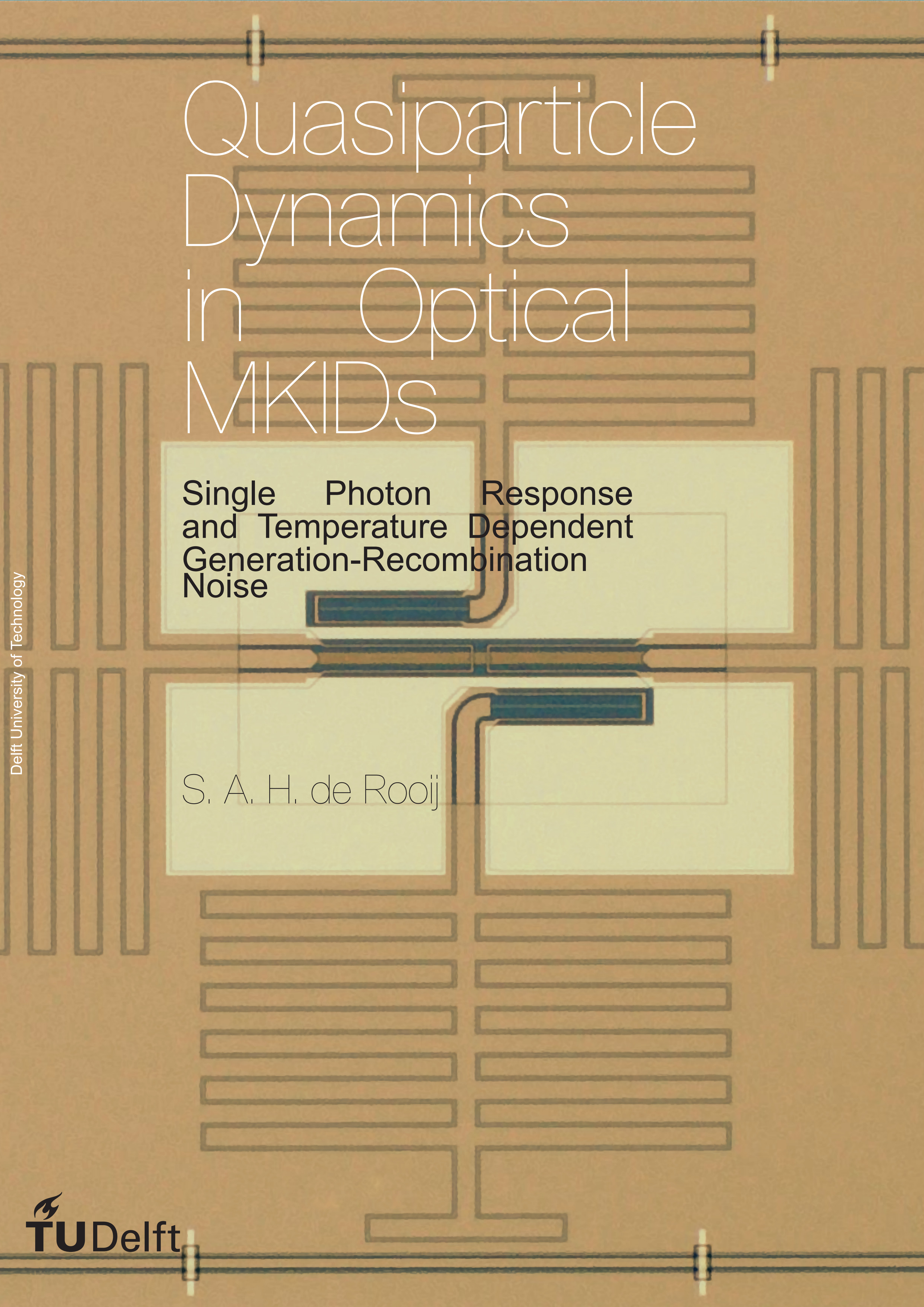

Quasiparticle Dynamics in Optical MKIDs

Single Photon Response and Temperature Dependent Generation-Recombination Noise

S. A. H. de Rooij

Delft University of Technology

Quasiparticle Dynamics in Optical MKIDs

Single Photon Response and Temperature Dependent Generation-Recombination Noise

by

S. A. H. de Rooij

to obtain the degree of Master of Science
at the Delft University of Technology,
to be defended publicly on Tuesday June 5, 2020 at 10:00 AM.

Student number:	4282760	
Project duration:	September 1, 2019 – June 5, 2020	
Thesis committee:	Dr. ir. P. J. de Visser,	SRON, daily supervisor
	Dr. A. Endo,	TU Delft, supervisor
	Prof. dr. ir. J. J. A. Baselmans,	SRON, TU Delft
	Prof. dr. G. A. Steele,	TU Delft

Cover image: microscope image of MKIDs on chip LT165, by courtesy of ing. D.J. Thoen

An electronic version of this thesis is available at `http://repository.tudelft.nl/`.

Preface

Nine months ago, I stood at the beginning of this master thesis project, enthusiastic to start a new, full-time deep-dive into something unknown to me. In my head, the applied physics knowledge was vivid, and the project management mindset from the Vattenfall Solar Team was fresh. I was more than ready to combine those two aspects into one large physics project.

Despite this enthusiasm and confidence, it became very clear to me that practising science requires more than just knowledge and a hands-on mindset. Already in the first few months of the project, I encountered obstacles that could not be overcome by opening another book or just trying harder. The critical question was not to proceed or not, but where to go. Which book to open, what to try and in which direction to move forward? I learnt that it is those kind of questions, that arise when you work on something new, something not already known, i.e. when practising science.

It is a messy, very non-linear process. Structuring it is hard, let alone long term planning. Having someone to share ideas with, discuss progress and help you in decisions, is therefore crucial. Pieter was exactly that person and I would like to thank him deeply for that. Thank you for introducing me to the field, for your inexhaustible source of ideas, for your patiences and thorough guidance. But most of all, thank you for showing me how you practise science.

Besides Pieter, I would like to thank the entire MKID-team at SRON and the TU Delft. The enthusiasm and critical mindset within the group is both motivating and inspiring. I also liked the daily work environment of the TeraHertz Sensing group very much, for which I would like to thank all its members. It is a pity that we can not enjoy each others company in these corona-crisis times.

In een wat bredere context, ter afsluiting van mijn studententijd, wil ik graag de Boze Mannen van de Raamstraat bedanken voor hun onbegrensde drang naar discussie, die ervoor gezorgd heeft dat mijn zweverige hoofd nog altijd met twee benen verbonden is met de grond. Daarnaast is ook dank voor mijn Gouden clubgenoten op zijn plaats. Dank voor jullie onredelijk vanzelfsprekende vriendschap. Nuna9 wil ik bedanken voor een onvergetelijk avontuur, maar nog meer voor het feit dat we een vriendengroep zijn geworden, ondanks (of misschien dankzij) alle stress die we moesten verduren.

Sarah, dankjewel voor je intensieve steun, vriendschap, gekkigheid en liefde.

Als laatste wil ik mijn familie bedanken. Pap, bedankt voor je steun en interesse in alles wat ik doe. Helen, bedankt dat je zo vanzelfsprekend een onderdeel van mijn leven bent. En mam, bedankt voor je onvoorwaardelijke steun en combinatie van verwondering en enthousiasme over wat ik dan ook maar vertel.

Steven de Rooij
Delft, June 2020

Abstract

Microwave Kinetic Inductance Detectors (MKIDs) are remarkable photon detectors, that have single photon detection and energy resolving capabilities in the near-infra red and higher frequency range. At lower frequencies, MKIDs are excellent radiation detectors as well, because of their high sensitivity and natural multiplexing capabilities, which enable large scale detector arrays.

In the (near) optical regime, MKIDs can use their single photon energy resolving capabilities for direct exoplanet detection, in missions like Hab-Ex [1] or LUVOIR [2]. This would enable atmospheric characterization, potentially finding habitual exoplanets. However, two aspects of the MKID still need improvement for this application [3]: the photon absorption efficiency must go from 30% to 50% and the resolving power must go from 8 to 100, both for wavelengths of 1 μm.

In this thesis, we study the single photon response and generation-recombination (GR) noise in optical NbTiN-Al hybrid MKIDs, to find knowledge gaps and opportunities to improve detector performance. For the single photon response, we set up a model starting from the Rothwarf-Taylor [4] and Mattis-Bardeen [5] equations, including the pair-breaking efficiency (η_{pb}) as only fit parameter. Both at high (220 mK and 250 mK) and low (120 mK) temperatures, the model predicted the single photon response of 4 different wavelengths correctly, with a fitted η_{pb} close to expected values (30%-70%), but somewhat high, which might be due to a non-thermal distribution of quasiparticles caused by read power [6]. In particular, the effect of phonon trapping was captured by the model, which was verified by considering MKIDs on substrate and membrane.

At lower temperatures (120 mK), a second exponential decay in both the amplitude and phase single photon pulse tail was observed, which is not explained by the model. This second decay was faster for higher read powers.

For the GR noise, also an unexpected feature was observed: the GR noise level dropped exponentially, when lowering temperature (<250 mK), for the amplitude, phase and cross power spectral densities (PSDs). High read powers mask this effect, due to the creation of excess quasiparticles [6, 7]. The noise drop was present in all analysed MKIDs, except for an MKID with an 150 nm (instead of 50 nm) thick Al film, which might be due to read power induced excess quasiparticles. When assuming the GR noise to be Poissonian, we show that the behaviour could be explained by a process which limits the quasiparticle lifetime, while keeping the quasiparticle density thermal.

We hypothesize the cause of both of these unpredicted measurements to be *quasiparticle trapping*, which is the localisation of quasiparticles. This process is known to degrade superconducting tunnel junction detectors [8] and limit quasiparticle lifetimes in MKIDs [9]. A secondary ion-mass spectroscopy (SIMS) analysis showed Fe contamination on the substrate-Al film interface, which is thought to be the quasiparticle trapping cause in our systems, consistent with the observation that increasing the film thickness diminishes the GR noise drop. To our knowledge, quasiparticle trapping has not be studied in steady state experiments, such as GR noise measurements.

Different models including quasiparticle trapping have been set up and can predict the amplitude PSDs, when assuming that trapped quasiparticles can not dissipate microwave power. However, comparison of the fitted model parameters with the trapping and detrapping rates calculated by Kozorezov et al.[10], showed a orders of magnitude difference. Combining this with the fact that amplitude, phase and cross PSDs show similar behaviour, implying that they relate to Cooper-pair fluctuations, led us to conclude that the trapping process can not be the cause of the observed behaviour. On-trap recombination most likely plays a role in the GR noise drop, but models including this process involve cyclic transitions and non-equilibrium steady states, greatly complicating the calculations. The second exponential decay could not be described by the trapping models, but also here on-trap recombination and Cooper-pair fluctuations must be considered.

A qualitative analysis on the MKID detector performance (both single photon and radiation power integration) showed that quasiparticle trapping effects can increase the energy resolving power and noise equivalent power at low temperatures, when this effect replaces the usual lifetime saturation due to excess quasiparticles [7].

Contents

1

Introduction

1.1. Motivation

The idea that light is made out of particles, was already advocated by the ancient Roman poet Lucretius in his *On the Nature of Things*, and remained the generally accepted picture until the seventeenth century, when René Descartes, Robert Hooke and Christiaan Huygens proposed that light is a wave. This started an active debate on the nature of light, as Isaac Newton still argued that light was composed of particles, because it only travelled in straight lines. In 1886, this debate seemed to be settled in favour of the wave-picture, by a combination of Maxwell's wave theory, which states that light is electromagnetic radiation, and a experiment by Heinrich Hertz, where radio waves were detected for the first time. However, at the end of the nineteenth century the debate started again, as Max Planck found that absorption or emission of energy in the form of radiation only take place in exact multiples of hf, where h is the Planck constant and f the light frequency. Albert Einstein subsequently proposed that radiation itself was made out of energy quanta that also have momentum. That implied that these quanta are particles, now called *photons*. In 1922, this was experimentally verified by Arthur Compton and the particle-wave debate on light was more alive than ever. Eventually, quantum mechanics settled this debate exactly in middle with the concept of particle-wave duality.

The ultimate proof of the particle nature of light is, of course, detecting it directly. In 1934, single photon detection became possible with the invention of photomultiplier tubes. Since then, many single photon detectors have been developed, such as the avalanche-photon detector (APD) or electron-multiplying CCDs, which are based on semiconductors. Superconductors are also used for single photon counting, for example in superconducting nano-wires (SNSPDs). Moreover, superconducting detectors are so sensitive that also the energy of the photon (i.e. colour) can be measured, such as in transition edge sensors (TES) and superconducting tunnel junctions (STJs). In the last two decades another energy resolving single photon detector has been developed: Microwave Kinetic Inductance Detectors (MKIDs), which we will study in this thesis. As an example, Figure 1.1 shows the detector response (measured in MKID phase) to an attenuated laser of four different colours ($E = hf = hc/\lambda$, with c the speed of light and λ the wavelength). The individual photons result in a detectable pulse, with a height proportional to the photon energy.

Since the first demonstration of MKID technology in 2003 [11], a wide range of applications has emerged, where astronomy is of particular interest. For lower energy radiation, such as terahertz, single photon detection is not possible (yet), but integrating the MKID signal over time still allows for very precise radiation measurements. Moreover, MKIDs are simple in design and have natural multiplexing capabilities, allowing for large scale photon detector arrays, needed for astronomical imaging [12].

For the low energy, terahertz regime, NIKA-2 is an instrument including almost 3000 MKIDs and was used recently in the IRAM 30 m telescope [13] in Spain, where it observed Pluto for testing purposes. Figure 1.2 shows the NIKA-2 instrument and the observation of Pluto.

DESHIMA (DEep Spectroscopic HIgh-redshift MApper, designed in Delft) is recently used on the ASTE (Atacama Submillimeter Telescope Experiment) telescope [14] in Chile. DESHIMA is a wide-band (332 GHz to 377 GHz) spectrometer that combines a 49-MKID array with an on-chip filterbank

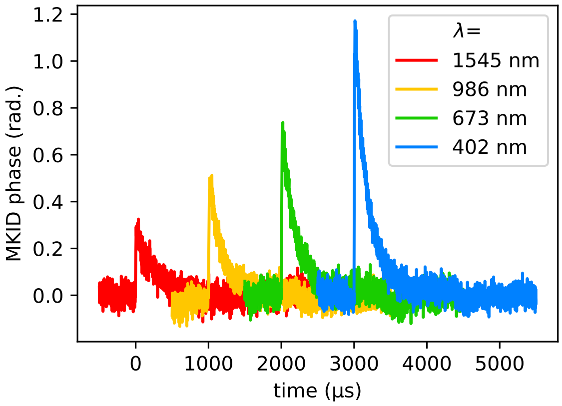

Figure 1.1: Single photon detection of four different photons, having different energies (see legend for their wavelengths). The pulses are from different time trace measurements and shifted to be 1 ms apart. Data is from LT139, KID6 at 220 mK and −96 dBm read power. See Chapter 2 for details.

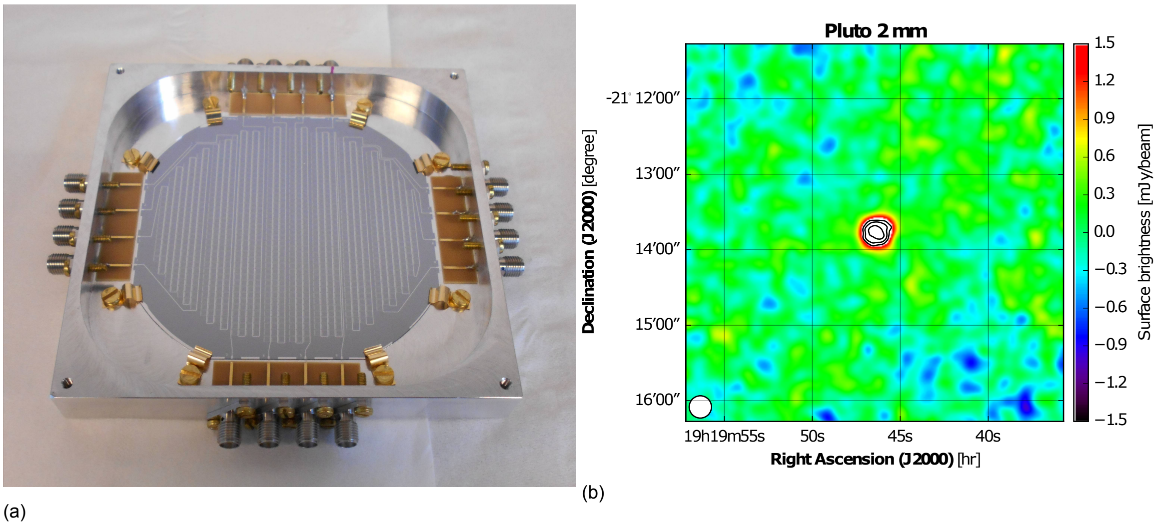

(a)

(b)

Figure 1.2: (a): Image of the front side of the NIKA-2 MKID array, with 16 connectors corresponding to 8 read lines. (b): Image of Pluto, measured with NIKA-2 on the IRAM 30 m telescope. Images are from [13].

[15] and is designed to observe distant galaxies, of which we can learn about the history of the cosmos.

For optical and near-infrared astronomy, the MKIDs high sensitivity offers the ability for direct imaging of exoplanets. In the Palomar Observatory of Caltech in California, DARKNESS (DARK-speckle Near-infrared Energy-resolving Superconducting Spectrophotometer) [16] is used for this purpose. However, it suffers from atmospheric distortion, as the observations are ground-based.
Space-based exoplanet observations, are planned by NASA (HabEx [1] and LUVOIR [2]) and recommended by Snellen et al. [17] to ESA. These missions open up the possibility of obtaining atmospheric spectra of exoplanets, as MKIDs have energy resolving capabilities at these wavelengths. Moreover, MKIDs have zero dark counts, which is necessary for these observations because the direct light coming from an exoplanet is very faint (in the order of photons per second). Potentially finding habitable exoplanets this way can eventually contribute to questions about the possibility of life outside of our solar system.

However, before MKIDs can be used for these missions, we are still faced with two challenges [3]. The first is the photon absorption efficiency, which is only about 30% for wavelengths of 1 μm, while at least 50% is needed for the 400 nm to 1.8 μm wavelength range. Furthermore, the energy resolution must be improved by about a factor 10. The resolving power, $R = \lambda/\Delta\lambda$, of the state of the art MKID detectors is about 8 at 1 μm (for example: [16, 18]), while $R = 100$ is needed.

1.2. MKID Operational Principle

The MKIDs working principle relies on the phenomenon of superconductivity. At low temperatures, below a critical temperature T_c (1.2 K for Al), the electrons in a metal pair up in so-called Cooper-pairs. The binding energy of such a Cooper-pair is called 2Δ and for conventional superconductor is given by $2\Delta = 3.52 k_B T_c$, where k_B is the Boltzmann constant [19]. This gives $\Delta = 180$ μeV for Al. This pairing gives rise to the superconducting phenomena, such as supercurrents (i.e. charge transport without resistance) and the Meissner effect (i.e. expulsion of magnetic fields inside superconductors). At non-zero temperature, not all electrons are paired in Cooper-pairs, but still some excitations exist. These excitations are electron-hole superpositions, or *quasiparticles*, with an energy $E \geq \Delta$ and behave like normal metal fermions.

In MKIDs, the superconductor is part of a microwave resonator. Through the use of a read out line, the resonator is driven at the resonance frequency, thus applying an AC field to the superconductor. The charge carriers in the superconducting material (Cooper-pairs and quasiparticles) get accelerated and decelerated by the changing field. Quasiparticles move with resistance, like in normal metals, and cause dissipation. The Cooper-pairs can however move without resistance and therefore get accelerated to the point where their inertia becomes significant. By acceleration or deceleration of the Cooper-pairs, kinetic energy is stored or extracted, which gives rise to *kinetic inductance*.

An incoming photon of energy $hf > 2\Delta$ can excite the superconductor by breaking Cooper-pairs, thus creating new quasiparticles. This causes two things to happen: the dissipation in the resonator goes up due to the extra quasiparticles and the kinetic inductance changes due to the broken Cooper-pairs. This process is illustrated in Figure 1.3 (a) and (b). The change in inductance results in a resonance frequency shift. This is illustrated in Figure 1.3 (c) as the resonance dips shift to the left, when incoming radiation increases. The dips also get wider and less deep, which is the result of more dissipation. When the input frequency to the read out line is constant, i.e. the original resonance frequency, the output of the read out line changes and the photon is detected. In normal operation, two variables are extracted from the MKID: amplitude, which is related to dissipation (i.e. dip width and depth, so quasiparticles) and phase, which is related to the inductance (i.e. resonance frequency, so Cooper-pairs). These variables are defined with respect to the MKID state without photon absorption and will be discussed in detail in the following chapter.
Optical photons have an energy in the range of electronvolts, which is typically orders of magnitude larger than Δ. Therefore, a few thousand quasiparticles are created when an optical photon is absorbed. As the amplitude and phase are proportional to the amount of created quasiparticles, the

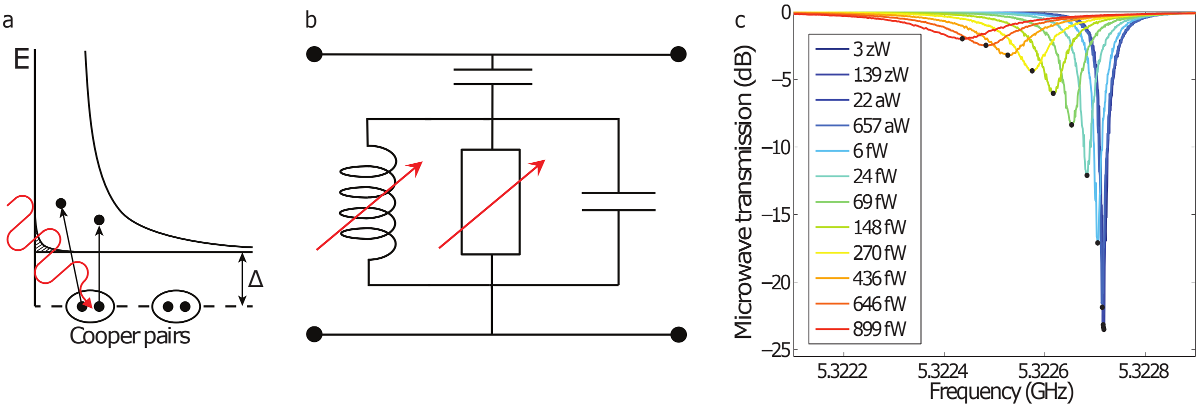

Figure 1.3: Schematics illustrating the MKID working principle. (a): A photon with energy $hf > 2\Delta$ breaks a Cooper-pair and creates two quasiparticles. (b): Simplified diagram of the MKID coupled to a read out line. The inductance and resistance of the MKID are variable, as these change upon photon absorption. (c): Frequency sweeps, measuring the resonance dip of the MKID at different incoming radiation powers at 1.54 THz. Images are from [20].

maximum value measured during the absorption of a single photon gives a measure for the photon energy, which is also seen in Figure 1.1. So, the relatively small value for Δ allows for the MKIDs energy resolving capabilities.

For a more detailed introduction to superconducting resonators and MKIDs, the reviews of Jonas Zmuidzinas [21] and Jochem Baselmans [22] are recommended. For a in-depth treatment of MKIDs, any one of the PhD theses from Pieter de Visser [20], Rami Barends [23] or Jiansong Gao [24] is recommended.

Quasiparticles lay at the heart of superconducting detectors (MKIDs, but also STJs, SNSPDs and TESs) and therefore a thorough understanding of their dynamics is crucial for further performance improvements. Also other superconductor applications can benefit from a better understanding of the behaviour of quasiparticles. For example, excess quasiparticles are a major source of relaxation and decoherence in several superconducting qubit implementations [25], yet their origin is unknown.

In thesis thesis, we will study the effects of quasiparticle-phonon interactions as well as the localisation of quasiparticles. We probe these dynamics via two measurements: single photon pulses, such as in Figure 1.1, and generation-recombination (GR) noise. In both measurements, we find deviations from standard MKID response theory, hypothesize on the origin of these deviations and discuss the impact on the detector performance.

1.3. Thesis Outline

In the following chapter, the MKID response to a single photon is discussed. First, the physics governing the MKID will be set out, with which a single photon response model is set up. After introducing the measurement setup and procedure, this model is compared to measurements and differences will be investigated and discussed. In particular, the pair-breaking efficiency (the ratio of the energy of the excess quasiparticles and the original photon energy) is obtained from the model as a fit parameter and compared to literature. Furthermore, a feature in the data at low temperatures, that is not explained by the model is discussed: a second exponential in the decay of the single photon excitation.

In Chapter 3, we will discuss the intrinsic noise in MKIDs: GR noise. Also here, we find an unexplained feature at low temperatures. The GR noise level decreases with decreasing temperature, where a constant level is expected. Below 170 mK the GR noise completely disappears in most chips.

Then, in Chapter 4 we will propose an explanation for the observed differences in models and measurements: quasiparticle trapping, i.e. the localisation of quasiparticles. We attribute this process to Fe contamination on the MKID-substrate interface. Different quasiparticle trapping models are explored and compared to experiment. Also the effect on the detector performance is discussed.

This thesis will end with conclusions along with recommendations for future work.

2

Single Photon Response

2.1. Introduction

As stated in the Introduction, the height of the single photon pulse is proportional to the energy of the incoming photon. Therefore, it can be used to determine the photon energy, after calibration. Calibration can, for example, be done with a laser which has a known, well-determined wavelength. Extracting the pulse height can simply be done by taking the maximum, of for example the MKID phase.
However, a more precise way to do it is to use a Wiener optimal filter, as used in [26] and described in more detail in [27] or [28]. Using this technique, a model pulse is calculated during calibration by averaging many single photon pulses, which were recorded during exposure to a laser with known wavelength. Then, the amplitude of a single pulse can be extracted by comparing its Fourier transform with the model spectrum, calculated by $AM(\omega) + N(\omega)$, where A is the wanted amplitude, $M(\omega)$ the Fourier transform of the model pulse and $N(\omega)$ the spectrum of the noise. This latter spectrum can be obtained from a time trace with no pulses in it.
Important to note here, is that the full single photon pulse is used to determine the amplitude. This is exactly why this method is more accurate than just taking the maximum of the pulse: it is less susceptible to noise.

The energy resolution (ΔE), or resolving power ($R = \lambda/\Delta\lambda$), is measured by making a histogram of the amplitudes and fitting a Gaussian distribution to it. A threshold for the amplitudes of different pulses in the histogram can be used to ensure that only direct photon absorption events are considered and indirect or other source energy absorption events are filtered out. An example of such a Gaussian fit is seen in Figure 2.1a. In this case, Mazin et al. [26] used the sum of two Gaussians, to ensure that the fit can follow part of the shoulder to the left as well. The calculate in R as the centre of the pulse (which relates to the photon energy of the laser) divided by the full width half maximum (FWHM) and is for this case 16 at $\lambda = 254$ nm.

With usage of a linear Wiener filter for the pulse amplitude, it is assumed that the individual single photon pulse shapes are not energy dependent. When the excess quasiparticles due to the incoming photon is small compared to thermal value, theory predicts a single exponential decay and justifies this assumption. However, at low temperatures (120 mK), we measure a non-single exponential decay, as illustrated in Figure 2.1b. Understanding this pulse shape, could lead to more accurate pulse models and therefore higher resolving power.
The goal of this chapter is to set out the physics underlying the MKID and with that, modelling the single photon response. This model will be compared with experimental data and deviations will be discussed.

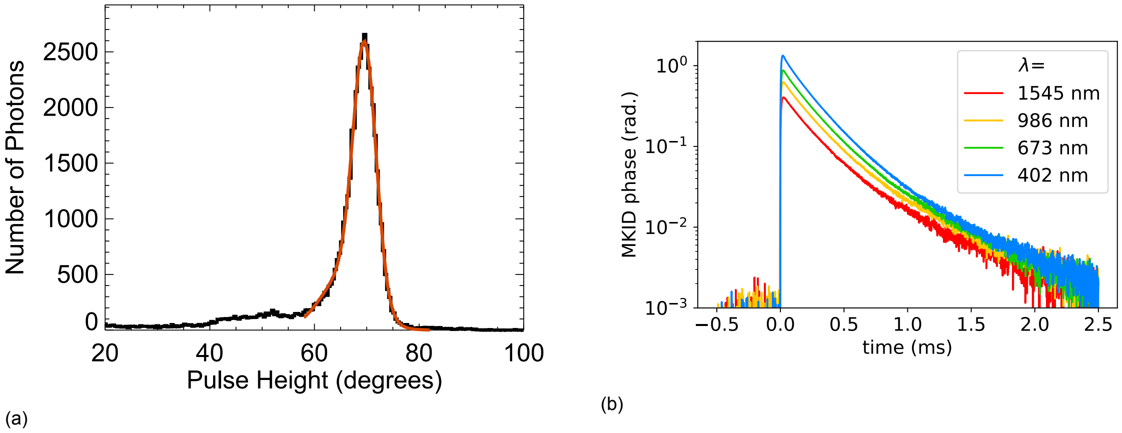

Figure 2.1: (a): Example of an histogram of pulse heights (amplitudes) (solid black) with a double Gaussian fit (red curve), showing a resolving power of $R = 16$ at $\lambda = 254$ nm. Figure from [26]. (b): Average single photon pulses from four different photon energies. Data taken at 120 mK, (Chip number LT139, KID1, P_{read} −96 dBm).

2.2. Theory: Single Photon Response Model

This section explains the theory of superconductivity needed for the single photon response model and sets out how this theory is implemented within the model. The first few subsections will cover the theoretical framework, and the following subsections will go into how the single photon response is calculated, including what parameters go into the model, how those are determined and what their sensitivity is. Lastly, some model validation and verification steps are described.

2.2.1. Superconductivity

The conventional theory of superconductivity is developed by Bardeen, Cooper and Schrieffer (BCS [29],[30]) in the late 1950's. Here, only the necessary aspects of this theory for this thesis will be addressed. For a more complete treatment, the book of Tinkham [19] (and specifically Chapter 3) is recommended.

The power of the BCS theory is the simplicity of the postulated picture of the electrons pairing up in so-called Cooper-pairs. Electrons with opposite spin and momentum have an attracting pairing potential, of energy 2Δ, which depends on the type of material. The origin of this attractive potential is a second order term in the phonon-electron interaction [19]. In the ground sate of a BSC superconductor all electrons are paired into Cooper-pairs. The Cooper-pairs are the charge carriers that cause the superconducting phenomena (e.g. current without resistance and the Meissner effect). This ground state can only exist in the limit of zero temperature ($T = 0$).

At non-zero temperatures, phonons are present in the superconductor and can break Cooper-pairs into two *quasiparticles*, when they have an energy of $\Omega \geq 2\Delta$. These quasiparticles both have a minimum energy of Δ, called the superconducting gap. The particles created in such a pair-breaking event are called quasiparticles because they are a superposition of a hole and an electron, but can be viewed as single fermionic particles. The opposite process of pair-breaking also takes place and is called recombination. As the temperature goes up, the density of quasiparticles goes up via,

$$n_{qp} = 4N_0 \int_0^\infty f(E;k_BT)N_s(E)dE = 4N_0 \int_\Delta^\infty \frac{f(E;k_BT)E}{\sqrt{E^2-\Delta^2}}dE, \tag{2.1}$$

where $f(E;k_BT)$ is the quasiparticle distribution, k_B is the Boltzmann constant and N_0 is the electron density of states at the Fermi level. $N_s(E) = \Re(E/\sqrt{E^2-\Delta^2})$ is the BSC normalised quasiparticle density of states. When the Fermi-Dirac distribution is used ($f_{FD}(E;k_BT) = 1/(\exp(E/k_BT)+1)$), and we consider low temperatures ($k_BT \ll \Delta$), n_{qp} can be approximated by [20],

$$n_{qp} \approx 2N_0\sqrt{2\pi k_BT\Delta}e^{-\Delta/k_BT}, \tag{2.2}$$

which reflects the exponential dependence of the quasiparticle density on temperature. The number of quasiparticles is given by $N_{qp} = Vn_{qp}$, where V is the superconductor volume.

As the presence of quasiparticles influences the electron-phonon interaction, the pairing potential Δ is temperature dependent. The BSC implicit expression,

$$\frac{1}{N_0 V_{sc}} = \int_{\Delta(T)}^{\Omega_D} \frac{1 - 2f(E; k_B T)}{\sqrt{E^2 - \Delta^2(T)}} dE, \tag{2.3}$$

gives an opportunity to calculate $\Delta(T)$ numerically. Here, V_{sc} is the potential energy describing the phonon-electron interaction and Ω_D is the Debye energy. V_{sc} is assumed to be isotropic and constant, up to the Debye energy, after which it is zero. This is called the BSC approximation, which is valid in the weak coupling regime, $\Delta \ll \Omega_D$, or $N_0 V_{sc} \ll 1$ [31].
As the temperature goes up, more quasiparticles will be present and the superconducting gap will be lowered, up to a point where it becomes zero. This point fixes a temperature, called the *critical* temperature (T_c), as $\Delta(T_c) = 0$. When we take $f(E; k_B T)$ to be the Fermi-Dirac distribution, set $T \rightarrow 0$, and assume $\Omega_D \gg k_B T_c$, Equation (2.3) reduces the well-known BSC relation $2\Delta_0 = 3.528 k_B T_c$, where Δ_0 is the superconducting gap at $T = 0$.

Because of the role of the superconductor in the MKID, we are interested what happens to the superconductor when an alternating electric field is applied to it, i.e. the AC response. In extension to Ohm's law, $\mathbf{j} = \sigma \mathbf{E}$, one can define a *complex conductivity*, $\sigma = \sigma_1 - j\sigma_2$. Here, σ_1 describes the dissipative part of the conductivity (via quasiparticles) and the imaginary part, σ_2, describes the response of the Cooper-pairs, which is inductive. This inductivity originates from the inertia of Cooper-pairs and is therefore called *kinetic inductance*.
Mattis and Bardeen [5] have calculated the complex conductivity with the microscopic BSC theory, in the local limit and the extreme anomalous limit, as,

$$\begin{aligned} \frac{\sigma_1}{\sigma_N} &= \frac{2}{\hbar\omega} \int_{\Delta}^{\infty} \frac{(f(E) - f(E + \hbar\omega))(E^2 + \Delta^2 + \hbar\omega E)}{\sqrt{(E^2 - \Delta^2)((E + \hbar\omega)^2 - \Delta^2)}} dE \\ &+ \frac{1}{\hbar\omega} \int_{min(\Delta - \hbar\omega, -\Delta)}^{-\Delta} \frac{(1 - 2f(E + \hbar\omega))(E^2 + \Delta^2 + \hbar\omega E)}{\sqrt{(E^2 - \Delta^2)((E + \hbar\omega)^2 - \Delta^2)}} dE \qquad (2.4a) \\ \frac{\sigma_2}{\sigma_N} &= \frac{1}{\hbar\omega} \int_{max(\Delta - \hbar\omega, -\Delta)}^{\Delta} \frac{(1 - 2f(E + \hbar\omega))(E^2 + \Delta^2 + \hbar\omega E)}{\sqrt{(\Delta^2 - E^2)((E + \hbar\omega)^2 - \Delta^2)}} dE. \qquad (2.4b) \end{aligned}$$

Here, σ_N is the normal state conductivity, $\hbar$ is the reduced Planck's constant and ω is the AC angular frequency. Note that the second integral in Equation (2.4a) only contributes when $\hbar\omega > 2\Delta$ and describes the process of pair-breaking by incoming radiation. The first integral in Equation (2.4a) describes the radiation absorption by quasiparticles.
To understand the limits in which these equations hold, we have to look at the length scales that determine the superconductor behaviour. Three length scales are important:

l: the mean free path of electrons. This is the average length that conduction electrons in the (non-superconducting) metal can travel, without scattering. As it says something about the resistance the electrons feel, it is not surprising that the normal state conductivity is proportional to this length ($\sigma_N \propto l$) [32, 33]. When thickness of the superconductor (d) is smaller than l, d becomes the limiting scattering length scale.

ξ_0: the BCS coherence length or 'size' of the Cooper-pair state. It is given by $\xi_0 = \hbar v_F / \pi\Delta_0$ [30], where v_F is the Fermi velocity. The coherence length is a measure for the length scale at which phenomena get a non-local character, and the word Cooper-pair 'size' is to be understood in that sense.

λ: the penetration depth of the magnetic field (not to be confused with the photon wavelength). First proposed by the London brothers [34] to explain the Meissner effect, λ is the exponential decay constant at which the magnetic field is expelled from the superconductor and is therefore called the penetration depth.

The mean free path and BCS coherence length both limit the non-local length scale, meaning we can define an effective coherence length, $1/\xi = 1/\xi_0 + 1/l$. The case in which $l \gg \xi_0$, and thus $\xi = \xi_0$ is

called the clean limit and analogous, $l \ll \xi_0$ or $\xi = l$, is called the dirty (or local) limit. In the latter case, the mean free path of the electrons limits the length scale of the non-local response.
This length scale should be compared to the penetration depth, λ, to determine if the response is local or non-local. So, when $\lambda \gg \xi$, the response is local and vice versa. The clean, non-local limit ($l \gg \xi_0$ and $\lambda \ll \xi_0$) is also called the extreme anomalous limit [20]. So, the Mattis-Bardeen equations are valid when either $l \ll \xi_0$ or $l \gg \xi_0$ and $\lambda \ll \xi_0$.
In this thesis, we study Al thin films (<150 nm) as our superconductor. As the coherence length in Al is about 1.3 µm [35], we are in the dirty limit, and the Mattis-Bardeen equations are valid.

2.2.2. Quasiparticle Dynamics

Now we know the essentials of superconducting theory to describe the MKIDs behaviour, we will focus on what actually determines the response of the MKID over time. This subsection will cover the basics needed to model the quasiparticle dynamics. The next section will cover how quasiparticles result in a response and what actually is measured in the MKID.

We will start from the master equation approach, first proposed by Rothwarf and Taylor [4]. They set up rate equations for the number of quasiparticles (N_{qp}) and phonons (N_ω) in a system without external energy deposition, in de following way,

$$\frac{dN_{qp}}{dt} = -\frac{RN_{qp}^2}{V} + 2\Gamma_B N_\omega, \tag{2.5a}$$

$$\frac{dN_\omega}{dt} = \frac{RN_{qp}^2}{2V} - \Gamma_B N_\omega - \Gamma_{es}(N_\omega - N_\omega^T). \tag{2.5b}$$

Here, V is the superconductor volume, $\Gamma_B = 1/\tau_{pb}$ is the pair breaking rate, $\Gamma_{es} = 1/\tau_{esc}$ the phonon escape rate and N_ω^T is the thermal equilibrium number of phonons in the superconductor. R is the recombination constant. Note that N_ω is the number of *pair-breaking* phonons, which means they have an energy $\Omega \geq 2\Delta$. Phonons with lower energy do not play a role in the quasiparticle dynamics. The steady state solution of these rate equations is,

$$N_{qp}^0 = \sqrt{\frac{2V\Gamma_B N_\omega^T}{R}}, \tag{2.6a}$$

$$N_\omega^0 = N_\omega^T. \tag{2.6b}$$

The first terms in both Equations (2.5a) and (2.5b) describe quasiparticle recombination, where two quasiparticles disappear (form a Cooper-pair) and one pair-breaking phonon is created. As quasiparticles recombine in pairs, this goes like $N_{qp}^2/2$ which is the number of ways to make pairs. If we disregard the other term in Equation (2.5a), which is valid when recombination is dominant, for example just after a large ($\delta N_{qp} \gg N_{qp}^0$) energy deposition, we can see that the general solution is of the form,

$$N_{qp}(t) = N_{qp}(0)\frac{V/R}{tN_{qp}(0) + V/R}, \tag{2.7}$$

where $N_{qp}(0)$ is the number of quasiparticles at $t = 0$. That means, that right after such a large energy deposition, N_{qp} behaves like $\propto 1/t$. On the other hand, when N_{qp} is close to equilibrium (still ignoring pair-breaking), we can linearise the first term ($N_{qp} = N_{qp}^0 + \delta N_{qp}$,so that $N_{qp}^2 \approx (N_{qp}^0)^2 + 2N_{qp}^0\delta N_{qp}$) and focus on deviations from equilibrium (δN_{qp}). In that way, we see $\delta N_{qp} \propto e^{-2t/\tau_{qp}}$, where $1/\tau_{qp} = \Gamma_R = RN_{qp}^0/V$. So, close to equilibrium, δN_{qp} exponentially decays with a time constant $\tau_{qp}/2$. The factor 2 appearing here denotes that τ_{qp} is the *single* particle lifetime, so that the bulk number δN_{qp} goes down with twice this rate. Kaplan et al. [36] calculated this quasiparticle lifetime for a thermal (Fermi-Dirac) quasiparticle distribution function low temperature ($T << T_c$) and for a quasiparticle of energy Δ to be,

$$\tau_{qp} = \frac{\tau_0}{\sqrt{\pi}}\left(\frac{k_BT_c}{2\Delta}\right)^{5/2}\sqrt{\frac{T_c}{T}}e^{\Delta/k_BT} = \frac{V\tau_0}{N_{qp}^0}\frac{N_0(k_BT_c)^3}{2\Delta^2}, \tag{2.8}$$

where τ_0 is the electron-phonon interaction time, which is a material parameter. In the second equality, Equation (2.2) is used. Note that for low temperatures, scattering is the dominant process for quasiparticles [36]. Therefore, the quasiparticles will quickly lose their energy in the form of phonons, until they reach superconducting energy gap, Δ. This justifies the choice for τ_{qp} at $E = \Delta$. With this expression, we can find R to be [31, 37],

$$R = \frac{V}{\tau_{qp} N_{qp}^0} = \left(\frac{2\Delta}{k_B T_c}\right)^3 \frac{1}{4\Delta N_0 \tau_0}. \tag{2.9}$$

The second term in Equation (2.5) describe pair-breaking events, where 2 quasiparticles are created and one phonon disappears. Kaplan et al. [36] also calculated phonon scattering and lifetimes for different materials. They show that for low temperatures, pair-breaking is the dominant phonon process. The last term in Equation (2.5b) describes phonon escape to (or inflow from, when $N_\omega^T > N_\omega$) a large phonon bath. This rate depends on superconductor and bath material and geometries. In Ref. [38] Steven B. Kaplan calculated film-substrate transparencies, η_{ph}, for various materials, which captures the material dependencies. For film thickness $d \gtrapprox \Lambda$, where Λ is the phonon mean free path against pair-breaking (approximately a few 100 nm for Al), the escape time is given by,

$$\tau_{esc} \approx \frac{4d}{\eta_{ph} v_{ph}}, \tag{2.10}$$

with v_{ph} being the average phonon velocity.

One important aspect of these equations we did not touch upon yet is *phonon trapping*, introduced by Rothwarf and Taylor [4]. It describes the event where a recombination process emits a 2Δ-phonon which afterwards breaks a pair. In other words, now we do not disregarding the phonon terms in Equation (2.5). Because the recombination process itself emits pair-breaking phonons, the overall δN_{qp} decay rate is lowered with a certain factor called the *phonon trapping factor*. Not surprisingly, this factor depends on the ratio of τ_{esc} and τ_{pb}. To see how exactly this factor comes in, we add an injection term (I) to the Rothwarf-Taylor equations:

$$\frac{dN_{qp}}{dt} = -\frac{RN_{qp}^2}{V} + 2\Gamma_B N_\omega + I, \tag{2.11a}$$

$$\frac{dN_\omega}{dt} = \frac{RN_{qp}^2}{2V} - \Gamma_B N_\omega - \Gamma_{es}(N_\omega - N_\omega^T), \tag{2.11b}$$

so that the new steady state values become:

$$N_\omega^0 = \frac{I}{2\Gamma_{es}} + N_\omega^T, \tag{2.12a}$$

$$N_{qp}^0 = \sqrt{\frac{V(1+\Gamma_B/\Gamma_{es})}{R} I + \frac{2V\Gamma_B N_\omega^T}{R}} = \sqrt{\frac{V(1+\Gamma_B/\Gamma_{es})}{R} I + (N_{qp}^T)^2}, \tag{2.12b}$$

where we defined N_{qp}^T as Equation (2.6a). Now, assuming I to be small ($\delta N_{qp} \ll N_{qp}^T$), we expand to first order and look at $\delta N_{qp} = N_{qp}^0 - N_{qp}^T$. We find,

$$\delta N_{qp} = \frac{V}{2RN_{qp}^T}\left(1 + \frac{\Gamma_B}{\Gamma_{es}}\right) I = \tau_{qp}^* I, \tag{2.13}$$

where we defined the *apparent* quasiparticle lifetime to be,

$$\tau_{qp}^* = \delta N_{qp}/I = \tau_{qp}(1 + \tau_{esc}/\tau_{pb})/2. \tag{2.14}$$

So, τ_{qp}^* includes the factor 2 from pair-wise recombination - that in this derivation formally arises from the linearisation, like in [37] - as well as the phonon trapping factor $(1 + \tau_{esc}/\tau_{pb})$.

2.2.3. MKID Model: From Quasiparticles to Amplitude and Phase

Now we know the basics of superconductivity and how the quasiparticles behave, it is time to see how the superconductor is used as a detector. An incoming photon breaks a certain amount of Cooper-pairs and creates thus twice as many quasiparticles (δN_{qp}) on top of the thermal level (N_{qp}^{T}). Via the Rothwarf-Taylor equations, Equation (2.5), we can numerically solve for the quasiparticle number over time ($N_{qp}(t)$). This subsection will go into how we can translate $N_{qp}(t)$ into the measured quantities amplitude (δA) and phase (θ), to predict the actual MKID response upon a single photon absorption. For a more detailed treatment see References [20, 23, 24].

As mentioned, the detector works on the principle of kinetic inductance, which is the inductance of a superconductor induced by the inertia of the Cooper-pairs. A change in number of Cooper-pairs (and quasiparticles), changes the inductance (and resistance) in the superconductor which can be measured. To translate the δN_{qp} into a change in σ, we use Equation (2.1), with the Fermi-Dirac distribution to define an effective quasiparticle temperature (T_{qp}^{eff}). We then use Equation (2.4) with $f(E) = f_{FD}(E; k_B T_{qp}^{eff})$ to calculate (σ_1, σ_2). This approach is justified by Gao et al. [39], who showed that a change in complex conductivity due to a temperature change is equivalent to a change due to external pair-breaking. This is experimentally verified in References [39, 40].
The effect of a complex conductivity in a circuit is captured by the *surface impedance*: $Z_s = R_s + jX_s = R_s + j\omega L_s$, where R_s is the surface resistance, X_s is the surface reactance and L_s is the surface inductance. In the dirty limit, this is given by [41]:

$$Z_s = \sqrt{\frac{j\mu_0\omega}{\sigma_1 - j\sigma_2}} \coth\left(\frac{d}{\lambda}\sqrt{1 + j\frac{\sigma_1}{\sigma_2}}\right), \tag{2.15}$$

where μ_0 is the magnetic permeability of vacuum. For low temperatures, $\sigma_2 \gg \sigma_1$, because the number of quasiparticles are exponentially low (Equation (2.2)). The kinetic inductance (due to Cooper-pairs) is thus much higher than the resistivity. This makes that we can approximate the resistance and inductance by [23],

$$R_s = \mu_0\omega\frac{\sigma_1}{2\sigma_2}\beta\lambda\coth\left(\frac{d}{\lambda}\right) \tag{2.16a}$$

$$L_s = \mu_0\lambda\coth\left(\frac{d}{\lambda}\right), \tag{2.16b}$$

where $\beta = 1 + \frac{2d/\lambda}{\sinh 2d/\lambda}$, which is 1 in the bulk limit and 2 in the thin film limit. Note that the penetration depth, λ, is dependent on σ_2, and in the low temperature limit ($\sigma_2 \gg \sigma_1$) is given by $\lambda = 1/\sqrt{\mu_0\omega\sigma_2}$ [42]. The temperature dependence of λ, can be calculated by the BCS expression [19],

$$\frac{\lambda(T)}{\lambda(0)} = \left(\frac{\Delta(T)}{\Delta(0)}\tanh\left(\frac{\Delta(T)}{2k_BT}\right)\right)^{-1/2}, \tag{2.17}$$

where $\lambda(0)$ is the penetration depth at zero temperature.

With these expressions for the superconducting element, we can predict how it behaves in a microwave circuit. In an MKID, the superconductor is part of an LC-resonator circuit where it plays the role of (kinetic) inductor and resistance. Knowing that, we can predict how the resonance frequency and quality factor (a measure for the resonator losses) are influenced, when the complex conductivity of the superconductor (σ_1, σ_2) changes, due to a change in quasiparticles.
The internal quality factor is given by [23],

$$Q_i = \frac{\omega L}{R} = \frac{1}{\alpha_k}\frac{\omega L_s}{R_s} = \frac{2}{\alpha_k\beta}\frac{\sigma_2}{\sigma_1}, \tag{2.18}$$

where α_k is the *kinetic induction fraction*, given by $\alpha_k = L_s/L$, where L is the total inductance in the circuit and L_s is the sheet inductance only caused Cooper-pairs (i.e. the kinetic inductance). The higher

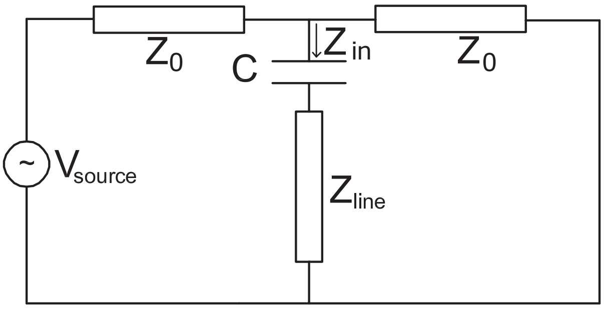

Figure 2.2: Representation of the microwave circuit, used to model its response. The top line represents the feedline to the resonator, with impedance Z_0. The resonator is coupled to the feedline with a coupler C, and the superconducting resonator itself is Z_{line}, which consists of a NbTiN capacitive part and an Al (kinetic) inductance part. The feedline 'sees' a combined impedance of Z_{in}. Diagram from [20]

this internal quality factor, the less energy is lost in resonator due to quasiparticles. Upon a change in σ, we have,

$$\delta\left(\frac{1}{Q_i}\right) = \frac{\alpha_k \beta}{2}\left(\frac{\delta\sigma_1}{\sigma_2} - \frac{\sigma_1 \delta\sigma_2}{\sigma_2^2}\right) \approx \frac{\alpha_k \beta}{2}\frac{\delta\sigma_1}{\sigma_2}, \tag{2.19}$$

where we used the low temperature limit, $\sigma_2 \gg \sigma_1$ and $\delta\sigma_1 \gg \delta\sigma_2$ (see for example [20, sec. 2.2]), in the last approximation.

For the resonance frequency of the circuit we know $\omega_0 \propto 1/\sqrt{LC}$. Therefore, we can infer (with Equation (2.16), [20]),

$$\frac{\delta\omega_0}{\omega_0} = \frac{\alpha_k \beta}{4}\frac{\delta\sigma_2}{\sigma_2}, \tag{2.20}$$

where we take the σ_2-dependence of λ into account.

Now we will discuss how the MKID measurable quantities are influenced. The circuit used for this analysis is seen in Figure 2.2. The resonator is represented by Z_{line} which is capacitively coupled to the feedline, with impedance Z_0. In this thesis, *hybrid* MKIDs are considered, because of the better noise characteristics [24, Sec. 5.6]. These are MKIDs with a lower gap superconductor (Al: 180 µeV) acting as the sensor and a higher gap superconductor (NbTiN, 2.1 meV) acting as a capacitive part. The quasiparticles in the Al-section can not transport to the NbTiN section, as this is a higher gap superconductor [24, Sec. 4.4]. For a calculation of Z_{in}/Z_0 see [20],[43] or [23]. Considering Figure 2.2, we can find from [44] that the *forward transmission* is given by,

$$S_{21} = \frac{2}{2 + Z_0/Z_{in}} = \frac{Q/Q_i + 2jQ\frac{\delta\omega}{\omega_0}}{1 + 2jQ\frac{\delta\omega}{\omega_0}}, \tag{2.21}$$

where Q is the loaded quality factor $1/Q = 1/Q_i + 1/Q_c$, with Q_c the coupling quality factor. $\delta\omega$ is the difference of driving frequency with the resonance frequency: $\delta\omega = \omega_{read} - \omega_0$.

This (complex) quantity S_{21} is measured in the setup at frequency ω_{read}. When the complex conductivity is constant (constant temperature and no energy depositions in the MKID), Equation (2.21) traces out a circle in the complex S_{21}-plane when the driving frequency (ω_{read}) is scanned. This is illustrated in Figure 2.3 as the red dots. Note that from Equation (2.21), we see that the most right point in the S_{21}-plane is $(1, 0)$ and the most left point is Q/Q_i, which we call S_{21}^{min}. That makes that the centre point of the circle is $x_c = (S_{21}^{min} + 1)/2$.

Now assuming an incoming photon, the complex conductivity changes. Therefore, Q_i and ω_0 change via Equations (2.19) and (2.20), respectively, which changes S_{21}. Keeping ω_{read} constant, a single photon response will look like the blue dots in Figure 2.3. Two things happen here: (1) a change in Q-factor, which lowers the radius of the resonance circle and (2) a change in resonance frequency which turns the resonance circle. We describe these changes by an amplitude A and phase θ, respectively.

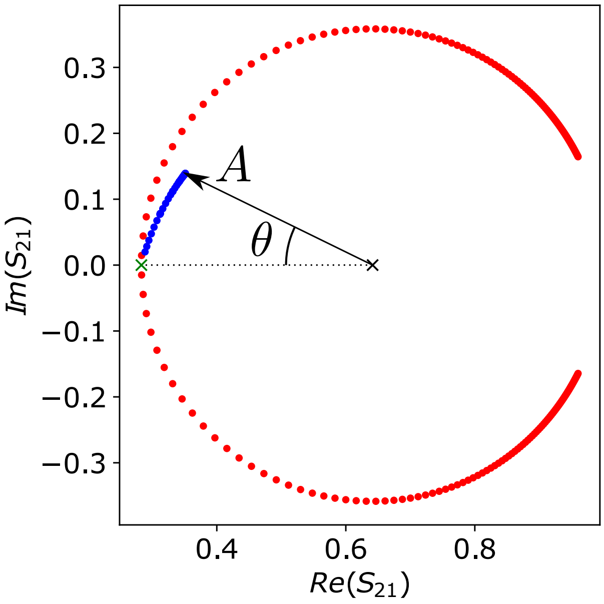

Figure 2.3: Simulated MKID response with resonance circle (red dots) and a single photon response at constant read frequency equal to the resonance frequency (blue dots). S_{21}^{min} is indicated by a green cross and x_c is indicated by a black cross. Amplitude and phase are visualised as well.

Defining amplitude and phase this way, we see that we get the following expressions,

$$A = \frac{\sqrt{(\Re(S_{21}) - x_c)^2 + \Im(S_{21})^2}}{1 - x_c}, \tag{2.22a}$$

$$\theta = \arctan\left(\frac{\Im(S_{21})}{x_c - \Re(S_{21})}\right). \tag{2.22b}$$

To see how the amplitude and phase are linked to a change in Q-factor and ω_0, it is instructive to note that from Equation (2.21),

$$|S_{21}|^2 = \frac{(Q/Q_i)^2 + 4Q^2\left(\frac{\delta\omega}{\omega_0}\right)^2}{1 + 4Q^2\left(\frac{\delta\omega}{\omega_0}\right)^2} \tag{2.23a}$$

$$\Re(S_{21}) = \frac{Q/Q_i + 4Q^2\left(\frac{\delta\omega}{\omega_0}\right)^2}{1 + 4Q^2\left(\frac{\delta\omega}{\omega_0}\right)^2} \approx \frac{Q}{Q_i}, \tag{2.23b}$$

$$\Im(S_{21}) = \frac{2Q\frac{\delta\omega}{\omega_0}(1 - Q/Q_i)}{1 + 4Q^2\left(\frac{\delta\omega}{\omega_0}\right)^2} \approx 2Q\frac{\delta\omega}{\omega_0}(1 - Q/Q_i), \tag{2.23c}$$

where the approximation is to first non-zero order in $\delta\omega/\omega_0$. From Equation (2.23b), we can also see that,

$$\delta\Re(S_{21}) = -\frac{Q_c Q_i}{(Q_c + Q_i)^2}\frac{\delta Q_i}{Q_i}, \tag{2.24}$$

where the delta denotes a change in Q_i. Note that only first order changes in both Q_i and $\delta\omega/\omega_0$ are taken into account. With that, and with $\delta A = 1 - A$ and $\tan(\theta) \approx \theta$ we find,

$$\delta A \approx \frac{2Q}{Q_i}\frac{\delta Q_i}{Q_i} = -2Q\delta\left(\frac{1}{Q_i}\right), \tag{2.25a}$$

$$\theta \approx 4Q\frac{\delta\omega}{\omega_0}. \tag{2.25b}$$

From these equations, it is clear that amplitude (mostly) probes the change in quality factor and thus changes in σ_1 see Equation (2.19), caused by quasiparticles. The phase mainly probes the change in resonance frequency and thus changes in inductivity, see Equation (2.20), caused by Cooper-pairs. In summary:

$$\delta A \rightarrow \delta Q_i \rightarrow \delta\sigma_1 \rightarrow \delta N_{qp}$$
$$\theta \rightarrow \delta\omega_0 \rightarrow \delta\sigma_2 \rightarrow \delta N_{CP}$$

Combining Equations (2.25a) and (2.25b) and Equations (2.19) and (2.20) we get,

$$\delta A = \alpha_k \beta Q \frac{\delta\sigma_1}{\sigma_2}, \tag{2.26a}$$
$$\theta = -\alpha_k \beta Q \frac{\delta\sigma_2}{\sigma_2}. \tag{2.26b}$$

Note that here $\delta\omega_0 = \omega_0^{new} - \omega_0^{old} = \omega_0 - \omega_{read} = -\delta\omega$. From these equations, we can derive [20, 23],

$$\frac{dA}{dN_{qp}} = -\frac{\alpha_k \beta Q}{|\sigma| V}\frac{d\sigma_1}{dn_{qp}}, \tag{2.27a}$$
$$\frac{d\theta}{dN_{qp}} = -\frac{\alpha_k \beta Q}{|\sigma| V}\frac{d\sigma_2}{dn_{qp}}. \tag{2.27b}$$

Here, the changes in amplitude and phase are to first order in complex conductivity. Also, $|\sigma| \approx \sigma_2$ is assumed, which is valid for low temperatures. These equations show that the responsivity of an MKID is (partly) determined by $\alpha_k\beta Q/|\sigma|V$ and can give guidance for the design of the detectors.

The following will explain the implementation of these equations in an MKID model, which is set up to predict the single photon response. The following gives an overview of the calculation steps, as it is coded.

1. The MKID simulation is initialised with parameters describing the superconducting state and MKID design. The superconducting state parameters include the effective quasiparticle temperature T, T_D, τ_0, τ_{pb}, $\lambda(0)$, N_0 and T_c and the design parameters include V,d,Q_c,α_k,τ_{esc},η_{pb} and (ω_0, T_0) which is the angular resonance frequency at a certain bath temperature T_0. The next section will go into how these parameters are determined.

2. The resonance frequency is calculated at this quasiparticle temperature, T, and the read frequency, ω_{read}, is set to this value. This is done via Equation (2.20), where the input pair (ω_0, T_0) gives the reference point $(\omega_0, \sigma_{2,0})$. Note that σ_2 is also dependent on the ω_{read}, see Equation (2.4). That means that when the read frequency is changed, also the resonance frequency changes. Therefore, the determination of ω_{read} is done iteratively.

3. The Rothwarf-Taylor equations, Equation (2.5), are numerically solved with the initial conditions given by,

   $$N_{qp}^{ini} = N_{qp}^0 + \eta_{pb}\frac{hf}{\Delta}, \tag{2.28a}$$
   $$N_{\omega}^{ini} = N_{\omega}^T = \frac{R(N_{qp}^0)^2\tau_{pb}}{2V}, \tag{2.28b}$$

   where N_{qp}^0 is calculated via Equation (2.1), R is given by Equation (2.9), and Δ is given by Equation (2.3) at temperature T. f is the frequency of the incoming photon.
   Here we assume that the quasiparticle generation is instantaneous, where in fact the deposited energy needs to be downconverted to the quasiparticle system.
   This downconversion process can be divided into three stages: (1) the photoelectron energy is downconverted via strong interacting electrons and holes (2) electron-phonon interactions become dominant and downconversion takes place via phonons as well and (3) quasiparticle-phonon interactions thermalize the quasiparticle distribution [45]. The first and second stages

are extremely fast (total of a few ns), compared to the third stage (of the order of quasiparticle lifetimes), which justifies our assumption. The third stage is described by Equation (2.5).
In the second stage, (high energy) phonon escape from the Al film, results in a photon-quasiparticles energy conversion efficiency of less than one. This is captured by η_{pb} in Equation (2.28) and is called the pair-breaking efficiency. Guruswamy et al. [33] calculated η_{pb} for different escape times and photon energies, and concluded that it was limited by about 59%.

4. To model the rise time of the single photon pulse, $N_{qp}(t)$ is adjusted in the following way. $\delta N_{qp}(t)$ is convolved with $A\exp(-t/\tau_{res})$, where A is a normalisation factor and $\tau_{res} = \frac{2Q}{\omega_0}$, the resonator ring time [46]. τ_{res} is in the order of microseconds for the MKIDs studied, $N_{qp}(t)$ is then given by $N_{qp}(t) = \delta\tilde{N}_{qp}(t) + N^0_{qp}$, where $\delta\tilde{N}_{qp}(t)$ is the convolved number of excess quasiparticles. Note that this is an artificial way to simulated the resonator response, as quasiparticle generation through energy deposition is very fast [45], as explained in the previous step.

5. $N_{qp}(t)$, is then translated to $\delta A(t)$ and $\theta(t)$ by doing the following for every time step:
   (a) an effective quasiparticle temperature T_{eff} is calculated iteratively with Equation (2.1);
   (b) Δ is calculated via Equation (2.3);
   (c) σ is calculated via Equation (2.4);
   (d) a new resonance frequency ω_0 and internal quality factor Q_i are calculated with Equations (2.18) and (2.20). Here, also a new β is calculated with the temperature dependent λ, see Equation (2.17);
   (e) S_{21} is calculated via Equation (2.21), where ω_{read} is kept constant and
   (f) lastly, $\delta A = 1 - A$ and θ are calculated with Equation (2.22).

   This gives the final output of the model: $\delta A(t)$ and $\theta(t)$.

2.2.4. Model Parameters

This section will go into what parameters are used, how they are determined and finally how sensitive the model is for each parameter. The parameters are divided into two categories: superconductor parameters, which define the superconducting state and design parameters, which are set by the design of the MKID. The natural units for the model are chosen to be: µeV, µs and µm.

Several parameters are determined from an S_{21}-*measurement* on the MKID that is performed to characterize it. In this measurement, the S_{21}-parameter is measured via a frequency sweep, such as the red circle in Figure 2.3. This is repeated for different temperatures, typically ranging from 100 mK to 420 mK. It is also repeated for different read powers P_{read}, which is the power that goes through the feedline (top line of Figure 2.2). In Figure 2.4, an example of an S_{21}-measurement, for one P_{read} is shown. The measurements of the resonance dips ($|S_{21}|$) give an opportunity to fit Equation (2.23a), and extract the resonance frequency and Q_i and Q_c factors at that temperature. We initialize the MKID simulation with the measured characteristics from the S_{21}-measurement at the same P_{read} at which the pulse measurements are done. In this way, it is possible to account for read power effects, like microwave excess quasiparticle generation [7] or redistribution of quasiparticles due to the read signal [6, 47], without explicitly including these effects in the model.

Superconductor Parameters

k_BT is the quasiparticle temperature, multiplied by the Boltzmann constant, which is 86.17 µeV K^{-1}. This is not chosen as the bath (cryostat) temperature (k_BT_{bath}), but is calculated from the measured quasiparticle lifetime. This is done to account for excess (non-thermal) quasiparticles, possibly micro-wave induced, which can become relevant at low temperatures [7]. Measuring this lifetime can be done in two ways: by fitting an exponential to the pulse decay, and via fitting a Lorentzian to the noise spectrum (see the next chapter for more details). Both give a τ^*_{qp}, Equation (2.14), which can be translated into a temperature with Equations (2.1) and (2.8). For pulse measurements at bath temperature higher than 200 mK, the noise measurement is used, and for lower temperature measurements the pulse fitting is used.

k_BT_D is the Boltzmann constant multiplied by the Debye temperature. For Al, this is a value of 37 meV.

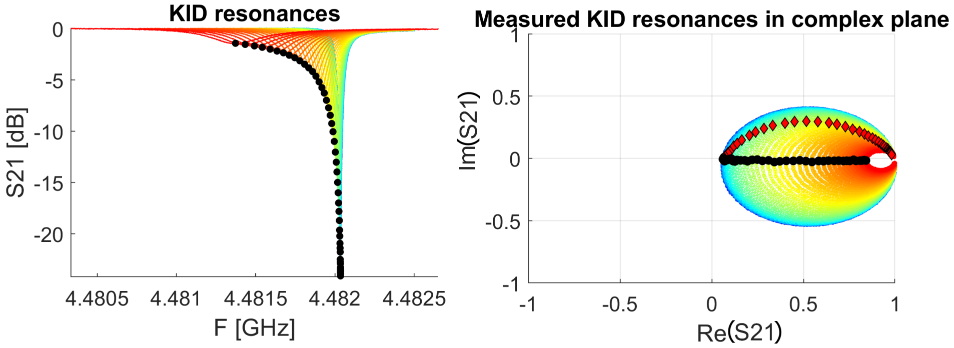

Figure 2.4: Example of a S_{21}-measurement. To the left, the resonance dips are shown ($|S_{21}|$) and to the right the complex components of S_{21} are seen. Colour represents temperature, with blue being low and red being high. The black dots indicate the resonance points.

τ_0 is the electron-phonon interaction time, which is theoretically calculated for Al to be 440 ns [36, 48]. Phonon trapping effects make it hard to verify this value via experiment, resulting in values ranging from (100 ± 20) ns [49] to 1.65 μs [37]. Film-to-film variations in the electron-phonon interaction strength influences the value of τ_0. Here, we neglect these variations by taking τ_0 constant. That implies that all differences in quasiparticle lifetimes are attributed to the phonon trapping effect, via τ_{esc}. In the high phonon trapping regime, this is justified by the fact that the apparent quasiparticle lifetime is not dependent on τ_0 [36, 37].

τ_{pb} is the phonon pair-breaking time. For Al, this is 0.28 ns [36, 48]. Also this value will be treated as a given constant.

$\lambda(0)$ is the magnetic penetration depth at 0 K. It is given by, $\lambda(0) = \lambda_L(0)\sqrt{\xi_0/l_e} = \sqrt{\hbar\rho_N/\mu_0\pi\Delta(0)}$, where λ_L is the London penetration depth [23, 34]. For an Al film of about 50 nm thick, this is $\sqrt{\hbar\rho_N/\mu_0\pi\Delta(0)} = 92$ nm [20, p. 38], which we will use here.

N_0 is the single spin electron density of states at the Fermi-level in Al and is taken to be $1.72 \times 10^4\ \mu\text{V}^{-1}\mu\text{m}^{-3}$ [20, 39].

k_BT_c is the Boltzmann constant multiplied by the critical temperature of Al, which is about 1.2 K. However, the T_c is influenced by a lot of parameters, for instance by the layer thickness. Therefore, of every chip, a separate DC-measurement is performed to determine the T_c.

Design Parameters

V is the superconductor volume. As all MKIDs studied in this thesis are NbTiN-Al hybrid MKIDs, the volume of the Al will be used as superconductor volume. This is justified by the fact that this section is the sensory part and quasiparticles cannot leave this volume.

d is the thickness of the Al film, which differs per chip. A typical value is 50 nm.

Q_c is the coupling quality factor which depends on MKID design, for example the distance of the feed-line to the MKID. It is extracted from the S_{21}-measurement. Note that the Q_c does not depend the quasiparticle density and therefore not on temperature, whereas the Q_i does (Equation (2.18)).

α_k is the kinetic induction fraction, which also depends on the geometry. It can be determined in several ways [24]. Here, it is done via a fit of Equation (2.20), where $\delta\omega_0/\omega_0$ is measured with the S_{21}-measurement at different temperatures and $\delta\sigma_2/\sigma_2$ is calculated for these temperatures with the Mattis-Bardeen equations, Equation (2.4). Only temperatures above 250 mK are considered, because at low temperatures the change in σ_2 is small, but ω_0 could still be influenced by other effects, which would have an effect on the fit.

$(\hbar\omega_0, k_BT_0)$ is a pair of resonance frequency (ω_0) at a certain temperature (T_0) needed to determine the resonance frequency at any temperature via Equation (2.20). It is taken to be the resonance frequency measured at the lowest temperature.

τ_{esc} is the phonon escape time. It strongly depends on the acoustic mismatch and the thickness of the substrate and the metal film [38]. Some of the MKIDs studied in this thesis are fabricated on a membrane, which drastically increases the escape time, as the phonons scatter of the back of the

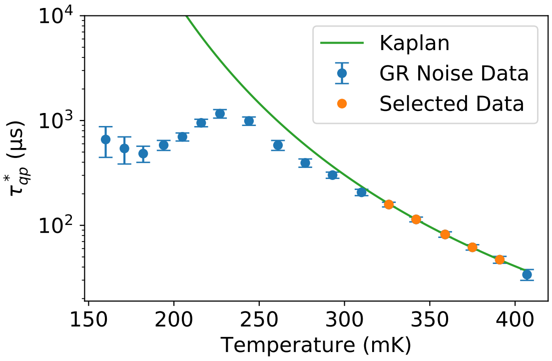

Figure 2.5: Example of a calculation of τ_{esc}, where τ^*_{qp} is calculated from a GR noise measurement. The higher temperature values are taken to calculate τ_{esc}, which in this case was 4.9 ns. The highest temperature point is not taken into account because the signal to noise ratio is not good enough, as at these high temperatures, the responsivity of the MKID goes down due to the (internal) quality factor. Also a Kaplan curve is shown with this phonon escape time, with the help of Equations (2.8) and (2.14).

membrane, back into the superconductor. This results in an increase of phonon trapping [38, 50]. τ_{esc} is estimated from a GR noise measurement at high temperatures (360 mK to 400 mK), to be sure that we are in a thermal regime, and highest available read power for the best signal to noise ratio. From this measurement the quasiparticle lifetime (τ^*_{qp}) is extracted over temperature and together with Equations (2.8) and (2.14), τ_{esc} is calculated. As an example, Figure 2.5 shows the GR noise extracted lifetimes and a Kaplan curve with the calculated τ_{esc} (see Equations (2.8) and (2.14)).

η_{pb} is the only free parameter of the model and reflects the ratio of added quasiparticles ($\delta N_{qp}(t = 0)$) and the incoming photon energy divided by the energy gap ($\hbar\omega_{ph}/\Delta$). It is bounded between 0 and 1 and is retrieved from a fit to a measured photon pulse, where the difference in maxima of the measured and predicted pulses is minimized. Among many parameters, it depends on τ_{esc}, as losing high energetic phonons during the photon down-conversion [45, 51] can decrease η_{pb} [33, 52]. For photon energy of 10 times the gap energy, η_{pb} has been calculated to be a maximum of 59% [33].

2.2.5. Sensitivity Analysis

To interpret the model outcome in a thorough way, it is instructive to look at the effects of each individual parameter on the final output. Three input parameters are calculated: k_BT,α_k and τ_{esc}. These will be discussed first. The parameters that have trivially the same effect, will be grouped.

k_BT influences the thermal quasiparticle number via Equation (2.1) and therefore the exponential decay via Equation (2.8). On top of that, the excess quasiparticles due to the photon will be relatively less, which leads to a lower single photon pulse.

α_k influences the phase via Equation (2.26b), so this will mainly influence the pulse height.

τ_{esc}/τ_{pb} is a ratio that determines the phonon trapping factor (Equation (2.14))). Altering it will change τ^*_{qp} and therefore the exponential decay rate. Note that τ_{pb} is used in the determination of τ_{esc} and altering τ_{pb} therefore has no effect on the results.

k_BT_D only appears in the calculation of Δ, Equation (2.3), which is used in many calculations. However, the Debye energy is orders of magnitude larger than the superconducting gap ($k_BT_D \gg \Delta$), and will therefore not influence Δ much, as the integrand in Equation (2.3) goes to 0 quickly as $E \to \infty$. On top of that, V_{sc} is calculated via Equation (2.3), at $T = 0$, such that it obeys the BSC relation, $\Delta_0 = 1.76k_BT_c$. Changing k_BT_D, will therefore have even less effect, as this will also change V_{sc}.

τ_0 appears both in the parameter calculations of k_BT, α_k and τ_{esc} and in the model calculations. In the model, it appears in τ_{qp}, Equation (2.8), and it will therefore alter the decay rate.

N_0 appears again in both the parameter calculations and the model, for instance in Equations (2.1) and (2.8). Note however that τ_{qp} depends also on N^0_{qp}, which linearly depends on N_0. Therefore, we expect that N_0 only influences the pulse height.

$\lambda(0)$ only appears in the calculation of β, Equation (2.17). As we analyse relatively thin films (50 nm),

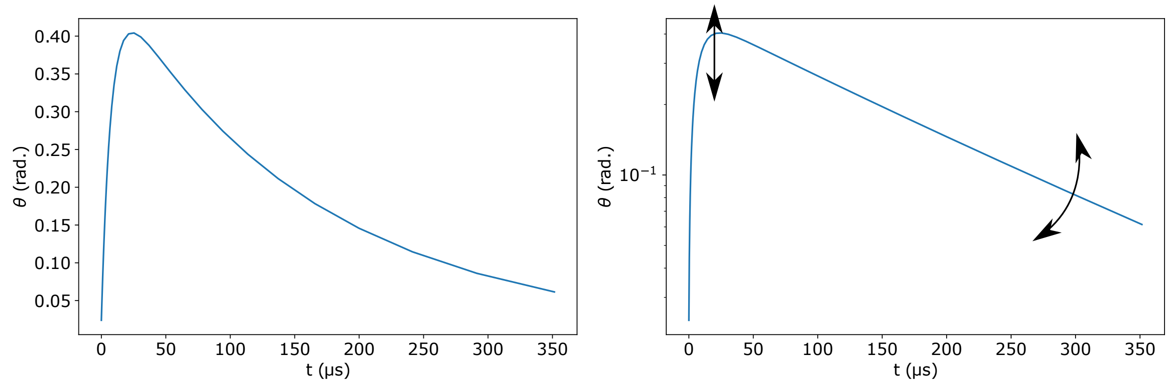

Figure 2.6: Predicted single photon response with parameters used as in Table 2.1 and a incoming 1545 nm photon. Left on a linear scale and right on a logarithmic scale to accentuate the exponential decay. The arrows in the right figure indicate the two main effects a change in parameters can have.

β is almost 2, and $\lambda(0)$ will have little effect on the result.

k_BT_c is only used in the model to calculate the recombination constant, Equation (2.9) and it will therefore alter the decay rate (note the power 3 in the equation). In the calculations of α_k and τ_{esc}, it is also used to determine the Δ_0 from the BCS relation $2\Delta_0 = 3.528k_BT_c$ and it will therefore also alter the pulse height.

V appears in the calculation for $N_{qp}^0 = Vn_{qp}^0$ and will therefore alter the pulse height directly. All other calculations are effectively done with the quasiparticle density and V will therefore not have any other effect.

d is only used in the calculation of β (V is an independent variable), but as we have seen, this will not have much of an effect.

Q_c is used in the calculation of Q in Equation (2.21). We see in Equations (2.25b) and (2.27b) that Q directly influences the responsivity, so we would expect a change in pulse height. However, when the Q factor is Q_i limited, there will be no effect as Q remains constant. So, we expect a slight change in pulse height for higher temperatures (~200 mK) and practically no change for low temperatures (see Equation (2.18)).

$(\hbar\omega_0, k_BT_0)$ will change the absolute resonance frequency and feedline frequency. As this pair is used as a base resonance and temperature pair for Equation (2.20), changing either of the two will have the same effect. Only relative changes to the resonance frequency, result in a θ change, thus altering one of these parameters will have no effect.

η_{pb} only changes the pulse height, as it influences the number of excess quasiparticles from the absorbed photon. This is a fit parameter which makes it dependent on all the input parameters of the model.

We will focus on the $\theta(t)$ output, as we will compare the measured phase with the model. To see the effect of each parameter, we vary it, while keeping the rest constant. As a starting point we will use the values seen in Table 2.1, which produce the single photon pulses seen in Figure 2.6, when a 1545 nm photon is absorbed. The arrows indicate the two main that change: the pulse height (θ^{max}) and the exponential decay constant (τ_{qp}^*). To quantitatively see the effect of the parameter change, we vary the parameter within the percentage of estimated uncertainty (see Table 2.1) and calculate the change in both θ^{max} and τ_{qp}^*. The result is seen in Table 2.1

The pulse height (θ^{max}) is most influenced by the uncertainty in V, followed by k_BT and α_k. The total uncertainty in θ^{max} is 0.08 rad, which translates to an uncertainty in η_{pb} of 6% (absolute percentage), as mentioned in Table 2.1. This error is the propagated error, using the methods as described. The error in η_{pb} is lager if these methods are not justified. In particular, when the method of calculating k_BT (via a pulse or GR noise lifetime) is changed to for example the bath temperature, η_{pb} can take values that are outside of this uncertainty interval.

For the decay rate (τ_{qp}^*), k_BT_c has a large influence due to the 3rd power in Equation (2.9) and the relatively high uncertainty in it. Also k_BT adds uncertainty into τ_{qp}^*, as this exponentially translates to N_{qp}^0 and therefore to τ_{qp}.

Table 2.1: Table of sensitivities for pulse height (θ^{max}) and decay rate (τ^*_{qp}) and parameters used for sensitivity analysis. These are typical values, which are also used in the comparison with data in the next section. No sensitivity means no significant effect. The uncertainty is estimated either by comparing different literature values, estimating measurement errors, analysing the calculation or a combination of these methods.

Parameter	Value	$\frac{d(\theta^{max})}{d(Param.)}$	$\frac{d(\tau^*_{qp})}{d(Param.)}$	Est. Uncert.
k_BT	19.9 µeV	−0.052 rad µeV^{-1}	−74.4 µs µeV^{-1}	0.8 µeV (4%)
α_k	0.0292	10.6 rad		3×10^{-3} (10%)
τ_{esc} (τ_{pb})	0.161 ns (0.28 ns)		3.5×10^5	2×10^{-5} µs (12%)
k_bT_D	37.3 µeV			1×10^1 µeV (0.02%)
τ_0	440 ns		362	0.22 µs (50%)
N_0	1.72×10^4 µeV^{-1} µm^{-3}	-2.2×10^{-5} rad µeV µm^3		1×10^2 µeV^{-1} µm^{-3} (0.5%)
$\lambda(0)$	92 nm			5 nm (5%)
k_BT_c	103 µeV	0.0036 rad µeV^{-1}	14.4 µs µeV^{-1}	5 µeV (5%)
V	12.4 µm	−0.032 rad µm^{-3}		2 µm^3 (16%)
d	50 nm			1 nm (2%)
Q_c	1.49×10^5	1.86×10^{-6} rad		1×10^3 (0.6%)
$\hbar\omega_0$ (k_BT_0)	20 µeV (10.3 µeV)			0.01 µeV (0.05%)
η_{pb}	0.56	0.69 rad		0.06 (propagated error)

2.2.6. Model Validation and Verification

To validate the workings of the model, first the individual functions are compared to literature. Then, the global model behaviour is compared to literature values, still without looking at any data. As verification, the simulated MKID behaviour is compared to standard MKID characterisation data, like the S_{21}-measurement.

For testing the individual functions, for example the function to calculate the complex conductivity, Equation (2.4), the behaviour is checked with literature values. In Figure 2.7, the behaviour of σ is calculated with the function for different temperatures and photon energies. These figures are in detail compared to [20, Ch. 2] as a validation of the function used to calculate them. The validation of other functions is done in a comparable way.

For the global model behaviour, we can see in Figure 2.3 that the general behaviour is correct. Moreover, it is possible to distil the model output to a value that can be compared to literature, for example the responsivity (dA/dN_{qp} and $d\theta/dN_{qp}$). With Equations (2.27a) and (2.27b), we have can theoretically estimate the responsivity, if we assume the approximations of Gao et al. [39],

$$\frac{d\sigma_1}{dn_{qp}} \simeq \frac{\sigma_N}{N_0\hbar\omega}\sqrt{\frac{2\Delta}{\pi k_B T}}\sinh(\xi)K_0(\xi), \tag{2.29a}$$

$$\frac{d\sigma_2}{dn_{qp}} \simeq \frac{-\pi\sigma_N}{2N_0\hbar\omega}\left[1+\sqrt{\frac{2\Delta}{\pi k_B T}}e^{-\xi}I_0(\xi)\right], \tag{2.29b}$$

where $\xi = \frac{\hbar\omega}{2k_BT}$, and $I_0(\xi)$, $K_0(\xi)$ are modified Bessel functions of the first and second kind, respectively. The approximations used are $\hbar\omega \ll \Delta$ and $k_BT \ll \omega$.

This theoretical estimation can be compared with the response that is simulated with the model. To calculate the responsivity from the model, the response to a small (a maximum of 10%) increase and decrease of N_{qp} from the thermal number is calculated. A spline interpolation of $A(N_{qp})$ and $\theta(N_{qp})$ gives an estimate for dA/dN_{qp} and $d\theta/dN_{qp}$ at the thermal quasiparticle number. In Figure 2.8 the results are shown. It is clear that the general behaviour of the responsivity over temperature is correct. The offset is thought to be caused by the difference in responsivity calculations. In Equation (2.29), the partial derivative with respect to n_{qp} is taken, where the model calculates the responsivity as a change

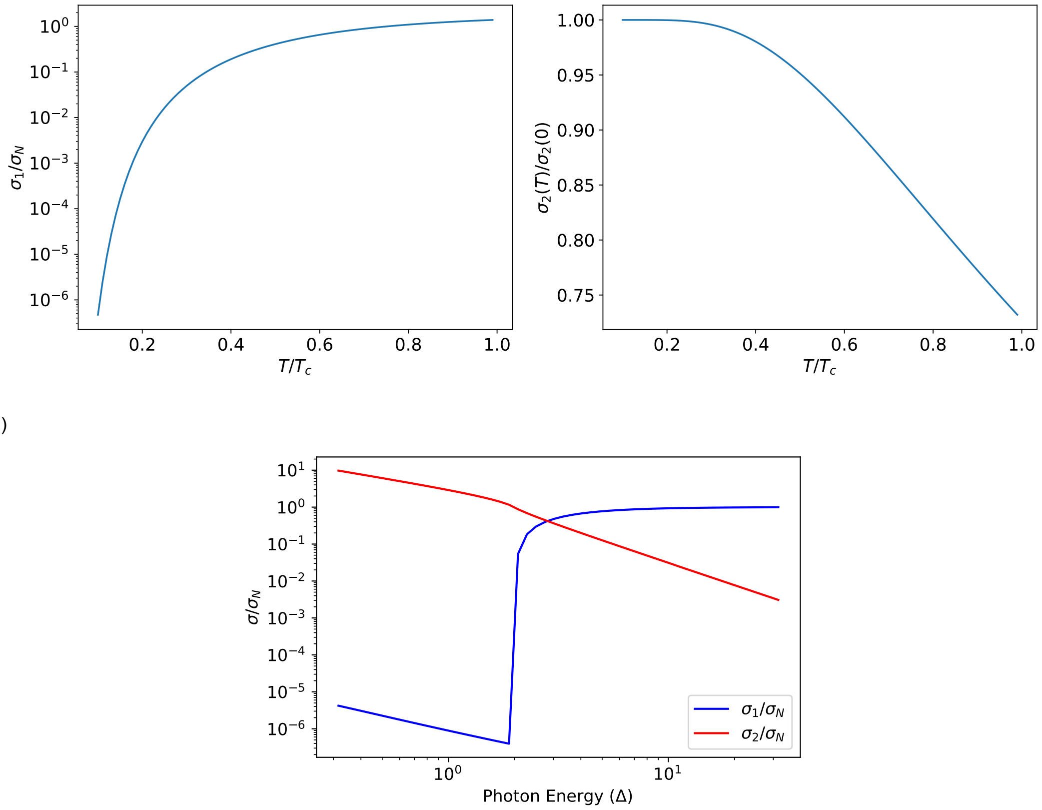

(a)

(b)

Figure 2.7: Behaviour of σ, calculated with the used model functions. (a): Temperature behaviour, with $\hbar\omega = \Delta/10$ (b): Incoming photon energy behaviour, with $T = T_c/8$. All figures are compared with [20, Ch. 2]

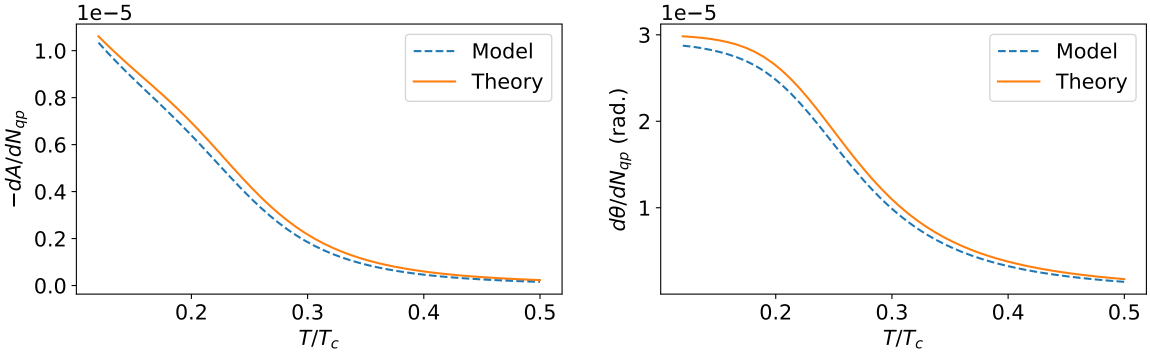

Figure 2.8: Responsivity behaviour of the model compared to theory (Equations (2.27a), (2.27b) and (2.29)). The parameters used are $\hbar\omega = \Delta/100$, and T_c = 12 K to make sure that the approximations hold.

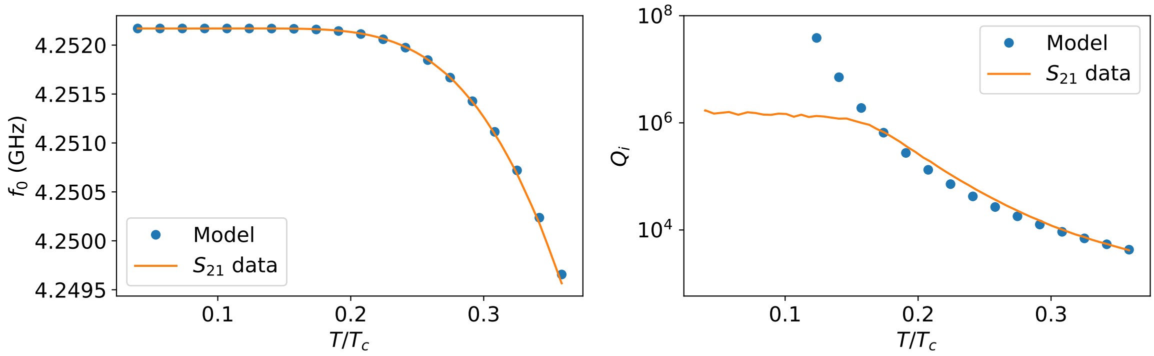

Figure 2.9: Comparison between S_{21}-measurement and MKID model for one specific MKID (LT165, KID1, $P_{read} = -95$ dBm). Left is the resonance frequency over temperature and right is the Q_i factor.

in both N_{qp} and quasiparticle temperature, as these are coupled in the model. A positive change in N_{qp}, causes the quasiparticle temperature to rise as well, resulting in a lower responsivity.

Lastly, as verification, we can compare the simulated MKID behaviour with characteristics measurements, like the S_{21}-measurement. From this measurement, we get Q_i-factors and resonance frequencies over temperature, which we can compare with the calculated values from the model. The model values are calculated in the same way as every time step for the single photon response, but with the thermal number of quasiparticles.
Figure 2.9 shows the results of this verification method. It is clear that the model behaves the same as the data, except for Q_i at low temperatures. This is expected as the model does not include loss mechanisms than other thermal quasiparticles, which exponentially decrease in number at lower temperatures (see Equation (2.1)). Other loss mechanisms can include excess quasiparticles [7], or two level systems (TLS) in thin oxide or contaminant layers between surface interfaces (Al-substrate, substrate-air or Al-air) [53, 54].
At higher temperatures, the calculated values for Q_i also deviate a bit from the measured ones. For the calculation, the bath temperature is used for the quasiparticle temperature. Therefore, this could indicate that the actual quasiparticle temperature is higher, possibly due to quasiparticle redistribution effect. As de Visser et al. [6] describe, the redistribution of quasiparticles due to the read out signal, causes a rise in internal quality factor above 200 mK, which is also seen in Figure 2.9.

2.3. Experimental Methods

2.3.1. Measurement Setup

The measurement setup that is used greatly resembles the one described in [20, Ch. 3] and in [55, 56]. Here, only a brief overview will be presented, with the goal of understanding the context of the measurements. All measurements presented in this thesis have been performed at SRON - Netherlands Institute for Space Research, in Utrecht. The microwave setup will be discussed first, after which the physical setup will follow.

As simplified schematic overview of the microwave measurement setup is showed in Figure 2.10. A microwave signal is created by a synthesizer with one certain angular frequency ω_{read} and power, after which it is split. One line goes to the (MKID) resonator (with power P_{read}) and acts as the read-out signal. It interacts with the MKID and is amplified by a low noise HEMT (high electron mobility transistor) amplifier. Then, the other line and MKID read-out line come together in the *IQ-mixer*, or quadrature mixer (*homodyne detection*). This device gives two outputs: *I*, which is the MKID signal and plain synthesizer signal mixed, and *Q* (not to be confused by the quality factor), which is the MKID signal and plain synthesizer signal mixed with a 90 degrees phase shift. This makes it possible to measure both the real and imaginary part of S_{21}. In order to translate I and Q to the complex S_{21}, the setup must be calibrated. A detailed description of this calibration can be found in [23].

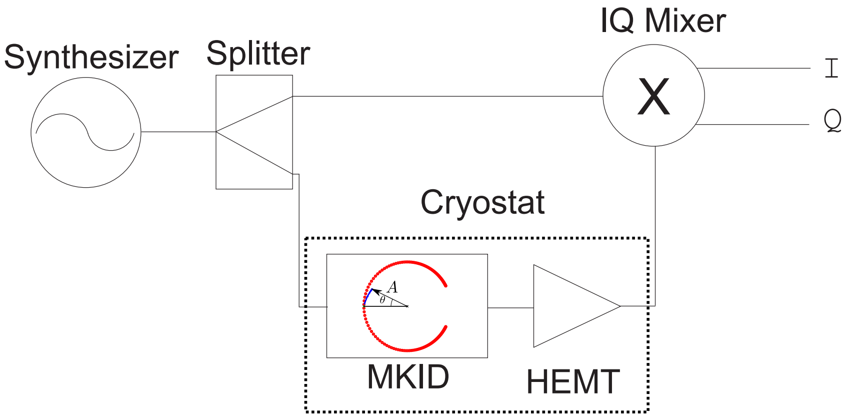

Figure 2.10: Schematic overview of the basic microwave measurement setup. See main text for explanation. Adjusted diagram from [43]

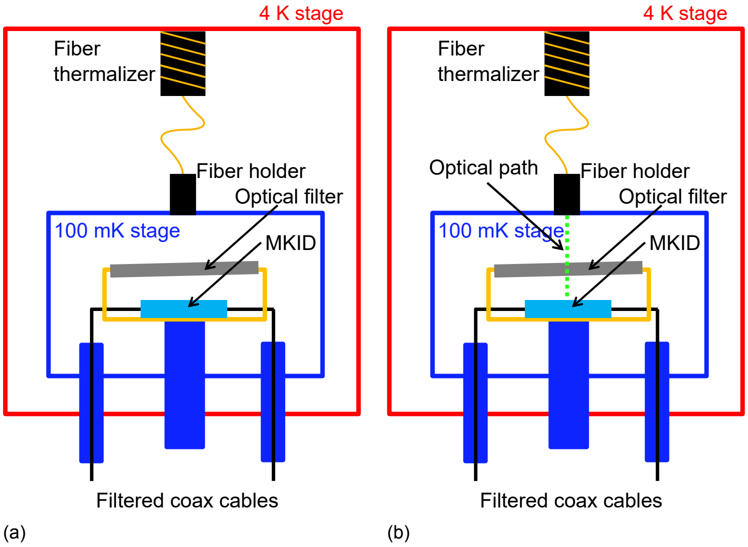

Figure 2.11: Overview of the last temperature stages of the setup. Adjusted diagram from [57]. (a): Dark (laser off) (b): Illumination

As the MKID works on the principles of superconductivity, the devices must be cooled down to below the critical temperature, preferably to one tenth of it. In order to achieve this, the physical setup entails different temperature stages. The cooler used, is a pulse tube pre-cooled adiabatic demagnetization refrigerator (ADR), which can reach temperatures below 100 mK, as described in [57]. The pulse tube pre-cooler has an intermediate temperature stage of 50 K and base temperature of 3.2 K. Further cooling is realised with a gadolinium gallium garnet (GGG), which reaches about 500 mK and ferric ammonium alum (FAA) salt pill, which eventually can reach a temperature of 30 mK [20]. Figure 2.11 shows the last temperature stages with the physical setup in it.
It is important to realise that thermal stray light from the 4 K stage can be absorbed by the MKID, which creates excess quasiparticles [58]. In Reference [55], it is treated in detail how this *box-inside-the-box* configuration can minimize stray light effects.

The 100 mK stage is sealed completely, as illustrated in Figure 2.11a, except for the tip of a laser fiber. The fiber is thermalized with a thermalization coil at the 4 K stage.

2.3.2. Measurement Procedure

In this thesis, the result of three measurements will be presented or used: (1) a S_{21}-measurement, (2) a single photon pulse measurement and (3) a GR noise measurement. The first was already discussed

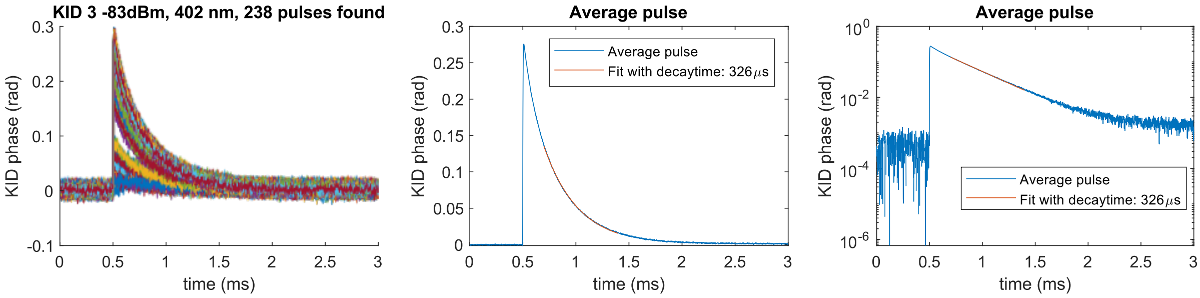

Figure 2.12: Example of measured individual single photon pulses (left) and the average after the double peak rejection, on linear (middle) and log-scale (right).

in Section 2.2.4 and the third measurement type will be discussed in Chapter 3. This subsection will go into the second measurement type: a single photon pulse measurement.

In such a measurement, the setup is in illumination operation (Figure 2.11b), with a laser of one of the four wavelengths (1545 nm, 986 nm, 673 nm and 402 nm). The laser power is attenuated to the point where single photon pulses are visible and do not overlap too much. A typical value for τ^*_{qp} is ∼300 µs and can go up to ∼3 ms [57, 59]. Therefore, the aim is to get about 100 photons per second, which translates to approximately 13 aW to 50 aW absorbed laser power, depending on the wavelength. The IQ-mixer sampled at 1 MHz with an analogue digital converter (ADC), so that the single photon pulse decay and rise time are clearly visible. The resonator ring time, which determines the pulse rise time, is typically in the order of microseconds.

IQ time traces (typically 40 traces of 1 second) are measured, and is translated to θ and δA. Only the phase is analysed here, because of the higher signal to noise ratio in this variable (Figure 2.8 already indicates a higher responsivity). A linear Wiener filter is used to calculate the amplitudes in the following way (see [27, 28] for details). The Fourier transform of pulse time trace, $D(f)$, is described by $D(f) = AM(f) + N(f)$, where A is the amplitude, $M(f)$ is the model pulse and $N(f)$ is noise spectrum, which is measured from dark time trace. The model pulse the average of all pulses. Then, the amplitude is extracted via,

$$A = \frac{\int_{-\infty}^{\infty} DM^*/|N|^2 df}{\int_{-\infty}^{\infty} |M/N|^2 df}, \tag{2.30}$$

where the star indicates the complex conjugate. The residuals of these optimal filters, given by $\chi^2 = \int_{-\infty}^{\infty} (D(f) - AM(f))^2/N^2(f) df$, are used to filter double pulses, where two or more photons arrive within a few ms. This is done again with an updated model pulse. On top of that, after the first pulse rejection, the pulses with an amplitude that differs from the average by more than 50% are also rejected. Figure 2.12 shows an example of the single photon pulses and their average after the double peak rejection. In this thesis, we will analyse the average single photon pulses (i.e. the updated model pulse), as the noise is the signal is reduced this way.

2.3.3. MKID Designs

For the single photon pulses, two chip designs (with multiple MKIDs on them) have been measured: LT139 and LT165. Their design will be discussed in this section.

LT139 is shown in Figure 2.13 (a), (b) and (c). The feedline is the outermost octagon in (a) and is a NbTiN co-planar wave-guide (CPW), with bridges (white stripes) over it to connect the ground planes on either side. Inside the octagon, eight hybrid MKIDs are placed, with their sensory Al section pointing towards the middle. This way, the laser can be focussed to the middle (indicated by the red circle) and the chance a photon gets absorbed by the Al is relatively high. The Al strips (of 50 nm thickness) are designed with a width of 1.6 µm, but have an actual width of 0.92 µm because of over-etching. The NbTiN film is etched away around the Al strips, to limit photon absorption in these sections. The capacitive part of the MKIDs consists of a meandering NbTiN CPW and the coupling to the feedline is done with an *elbow* geometry, like described in [24]. Each MKID is designed to have a unique resonance frequency (by varying the capacitive and inductive part), so that they can be read out individually. The processing is done on a Sapphire wafer, as a semiconductor wafer would absorb the laser photons and heat up.

LT169 is shown in Figure 2.13 (d),(e) and (f). The feedline resembles the one of LT139. Inside are 4 MKIDs, coupled to the feedline with a T-shaped CPW. The capacitive parts are of a double sided interdigitated capacitor (IDC) design. The four sensory Al parts come again together in the middle for a higher chance of photon absorption. The Al strip is 50 nm thick, 2 µm wide and 312 µm long. The processing is done on a silicon wafer. A 110 nm SiN film is deposited in the middle, on top of which the Al strips lay. A KOH etch then etches the (middle of the) backside of the Si wafer, and leaves the SiN intact. In this way, the middle two MKIDs, with their Al strips pointing left and right, effectively lay on a 110 nm thick SiN membrane. As stated earlier, this will greatly enlarge τ_{esc}, and with it the phonon trapping factor. The other two MKIDs, with the IDCs pointing north and south, do not lay on the membrane. The membrane can be observed as the middle dark brown bar, on top of which the Al is seen as thin white lines (Figure 2.13 (e)).

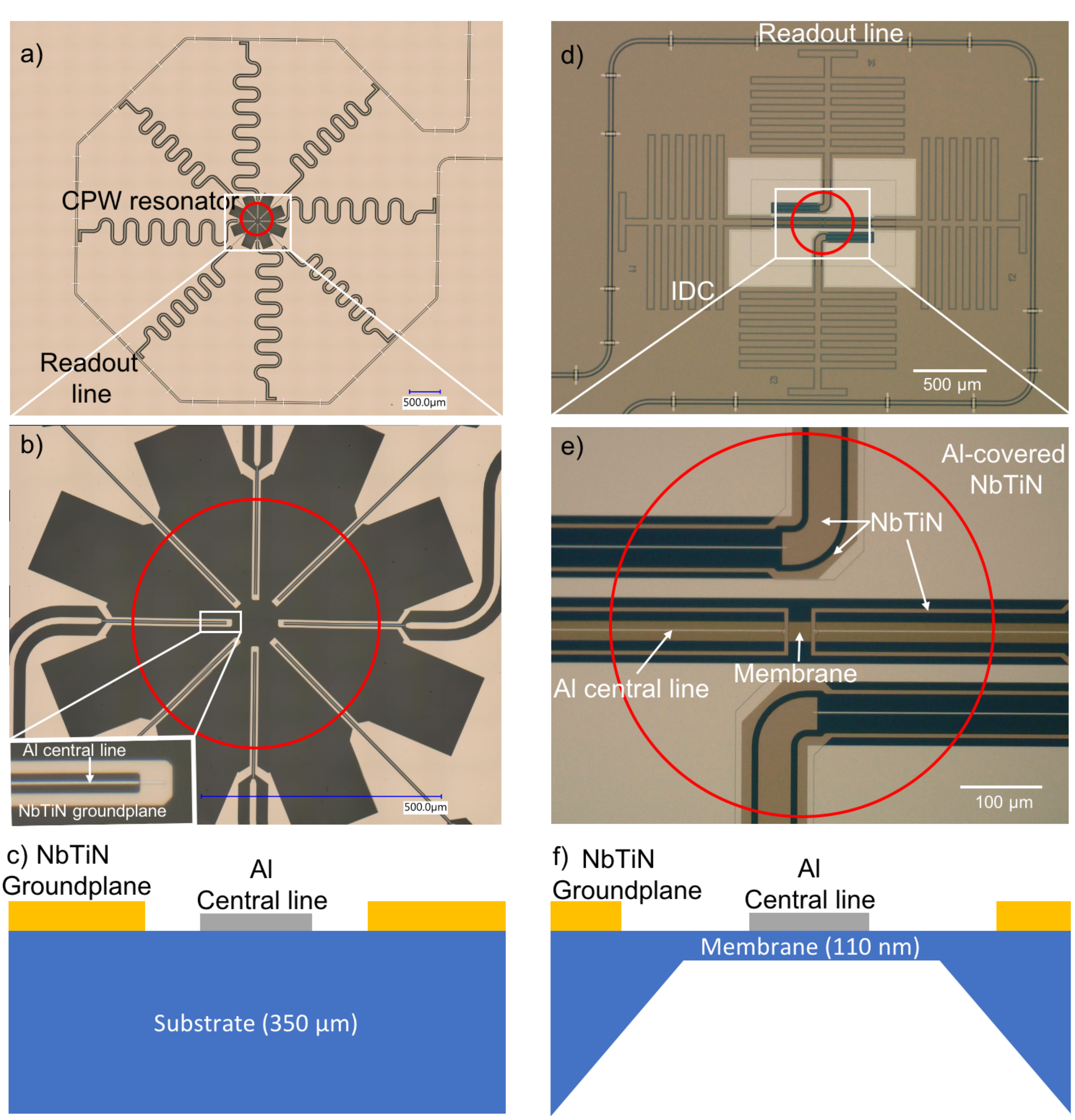

Figure 2.13: Chip design of LT139 ((a),(b) and (c)) and LT165 ((d),(e) and (f)). (a) and (d) are overview microscope images, and (b) and (e) are zoom-ins of the middle parts. The red circles have a diameter of 500 µm. (c) and (f) are schematic side views of the sensitive Al part of a substrate MKID and membrane MKID respectively. Image from P. J. de Visser via private communication.

2.4. Results and Discussion

In this section, the single photon pulses predicted by the model described in Section 2.2.3, will be compared to data, which is measured with the procedure explained in the previous section. First the data of LT139 is presented, which are MKIDs on a substrate. Then, the data of LT165 is discussed, which has MKIDs on both substrate and membrane. That allows us to see the effect of phonon trapping. Of both chips, low temperature (120 mK) and high temperature (220 mK and 250 mK) data is available and some for multiple values of P_{read}. The full data set with model comparison can be found in Appendix C.

2.4.1. Optical MKIDs on substrate

The high temperature (220 mK) data for KID6 of LT139 is shown in Figure 2.14, along with the model prediction. The used parameters are given in Table 2.2. The effective quasiparticle temperature is calculated with the lifetime from a GR noise measurement and the pair-breaking efficiency is fitted to the 986 nm pulse height.

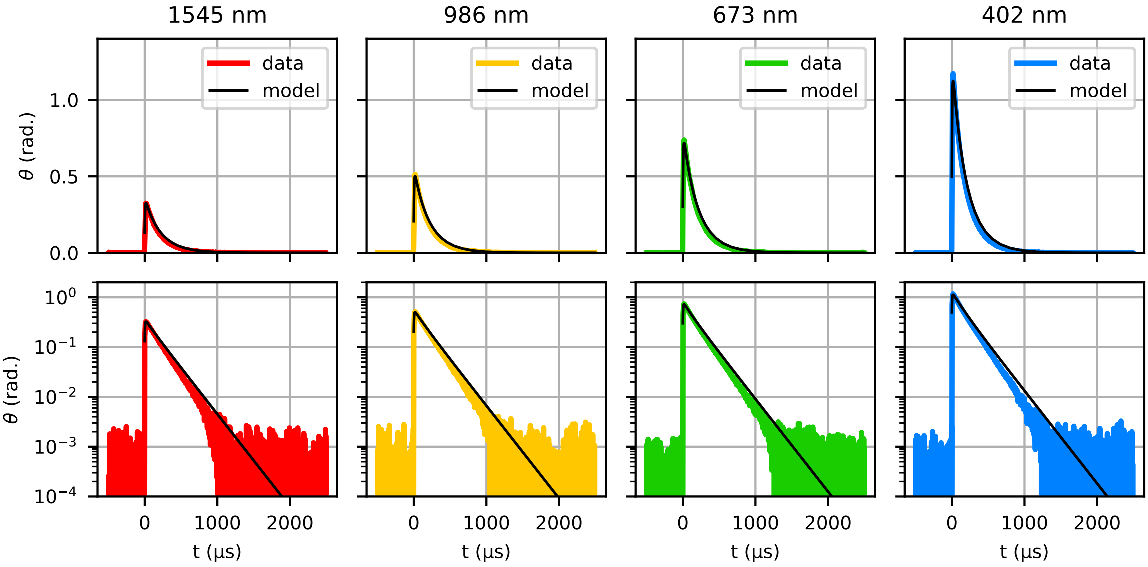

Figure 2.14: Average single photon pulses of different wavelengths, for LT139, KID6 at −96 dBm read power and 220 mK. Model predictions are added as solid black lines. The pair-breaking efficiency is fitted to the 986 nm measured peak. Both linear and log scale is shown.

It is clear that the model can predict the single photon pulse in this case quite well. A single set of parameters can predict the pulse height for different incoming photon wavelengths. Moreover, the exponential decay is also quite well accounted for. This decay is mainly determined by the effective quasiparticle temperature, which is based on a noise measurement (see Section 3.3) for these model curves.

η_{pb} has value of around 53%, with an error margin of 6% (see Section 2.2.5). This value is relatively high compared to the theoretical maximum of 59% calculated by Guruswamy et al. [33]. This could be an effect of quasiparticle redistribution due to read power [6]. At these temperatures, this effect increases Q_i compared to a thermal quasiparticle distribution. Also in Figure 2.9, at 220 mK, the measured Q_i is higher than the predicted value. A higher Q_i results a larger photon response, which would lower the fitted pair-breaking efficiency.

Furthermore, the pulses at lower wavelengths seem to be larger than the predicted pulses, which are calculated with η_{pb} from a fit to the 986 nm pulse. In fact, when the pair-breaking efficiency is fitted to the 402 nm pulse, the result is 58% and for the 1545 nm, it results in 55%, both for −96 dBm read power. For the higher read power, −92 dBm, the spread in fitted pair-breaking efficiency is 50 % to 53 %, but with an opposite wavelength dependence, also seen in Figure 2.15. This suggests that these deviations are the effect of read power, possibly the redistribution of quasiparticles, altering the $f(E)$

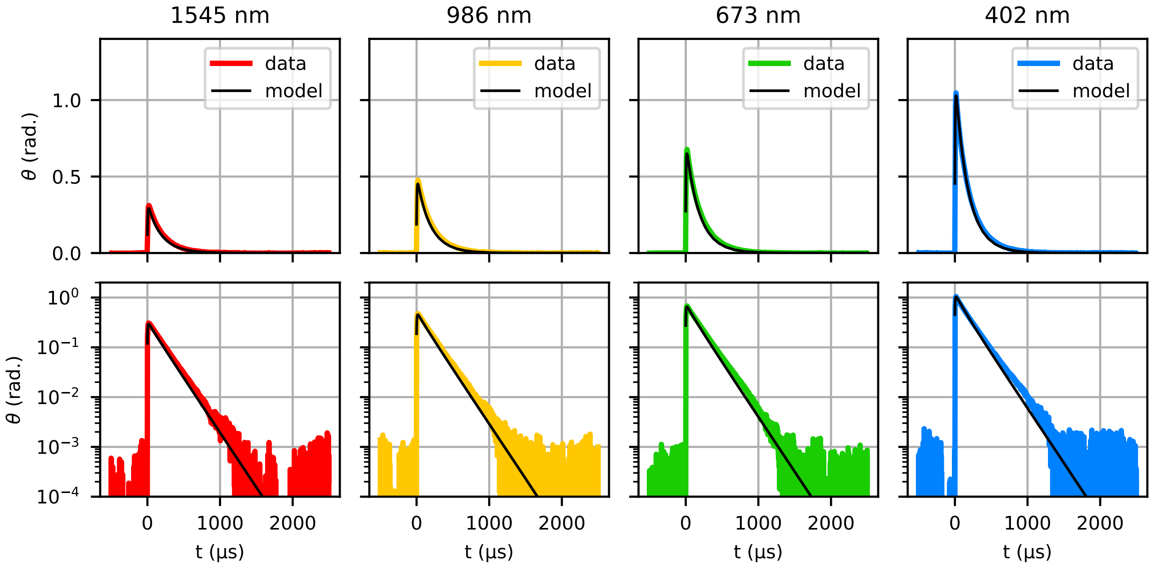

Figure 2.15: Average single photon pulses of different wavelengths, for LT139, KID6 at −92 dBm read power and 220 mK. Model predictions are added as solid black lines. The pair-breaking efficiency is fitted to the 986 nm measured peak. Both linear and log scale is shown.

in the Mattis-Bardeen equations.

Moreover, the pair-breaking efficiency seems to decrease with increase read power, as seen in Table 2.2. It is important to realise that η_{pb} is fitted to the data, and thus is subject to all model parameters and shortcomings, in particular to read power effects. The data shows that higher read powers lead to a decrease in peak height. This could be the result of microwave induced excess quasiparticles as described in [7, 57], which also explains the somewhat higher effective quasiparticle temperature in Table 2.2 for higher read power.

At lower temperature (120 mK) for the same KID6 and −96 dBm, the results are presented in Figure 2.16. The parameters used are also in Table 2.2. For the lower temperatures, no reliable GR noise data is available. Therefore, k_BT is determined via an exponential fit to the 402 nm single photon pulse. The decay does not follow a single exponential at these temperatures, but follows a *second exponential decay* after about 1 ms, with a longer decay time. The first part of the decay is modelled in a correct way, as is the pulse height (see linear plots in Figure 2.16). Furthermore, from these plots it is clear that the second exponential decay starts around same value θ for all wavelengths, which is in this case 0.2 rad.

As the second exponential decay is not predicted by the model, we can conclude that the cause of this behaviour is not a non-linearity that is included the model. The model includes the intrinsic non-linearity of the recombination process [4, 37], caused by the squared term in Equation (2.5). It also includes phase non-linearity due to high MKID responses, where the approximation $\tan(\theta) \approx \theta$ is not valid.

To get a closer look at this behaviour, Figure 2.18 shows the single photon pulses for different read powers. Again, the trend of lower pulse height with increasing read power is seen in the linear scale figure. From the log scale graph, it is clear that the two exponential decays average out towards one exponential decay for higher read powers, although it does not completely disappear. Fitting exponential functions to the two parts, for different read powers, results in Figure 2.17, where this averaging is also visible.

It is possible that the increase of read power masks this second exponential behaviour by generating excess quasiparticles [7], which effectively increases the quasiparticle temperature. From Figure 2.14, we know that at higher temperatures, the second exponential decay is not seen. As a test for this hypothesis, we can look at the behaviour of the internal quality factor and resonance frequency at 120 mK for this MKID, which is measured in the S_{21}-measurement. Excess quasiparticles would imply a lower

Table 2.2: Used parameters for model predictions of LT139, KID6 and KID7. Values that are the same for these MKIDs are shown in a separate table. The effective quasiparticle temperature (k_BT) is calculated with the lifetime from a GR noise measurement for 220 mK and a exponential fit to the 402 nm single photon pulse is used for 120 mK. The pair-breaking efficiency is determined by a fit to the 986 nm pulse.

MKID	KID6	KID6	KID6	KID7
Temperature (mK)	220	220	120	120
P_{read} (dBm)	−92	−96	−96	−96
Parameter				
Q_c	1.22×10^5	1.15×10^5	1.15×10^5	8.72×10^4
$\hbar\omega_0$ (µeV)	21.2	21.2	21.2	21.4
k_BT_0 (µeV)	10.3	10.3	10.3	10.4
k_BT (µeV)	19.6	19.2	18.8	19.3
V (µm^3)	24.6	24.6	24.6	24.4
α_k	0.0588	0.0591	0.0591	0.055
τ_{esc} (ns)	0.149	0.149	0.149	0.214
η_{pb}	0.512	0.56	0.562	0.51

Parameter	Value
d (nm)	50
k_BT_c (µeV)	103
k_bT_D (meV)	37.3
τ_0 (ns)	440
τ_{pb} (ns)	0.28
$\lambda(0)$ (nm)	92
N_0 (µeV^{-1} µm^{-3})	1.72×10^4

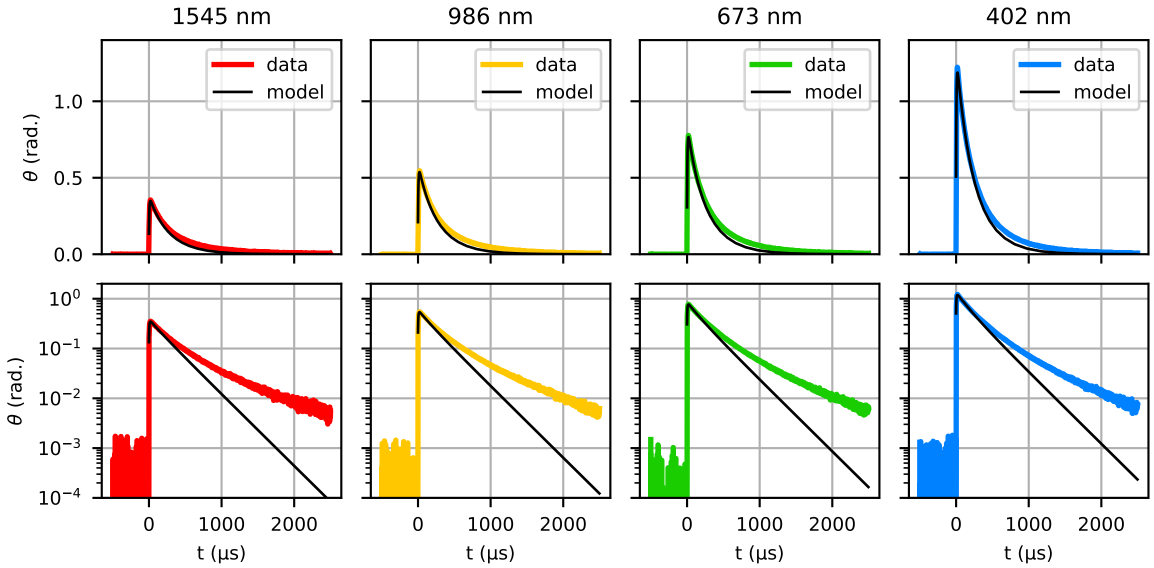

Figure 2.16: Average single photon pulses of different wavelengths, for LT139, KID6 at −96 dBm read power and 120 mK. Model predictions are added as solid black lines. The pair-breaking efficiency is fitted to the 986 nm measured peak. Both linear and log scale is shown.

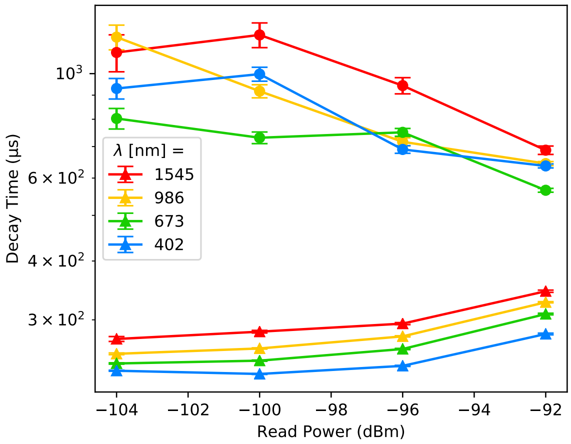

Figure 2.17: Exponential decay constants of the first (△) and second (○) decays in the single photon phase response of LT139 KID6 at 120 mK for different wavelengths (see legend) and at different read powers. The errorbars denote the fit error and for the first decay, the window of 30 µs to 100 µs is chosen, where for the second decay 2 ms to 2.5 ms is used.

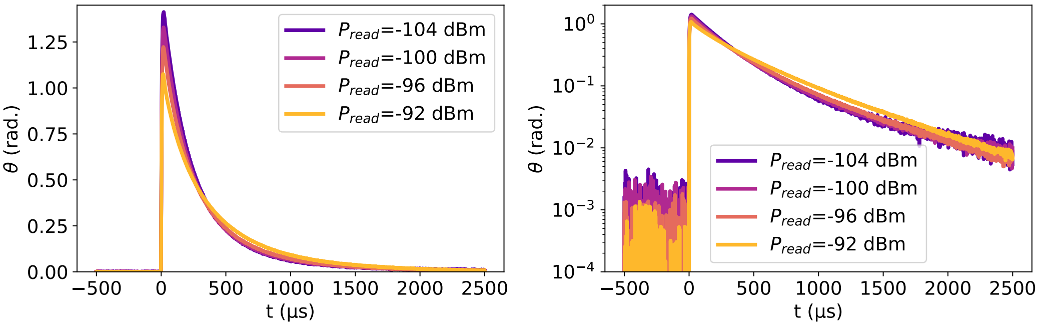

Figure 2.18: Averaged single photon pulses (402 nm) for LT139 KID6, at 4 different read powers, both linear (left) and log scale (right).

internal quality factor (as quasiparticles dissipate resonator energy) and a lower resonance frequency (as less Cooper-pairs are present). This follows the methods of [6], which shows that the microwave power causes a non-thermal distribution of quasiparticles.

Figure 2.19 shows that the resonance frequency slightly goes down with increasing read power, at 120 mK. However, the internal quality factor goes up with increasing read power. A possible explanation for this may be that the Q_i saturation is caused by TLS losses, which go down with increasing read power [60]. Either way, we cannot conclude that the masking of the second exponential decay is described by a simple increase in quasiparticle temperature. In order to understand this, a full energy dependent model could be adopted [6, 47], but this is out of the scope of this thesis.

As an further investigation, also the scaled (to match the height of the phase pulse) amplitude response is plotted together with phase response in Figure 2.20. Note that the second exponential decay is most visible in this chip, compared to LT165. The lowest read power (−104 dBm) is used, to make the second exponential decay even more visible. Because of the low signal to noise ratio in the amplitude, a moving average is used to make the tail behaviour visible.

The amplitude response shows a second exponential decay as well. The decay constant seems to be the same as for phase, however the signal to noise ratio in amplitude does not allow for this statement to be confirmed. Furthermore, the second decay starts later than it does in phase.

In KID7 of LT139 this second exponential decay is also seen, see Figure 2.21 and Table 2.2. Here, it seems that the second decay rate is dependent on the wavelength of the incoming photon. The higher the photon energy, the smaller this exponential decay constant. However, this could be an effect of the post-processing of the data. The measured time traces are corrected for offsets by subtracting the

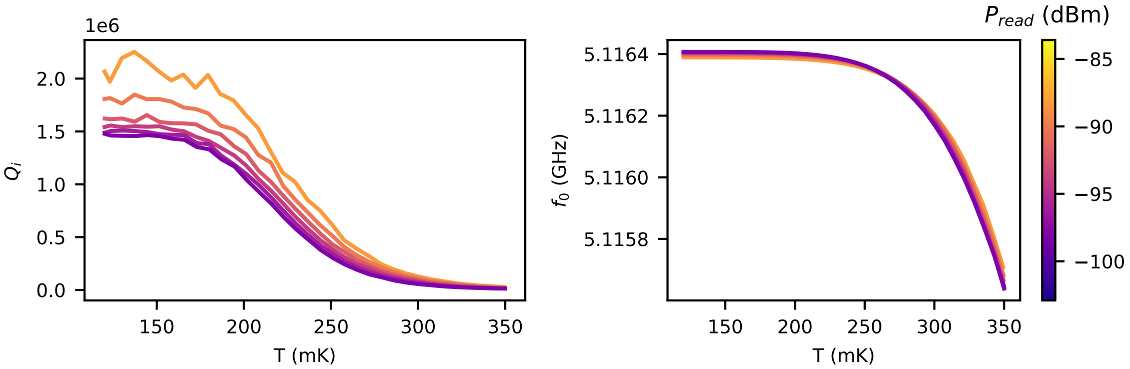

Figure 2.19: Resonance frequency (left) and internal quality factor (right) as a function of read out power, measured by a S_{21}-measurement for LT139, KID6.

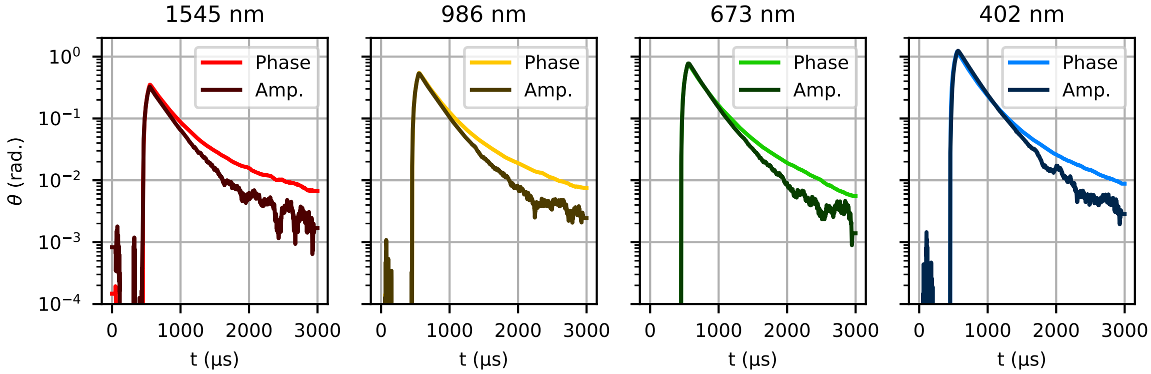

Figure 2.20: Amplitude and phase single photon responses for 4 different wavelengths. The amplitude is normalized to the height of the phase pulse and both data series are smoothed with a moving average, at window size 100 μs. Data is from LT139, KID6 at −104 dBm, 120 mK.

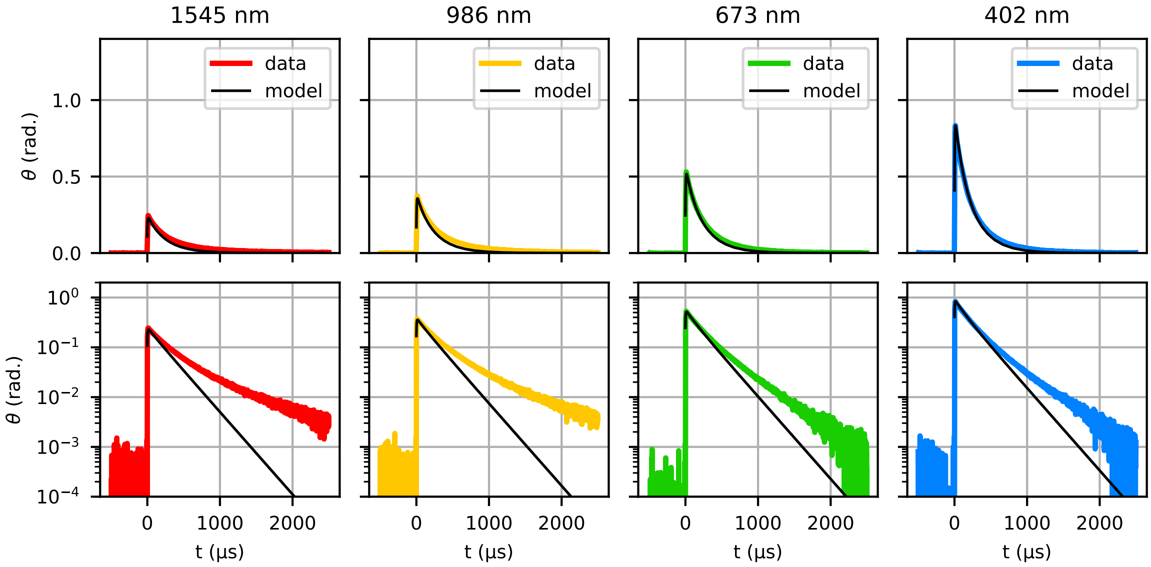

Figure 2.21: Average single photon pulses of different wavelengths, for LT139, KID7 at −96 dBm read power and 120 mK. Model predictions are added as solid black lines. Both linear and log scale is shown.

average of the parts where there is no pulse. These parts are selected by a threshold, which means part of the pulse tails is still in the average and a too large value is subtracted from the data. When averaging over the first 500 μs in Figure 2.21, all averages are negative, with −0.17 mrad, −0.43 mrad, −0.88 mrad and −0.71 mrad for 1545 nm, 986 nm, 673 nm and 402 nm, respectively. This offset effectively increases the second exponential decay rate and seems higher for the 402 nm and 673 nm pulses. However, the average standard deviations in these sections is 2 mrad, which makes it hard to conclude that the averages are the cause.

The lower pulse heights of KID7 compared to KID6, is explained by the model, without adjusting η_{pb} much. Comparing the parameters in Table 2.2, we see that Q_c is lower, which limits the quality factor Q. In turn, Q lowers responsivity, as Equation (2.27) states. On top of that, α_k is also a bit lower, which lowers the pulse height even more.

2.4.2. Phonon Trapping Effects

For LT165, we will look at KID2 and KID3, of which the former is on a membrane and the latter is not. The high temperature (250 mK) data with model predictions, is shown in Figure 2.22. Only the 1545 nm data is available for this temperature. The used parameters are in Table 2.3.

We can clearly see the effect of phonon trapping by the much longer decay time for KID2. Also the escape times in Table 2.3 show that phonon trapping is much higher in KID2 than in KID3.

Besides that, the effective quasiparticle temperature is also higher at KID2, which might indicate that MKIDs on a membrane are more susceptible to microwave power heating [6].

A difference in pulse height is apparent and reflected by η_{pb}, in Table 2.3. That η_{pb} is higher for KID2 than for KID3, is not surprising, since in the downconversion process, less high-energetic phonon get lost, which makes the process more efficient [33, 61].

For the low temperature (120 mK) data, Figures 2.23 and 2.24 show the single photon pulses and model predictions with parameters listed in Table 2.3.

In KID2, the pair-breaking efficiency is even higher: 69 %. This is not physically possible because of the calculated maximum of 59 % by Guruswamy et al. [33]. However, as stated before, when interpreting the value of η_{pb}, it should be kept in mind that it is dependent on all model input parameters and model shortcomings.

Also in these MKIDs, a second exponential decay is visible. In KID3, it starts earlier (in time) than in

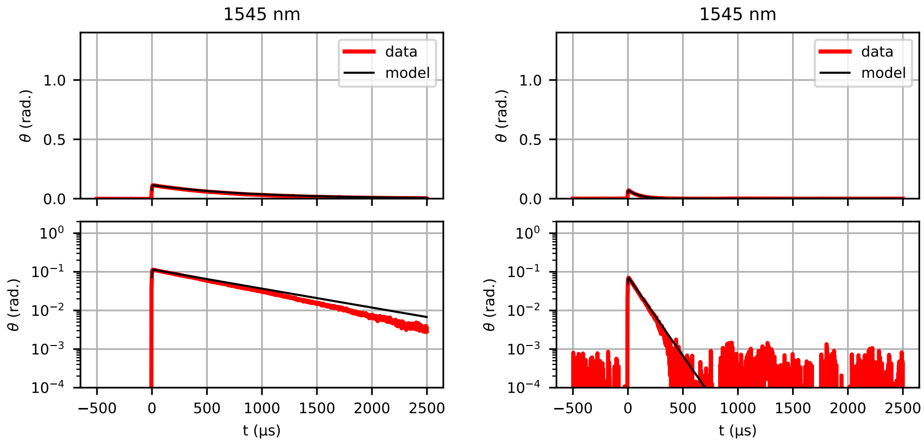

(a) KID2, −85 dBm

(b) KID3, −83 dBm

Figure 2.22: Single photon response model results for LT165 at 250 mK.

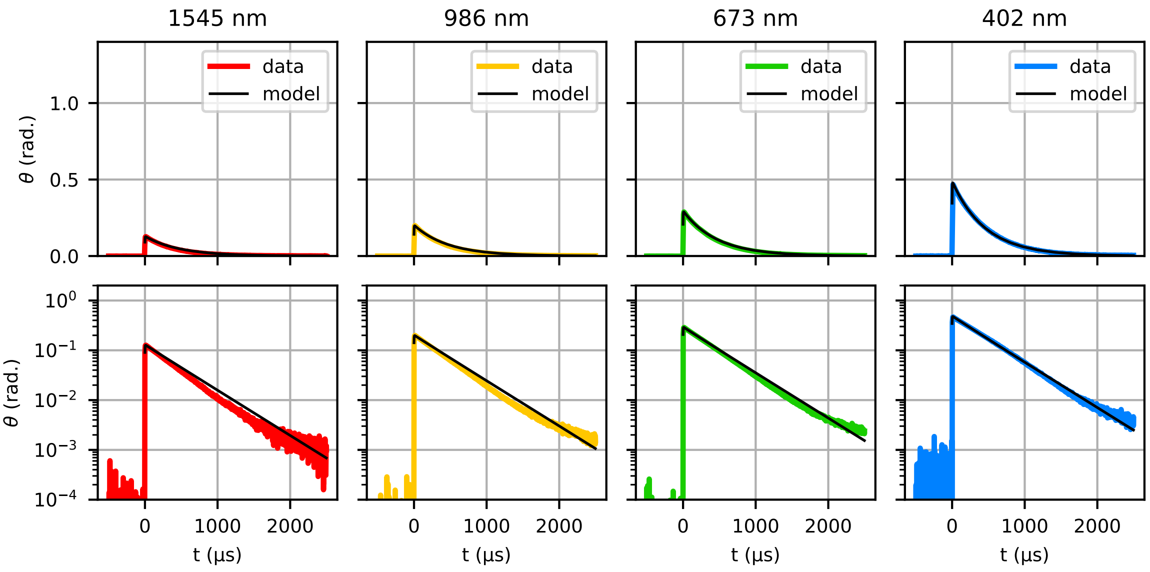

Figure 2.23: Average single photon pulses of different wavelengths, for LT165, KID2 at −85 dBm read power and 120 mK. Model predictions are added as solid black lines. Both linear and log scale is shown.

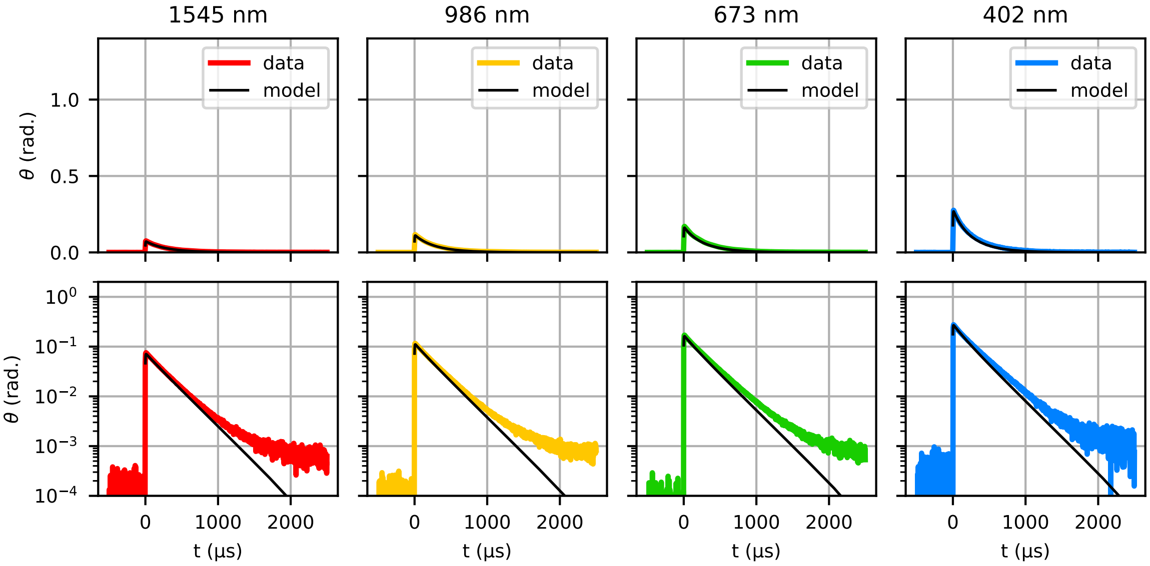

Figure 2.24: Average single photon pulses of different wavelengths, for LT165, KID3 at −83 dBm read power and 120 mK. Model predictions are added as solid black lines. Both linear and log scale is shown.

Table 2.3: Used parameters for model predictions of LT165, KID2 and KID3 at 120 mK and 250 mK. The effective bath temperature (k_BT) is calculated an exponential fit to the 402 nm single photon pulse. Parameters that are the same for these MKIDs are in a separate table.

MKID Temperature (mK) P_{read} (dBm)	KID2 120 −85	KID3 120 −83	KID2 250 −85	KID3 250 −83
Parameter				
Q_c	4.76×10^4	3.8×10^4	4.76×10^4	3.8×10^4
$\hbar\omega_0$ (μeV)	17.8	18.6	17.8	18.6
k_BT_0 (μeV)	4.3	4.3	4.3	4.3
k_BT (μeV)	24.4	19.6	22.7	21.8
α_k	0.0643	0.0587	0.0643	0.0587
τ_{esc} (ns)	4.9	0.138	4.9	0.138
η_{pb}	0.686	0.329	0.496	0.382

Parameter	Value
V (μm^3)	27
d (nm)	50
k_BT_c (μeV)	108
k_bT_D (meV)	37.3
τ_0 (ns)	440
τ_{pb} (ns)	0.28
$\lambda(0)$ (nm)	92
N_0 (μeV^{-1} μm^{-3})	1.72×10^4

KID2. This should be considered in light of the different (first) decay times, τ_{qp}^*. The second exponential decays seems to start at about the same θ in the decay. Therefore, as KID2 has a longer first decay time due to phonon trapping, the second decay starts later. However, the data we are looking at is susceptible to read power effects, as we have seen. Therefore, comparing different MKIDs in such a way can only be justified if these read power effects are also considered.

2.5. Conclusion

In this chapter, we have set out a way to model the response of an MKID and with that, touched upon the physics that governs these detectors. Via the Rothwarf-Taylor equations, we found a way to model the time evolution of the number of excess quasiparticles (broken Cooper-pairs) generated by a single photon. We saw how the number of quasiparticles influences the complex conductivity of the Al section and how this changed the resonance frequency and quality factor of the resonator. The measurable S_{21}-parameter (which depends on the quality factor and resonance frequency) lead us to the two MKID variables that define the output of the detector: amplitude and phase.

For the implementation of the model, we considered all the different input parameters and fit parameter (the pair-breaking efficiency, η_{pb}), and how to pin them down. A sensitivity analysis showed that the single photon pulse height output is most influenced by the uncertainty in the volume (followed by the kinetic induction fraction and the effective quasiparticle temperature). The decay rate of the single photon pulse is most influenced by the uncertainty in the critical temperature.

With local and global validation methods, we saw that the model behaves as expected. As a verification, we compared the model resonance frequency and internal quality factor with real MKID data and saw an expected resemblance.

We tested the model with the data of different MKIDs, of which one was on a membrane. The model can explain the data in all cases quite well, considering the model has only one fit parameter (η_{pb}), with values in the range of expected pair breaking efficiencies (30%-70%), although somewhat high for most MKIDs. That might be caused by redistribution of quasiparticles due to read power [6]. Also the effect of phonon trapping could be well explained by the model, with fitted phonon trapping factors varying from 1.5 to 18.5. As to read power effects, we saw in the data a consistent decrease in pulse height with increasing read power. Also the decay rates depend on read power, but to understand this, a full energy dependent treatment is needed [6, 33, 47].

At low temperatures (120 mK) all the MKIDs show a second exponential decay, with a longer decay time. This is not captured by the model and is thus not caused by non-linearities that are included in the model, such as recombination non-linearity [4] or large phase non-linearities. This second exponential decay is also present in the amplitude response, but starts later. Furthermore, at different wavelengths the onset of the second exponential decay was observed to be at the same values for θ. What the cause of this second exponential decay is, remains an open question.

3

Generation-Recombination Noise

3.1. Introduction

In the previous chapter, we saw that the known theory governing the MKIDs - superconducting theory and the Rothwarf-Taylor master equation approach to quasiparticle dynamics - could very well describe the single photon response. Also phonon trapping could be explained and quantitatively modelled. However, when going to lower temperatures (120 mK), we observed an unexplained second exponential decay, which was longer than the initial decay (3 ms instead of ~400 µs). As the process that causes this behaviour dominates close to equilibrium (where N_{qp} is close to N_{qp}^T), we will look in this chapter at the system in equilibrium (or, at least in steady state). In other words, we will focus on dark observations, without photon absorption.

When there is no energy deposited in the MKID, and we measure in normal detector operation (ω_{read} on resonance, extracting dA and θ), the noise in the system is captured. This noise typically comes from different sources, such as the amplifier, the MKID surroundings (TLS noise, [60]) or thermal fluctuations within the MKID (generation-recombination (GR) noise [46]). The latter one is intrinsic to the superconducting detector and therefore contains information about the quasiparticle dynamics, by the fluctuation-dissipation theorem [37, 62].

GR noise originates from the process of pair-breaking by a (thermal) phonon, i.e. the generation of two quasiparticles. Recombination of quasiparticles is the opposite process, which emits a phonon at an energy of the sum of the two quasiparticles energies (in most cases 2Δ). In equilibrium, these processes are on (time) average in balance, so that the average quasiparticle number is constant (and can be calculated via Equation (2.1)). In real time, however, these processes constantly take place and cause GR noise, which contains information on the MKID equilibrium state. Investigating this, could give more insight into the processes close to equilibrium, responsible for the second exponential decay.

Besides that, there is one more reason to focus on the GR noise in the detectors. The dark measurement data of the detectors contains an unexplained feature. Namely, when the temperature is lowered, the fluctuations exponentially decrease in level, to the point where the noise is measurable. Conventional GR noise theory predicts a constant level, which also has been measured previously [46]. A *GR noise level drop* as observed here is not reported in literature. The next chapter will go into a probable cause of this behaviour.

This chapter will first go into the conventional GR noise theory. Then, the experimental methods to measure GR noise are set out, after which the results will be shown. The focus will lie on the GR noise drop and its dependencies on different quantities, including phonon trapping, MKID geometry and read power. The chapter will close with conclusions on the observed data and a discussion.

3.2. GR Noise Theory

This section will cover the connection between the quasiparticle dynamics and detector fluctuations. It follows largely the efforts of Wilson en Prober [37]. For more details, this paper is recommended.

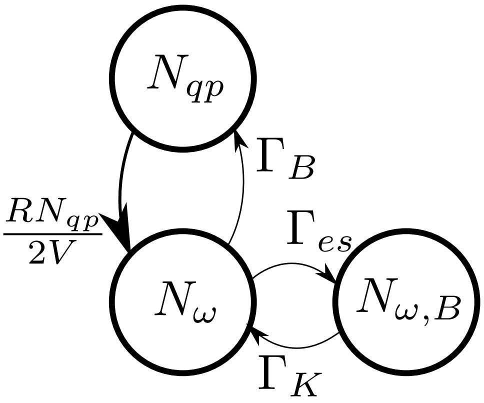

Figure 3.1: Diagram illustrating the master equations in Equation (3.1). The rates for each transition is given next to the arrow indicating it. A thicker arrow indicates a transition with shot size 2.

To model the quasiparticle dynamics, we use the master equation approach with three levels: (1) the number of quasiparticles (N_{qp}), (2) the number of pair-breaking ($\Omega \geq 2\Delta$) phonons in the superconducting film (N_ω) and (3) the number of pair-breaking phonons in the bath ($N_{\omega,B}$), which could for example be the substrate. These levels are illustrated in Figure 3.1, along with the transitions between the particle levels. The rate equations we set up this way, look like,

$$\frac{dN_{qp}}{dt} = 2\left(-\frac{RN_{qp}^2}{2V} + \Gamma_B N_\omega\right), \tag{3.1a}$$

$$\frac{dN_\omega}{dt} = \frac{RN_{qp}^2}{2V} - \Gamma_B N_\omega - \Gamma_{es} N_\omega + \Gamma_K N_{\omega,B}, \tag{3.1b}$$

$$\frac{dN_{\omega,B}}{dt} = \Gamma_{es} N_\omega - \Gamma_K N_{\omega,B}, \tag{3.1c}$$

where $\Gamma_B = 1/\tau_{pb}$, $\Gamma_{es} = 1/\tau_{esc}$, R and V are the same as in Equation (2.5) and Γ_K is the rate at which phonons from the bath come into the film. The recombination rate (the first terms in Equations (3.1a) and (3.1b)) is proportional to $N_{qp}^2/2$, which is the number of ways to combine two quasiparticles. The factor 2 in front of the terms in Equation (3.1a), accounts for the fact that two quasiparticles participate in a single pair-breaking or recombination process. In other words, the transition from N_{qp} to N_ω has a *shot size* of 2. Figure 3.1 also includes the transition rates. We can make the approximation that the bath is large ($N_{\omega,B} \gg N_\omega$) and therefore that $N_{\omega,B}$ is approximately constant ($\frac{N_{\omega,B}}{dt} = 0$). Then, we can simplify the rate equations by setting $\Gamma_{es} N_\omega^T = \Gamma_K N_{\omega,B}^T$, where the superscript T denotes thermal equilibrium. That way we arrive at,

$$\frac{dN_{qp}}{dt} = -\frac{RN_{qp}^2}{V} + 2\Gamma_B N_\omega, \tag{3.2a}$$

$$\frac{dN_\omega}{dt} = \frac{RN_{qp}^2}{2V} - \Gamma_B N_\omega - \Gamma_{es}(N_\omega - N_\omega^T), \tag{3.2b}$$

$$\tag{3.2c}$$

by which we recovered Equation (2.5). With these equations, we can find the steady state values in terms of N_ω^T, as found in Equation (2.6). N_ω^T is calculated by inverting Equation (2.6a) and calculating N_{qp}^0 with Equation (2.1).

Now the steady state values are known, we can calculate the fluctuations around these steady state values. In order to do this, we write down the transition probabilities with their shot sizes (δn) as,

$$p_{12} = RN_{qp}^2/2V \qquad \delta n_{12} = 2, \tag{3.3a}$$

$$p_{21} = \Gamma_B N_\omega \qquad \delta n_{21} = 1, \tag{3.3b}$$

$$p_{23} = \Gamma_{es} N_\omega \qquad \delta n_{23} = 1, \tag{3.3c}$$

$$p_{32} = \Gamma_{es} N_\omega^T \qquad \delta n_{32} = 1. \tag{3.3d}$$

Here we use the level numbers as defined in the first paragraph of this section. With these transition probabilities, we can calculated the $\mathbf{M}$ and $\mathbf{B}$ matrices as described in [37] and [63], with

$$M_{ij} = \sum_k \delta n_{ik} \left(\frac{\partial p_{ik}}{\partial N_j} - \frac{\partial p_{ki}}{\partial N_j} \right) \Bigg|_{\{N_i\}=\{N_i^0\}}, \tag{3.4a}$$

$$B_{ii} = \sum_{k \neq i} \delta n_{ik}^2 (p_{ki} + p_{ik}), \tag{3.4b}$$

$$B_{ij} = -\delta n_{ij} \delta n_{ji} (p_{ij} + p_{ji}). \tag{3.4c}$$

The matrix $\mathbf{M}$ describes the first order moments of the system (i.e. average occupation numbers) and $\mathbf{B}$ describes the second order Fokker-Planck moments (i.e. the fluctuations around the average number). The eigenvalues of $\mathbf{M}$ give the relevant rates governing the system. For the system under consideration and taking $N_\omega^T = N_\omega^0$, they become,

$$\mathbf{M} = \begin{pmatrix} \frac{2RN_{qp}^0}{V} & -2\Gamma_B \\ -\frac{RN_{qp}^0}{V} & \Gamma_{es} + \Gamma_B \end{pmatrix}, \tag{3.5a}$$

$$\mathbf{B} = \frac{R(N_{qp}^0)^2}{V} \begin{pmatrix} 4 & -2 \\ -2 & 1 + \Gamma_{es}/\Gamma_B \end{pmatrix}. \tag{3.5b}$$

With these matrices we can calculated the noise properties (up to the second moment) of the system. The quantity we are interested in is the power spectral density (PSD) of the number of quasiparticles, as this is measurable in the MKID via amplitude and phase fluctuations. The power spectral density matrix is given by,

$$\mathbf{G}(\omega) = 2\Re\left\{(\mathbf{M} + j\omega\mathbf{I})^{-1}\mathbf{B}(\mathbf{M}^T - j\omega\mathbf{I})^{-1}\right\}, \tag{3.6}$$

where $\mathbf{I}$ is the identity matrix of the same dimensions as $\mathbf{M}$ and $\mathbf{B}$, ^{T} means the transpose, $^{-1}$ is the inverse and ω is the angular frequency of the fluctuations. The upper left element of this matrix will give the power spectral density of N_{qp}, denoted by $S_{N_{qp},N_{qp}}(\omega)$. In the considered case, it is given by,

$$S_{N_{qp},N_{qp}}(\omega) = \frac{2\alpha_1 \tau_1 N_{qp}^0}{1 + (\omega\tau_1)^2} + \frac{2\alpha_2 \tau_2 N_{qp}^0}{1 + (\omega\tau_2)^2}, \tag{3.7}$$

with,

$$\alpha_1 = 2\frac{\tau_1 - \tau_{esc}}{\tau_1 - \tau_2} \qquad \alpha_2 = 2\frac{\tau_{esc} - \tau_2}{\tau_1 - \tau_2},$$

where τ_1 and τ_2 are the reciprocals of the eigenvalues of $\mathbf{M}$. When integrating $S_{N_{qp},N_{qp}}(\omega)$ over frequency, we recover the the variance of the fluctuations of N_{qp}, which gives $\langle \Delta N_{qp}^2 \rangle = \sigma_{N_{qp}}^2 = N_{qp}^0$. So, GR noise is *Poissonian*.

Equation (3.7) is an exact solution, which consists of two Lorentzian spectra. However, when physical numbers for the rates are considered, we see that $RN_{qp}^0/V \ll \Gamma_B + \Gamma_{es}$, as both the pair-breaking rate and the phonon escape time are orders of magnitude smaller than the recombination rate (see for example Tables 2.2 and 2.3). With this approximation we can find the eigenvalues of $\mathbf{M}$ to be [64],

$$\tau_1 = \frac{1}{2}\frac{V}{RN_{qp}^0}(1 + \tau_{esc}/\tau_{pb}), \tag{3.8a}$$

$$\tau_2 = \frac{\tau_{esc}\tau_{pb}}{\tau_{esc} + \tau_{pb}}. \tag{3.8b}$$

Notice that τ_1 is equal to τ_{qp}^* in Equation (2.14), which includes the phonon trapping factor. Generally, τ_1 represents the quasiparticle lifetime and τ_2 the phonon lifetime in the film. With these values, the first Lorentzian in Equation (3.7) dominates the second and $\alpha_1 \approx 2$. This way, we find the main result of this section,

$$S_{N_{qp},N_{qp}}(\omega) \approx \frac{4\tau_{qp}^* N_{qp}^0}{1 + (\omega\tau_{qp}^*)^2}. \tag{3.9}$$

This tells us that GR noise manifests itself with an approximate single Lorentzian PSD. This spectrum has flat noise level of $4\tau_{qp}^* N_{qp}^0$ and a roll-off given by the apparent quasiparticle lifetime. We will use the term *flat noise level* (FNL) as the (approximately) frequency independent part of a spectrum, located at lower frequencies than the roll-off frequency. For a Lorentzian expression, this is given by the numerator.
As $\tau_{qp}^* \propto 1/N_{qp}$, the FNL is constant over temperature. In contrast, the roll-off will move to lower frequencies when the temperature is lowered, as N_{qp} goes down with temperature and τ_{qp}^* goes up.

Before we discuss how this spectrum is measured, we want to stop and make a few comments about this theory. First, it is instructive to see that in calculating the matrix $\mathbf{M}$, Equation (3.5a), the actual procedure we perform is the linearisation of the master equations. Specifically, in Equation (3.1) the quadratic term is linearised, which results in the factor 2 in the upper-left element of Equation (3.5a). The linearisation also explains why the eigenvalues of $\mathbf{M}$ give the relevant time constants of the system. Furthermore, this insight makes it clear how exactly the noise in the detector gives information about the quasiparticle dynamics. It is a version of the fluctuation-dissipation theorem [62]. Besides that, it makes us aware of the fact that this linearisation must be appropriate in order for this method to work. In our specific system, the linearisation requires that the fluctuations δN_{qp} are small compared to the average value, $\delta N_{qp} \ll N_{qp}^0$, such that the decay rate is approximately constant. For Poissonian processes, this is justified if the occupation numbers are large [37].
Secondly, systems in *equilibrium*, have a symmetric correlation matrix,

$$\sigma^2 = \left\langle \Delta\mathbf{a}(t) \cdot \Delta\mathbf{a}^T(0) \right\rangle = \left\langle \Delta\mathbf{a}(0) \cdot \Delta\mathbf{a}^T(t) \right\rangle = \frac{1}{2}\mathbf{M}^{-1}\mathbf{B}, \tag{3.10}$$

where $\mathbf{a} = (\{N_i\})$ and $\Delta\mathbf{a}$ means the deviation from the steady state values. This is due to microscopic reversibility [65] and also implies *detailed balance*, $p_{ij}^0 = p_{ji}^0$. However, a system in steady state, obeys the less strict condition $\sum_{i\neq j} p_{ij}^0 = \sum_{i\neq j} p_{ji}^0$, which in general does not imply detailed balance. If the occupation levels are connected via paired transitions (such as in Figure 3.1), this reduces to detailed balance. But if one introduces an extra transition say, from N_{qp} to $N_{\omega,B}$, cyclic transitions are possible and non-equilibrium steady state solutions are present. Van Vliet [66] describes such transitions in a semiconductor and notes that systems out of equilibrium can exhibit super-Poissonian noise ($\langle \Delta N^2 \rangle > N^0$) and quasiequilibrium systems (steady state and detailed balance) can only exhibit (sub-) Poissonian noise ($\langle \Delta N^2 \rangle \leq N^0$).

Finally, we make the connection from N_{qp} to A and θ, as that is what is actually measured. The PSD of the number of quasiparticles is given in Equation (3.9). With the responsivities dA/dN_{qp} and $d\theta/dN_{qp}$, which are given in Equation (2.27), we may write [46],

$$S_{A,A}(\omega) = S_{N_{qp},N_{qp}}(\omega)\frac{(dA/dN_{qp})^2}{1+(\tau_{res}\omega)^2}, \tag{3.11a}$$

$$S_{\theta,\theta}(\omega) = S_{N_{qp},N_{qp}}(\omega)\frac{(d\theta/dN_{qp})^2}{1+(\tau_{res}\omega)^2}, \tag{3.11b}$$

$$S_{\theta,A}(\omega) = S_{N_{qp},N_{qp}}(\omega)\frac{dA \cdot d\theta/dN_{qp}^2}{1+(\tau_{res}\omega)^2}, \tag{3.11c}$$

(3.11d)

where $S_{\theta,A}(\omega)$ is the *cross PSD* of the amplitude and phase. The division by $(1+(\tau_{res}\omega)^2)$ ensures a roll-off in the PSDs with the resonator ring time ($\tau_{res} = \frac{2Q}{\omega_0}$) which is typically in the order of microseconds, and will thus not influence the spectrum much in most cases. So, the GR noise spectrum measured in A, θ or cross (A, θ) will approximately be given by Equation (3.9) times the appropriate responsivities. In Equation (2.27), these responsivities are expressed in terms of the temperature dependent variables Q and σ_1,σ_2.
The measured PSDs of θ and A can contain contributions from other autocorrelated noise sources. For example, TLS noise, is known to have a $1/\sqrt{f}$-character, mainly in the PSD of θ [60]. The cross PSD effectively eliminates these other noise sources, as only amplitude-phase correlated noise is captured. As the amplitude mainly probes quasiparticles and phase Cooper-pairs, the cross PSD is a probe for

(anti-)correlations in those numbers. Therefore, it probes generation and recombination processes directly.

3.3. Experimental Methods

Most of the experimental methods are already addressed in Section 2.3. Here, only the measurement procedures for GR noise measurements will be discussed, along with the used MKID designs.

3.3.1. Measurement Procedure

For the GR noise measurements, the laser is off (Figure 2.11a) and the setup is at a certain bath temperature, usually in the range of 100 mK to 400 mK. The MKID is driven at resonance frequency with P_{read} and the Q and I from the IQ-mixer are measured and translated to A and θ. Two time traces are recorded: one at 50 kHz, for 40 s and one at 1 MHz for 200 ms. This is done to limit data size, while ensuring a wide frequency coverage in the PSDs. For both time traces a PSD is calculated, after which they are stitched together.

The time traces typically contain pulses, caused by external energy sources that could not be shielded off. These include cosmic rays [67] and non-shielded stray light [58]. As the amplitude of such pulses is large compared to the noise, they have a dominating effect on the PSDs and thus contaminate the noise measurement. Therefore, the time traces are filtered in the following way.
After correcting for an offset by subtracting the mean, the time traces are divided into 32 equal sections. Each section is either rejected or a PSD is calculated from it. All the calculated PSDs are later averaged. The rejection criterion is as follows. First, the section is smoothed using the *smooth* function in MATLAB, which is a moving average with the span chosen to be $\tau_{qp}^{*}/2$. This lifetime is estimated by the user. Then, for the 50 kHz data, a linear correction is subtracted from the data, to ensure that low frequency variations in the bath temperature or other drifts in the system cannot influence the rejection procedure. A section is then rejected if either the smoothed data or the raw data contains a data point above a threshold. This threshold is selected to be a multiple of the standard deviation of the smoothed or raw data, respectively. The minimum standard deviation of the full time trace and of the segment is used. In Figure 3.2, an example of this procedure is illustrated. The individual segments do not align after peak rejection, because of the linear correction.
For the data presented here, the threshold is chosen to be 5 times the standard deviation. This is the result of a trade-off between throwing out too much data and the effect of the energy deposition pulses in the time traces. See Appendix B for details on this trade-off.

After the pulse rejection, the PSDs of the individual segments are calculated with the MATLAB *pwelch* function for the amplitude and phase PSDs and with the *cpsd* for the cross PSD. It is instructive to note that a power spectral density is the Fourier transform of the (auto-) correlation via the Wiener-Khinchin theorem, when the process is wide-sense-stationary[1]. Thus when we assume $A(t)$ and $\theta(t)$

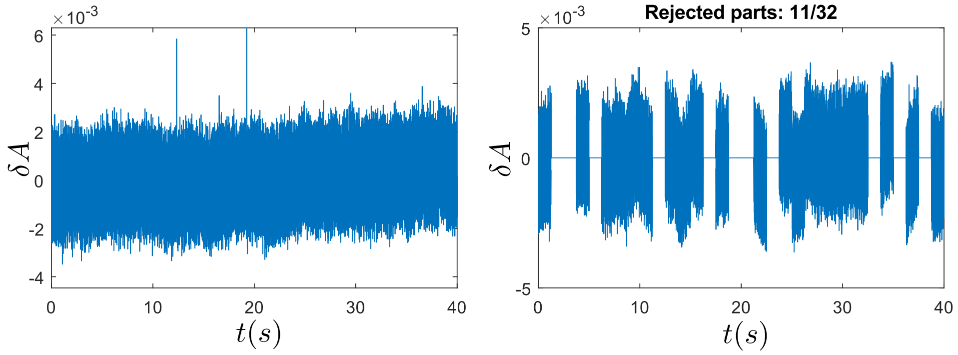

Figure 3.2: *(Left)*: Example of a smoothed and offset corrected 50 kHz amplitude time trace. *(Right)*: Same time trace after pulse rejection.

---

[1] This requires the first moment and autocovariance to be time invariant and that the second moment is finite for all times [68, p. 152]

to be mathematical functions,

$$S_{A,A}(\omega) = \int_{-\infty}^{\infty}\left[\int_{-\infty}^{\infty} A(t)A(t-\tau)dt\right]e^{-j\omega\tau}d\tau, \tag{3.12a}$$

$$S_{\theta,\theta}(\omega) = \int_{-\infty}^{\infty}\left[\int_{-\infty}^{\infty} \theta(t)\theta(t-\tau)dt\right]e^{-j\omega\tau}d\tau, \tag{3.12b}$$

$$S_{\theta,A}(\omega) = \int_{-\infty}^{\infty}\left[\int_{-\infty}^{\infty} A(t)\theta(t-\tau)dt\right]e^{-j\omega\tau}d\tau. \tag{3.12c}$$

$$\tag{3.12d}$$

Note that $S_{\theta,A}(\omega) = S_{A,\theta}(\omega)$, when $\int_0^\infty A(t)\theta(t-\tau)dt = \int_0^\infty \theta(t)A(t-\tau)dt$. Or in other words, when the cross correlation function is symmetric, which is the case for real variables.
Lastly, the spectra are down sampled to 30 points per decade in frequency, to reduce data storage and visibility at high frequencies.

An example of the PSDs retrieved this way is shown in Figure 3.3, as the blue lines in the upper right, upper left en lower left figures. These spectra are subject to other noise sources than GR noise, where the two most prominent noise sources are TLS and (HEMT) amplifier noise. TLS manifests itself mostly in the phase and has a $1/\sqrt{f}$-character. Amplifier noise manifests itself in both the amplitude and phase with a white characteristic [60]. To suppress amplifier noise, the high frequency (3×10^2 Hz to 2×10^5 Hz) maximum is subtracted from the PSDs, if the average in that range is lower than the average in 3×10^2 Hz to 1×10^4 Hz. If it is higher (such as in Figure 3.3), the minimum in that lower frequency range is subtracted.
To compensate for TLS, $A/\sqrt{f}$ is subtracted from the noise, where A is determined by the average of the first 4 data points. Figure 3.3 shows the effects of these compensation steps on the PSDs.

Lastly, to distil quantitative characteristics from these PSDs, a Lorentzian spectrum, Equation (3.9), is fitted with the Python *scipy.optimize.curve_fit* function, which uses a non-linear least squares method. The fitting range is set to start from 10 Hz and end at the minimum of the PSD in the range of 3×10^2 Hz to 2×10^4 Hz. The output gives the lifetime (τ_{qp}^*) and the flat noise level (FNL). The lower right plot in Figure 3.3 also shows the fitted Lorentzians.
As the measured spectra follow Equation (3.11), the FNLs of the spectra are dependent on the responsivities, which in turn are dependent on temperature. To extract the quasiparticle fluctuations the FNLs are divided by the appropriate responsivities, which are calculated as follows. From Equation (2.25) we know,

$$\frac{dA}{d(1/Q_i)} = -2Q, \tag{3.13a}$$

$$\frac{d\theta}{d(\delta\omega/\omega_0)} = 4Q. \tag{3.13b}$$

We can therefore calculate the responsivities via,

$$\frac{dA}{dN_{qp}} = \frac{dA}{d(1/Q_i)}\frac{d(1/Q_i)}{N_{qp}} = -2Q\frac{d(1/Q_i)}{N_{qp}}, \tag{3.14a}$$

$$\frac{d\theta}{dN_{qp}} = \frac{d\theta}{d(\delta\omega/\omega_0)}\frac{d(\delta\omega/\omega_0)}{dN_{qp}} = 4Q\frac{d(\delta\omega/\omega_0)}{dN_{qp}}. \tag{3.14b}$$

Here, $\frac{d(1/Q_i)}{N_{qp}}$ and $\frac{d(\delta\omega/\omega_0)}{dN_{qp}}$ are calculated via the measured $Q_i(T)$ and $\frac{\delta\omega}{\omega_0}(T)$ from the S_{21}-measurement, where ω_0 is the resonance frequency at the lowest temperature (50 mK). $N_{qp}(T)$ is calculated from Equation (2.1), with a quasiparticle temperature equal to the bath temperature. The high temperature values are used, to make sure we are in a thermal regime and that Q_i and $\delta\omega/\omega_0$ vary significantly with changing temperature.
The effect of the responsivities on the PSDs becomes apparent at higher temperatures. There, quasiparticles degrade Q_i to the point where Q_i limits Q and Q starts to drop with increasing temperature. This degrades the responsivity as Equation (3.14) shows. This is seen from Figure 3.4, where the compensation starts to show above 250 mK.

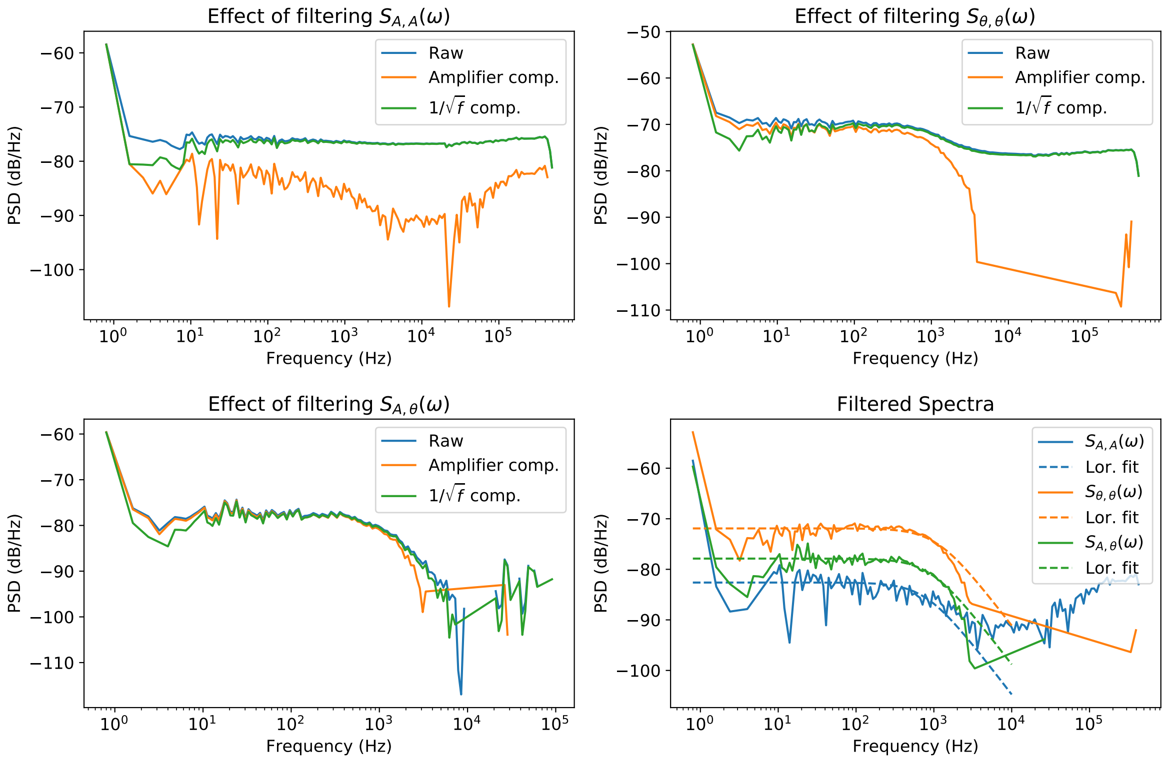

Figure 3.3: Effect of subtracting TLS and amplitude noise on PSDs: amplitude *(upper left)*, phase *(upper right)* and cross *(lower left)*. *(Lower right)*: the PSDs when subtracting both noise sources and with Lorentzian fits. The data is from LT165, KID1, −101 dBm read power and 330 mK.

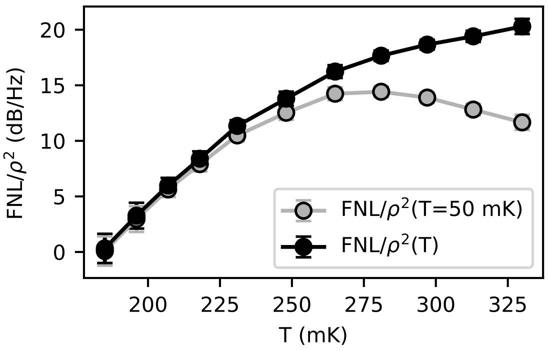

Figure 3.4: The FNLs calculated from cross PSDs via the Lorentzian fit. The FNLs are divided by the square of the low temperature (50 mK) responsivity (ρ) value and temperature dependent responsivity. Data is from LT165, KID2 at minimal (−101 dBm) read power.

3.3.2. MKID Designs

For an extensive analysis of the GR noise in different MKIDs, 7 chips have been analysed, each containing multiple MKIDs. To reduce the data size, only relevant MKIDs with good performance (i.e. quality factors) are measured. This section will briefly explain the chip designs. Table 3.1 summarizes all the different chip designs.

LT132 This chip contains 30 hybrid MKIDs, with different NbTiN and Al lengths. At 15 MKIDs (the top ones in Figure 3.5), before the NbTiN deposition, a SiO_2-patch was placed on the location where the Al is later deposited. After etching of the NbTiN, this patch is removed, and the Al is deposited and etched. This is ensures a pristine surface underneath the Al. The Al sections are 1.25 µm wide and 0.3 mm to 1.6 mm long. The capacitive NbTiN section is a meandering CPW. The processing is done on a Sapphire wafer. Figure 3.5a provides an overview of the chip design and Figure 3.5b shows a zoom-in on one of the MKIDs.

LT139 is discussed in Section 2.3.3.

LT145 is an exact copy of LT139, except with an 150 nm Al film, instead of 50 nm.

LT165 is discussed in Section 2.3.3.

LT165W2 is an exact copy of LT165, except with an 25 nm Al film, instead of 50 nm.

LT179 contains 16 hybrid MKIDs (see Figure 3.5c), with all different Al and capacitive sections. The capacitive NbTiN is shaped in a double sided IDC, such as in LT165. The Al lengths vary from 0.12 mm to 1.6 mm. The Al width is 0.6 µm and thickness is 40 nm. At the end of the Al strip, a wide band, twinslot antenna is placed with a micro lens on top (such as described in Reference [69]), to couple TeraHertz radiation to the MKIDs. This antenna is visible in Figure 3.5d. We will only look at dark measurements, so this will have no effect on the data analysed here. All MKIDs are processed with the SiO_2 patch, as described for LT132.

LT179Wide is an exact copy of LT179, except with a Al line width of 1.5 µm instead of 0.6 µm

Table 3.1: Overview of parameters of the different chips presented in this thesis.*= not measured, but assumed.

Chip	Al Thickness (nm)	Al Width (µm)	Al Length (mm)	Capacitor design	Substrate (membrane)	$Si0_2$ Patch	T_c (K)
LT132	50	1.25	0.3 to 1.6	CPW	c-Sapphire	15/30	1.24
LT139	50	0.92	0.26 to 0.53	CPW	c-Sapphire	No	1.20
LT145	150	0.92	0.26 to 0.53	CPW	c-Sapphire	No	1.12
LT165	50	2	0.3	double IDC	Si (SiN)	Yes	1.255
LT165W2	25	2	0.3	double IDC	Si (SiN)	Yes	1.35
LT179	40	0.6	0.12 to 1.6	double IDC	c-Sapphire	Yes	1.2*
LT179Wide	40	1.5	0.12 to 1.6	double IDC	c-Sapphire	Yes	1.2*

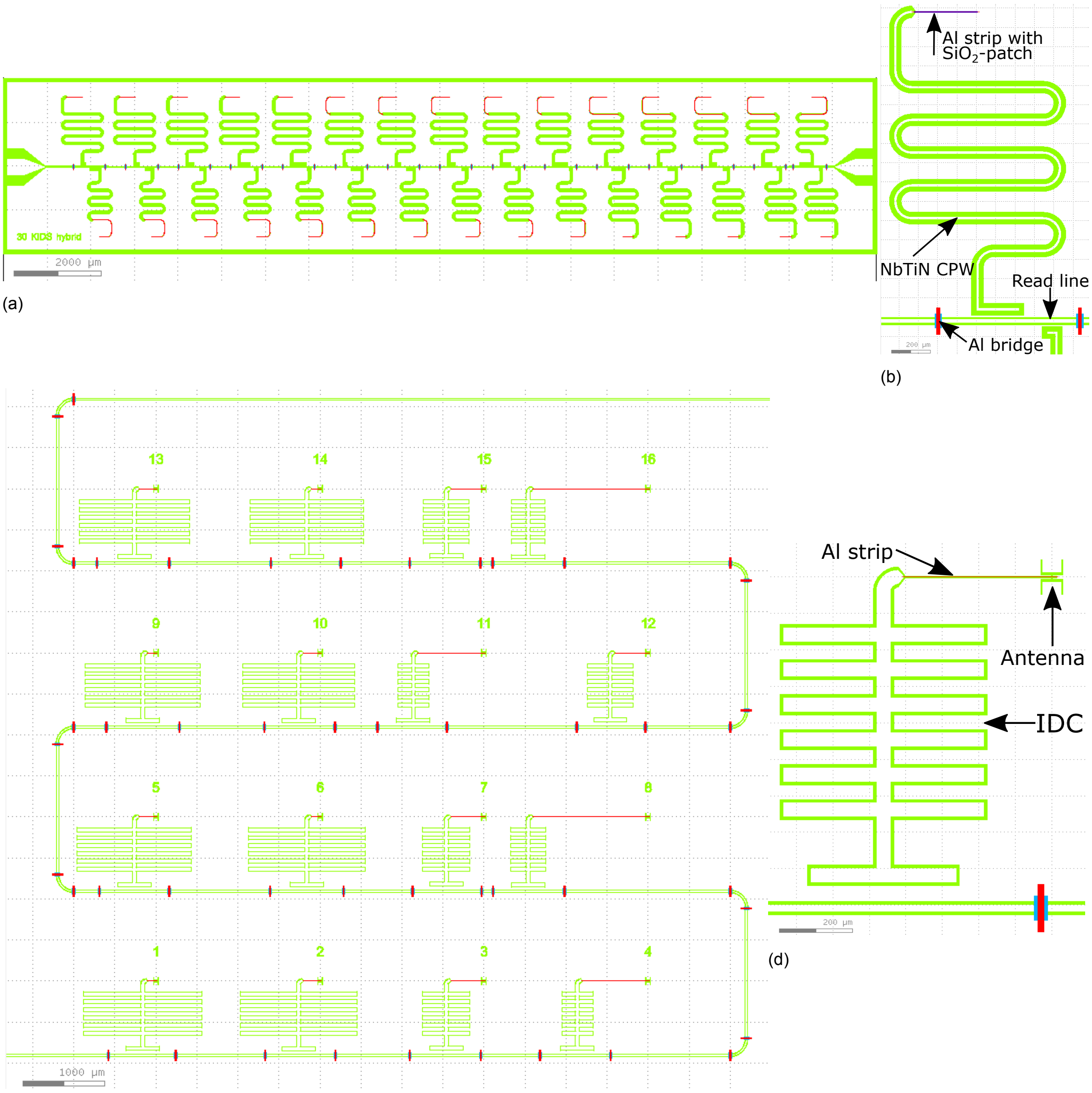

(a)

(b)

(c)

(d)

Figure 3.5: (a): Overview of LT132, red is Al, blue SiO$_2$, green is substrate, light blue is polyamide and white is NbTiN. (b): Zoom-in of one of the MKIDs in LT132, with the SiO$_2$ patch. (c): Overview of LT179. (d): Zoom-in of one of the MKIDs in LT179, with the twinslot antenna at the end of the Al strip.

3.4. Results and Discussion

Our focus will lay on when and how the unpredicted noise level drop is present, with respect to different MKID variables. First, the effect of phonon trapping will be discussed, by comparing measurements on substrate and membrane. Then, geometric parameters will be addressed, which includes: Al strip length, thickness and width. The effect of the SiO$_2$ will be discussed shortly. Lastly, read power effects to the GR noise drop are discussed, after which a discussion and conclusion of this chapter will be given. All the data sets analysed are presented in Appendix D.

3.4.1. Phonon Trapping

As we saw in Sections 2.2.2 and 2.4.2, phonon trapping causes an increase in quasiparticle lifetime, via the phonon trapping factor (Equation (2.14)). Therefore, from Equation (3.9), we see that we would expect a higher FNL, when phonon trapping is higher.

In LT165, KID2 is on a 110 nm membrane, increasing the phonon trapping factor, and KID3 is not.

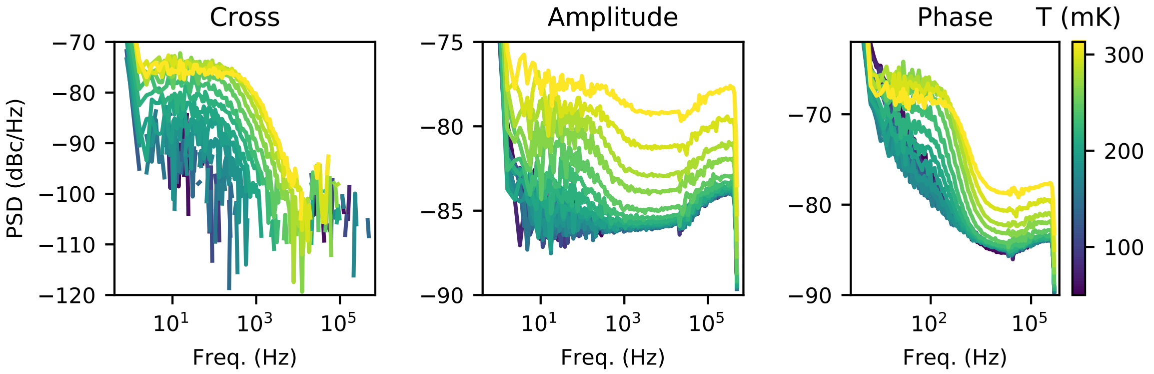

(a) KID2

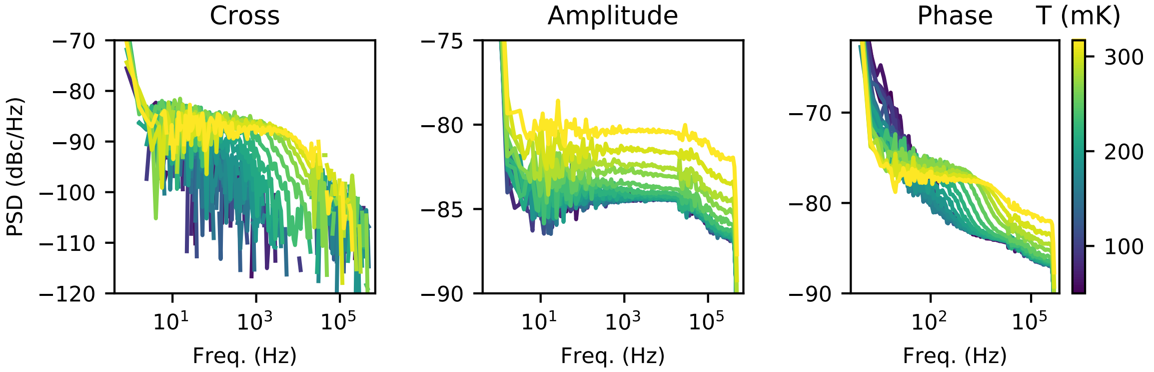

(b) KID3

Figure 3.6: Raw spectra for KID2 (a) and KID3 (b) of LT165, for the lowest available read power (−101 dBm for KID2 and −99 dBm for KID3).

The raw cross, amplitude and phase spectra are shown in Figure 3.6. The lowest available read power is chosen, to minimize any possible read power effects. At high temperatures, a decrease in noise level is visible, which is caused by the lower responsivity. Also, the amplifier noise is present in the amplitude and phase PSDs, as a high frequency flat level. TLS is seen in the low temperature phase spectra as a $1/\sqrt{f}$-feature. In the cross spectra these other noise sources are very much suppressed. The GR noise drop is clearly and consistently visible in all three PSDs (amplitude, phase and cross) as the noise levels (FNLs) go down with temperature.
Figure 3.7, gives the results of the Lorentzian fits to the spectra, after TLS and amplitude noise are subtracted. At high temperatures, the FNL is much higher for the membrane MKID, than for the substrate MKID, as expected. When we take the high temperature FNL of KID3 to be 9 dBc/Hz/rad and of KID2 20 dBc/Hz/rad (indicated by the dashed lines), we calculate a factor 12.6 higher FNL for KID2. Looking at values of τ_{esc} and τ_{pb} in Table 2.3, we see the phonon trapping factor $(1+\tau_{esc}/\tau_{pb})$ is a factor 12.4 higher. Therefore we see that phonon trapping causes a higher FNL, as explained by Equation (3.9).

For lower temperatures, the FNL drop is clearly visible in all the three PSDs, which is not explained by theory. From Equation (3.9) we would expect the FNL to be constant over temperature. As a reference, Figure 3.8 shows the expected behaviour. These amplitude PSDs at different temperatures, measured by de Visser et al. [46] on full Al MKIDs (not hybrids), show a constant FNL over temperature. These spectra can be compared to the PSDs in Figure 3.6 where a FNL drop is visible. In KID2, it is more apparent due to the higher FNL at high temperatures, and starts earlier (at approximately 300 mK). Only the Lorentzian fits with a relative error of 23% in lifetime are shown, which ensures that there is a Lorentzian shape present in the spectrum. That means that below 200 mK, there is no GR signature present in the spectra. A higher read power could help with resolving the spectra a bit more, as the TLS

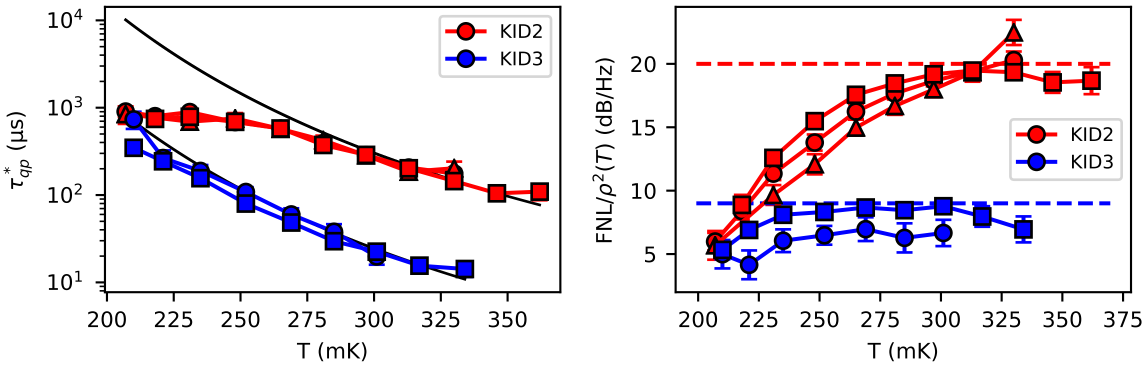

Figure 3.7: Lifetime and FNL for KID2 and KID3 of LT165, for the lowest available read power (−101 dBm for KID2 and −99 dBm for KID3), retrieved from a Lorentzian fit to the spectra (○: cross, △: amplitude and □: phase). Errorbars indicate the statistical error in the Lorentzian fit. The amplitude fits for KID3 are missing because they do not meet this requirement. The FNLs are divided by the appropriate responsivities (denoted by $\rho(T)$) as described in Section 3.3. The solid black lines in the lifetime plot are Kaplan curves (Equations (2.8) and (2.14)) where the τ_{esc} is used from Table 2.3. The dashed lines indicate 20 dBc (red) and 9 dBc (blue).

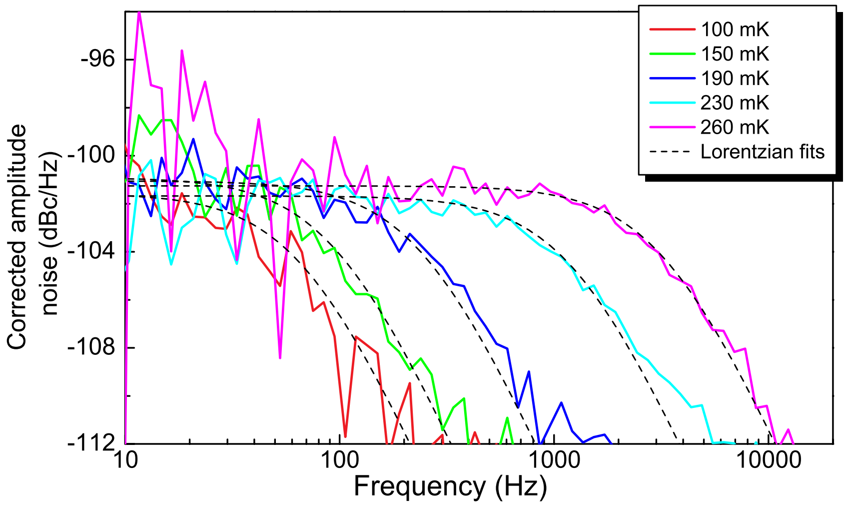

Figure 3.8: Amplitude PSDs at different temperatures measured by de Visser et al. [46] for full Al MKIDs. The PSDs are corrected for other noise sources by subtracting a measured PSD with an off-resonance read signal. Image from [46].

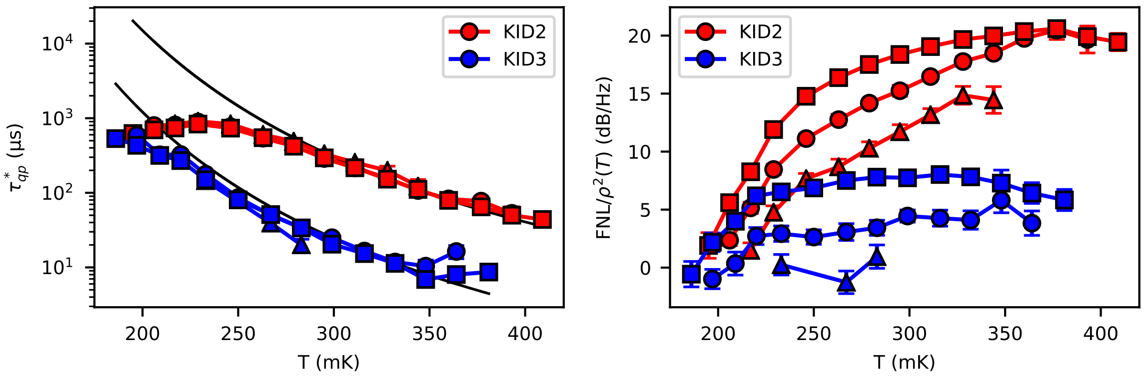

Figure 3.9: Lifetime and FNL for KID2 and KID3 of LT165, (○: cross, △: amplitude and □: phase) at at −91 dBm for KID2 and −89 dBm read power for KID3. The FNLs are compensated for responsivity ($\rho(T)$) as described in Section 3.3. The solid black lines in the lifetime plot are Kaplan curves (Equations (2.8) and (2.14)) with the calculated τ_{esc} in Table 2.3.

noise goes down with read power [60] and the amplifier noise will be lower, relative to the increased signal. Figure 3.9 shows the same data analysis, but at −91 dBm for KID2 and −89 dBm for KID3. Here, the GR noise spectra can be fitted a bit better, but still disappear below 180 mK.

The lifetimes seen in Figure 3.7 are the same for cross, amplitude and phase spectra. As we saw in Section 2.4.2, phonon trapping increases the lifetime by the phonon trapping factor (relative factor 12 in this case), which is also apparent here. Moreover, the lifetimes seem to saturate to 800 µs for lower temperatures, which is most visible in the KID2 data. The start of this saturation, which is the start of the deviation with the Kaplan curves (solid black lines), happens at approximately the same temperature as the FNL drop (300 mK).

3.4.2. Al Length

LT179 has the most variation in Al length, which is ranging from 0.12 mm to 1.6 mm. As the cross PSDs suffers the least from other noise sources and the GR noise drop is visible in all three spectra, we will focus on the cross PSDs. In Figure 3.10, the lifetimes and responsivity compensated FNLs from the Lorentzian fits are displayed. Only fits with an relative error of less than 21% in lifetime are shown.

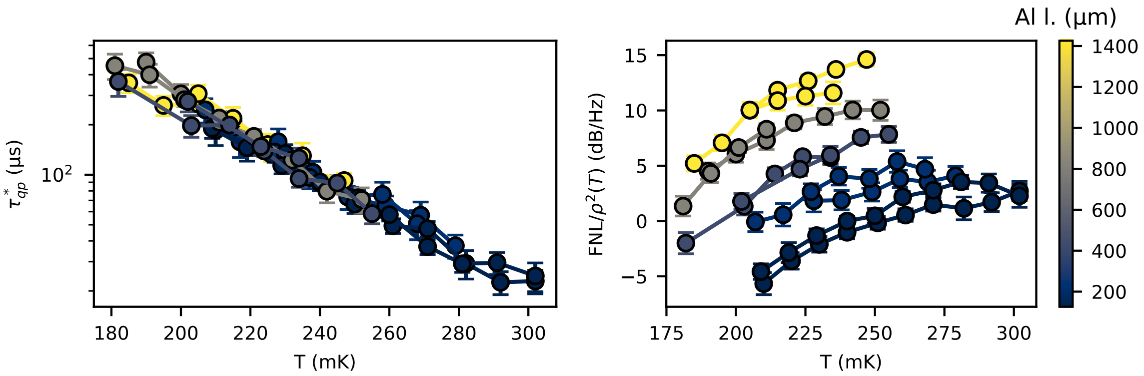

Figure 3.10: Lifetimes (left) and FNLs (right) of LT179 cross PSDs for MKID numbers: 1,2,4,5,8,9,11,12,13,15, at the lowest available read powers, ranging from −110 dBm to −119 dBm. Colour represents Al length with the scale shown on the right. The FNLs are compensated for responsivity, indicated by the $\rho^2(T)$

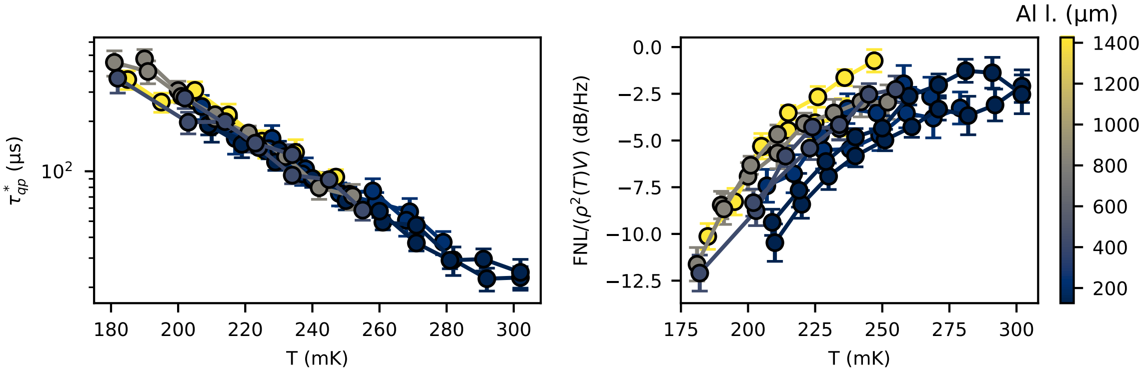

Figure 3.11: Lifetimes (left) and FNLs (right) of LT179 cross PSDs for MKID numbers: 1,2,4,5,8,9,11,12,13,15, at the lowest available read powers, ranging from −110 dBm to −119 dBm. Colour represents Al length with the scale shown on the right. Only fits with an relative error of less than 21% are shown. The FNLs are compensated for responsivity (ρ) and volume (V).

The lifetimes of the KIDs are almost identical, whereas the FNLs clearly increase for longer Al strips. This is expected, as the FNL is proportional to $\tau^*_{qp}N_{qp}$ (Equation (3.9)) and N_{qp} is proportional to Al volume. To check this expected dependence, we again divide the FNLs by volume and retrieve Figure 3.11. We see that the FNL volume dependence of about 15 dB Hz^{-1} for the Al length range we are considering, decreased to about 5 dB Hz^{-1}.

In Section 3.4.6, we will see that read power effects can have a significant effect on the high temperature FNLs, sometimes as large as 10 dB Hz^{-1}. The lowest available read power differs per MKID, ranging from −110 dBm to −119 dBm. Moreover, we do not have an appropriate measure for MKID read power effects, as these differ for MKID geometry. Therefore, comparing these FNLs from different MKIDs with an accuracy of 5 dB Hz^{-1} is difficult.
However, there is still an Al length dependence seen in Figure 3.11. Therefore, if this is attributed to read power effects, there must be a read power effect that is Al length dependent as well. A hint on this dependence can be found in the kinetic inductance fractions of these MKIDs, seen in Figure 3.12. The smaller the length, the lower the kinetic induction fraction, which is explained by the fact that also the NbTiN capacitive section has an non-zero inductance. This could suggest that the Al length dependence on the FNL seen in Figure 3.11 is due to read power effects. However to verify this hypothesis, a detailed analysis on read power dissipation by quasiparticles versus Al length is needed.

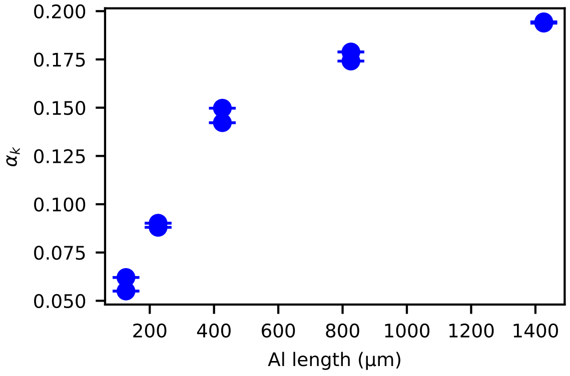

Figure 3.12: Kinetic induction fractions of the MKIDs analysed of LT175 versus Al length with errorbars. The calculation method is described in Section 2.2.4, and is done at the lowest available read powers.

3.4.3. Al Thickness

We have two pairs of chips that have an equivalent design, but different Al film thickness: LT165 and LT165W2 (50 nm and 25 nm) and LT139 and LT145 (50 nm and 150 nm). These will be discussed in that order. We will again only look at cross PSDs.

Apart from the volume, films with a different thickness, will have different phonon escape times, as discussed in Section 2.2.2. For KID2, the calculated escape times are 4.9 ns for the 50 nm and 2.5 ns for the 25 nm film, which is consistent with Equation (2.10). Moreover, thinner Al films have a higher critical temperature [70], which have been measured to be 1.255 K and 1.35 K for the 50 nm and 25 nm films, respectively.

All of these three parameters (V,τ_{esc} and k_BT_c) influence the FNL, as,

$$4\tau^*_{qp}N_{qp} = V\tau_0N_0\frac{(k_BT_c)^3}{\Delta^2}(1+\tau_{esc}/\tau_{pb}), \tag{3.15}$$

where we used Equations (2.8) and (2.14). As k_BT_c is changing, also Δ changes via Equation (2.3), which at low temperatures gives $\Delta \propto T_c$. To see the effect of film thickness, we compare the cross PSD FNLs of LT165 and LT165W2 for KID2 at the lowest read powers, both −101 dBm. We divide the FNL by responsivity squared (to get the quasiparticle fluctuations) and by the phonon trapping factor, volume and by $(k_BT_c)^3/\Delta^2$, to compensate for the thickness variation effects. The result is seen in Figure 3.13.

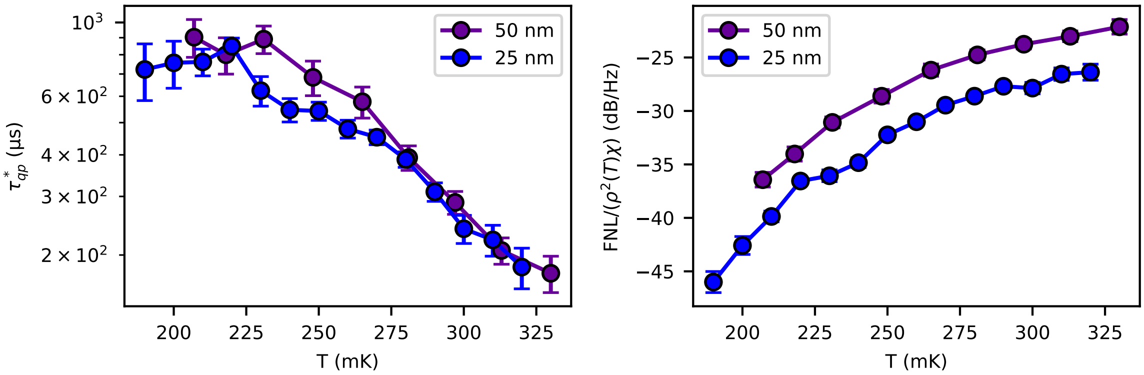

Figure 3.13: Lifetime (left) and FNL (right), compensated for responsivity (ρ) and $\chi = V(1+\tau_{esc}/\tau_{pb})(k_BT_c)^3/\Delta^2$, from cross PSDs for LT165 (50 nm Al thickness) and LT165W2 (25 nm Al thickness), both KID2, and both −101 dBm read power. Only fits with a relative error of less than 22% in lifetime are shown.

It is clear that the temperature behaviour of the FNL drops is the same. The FNL of the 25 nm film is in general a bit lower; about 4 dB Hz^{-1}. It is not known what causes this offset, although it is in range of what read power effects can cause.

The other set of chips, LT139 and LT145, of 50 nm and 150 nm respectively, have a measured T_c of 1.24 K and 1.12 K. For KID7 of each chip, the escape times are calculated (see Section 2.2.4) to be (0.21 ± 0.10) ns for LT139 and (1.0 ± 0.2) ns for LT145. Within the error bounds, it is consistent with Equation (2.10). The relatively large error is the result of sparse data, as the there are only a few temperature points (6, from 120 mK to 320 mK) for these chips. Figures 3.14 and 3.15 show the lifetimes and compensated FNLs for two different read powers.

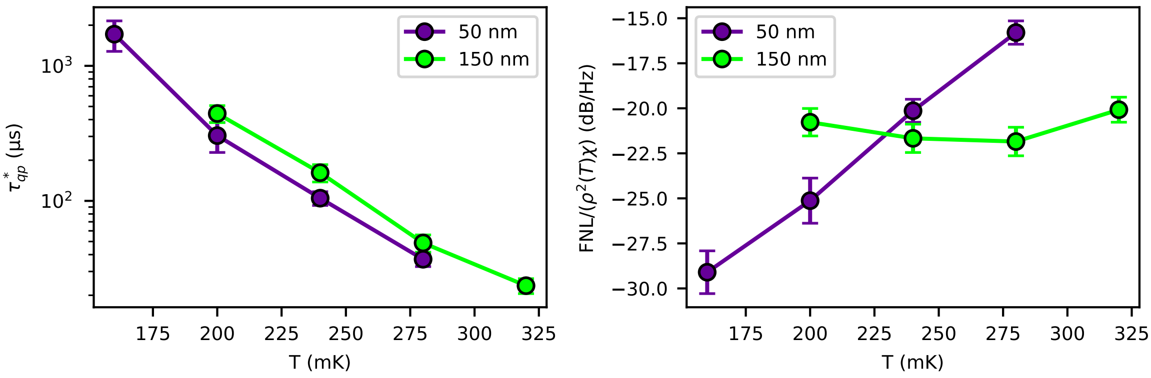

Figure 3.14: Lifetime (left) and FNL (right), compensated for responsivity (ρ) and $\chi = V(1 + \tau_{esc}/\tau_{pb})(k_B T_c)^3/\Delta^2$, from cross PSDs for LT139 (50 nm Al thickness) and LT145 (150 nm Al thickness), both KID7, and −104 dBm and −92 dBm read power, respectively. Only fits with a relative error of less than 30% in lifetime are shown.

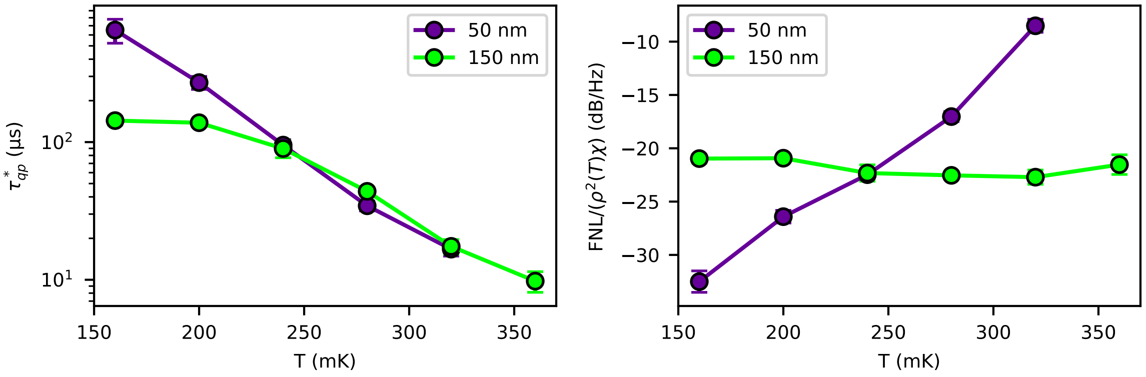

Figure 3.15: Lifetime (left) and FNL (right), compensated for responsivity (ρ) and $\chi = V(1 + \tau_{esc}/\tau_{pb})(k_B T_c)^3/\Delta^2$, from cross PSDs for LT139 (50 nm Al thickness) and LT145 (150 nm Al thickness), both KID7, and −96 dBm and −80 dBm read power, respectively. Only fits with a relative error of less than 30% in lifetime are shown.

The most important observation is that there is no GR noise drop visible in LT145, whereas there is in LT139. The same behaviour is also observed in all the other MKIDs in these chips. So, at these variations of film thickness, the GR noise drop is dependent on film thickness.
Another observation is that in LT145, lifetime saturation to about 150 µs is visible, whereas at LT139 it is not. We will revisit this observation in Section 3.4.6.

3.4.4. Al Width

The effect of the Al width to the GR noise drop can be seen from LT179 and LT179Wide, as those chips are identical except for the Al width, which are 0.6 µm and 1.5 µm, respectively. We will compare the lifetimes and FNLs, compensated for responsivity and volume, for the lowest read powers.

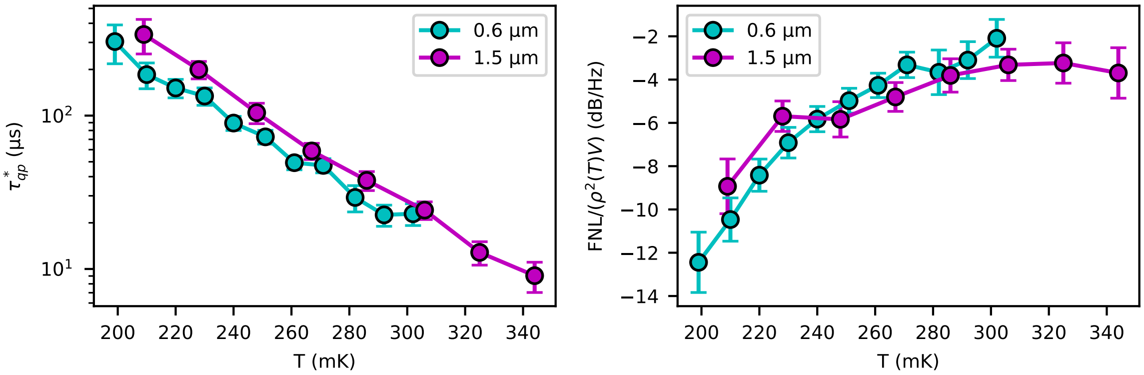

Figure 3.16: Lifetime (left) and FNL (right), compensated for responsivity and volume, from cross PSDs for LT179 (0.6 µm Al width) and LT179Wide (1.5 µm Al width), both KID8 at lowest read powers −100 dBm and −98 dBm, respectively. Only fits with a relative error of less than 30% in lifetime are shown.

Figure 3.16 shows the results for KID8 of these chips. No apparent Al width effect on the GR noise drop is visible, as the temperature behaviour is similar. The same is observed in the other MKIDs in these chips, at low read powers.

3.4.5. Substrate Roughness

LT132 the first 15 MKIDs are processed with a SiO_2 (KID1-15) and the others are not (KID16-30). The purpose of this intermediate processing step is to decrease the substrate roughness, having a more pristine surface underneath the Al.

The individual MKIDs differ in Al length, so we compensate the FNLs for responsivity and volume, to see the effect of a SiO_2 patch. Figure 3.17 shows the compensated FNLs and lifetimes from fits to the cross PSDs of 6 selected MKIDs (3 with, and 3 without patch), all at minimal read power. The MKIDs with the smallest Al length have been selected.

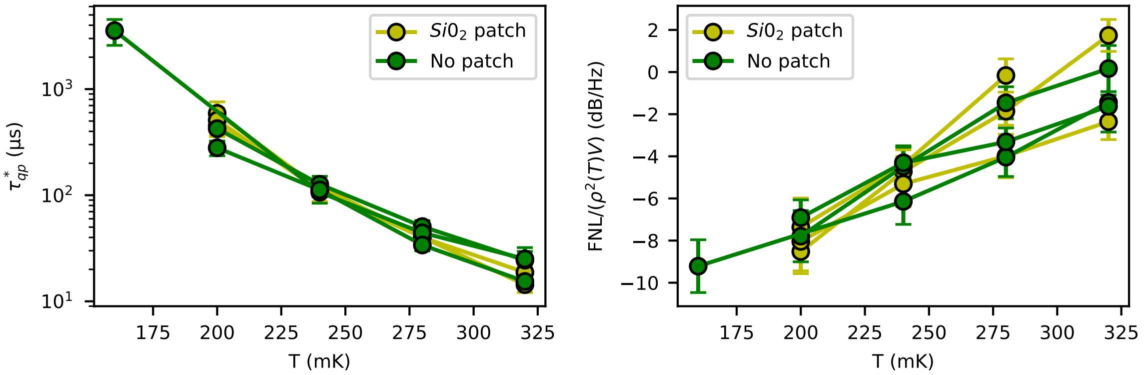

Figure 3.17: Lifetime (left) and FNL (right), compensated for responsivity (ρ) and volume (V), from cross PSDs for LT132, KID1,2,4 (with patch) and KID16,17,19 (without patch), at lowest read powers. These are −97 dBm, −99 dBm, −91 dBm, −94 dBm, −94 dBm and −88 dBm, respectively. Only fits with a relative error of less than 30% in lifetime are shown.

There is no clear effect on the lifetimes and FNLs due to the SiO_2 patch visible.

3.4.6. Read Power

Until now, we mostly looked at the lowest read powers, to avoid as much of read power effects as possible. In this section, we will look at higher read powers, to see how the GR noise drop changes. The known effects of read power are creation of excess quasiparticles, noticeable at low temperatures [7] and redistribution of quasiparticles [6] and phonons [71, 72] in energy. At very high read powers, the current in the superconducting Al broadens the density of states [73], which causes a frequency

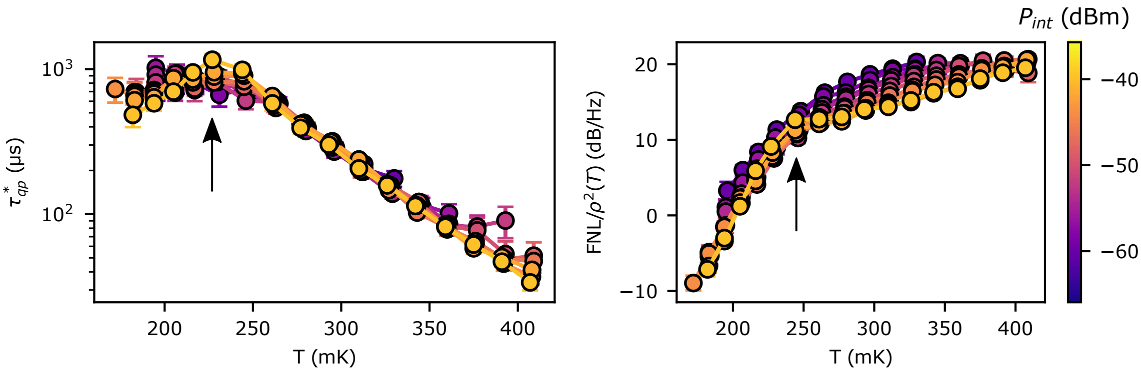

Figure 3.18: Lifetime (left) and FNL (right), compensated for responsivity (ρ), from cross PSDs for LT165, KID2 (on a membrane). Only fits with a relative error of less than 25% in lifetime are shown. The arrows indicate the peak in lifetime and sharp knee in the FNL drop.

shift in the resonator. This leads to an asymmetric S_{21}-dip, as the supercurrent is dependent on the frequency detuning of the read signal with respect to the resonance frequency. Eventually this leads to bifurcation, where S_{21} has not a uniquely defined value in a range of frequencies [74]. For the measurements presented in this thesis, the read power is varied to just before the point of bifurcation. We will first look at power effects in LT165, as the GR noise drop is most prominent in these MKIDs. Then, we will consider the power effects in LT179 and LT179Wide and lastly LT145, which does not show a GR noise drop.

In this section, the read powers will be translated to *internal* power, to ensure better MKID to MKID comparisons. Internal power is the stored energy in the resonator (the full resonator, not just the Al section) times the resonance frequency and given by [20],

$$P_{int} = \frac{Q^2}{\pi Q_c} P_{read}. \tag{3.16}$$

As Q is temperature dependent, P_{int} is temperature dependent as well. Here, the value at minimal temperature (~120 mK) will be used.

For KID2 in LT165 (on a membrane), the lifetimes and responsivity compensated FNLs are seen in Figure 3.18. For the lifetime, a peak around 230 mK becomes visible at higher read powers, which was also seen when comparing Figures 3.7 and 3.9. Moreover, the FNL drop gets a knee shape (also at 230 mK) at higher read powers, instead of a gradual decay seen at lower read power. At the intermediate temperatures (~320 mK) the difference in FNL is quite high (approximately 6 dB Hz^{-1}), whereas for higher temperatures the FNLs coincide. In general, at all MKIDs, a lower FNL (compensated for responsivity) is observed for higher read powers.

For LT179 KID8, a similar behaviour is seen in Figure 3.19. Higher power leads to a peak in lifetime and a sharp knee behaviour in FNL. However, at this MKID, the higher read out power causes the FNL to rise as well, before dropping. This could be an effect of the current in the Al coming close to the bifurcation limit, but further analysis is needed to confirm this. The internal power is still lower than in Figure 3.18, but as mentioned, this is the total resonator power and the power in just the Al strip is different. To make a full comparison, an analysis on the power behaviour inside the hybrid MKID resonators is needed.

For the same MKID geometry, but with a wider Al strip (1.5 µm instead of 0.6 µm), the lifetimes and compensated FNLs look like Figure 3.20. We see that at higher powers, the lifetime saturates to a lower value. The other MKIDs in LT179Wide also show a decrease in GR noise drop and lifetime saturation with increasing read power.

Moreover, there seems to be a cross-over regime in the read power where the FNL increases with decreasing temperature. This regime coincides with the onset of the decrease in lifetime saturation.

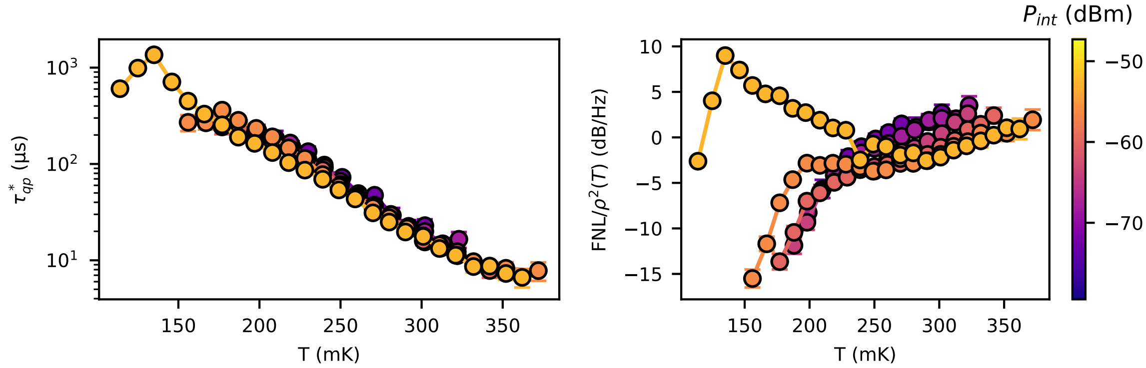

Figure 3.19: Lifetime (left) and FNL (right), compensated for responsivity, from cross PSDs for LT179, KID8 for different read powers. Only fits with a relative error of less than 22% in lifetime are shown.

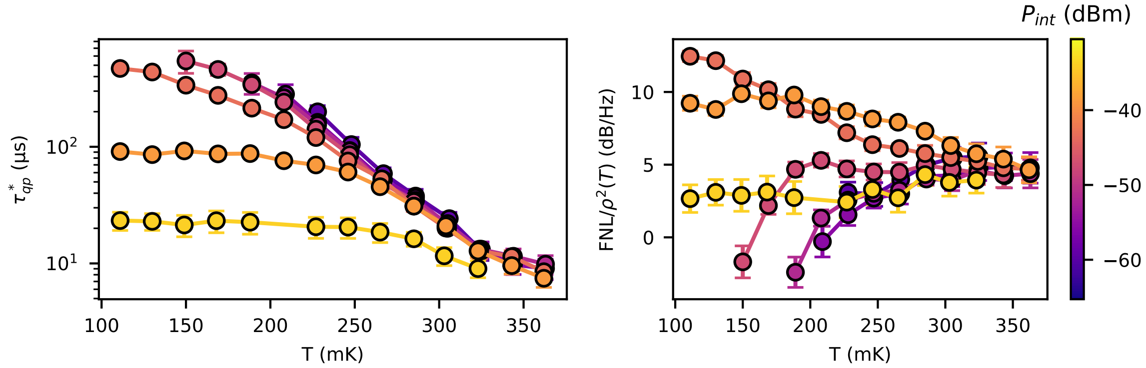

Figure 3.20: Lifetime (left) and FNL (right), compensated for responsivity (ρ), from cross PSDs for LT179Wide, KID8 for different read powers. Only fits with a relative error of less than 22% in lifetime are shown.

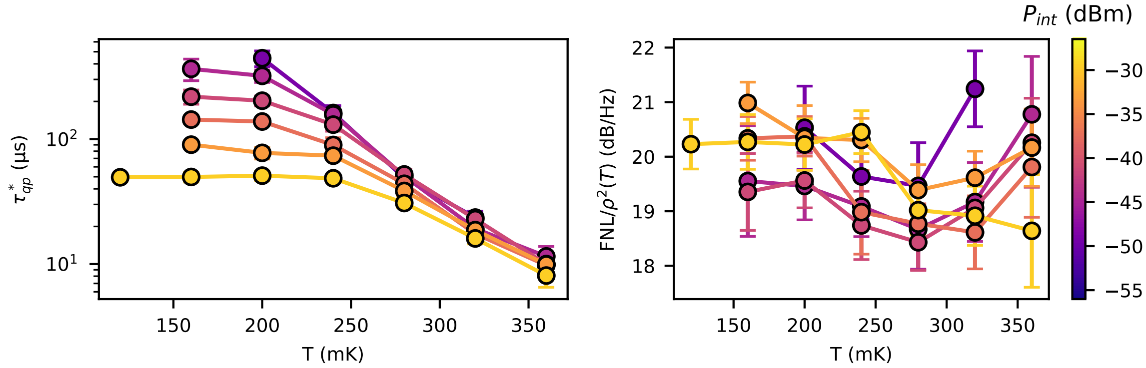

Figure 3.21: Lifetime (left) and FNL (right), compensated for responsivity, from cross PSDs for LT145, KID7 for different read powers. Only fits with a relative error of less than 22% in lifetime are shown.

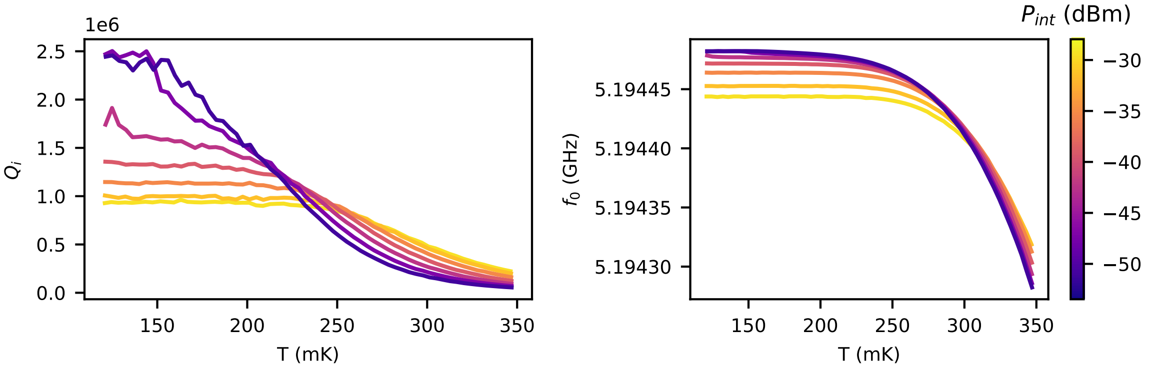

Figure 3.22: Internal quality factor (left) and resonance frequency (right) for LT145, KID7 for different read powers. Data is from a S_{21} measurement.

In LT145, with a 150 nm thick Al film, there is also a decrease in saturation lifetime visible (Figure 3.21), but without a GR noise drop. This resembles data presented in Reference [7], where they attribute the decrease in saturation lifetime to creation of excess quasiparticles by the microwave read out signal. Further inspection of the internal quality factor and resonance frequency from the S_{21}-measurements, Figure 3.22, shows that at low temperatures, the quality factor and resonance frequency simultaneously decrease. This indicates a higher effective quasiparticle temperature, as argued in [6], and thus a higher quasiparticle number, i.e. microwave induced excess quasiparticles. This behaviour of Q_i and f_0 is generally not seen in the MKIDs of other chips, that do show a GR noise drop.

Reconsidering the conclusion that the film thickness plays a role in the occurrence of the GR noise drop, we see that it could be the case that the GR noise drop in LT145 is masked by the power effects. It is possible that the power in the Al strip creates excess quasiparticles at a higher level than the GR noise drop occurs, resulting in a constant FNL. Again, an analysis on the MKID internal power is needed to confirm this.

3.5. Discussion

Now we know how the GR noise drop behaves with respect to phonon trapping, MKID geometry, substrate roughness and read power, we will analyse the GR noise drop itself in more detail. In this section, we will combine the lifetime and FNL data to see if we can grasp the quasiparticle dynamics and guide us to a possible explanation.

First of all, it is instructive to interpret the (responsivity compensated) FNL as $4\tau^*_{qp}N_{qp}$, where τ^*_{qp} is given by the roll-off of the same cross PSD. By this interpretation we assume the quasiparticle noise to be Poissonian ($\langle \Delta N^2_{qp}\rangle = N_{qp}$). By doing so, we can calculate the number of quasiparticles, analogous to [46], by dividing the FNL with $4\tau^*_{qp}$, where the measured lifetime, extracted from the Lorentzian fit. By using the cross PSDs, we ensure that we probe quasiparticle-Cooper-pair fluctuations, with the lowest contributions of other noise sources. The calculated N_{qp} will therefore represent the total number of quasiparticles in the system. We can compare this number divided by Al volume with the thermal density of quasiparticles given by Equation (2.1). The exact numbers are susceptible to errors in the amplitude and phase responsivities. However, the temperature behaviour can still be recovered this way. Figure 3.23 shows the results of such a calculation for the membrane MKID in LT165 and the KID7 of LT145, where no GR noise drop is present.

From LT165 (left), it is clear that the number of quasiparticles is close to thermal behaviour during the GR noise drop, for all read powers. This resemblance supports our assumption of Poissonian noise. From this, we can conclude that in this MKID, the read power does not cause excess quasiparticles, for temperatures as low as 170 mK . Furthermore, this means that the peak in lifetime and sharp knee in FNL are coupled and caused by the same read power effect.

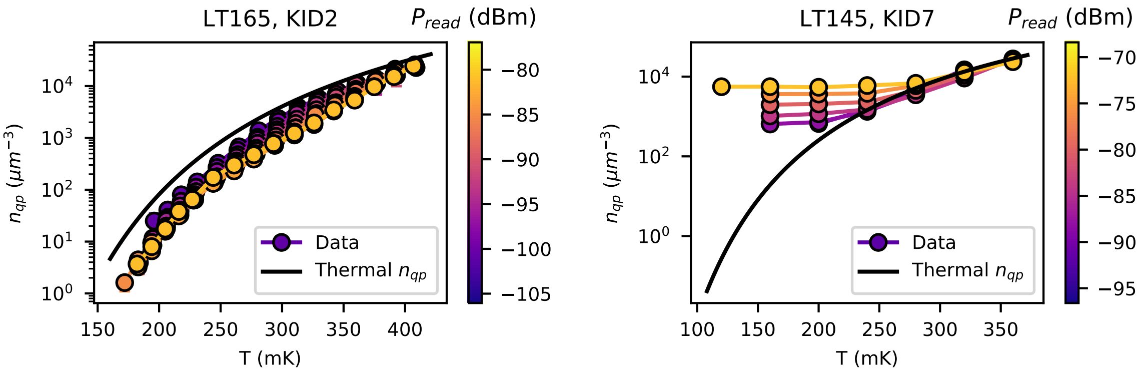

Figure 3.23: Calculated n_{qp} via lifetime and responsivity compensated FNLs for different read powers, of LT165, KID2 (left) and LT145 KID7 (right).

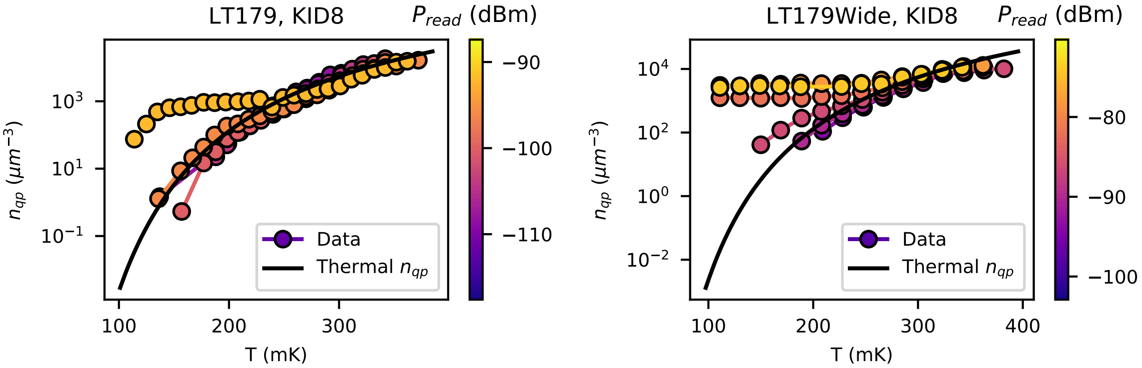

Figure 3.24: Calculated n_{qp} via lifetime and responsivity compensated FNLs for different read powers, of LT179, KID8 (left) and LT179Wide KID8 (right).

Extending this reasoning, we see that the GR noise drop is caused by a process that saturates the quasiparticle lifetime, while keeping the quasiparticle number thermal. This contrasts the lifetime saturation in LT145, which is dependent on read power. As we have seen, there the read power creates excess quasiparticles, which is also depicted in Figure 3.23 (right).
To check the rising FNLs in LT179 (Figures 3.19 and 3.20), the same analysis is done on these MKIDs and is shown in Figure 3.24. From this figure, it is clear that the number of quasiparticles does not increase, but saturates only at the highest power. From this analysis (assuming the noise to be Poissonian), the rise in FNL seems thus to be caused by a rise in lifetime, while the quasiparticle number is constant.

Another way to check if the number of quasiparticles is thermal, is looking at the internal quality factor. Via Equation (2.18), the ratio σ_2/σ_1 can be calculated, which can be translated to a quasiparticle density via Equations (2.1) and (2.4). Figure 3.25 shows these calculations as the green solid line, for the highest read powers in LT165 KID2 and LT145 KID7.
For LT145, we see that Q_i also describes the excess quasiparticles created by the read power, as expected. For LT165, the predicted n_{qp} from Q_i follows the thermal behaviour, up to a point where it saturates, around 250 mK. This saturation begins a slightly later than the GR noise drop (at 300 mK, see Figure 3.7), which might indicate that the quasiparticle number is thermal during the GR noise drop. However, as the internal quality factor saturates close to the onset temperature, it is hard to justify this claim.
The cause of this Q_i saturation is most likely not due to excess quasiparticles generated by read power, as Q_i does not decrease with decreasing power. Instead, it increases as seen in Figure 3.26. This is a sign of TLS noise [60], and Q_i could be limited by by this loss mechanism. The dashed line in Figure 3.23

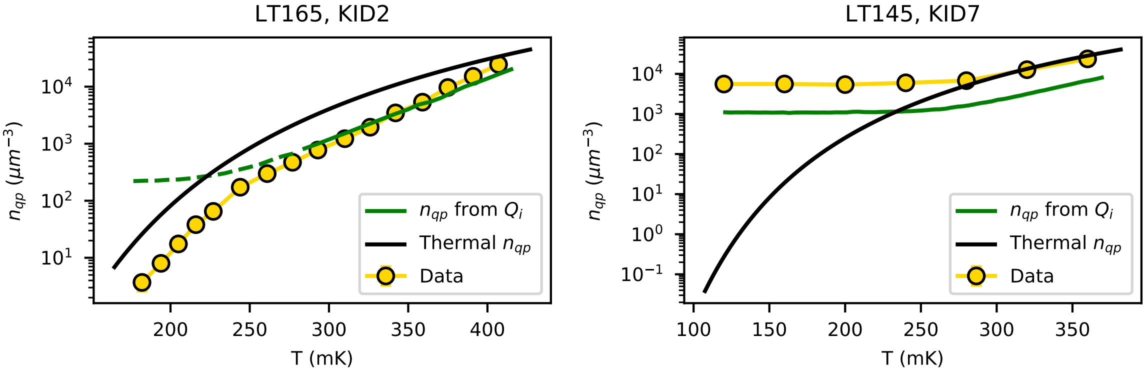

Figure 3.25: Calculated n_{qp} via lifetime and responsivity compensated FNLs of LT165, KID2 (left) and LT145 KID7 (right), at −81 dBm and −72 dBm read power, respectively. Also the quasiparticle density via Q_i is included as a green solid line. The dashed line indicates that the Q_i factor is not limited by losses int he quasiparticle system.

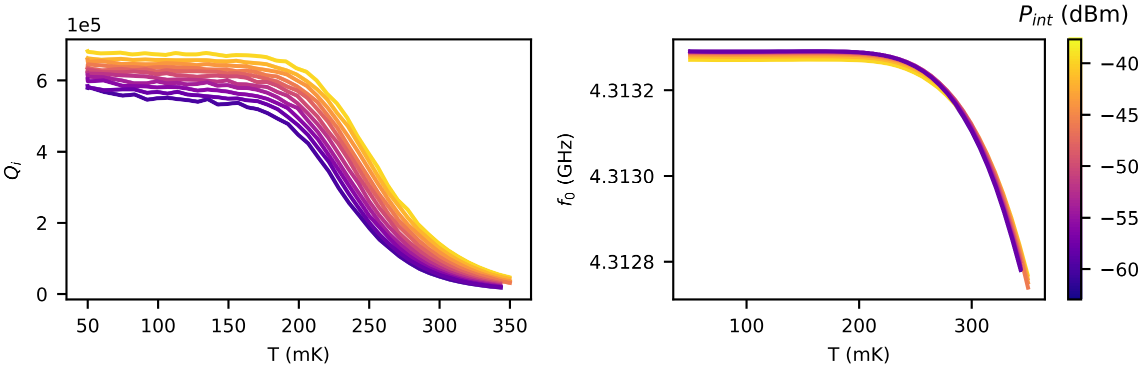

Figure 3.26: Internal quality factor (left) and resonance frequency (right) for LT165, KID2 for different read powers. Data is from a S_{21} measurement.

indicates that Q_i is limited by another process than quasiparticle losses.

3.6. Conclusion

In this chapter we have seen that the generation-recombination (GR) noise is most effectively probed by the amplitude-phase cross PSD. This spectrum can be approximated by a single Lorentzian spectrum, where the roll-off is given by the apparent quasiparticle lifetime (τ^*_{qp}) and the flat noise level (FNL) by $4\tau^*_{qp}N_{qp}$ times the amplitude and phase responsivities. Conventional GR noise theory predicts this FNL to be constant over temperature.

In the data, we saw a drop in the FNL, which cannot be explained by the quasiparticle-phonon fluctuation theory [37]. This GR noise drop was seen in multiple devices and we saw that phonon trapping makes the effect more visible, as GR noise is more prominent at higher phonon trapping. Moreover, we saw that the MKID Al length did not have a significant effect, when taking the responsivity and volume changes into account. Also the Al width and the usages of a SiO$_2$ patch during processing, making the substrate under the Al less rough, did not have a significant effect on the GR noise drop.
As for Al film thickness, we saw that going from 25 nm to 50 nm did not have an effect. However, going from 50 nm to 150 nm for MKIDs on substrate, the GR noise drop vanished.
When increasing read power, a peak in lifetime and sharp knee in the GR noise drop appears at 250 mK. Even higher read power can mask the GR noise drop by creating excess quasiparticles. There is a cross over regime, where the FNL can increase with decreasing temperature. Also in the 150 nm Al device, the GR noise drop could be masked by read power induced excess quasiparticles.

With a further analysis, where we assume the noise to be Poissonian, we concluded that the GR noise drop is a result of a process that limits the lifetime, while keeping the number of quasiparticles thermal. This also implies that the peak in lifetime and sharp knee shape in FNL caused by read power, is the same effect.

4

Quasiparticle Trapping

4.1. Introduction

In the previous two chapters we observed two unexplained features in the MKID behaviour: a second exponential decay in the single photon response and a disappearance of GR noise, both at low temperatures and low read power. We will briefly summarize these observations here, before introducing an explanation: *quasiparticle trapping*.

1. Second exponential decay (Chapter 2):
    - only observed at 120 mK (not at >200 mK);
    - longer than the first decay (∼3 ms instead of ∼300 µs);
    - in both amplitude and phase, but later in amplitude;
    - the onset at the same θ for different excitation photon wavelengths;
    - increasing read power leads to a faster second decay, making it less visible.
2. GR noise drop (Chapter 3):
    - started at around 200 mK to 300 mK;
    - phonon trapping makes the effect more visible, as it increases GR noise;
    - in all three PSDs (amplitude, phase and cross);
    - Al length, width and substrate roughness does not have an effect
    - increasing the Al thickness for 50 nm to 150 nm diminishes the drop, which could be an effect of read power;
    - increasing read power leads to a peak in lifetime and sharp knee in the GR noise drop. Even higher read power leads to excess quasiparticles, eventually masking the effect;
    - when assuming the noise to be Poissonian, the GR noise drop can be explained by a process that limits the lifetime, while keeping the quasiparticle number thermal.

Figure 4.1 shows both phenomena qualitatively and Figures 4.2 and 4.3 show the GR noise levels and lifetimes, including the lifetimes from the pulse measurements. At high temperature (220 mK) the pulse measurements coincide with the lifetimes from GR noise, for all chips. At low temperature (120 mK) it is not clear which decay rate relates to the GR noise values, as GR noise generally disappears at these temperatures. In LT139, the second exponential decay seems to relate to the GR noise lifetime, whereas, for LT165 KID2 and KID3, shown in Figure 4.3, it is not clear which of the two decay rates correspond to the GR noise lifetimes. For comparison, the lifetime behaviour of LT145 KID1, where no GR noise drop is present, is depicted in Figure 4.2. Here, the pulse lifetimes (single exponential) coincide with the GR noise saturation lifetimes.

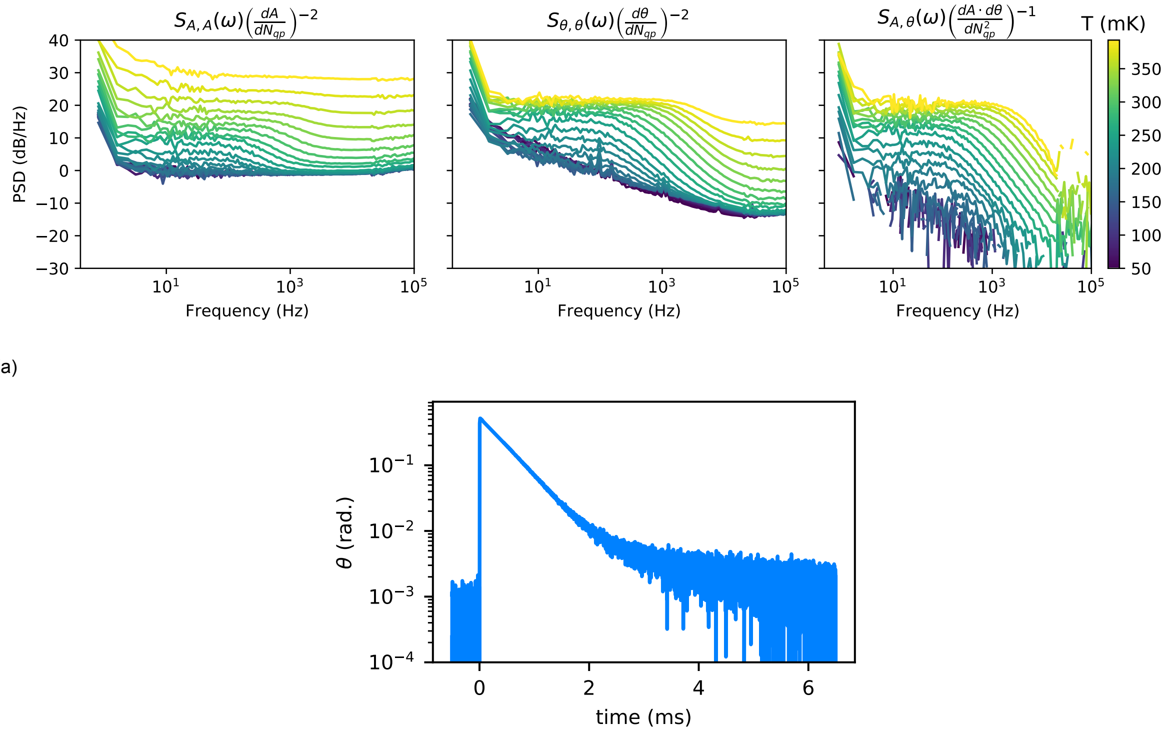

(a)

(b)

Figure 4.1: GR noise drop and second exponential decay for LT165 KID2, at −89 dBm read power. (a): measured amplitude, phase and cross PSDs at different temperatures. The spectra are divided by the appropriate responsivity squared, as indicated by the titles. (b): Averaged single 402 nm photon response at 120 mK.

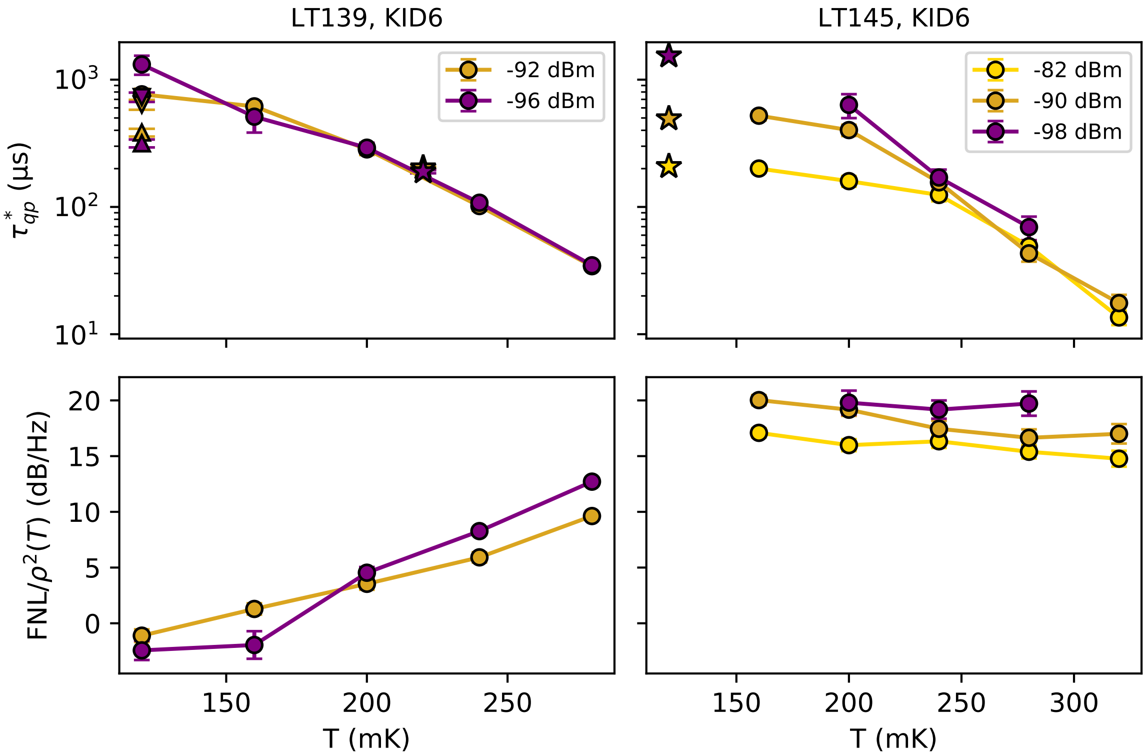

Figure 4.2: Lifetimes and FNLs (divided by responsivity squared) of LT139 KID6 and LT145, KID1. (○): cross PSD GR noise data, (△): pulse data, first decay, (∇): pulse data, second decay and (⋆): pulse data, single decay. The pulse lifetimes are averaged over the available wavelengths and the errorbars represent statistical error in the (Lorentzian and exponential) fits.

The hypothesis for both unexplained features is *quasiparticle trapping*. In an ordinary superconductor, quasiparticles (with energy $E = \Delta$) can move around and diffuse within the superconductor. When traps are introduced, quasiparticles can locally lose some energy at these traps, and therefore become localised (i.e. trapped). In the design of superconducting qubits, quasiparticle trapping can be used to confine excess quasiparticles to non-critical regions to enhance coherence times [75, 76]. Figure 4.4d shows the measured qubit decay rate at different external magnetic fields, which induce quasiparticle trapping states. In superconducting tunnel junction (STJ) devices, a lower gap superconductor can be used to spatially engineer the superconducting gap energy, trapping quasiparticles before tunnelling and thereby increasing charge separation [77]. For transition edge sensors, quasiparticle trapping can be used to enlarge the absorber area, without increasing the sensor heat capacity [78].
Besides these opportunities to improve performance of superconducting devices, quasiparticle trapping is also known to degrade detector performance. For example, in STJ X-ray detectors, quasiparticle trapping due to impurities is thought to limit the responsivity at low temperatures [8, 79–81], as seen in Figure 4.4a. In MKIDs, quasiparticle trapping into subgap states due to disorder could result in an anomalous electrodynamical response as shown by Gao et al. [82].
Moreover, Barends et al. [83] have shown that disorder leads to limited quasiparticle lifetimes at low temperatures, by implanting Al MKID films with Mn and Al-ions, as seen in Figure 4.4b. Grünhaupt et al. [84] found that disorded granular Al superconducting resonators exhibit long lived excitations, as shown in Figure 4.4c, which they attribute to quasiparticle trapping.

These last two features of quasiparticle trapping led us to the proposed hypothesis. Specifically, in Chapter 3, we saw that we could explain the observed GR noise drop, by postulating a process that limits the quasiparticle lifetime and keeps the quasiparticle density thermal. The observation in Figure 4.4b suggests that quasiparticle trapping results in a limited lifetime. Besides that, the observation in Figure 4.4c, is qualitatively very similar to the observation of the second exponential decay in Chapter 2 (compare Figures 4.1b and 4.4c), which also is observed to be read power dependent.

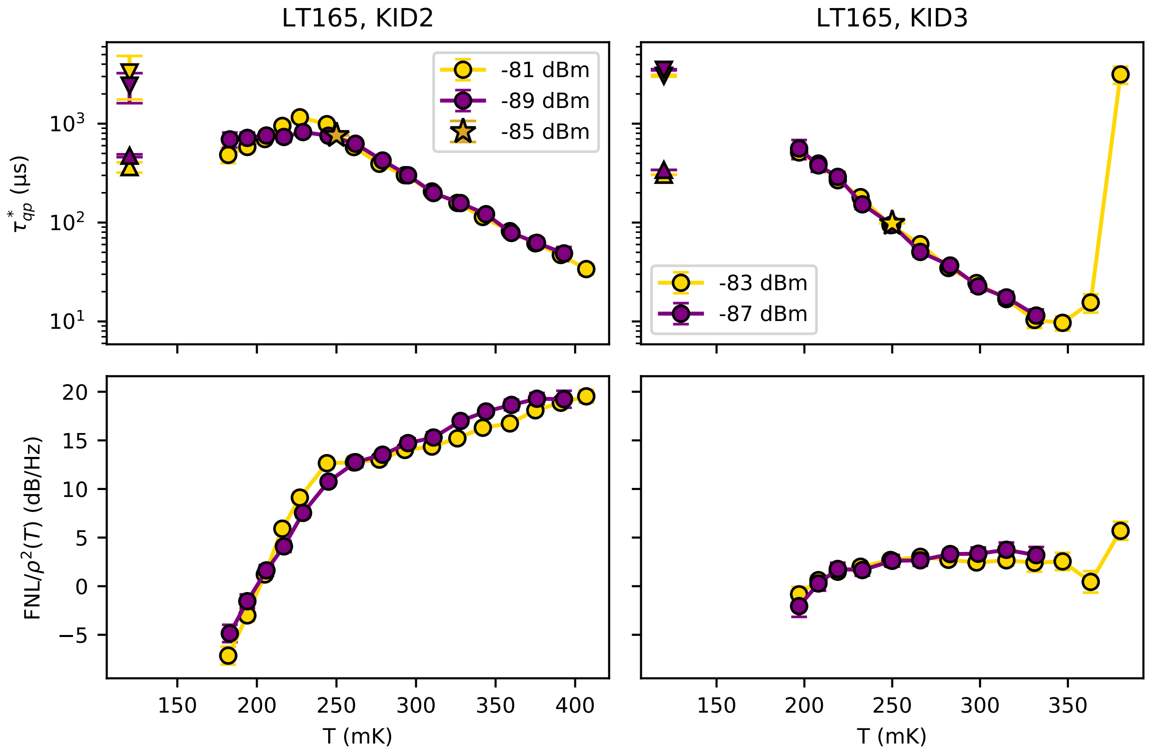

Figure 4.3: Lifetimes and FNLs (divided by responsivity) of LT165 KID2 and KID3. (○): cross PSD GR noise data, (△): pulse data, first decay, (∇): pulse data, second decay and (⍰). The pulse lifetimes are averaged over the available wavelengths and the errorbars represent statistical error in the (Lorentzian and exponential) fits.

Because there are no obvious trapping locations in the Al films used in this thesis, a SIMS (Secondary Ion Mass Spectroscopy) analysis was performed, as discussed in Appendix A. This showed Fe contamination between the wafer and the Al films, which is likely to cause quasiparticle trapping due to its ferromagnetic properties. Quasiparticle traps located at the interface of the Al and the wafer are consistent with observations in Chapter 3. There, we saw that Al length and width did not have a measurable effect on the GR noise drop, but Al thickness did (see Figure 4.2, LT139: 50 nm and LT145: 150 nm Al films). With traps located on the Al-wafer interface, increasing the Al thickness is indeed the only way to lower the effective trap concentration, diminishing quasiparticle trapping effects[1].

In this chapter, we will try to model the GR noise behaviour by introducing quasiparticle trapping terms into the Rothwarf-Taylor equations. Probing quasiparticle trapping processes in steady state has, to our knowledge, never been done. All above mentioned quasiparticle trapping experiments study the decay of quasiparticles after the superconductor is excited, neglecting quasiparticle generation. GR noise probes the quasiparticle fluctuations in steady state, where generation processes can not be neglected. Measuring fluctuations enables us to directly probe the quasiparticle dynamics, as the PSDs give us both the quasiparticle lifetime and a FNL, from which we can infer the quasiparticle density, as done in Section 3.5.

Moreover, as we study MKIDs we probe the average quasiparticle density and are therefore not susceptible to quasiparticle diffusion effects. In contrast, diffusion plays an important role in STJs and superconducting qubits, as the quasiparticles must interact with a localised devices feature, such as a Josephson junction.

First, the theory needed for this modelling will be discussed, after which different quasiparticle trapping models are compared to the GR noise data. We will use mostly the data from LT165, as the GR noise drop is most prominent there due to phonon trapping (not to be confused with quasiparticle trapping) and the data set is quite extensive. The single photon response will briefly be discussed, along with

---

[1] However, keep in mind that we saw in Chapter 3 read power effects could also mask the GR noise drop.

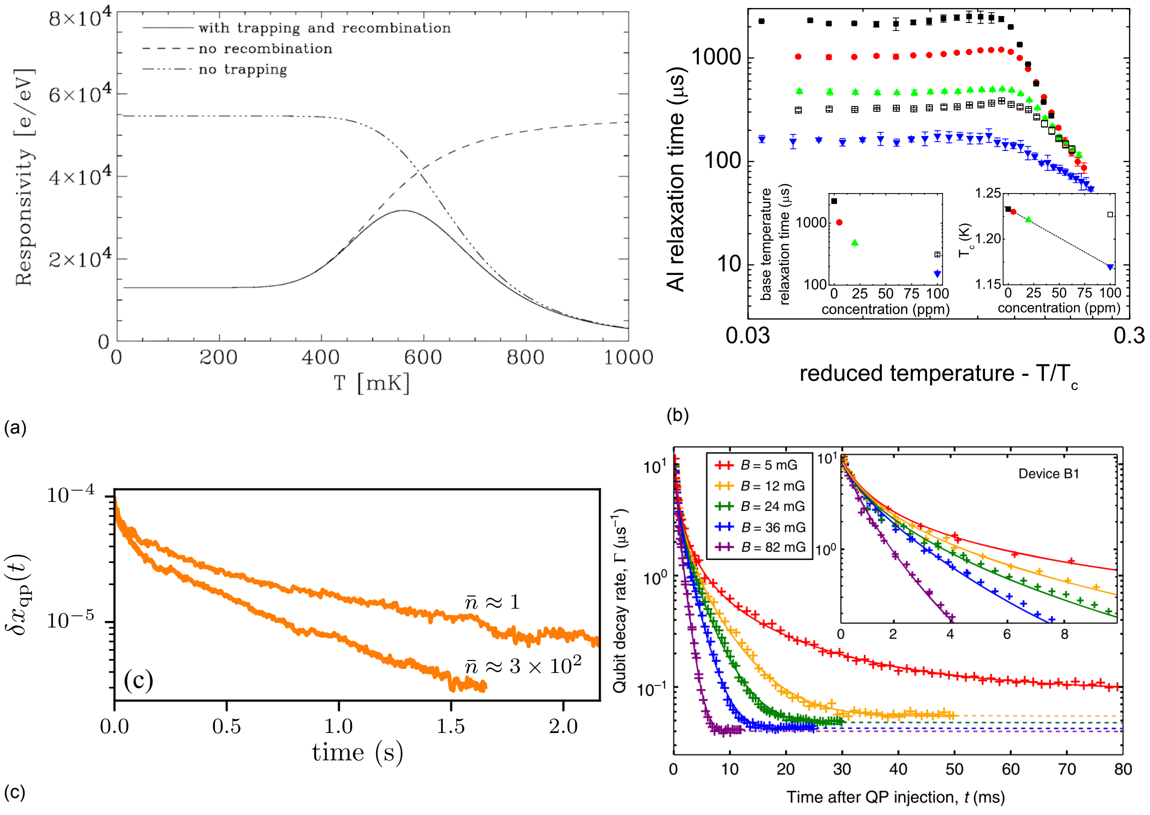

(a)

(b)

(c)

(d)

Figure 4.4: Quasiparticle trapping phenomena in literature. (a): Modelled STJ responsivity versus temperature including and excluding trapping. Image from Hijmering et al.[81] (b): Quasiparticle lifetimes from pulse measurements done by Barends et al.[83] at different temperatures for full Al MKIDs, with Mn ion-implantation of concentrations: 0 (■), 5(●), 20 (▲), and 100 (▼) ppm and 100 ppm Al (□). The left inset shows the relaxation time at 325 mK versus ion concentration. The right inset shows the decrease in critical temperature versus Mn implantation (Al implantation does not affect T_c). Image from [83]. (c): Excess quasiparticle decay after granular Al MKID excitation as measured by Grünhaupt et al.[84], for two internal resonator powers, with respectively 1 and 300 circulating photons. Image from [84]. (d): Qubit decay rates after a quasiparticle injection for different external magnetic fields versus time. A stronger magnetic field induces more quasiparticle trapping states. Inset is a zoom-in of top left corner. Image from Wang et al.[75].

possible effects of quasiparticle trapping on the MKID performance.

4.2. Theory

Quasiparticle trapping can have a number of different causes. Engineering quasiparticle traps can be done with normal metal sinks [85], Andreev bound states in weak links [86], superconducting gap engineering [77, 87] or via an external magnetic field, which induces Meissner and vortex states [75, 76]. However, in our case, the presumed quasiparticle trapping is not engineered. Material properties can induce quasiparticle trapping as well, via different mechanisms. We will first give a brief overview of the existing literature on the various mechanisms.

The presence of **impurities** in the superconducting film is one of the possible causes. Impurities can be either magnetic or non-magnetic. In the **magnetic** case, when impurity concentrations are low, Yu-Shiba-Rusinov states [88–90] appear, which are localised electronic states, enabling quasiparticle trapping [91]. At higher concentrations, a subgap band can form via hybridization, which merges eventually with the continuum at even higher concentrations. In this regime, the superconducting gap is lowered, which eventually leads to a *gapless* superconductor [90], as calculated by Abrikosov and Gor'kov [92, 93]. Zittartz, Bringer and Müller-Hartmann [94] have calculated the (subgap) band structure due to the magnetic impurities. From this, Kozorezov et al. [10] have calculated relevant rates for detector performance, which can be used for phenomenological models of superconducting detectors,

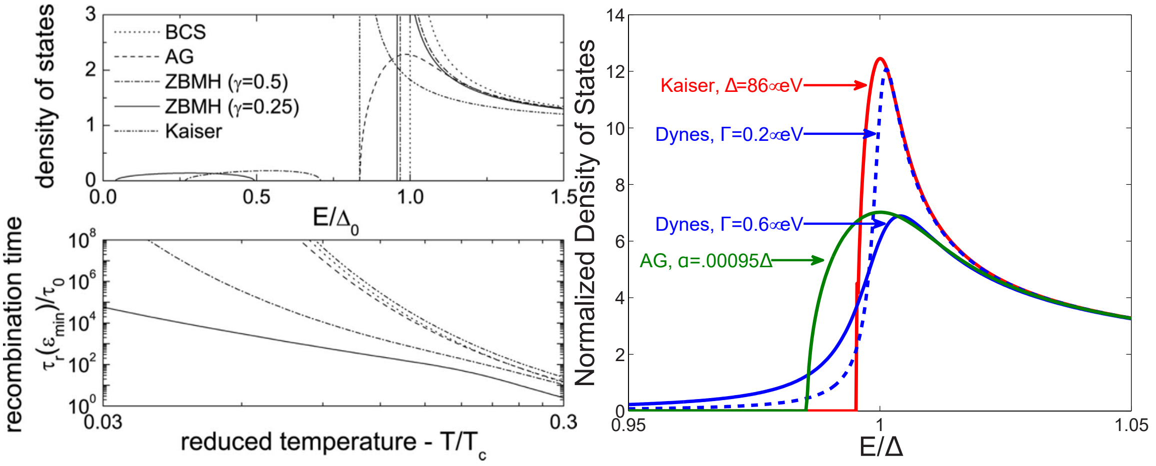

(a) (b)

Figure 4.5: Density of states from different theoretical calculations. *(a)*: DOS and recombination times from BSC compared to Abrikosov-Gor'kov [92, 93], Zittartz, Bringer and Müller-Hartmann [94] and Kaiser [99]. Image from Reference [83]. *(b)*: DOS for Kaiser, Abrikosov-Gor'kov and Dynes [100] for two parameters. Image from Reference [98].

such as in Reference [81]. They estimate that low concentrations (∼10 ppm) can already have a dominating effect on the quasiparticle dynamics at low temperatures. As Fe contamination is found at the substrate-Al film interface, magnetic impurities are the most probable cause for the devices studied in this thesis. The effect of the (non-homogeneous) spatial distribution of these impurities is however not clear.

Non-magnetic impurities as ordinary scatters can only have an effect on the anisotropic part of the superconducting gap, due to time-reversal symmetry as stated by the Anderson theorem [95], which is small [96]. Only at large concentrations, the disorder in the material causes variations in the gap energy, creating superconducting islands [97]. A non-magnetic impurity can also be created by magnetic impurities, with an equal populated spin up en spin down state (such as in AlMn alloys [98]) making it non-magnetic after hybridization. Kaiser [99] has calculated the gap reduction, for this case. Alternatively, the smearing of the density of states (DOS) gap-edge singularity can be described by the Dynes parameter [100], which lowers the gap and describes subgap states when non-zero. Figure 4.5 shows the DOS calculated by different theories.

Another cause of quasiparticle trapping can be **spatial inhomogeneities of the superconducting gap**, Δ. Larkin and Ovchinnikov [101] have calculated the DOS smearing for this type. It turns out to be essentially the same as for magnetic impurities, which is argued to be universal for all depairing mechanisms [19]. Apart from lowering the superconducting energy gap, disorder in Δ results in a exponential subgap tail in the DOS [96, 102, 103], consisting of localised states, even for low disorder. Quasiparticles can relax into this tail, when close to these trapping states, and therefore become localised.

Lastly, also **combinations of these mechanisms** are possible. For example in Reference [104], trapping via normal islands and magnetic impurities is discussed. From this it is inferred that in systems with a spatially non-homogeneous gap and impurities (both magnetic and non-magnetic), multiple subgap states emerge. For the case of Mn doped Al films, this could explain the results found by Barends et al.[83] who found quasiparticle lifetimes limited by non-magnetic Mn impurities and O'Neil et al.[105] who found subgap states in AlMn-alloys.

Regardless of the cause, the dominant quasiparticle trapping effects on pulse and noise measurements, can be described in a relatively simple, phenomenological way. It can be modelled by adding an extra level: N_t, the number of trapped quasiparticles, to the the Rothwarf-Taylor equations, Equation (2.5). This method has proven fairly successful in qualitatively explaining long lived excitations in superconducting resonators [84] and quantitatively describing responsivity at low temperature in STJs [79–81, 106] and quasiparticle dynamics in qubits [75]. All these applications focus on the non-equilibrium response of the detector. Here, we model the steady state behaviour of the MKIDs, i.e. the GR noise. For this, we use the framework provided by Wilson and Prober already addressed in

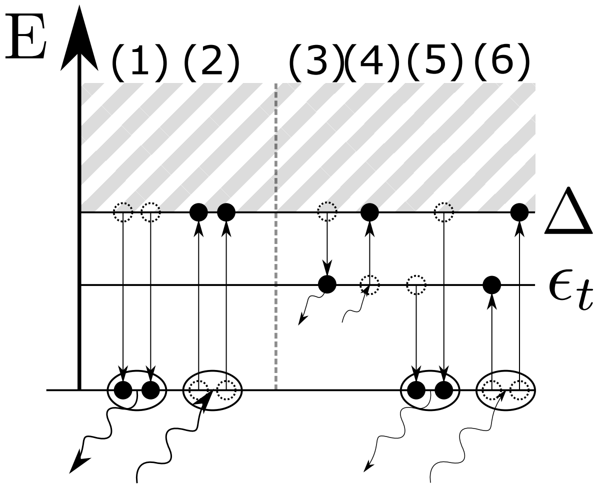

Figure 4.6: Relevant quasiparticle-phonon processes: (1) recombination, (2) pair-breaking, (3) trapping, (4) detrapping, (5) on-trap recombination and (6) on-trap pair-breaking. The wiggle arrows indicate involved phonons, and their length and thickness indicate their relative energy.

Section 3.2, starting from the altered Rothwarf-Taylor equations.

After the new level, N_t, is added, it can be coupled to the other levels in several ways, as depicted in Figure 4.6. The most obvious is the coupling to the free quasiparticle level, N_{qp}, via a trapping and detrapping term ((3) and (4)), which will be discussed in Sections 4.3, 4.4 and 4.6. Other possible processes also involve the phonon level (or equivalently Cooper-pair level) and include on-trap pair-breaking (6), where a phonon breaks a Cooper-pair into a trapped and a free quasiparticle, and on-trap recombination (5), which is the reverse process. Those will be discussed in Section 4.7.

It is important to realise that the resulting rate equations include the quasiparticle generation (i.e. pair-breaking) terms. In modelling excitation behaviour, these generation terms can be neglected when phonon effects are accounted for via the phonon trapping factor. However, when looking at the system in steady state (i.e. GR noise) these terms cannot be neglected as they are of the same order as recombination processes.

From the resulting rate equations, the steady state values (N_{qp}^0 and N_t^0) are calculated. With these values, the transition probabilities between the levels can be written down, like in Section 3.2. To keep the resulting $\mathbf{M}$ and $\mathbf{B}$ matrices simple (i.e. two-dimensional), the third level is chosen as N_C, the number of Cooper-pairs, instead of the number of pair-breaking phonons. The phonon effects are accounted for by multiplying the recombination constant (R) by the phonon trapping factor (resulting in R^*) as calculated in Section 3.2. With these transition rates, the $\mathbf{M}$ and $\mathbf{B}$ matrices and the fluctuation spectra are calculated.

The resulting power spectral density matrix, $\mathbf{G}(\omega)$ (see Equation (3.6)), now includes the (cross-) fluctuations for both the N_{qp} and N_t level, when choosing N_C as the dependent variable. The question now arises which fluctuations we should look at when comparing it to the measured cross-, amplitude or phase PSDs. From Section 2.2.3, we know that amplitude mainly probes the quasiparticle number and phase the (broken) Cooper-pairs. Extending this reasoning, we could argue that the amplitude fluctuations should relate to the free quasiparticle number, if we assume that trapped quasiparticles cannot absorb the microwave read out signal. This assumption implies that the trapping state has a smaller linewidth than the microwave photon energy (21 µeV for 5 GHz) and the trap energy is sufficiently deep inside the superconducting gap, so that the quasiparticles inside it cannot be excited to the continuum by the microwave photons. Likewise, phase relates to Cooper-pair fluctuations and the cross PSDs relates to Cooper-pair- free quasiparticle fluctuations. Or more precisely, updating Equation (3.11),

$$S_{A,A}(\omega) \approx S_{N_{qp},N_{qp}}(\omega)\left(\frac{dA}{dN_{qp}}\right)^2, \tag{4.1a}$$

$$S_{\theta,\theta}(\omega) \approx S_{N_C,N_C}(\omega)\left(\frac{d\theta}{dN_C}\right)^2 = \left[S_{N_{qp},N_{qp}} + S_{N_{qp},N_t} + S_{N_t,N_{qp}} + S_{N_t,N_t}\right]\left(\frac{d\theta}{dN_{qp}}\right)^2, \tag{4.1b}$$

$$S_{\theta,A}(\omega) \approx S_{N_C,N_{qp}}(\omega)\frac{dA}{dN_{qp}}\frac{d\theta}{dN_C} = \left[S_{N_{qp},N_{qp}} + S_{N_{qp},N_t}\right]\frac{dA \cdot d\theta}{dN_{qp}^2}. \tag{4.1c}$$

Here, we used[2] that $N_C \propto -(N_{qp} + N_t)/2$ and Equation (3.12) in the last equality, to ensure the spectra can be calculated with N_{qp} and N_t as independent variables and the responsivities from Section 3.3 can be used.

Alternatively, assuming trapped quasiparticles can absorb microwave power and thus amplitude probes the *total* number of quasiparticles, we recover Equation (3.11), with the substitution $N_{qp} \to N_C/2$,

$$S_{A,A}(\omega) \approx S_{N_C,N_C}(\omega)\left(\frac{dA}{dN_C}\right)^2 = \left[S_{N_{qp},N_{qp}} + S_{N_{qp},N_t} + S_{N_t,N_{qp}} + S_{N_t,N_t}\right]\left(\frac{dA}{dN_{qp}}\right)^2, \tag{4.2a}$$

$$S_{\theta,\theta}(\omega) \approx S_{N_C,N_C}(\omega)\left(\frac{d\theta}{dN_C}\right)^2 = \left[S_{N_{qp},N_{qp}} + S_{N_{qp},N_t} + S_{N_t,N_{qp}} + S_{N_t,N_t}\right]\left(\frac{d\theta}{dN_{qp}}\right)^2, \tag{4.2b}$$

$$S_{\theta,A}(\omega) \approx S_{N_C,N_C}(\omega)\frac{dA \cdot d\theta}{dN_C^2} = \left[S_{N_{qp},N_{qp}} + S_{N_{qp},N_t} + S_{N_t,N_{qp}} + S_{N_t,N_t}\right]\left(\frac{dA \cdot d\theta}{dN_{qp}^2}\right). \tag{4.2c}$$

This implies that phase, amplitude and cross PSDs, all relate to fluctuations in N_C, and after dividing by responsivity should be equal.

In the following sections, we will look at all three spectra ($S_{N_{qp},N_{qp}}(\omega)$, $S_{N_C,N_C}(\omega)$ and $S_{N_C,N_{qp}}(\omega)$) for completeness. The data shows that the amplitude, phase and cross behave very similarly (e.g. Figure 3.7), suggesting that at least part of the trapped quasiparticles can absorb the microwave radiation.

4.3. Trapping and Detrapping

In the most basic quasiparticle trapping model an extra level of trapped quasiparticles, N_t, is added to the Rothwarf-Taylor equations and coupled to the free quasiparticle level with a trapping and detrapping term. These terms are depicted in Figure 4.6 as (3) and (4). This case is also discussed in the paper by Wilson and Prober [37], which we will largely follow in this section. The resulting rate equations are,

$$\frac{dN_{qp}}{dt} = -\frac{RN_{qp}^2}{V} - \Gamma_t N_{qp} + \Gamma_d N_t + 2\Gamma_B N_\omega, \tag{4.3a}$$

$$\frac{dN_t}{dt} = \Gamma_t N_{qp} - \Gamma_d N_t, \tag{4.3b}$$

$$\frac{dN_\omega}{dt} = \frac{RN_{qp}^2}{2V} - \Gamma_B N_\omega - \Gamma_{es}(N_\omega - N_\omega^T), \tag{4.3c}$$

$$N_\omega^T = \frac{R(N_{qp}^T)^2}{2\Gamma_B V}. \tag{4.3d}$$

(4.3e)

Here, the rates are used as introduced in Section 2.2.2, with the addition of Γ_t and Γ_d, which are the trapping and detrapping rate, respectively. The expression for N_ω^T is determined by the solved steady state Rothwarf-Taylor equations (Equation (2.5)). N_{qp}^T is given by Equation (2.1), the thermal number of quasiparticles. Notice that the terms are grouped in columns for recombination, trapping and detrapping, pair-breaking and phonon escape.

---

[2] Note that we only take the proportionality of N_C and N_{qp},N_t into account. Actually, $N_C = N_C^{max} - (N_{qp} + N_t)/2$, where N_C^{max} is the total amount of electrons in the systems, divided by two. However, the extra terms that this expression produces, only have a DC (zero frequency) contribution.

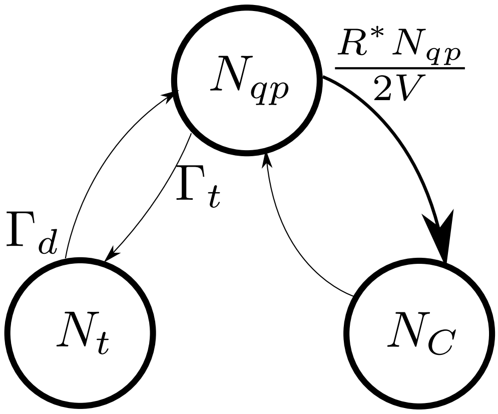

Figure 4.7: Diagram illustrating the different transitions between the levels (free, trapped quasiparticles and Cooper-pairs) for the trapping-detrapping fluctuation model. Next to the arrows are the transition rates. When a rate is missing, the equilibrium value of the opposite rate is used, as given by the transition probabilities. A thick arrow means that the transition has shot noise of 2.

In steady state, the rate equations in Equation (4.3) result in a thermal quasiparticle number ($N_{qp}^0 = N_{qp}^T$) and phonon number ($N_\omega^0 = N_\omega^T$). The trapped quasiparticle number is given by, $N_t^0 = \frac{\Gamma_t}{\Gamma_d} N_{qp}^T$. With these steady state values, we can calculate the $\mathbf{M}$ and $\mathbf{B}$ matrices as follows.
The transition probabilities and shot sizes are,

$$p_{12} = \Gamma_t N_{qp} \qquad \delta n_{12} = 1, \tag{4.4a}$$
$$p_{13} = R^* N_{qp}^2/(2V) \qquad \delta n_{13} = 2, \tag{4.4b}$$
$$p_{21} = \Gamma_d N_t \qquad \delta n_{21} = 1, \tag{4.4c}$$
$$p_{31} = R^* (N_{qp}^T)^2/(2V) \qquad \delta n_{31} = 1. \tag{4.4d}$$
$$\tag{4.4e}$$

The numbers indicate the different levels, where we use: (1): free quasiparticles, (2): trapped quasiparticles and (3): the number of Cooper pairs. The phonon effects are accounted for via the effective recombination constant of $R^* = R/(1 + \tau_{esc}/\tau_{pb})$, as described in Section 3.2. When choosing the free and trapped quasiparticle numbers as independent variables, the resulting matrices are,

$$\mathbf{M} = \begin{pmatrix} \Gamma_R^* + \Gamma_t & -\Gamma_d \\ -\Gamma_t & \Gamma_d \end{pmatrix}, \tag{4.5a}$$
$$\mathbf{B} = \begin{pmatrix} 2(\Gamma_R^* + \Gamma_t)N_{qp}^0 & -(\Gamma_t N_{qp}^0 + \Gamma_d N_t^0) \\ -(\Gamma_t N_{qp}^0 + \Gamma_d N_t^0) & 2\Gamma_d N_t^0 \end{pmatrix}, \tag{4.5b}$$
$$= 2N_{qp}^0 \begin{pmatrix} \Gamma_R^* + \Gamma_t & -\Gamma_t \\ -\Gamma_t & \Gamma_t \end{pmatrix}. \tag{4.5c}$$

Here, $\Gamma_R* = 2R^* N_{qp}^0/V = 1/\tau_{qp}*$ and in the last step for $\mathbf{B}$, the principle of detailed balance is used which is justified as the transitions are connected in pairs, as depicted in Figure 4.7. When calculating the correlation matrix via Equation (3.10), it is found that $\sigma_{N_{qp}}^2 = N_{qp}^0$ and $\sigma_{N_t}^2 = N_t^0$, which means that the noise in both levels is still Poissonian, as expected from the fact that the transitions are paired.
Following Wilson and Prober [37], the relevant rates governing the system can be calculated as the eigenvalues of $\mathbf{M}$. When assuming the trapping and detrapping rates to be much higher than the recombination rate, $\Gamma_t + \Gamma_d \gg \Gamma_R^*$, these rates are given by,

$$\frac{1}{\tau_1} = \frac{\Gamma_d}{\Gamma_d + \Gamma_t}\Gamma_R^*, \qquad \frac{1}{\tau_2} = \Gamma_d + \Gamma_t. \tag{4.6}$$

The quasiparticle fluctuation spectrum is given by,

$$S_{N_{qp},N_{qp}} = \frac{4N_{qp}^0}{\Gamma_d + \Gamma_t}\left(\frac{\tau_1 \Gamma_d}{1 + (\omega\tau_1)^2} + \frac{\tau_2 \Gamma_t}{1 + (\omega\tau_2)^2}\right). \tag{4.7}$$

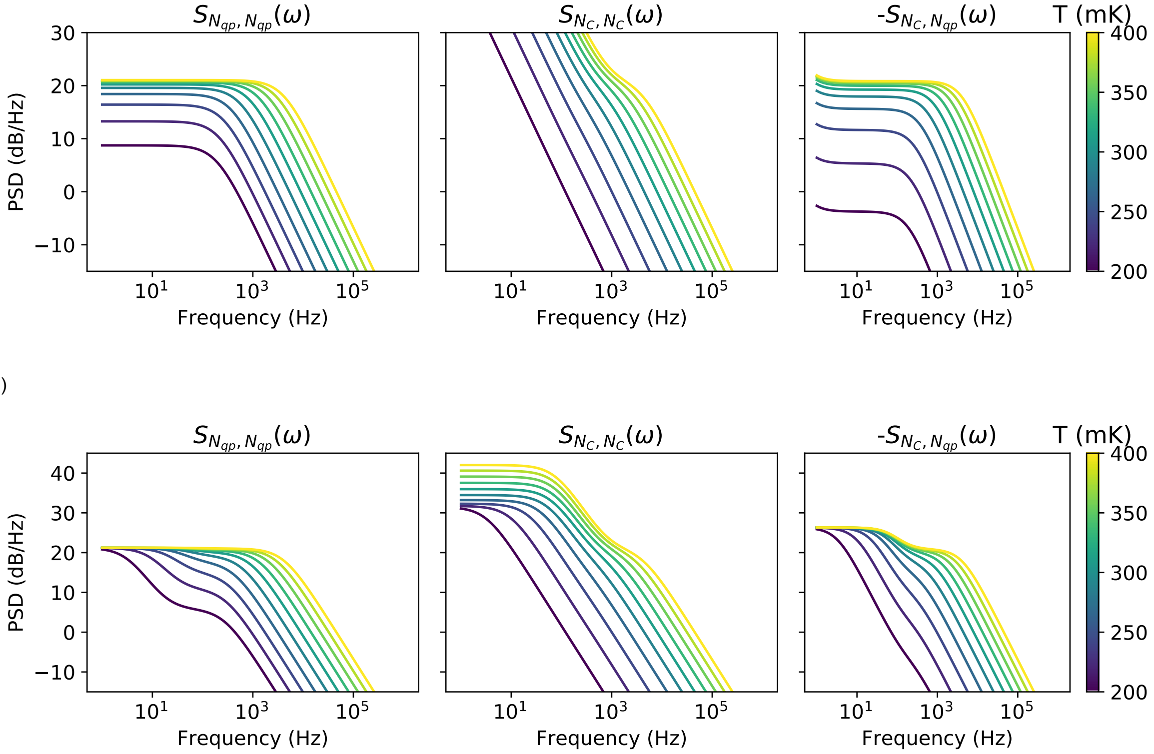

(a)

(b)

Figure 4.8: Calculated PSDs from the trapping model, with the trapping rate is set to 1/(900 µs). (a): detrapping rate is 1/(1 × 10^5 ms). (b): detrapping rate is 1/(2 ms).

For $\Gamma_d \gg \Gamma_t$, this results in Equation (3.9) and thus behaves as if no trapping is present. In the opposite situation, $\Gamma_d \ll \Gamma_t$, the spectrum results in,

$$S_{N_{qp},N_{qp}} = \frac{4\tau_t N_{qp}^0}{1+(\omega\tau_t)^2}, \tag{4.8}$$

where $\tau_t = 1/\Gamma_t$. In this case, the traps can be viewed as quasiparticle sinks. For intermediate values of Γ_d and Γ_t, the spectrum is of a double Lorentzian shape.

We can now see how this model can describe the behaviour we have seen in the temperature dependent GR noise (Chapter 3). For low temperatures, the lifetime saturates and the FNL drops. We have seen in Section 3.5, that this drop is likely due to a saturating lifetime with a thermal quasiparticle number. This is exactly what Equation (4.8) describes.
For higher temperatures, we observed the expected thermal behaviour: an increasing lifetime and constant FNL. This is automatically accounted for when we choose $\Gamma_t = 1/\tau^*_{qp,sat}$, where $\tau^*_{qp,sat}$ is the saturation lifetime. In the case of $\Gamma_t + \Gamma_d \ll \Gamma^*_R$, recombination dominates and the GR noise temperature behaviour is thermal (i.e. no trapping).

Putting this reasoning to the test, we set the trapping rate to 1/(900 µs) and the detrapping rate to a value much lower: 1/(1 × 10^5 ms), such that $\Gamma_d \ll \Gamma_t$ holds. Furthermore, the escape time and other parameters used for R^* are obtained with the methods set out in Section 2.2.3. We numerically calculate $\mathbf{G}(\omega)$ via Equation (3.6) and from that, $S_{N_{qp},N_{qp}}(\omega)$, $S_{N_C,N_C}(\omega)$ and $S_{N_C,N_{qp}}(\omega)$ for different temperatures. The spectra obtained this way are shown in Figure 4.8a.

For $S_{N_{qp},N_{qp}}(\omega)$, we see that this gives the expected behaviour: a lifetime saturation and FNL drop. However, the spectra $S_{N_C,N_C}(\omega)$ do not resemble data. $-S_{N_C,N_{qp}}(\omega)$ behaves similar to $S_{N_{qp},N_{qp}}(\omega)$, but

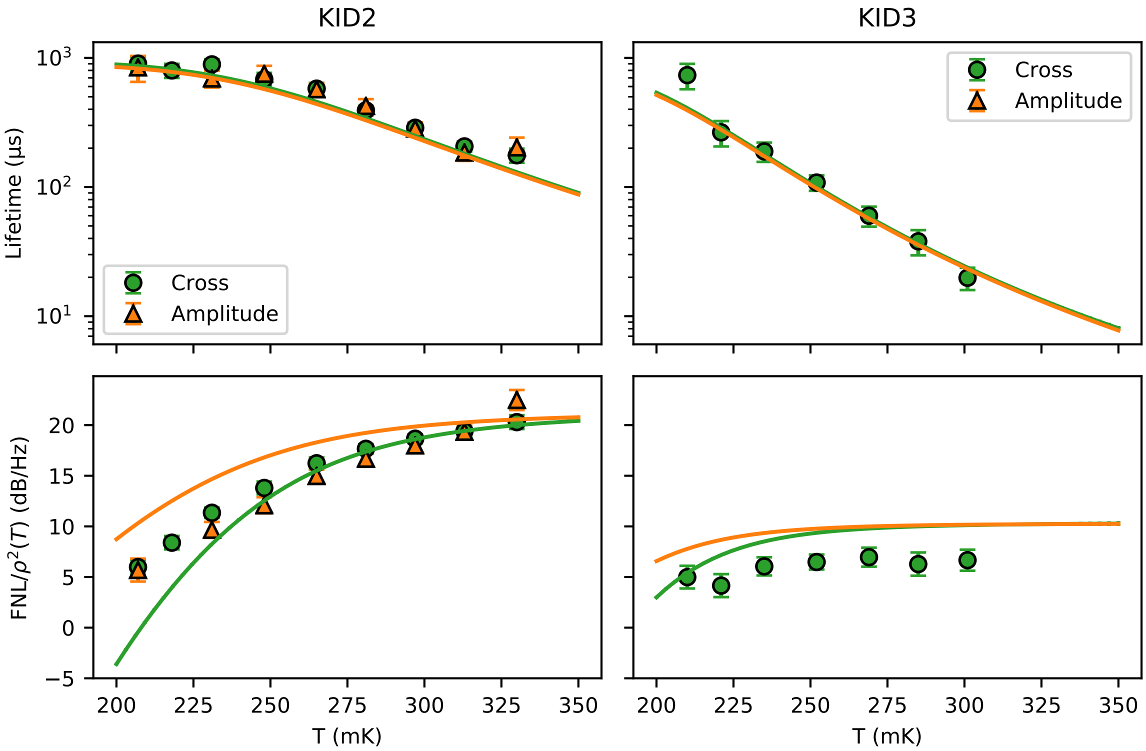

Figure 4.9: Lifetime and FNLs (divided by the appropriate responsivity squared: $\rho^2(T)$) from cross (●) and amplitude (▲) PSDs of LT165 KID2 and KID3 at −101 dBm and −99 dBm, respectively. The orange lines give the model predictions from the $S_{N_{qp},N_{qp}}$ spectra and the green lines are from the $-S_{N_C,N_{qp}}$ spectra as seen in Figure 4.8a. As model input, a trapping rate of 1/(900 µs) and detrapping rate of 1/(1 × 10^8 µs) are used.

with a faster FNL drop. For the case that trapped quasiparticles contribute to an amplitude response, the measured cross, amplitude and phase spectra all relate to $S_{N_C,N_C}(\omega)$ (Equation (4.2)). Thus, in that case, we conclude that this model cannot describe the data (compare Figure 4.8a with Figure 4.1).
In the other case, when trapped quasiparticle do not show up in the amplitude response, $S_{N_{qp},N_{qp}}(\omega)$, $S_{N_C,N_C}(\omega)$ and $-S_{N_C,N_{qp}}(\omega)$ relate to amplitude, phase and cross PSDs, respectively (Equation (4.1)). Again, for $S_{N_C,N_C}(\omega)$, we see that this model does not predict the phase PSDs properly. For $S_{N_{qp},N_{qp}}(\omega)$ and $-S_{N_C,N_{qp}}(\omega)$ spectra, however, we can extract lifetime and flat noise levels, via the same fitting procedure as explained in Section 3.3. Comparing these to the extracted lifetimes and FNLs of the measured amplitude and cross PSDs (via the methods set out in Section 3.3) results in Figure 4.9.

We see that the behaviour (lifetime saturation and FNL drop) is indeed correctly described by the model, for these cases. The FNLs from the model are too high, which is likely to be caused by an inaccuracy in the responsivity, with which the measured FNLs are compensated. The missing amplitude data for KID3 is because of the bad signal to noise ratio in this variable (on substrate). Furthermore, we see that the predicted FNL drop in cross is too steep. In the data, the amplitude and cross PSDs show a comparable FNL drop, whereas the model predicts a steeper drop in cross.

Despite the relatively good agreement with the amplitude data, this trapping model has its shortcomings. The detrapping rate is effectively set to zero to ensure a single Lorentzian spectrum at low temperatures. However, by doing so, the traps become quasiparticle sinks. The trapped quasiparticle number is given by $N_t^0 = \Gamma_t N_{qp}^0/\Gamma_d$ which goes to infinity for a detrapping rate of zero. Of course, we could increase the detrapping rate to an acceptable level. Increasing the detrapping rate results in a low frequency feature, as depicted in Figure 4.8b where we set Γ_d to 1/(2 ms). This is the double Lorentzian shape, anticipated in Equation (4.7). Γ_d can be set to about a maximum of 1/(15 ms), before the model and measured spectra start to differ noticeably, which still results in trapped quasiparticle number on the order of 1 × 10^8. Despite this number being really large (there are about 1 × 10^{12} Cooper-pairs at zero temperature present in the 27 µm^3 volume), it is still within the number of Fe atoms calculated from the SIMS analysis, which is 9 × 10^8 for 450 ppm (see Appendix A).

It is important to realise that the number of Fe atoms is not necessarily equal to the number of effective traps, as the Fe atoms could be clumped together in larger fragments. It is not clear how many trapping states such configurations would induce, if at all. Therefore, the number 9 × 10^8 should be regarded as an upper limit to the number of traps.

Furthermore, we saw that the phase spectra could not be accounted for by the model and the predicted FNL drop is too steep for the cross PSD. Moreover, when we assume trapped quasiparticles to contribute to the losses, all three spectra could not be described. Remember that we see in the data that amplitude, phase and cross PSDs show similar behaviour, suggesting that trapped quasiparticles do contribute to the losses.

These shortcomings can be attributed to the fact that we set-up this model by looking at the free quasiparticle fluctuations ($S_{N_{qp},N_{qp}}$). Indeed, comparing this spectrum with the amplitude PSDs, results in the correct behaviour. However, the response of an MKID (at least in phase and cross) depends also on the Cooper-pair fluctuations, as we saw in Section 4.2. The low detrapping rate, results in a very high trapped quasiparticle number, which also makes the fluctuations large, as the noise is still Poissonian. Therefore, when including the trapped quasiparticles in the observable fluctuation level, the fluctuations become very large, with a very small roll-off frequency corresponding to the small detrapping rate.

In conclusion, this trapping model can follow the amplitude data when assuming trapped quasiparticles do not contribute to quasiparticle loss and the traps are effectively quasiparticle sinks ($\Gamma_d \ll \Gamma_t$). However, the predictions for cross- and phase PSDs deviate from measurements. Moreover, when trapped quasiparticle do contribute to the losses, this model cannot follow the data of all three variables (amplitude, phase and cross). The reason for these deviations lies in the fact that the model was set up, regarding the free quasiparticle fluctuations, where in fact the MKID response is determined by the all three levels (trapped and free quasiparticles and Cooper-pairs).

4.4. Finite Number of Traps

In the previous section, we found that in order to follow the data the traps should act as sinks, effectively trapping all quasiparticles. In an attempt to set up a physically more correct model, we introduce a trapping rate that is dependent on the number of trapped quasiparticles. More precisely, $\Gamma_t = \Upsilon(N_t^{max} - N_t)$, where Υ is a trapping constant and N_t^{max} is the number of trapping states in the system. A similar approach is studied in Poelaert et al. [106] in the case for STJs. The resulting rate equations are,

$$\frac{dN_{qp}}{dt} = -\frac{RN_{qp}^2}{V} - \Upsilon(N_t^{max} - N_t)N_{qp} + \Gamma_d N_t + 2\Gamma_B N_\omega, \tag{4.9a}$$

$$\frac{dN_t}{dt} = \Upsilon(N_t^{max} - N_t)N_{qp} - \Gamma_d N_t, \tag{4.9b}$$

$$\frac{dN_\omega}{dt} = \frac{RN_{qp}^2}{2V} - \Gamma_B N_\omega - \Gamma_{es}(N_\omega - N_\omega^T), \tag{4.9c}$$

$$N_\omega^T = \frac{R(N_{qp}^T)^2}{2\Gamma_B V}. \tag{4.9d}$$

The steady state free quasiparticle and phonon numbers are again thermal and the steady state trapped quasiparticle number is given by $N_t^0 = N_t^{max}/(1 + \Gamma_d/(\Upsilon N_{qp}^T))$. Substituting value in the trapping rate gives, $\Gamma_t = \Upsilon N_t^{max}/(1 + \Upsilon N_{qp}^T/\Gamma_d)$. For high temperatures, where $\Gamma_d \ll \Upsilon N_{qp}^T$, N_t^0 is approximately equal to N_t^{max}, i.e. all traps are occupied. In that case, $\Gamma_t = \Gamma_d N_t^{max}/N_{qp}^T$, i.e. an exponential increase in the trapping rate when the temperature is lowered.

In the opposite regime, $\Gamma_d \gg \Upsilon N_{qp}^T$, N_t^0 is equal to $\Upsilon N_t^{max} N_{qp}^T/\Gamma_d$. The trapping rate then becomes, $\Gamma_t = \Upsilon N_t^{max}$, which is constant. Therefore, in this regime the previous model is recovered. When N_t^{max} and Υ are fixed, the detrapping rate controls the onset of the high en low temperature trapping regimes.

The transition rates for this case are,

$$\begin{aligned}
p_{12} &= \Upsilon(N_t^{max} - N_t)N_{qp} & \delta n_{12} &= 1, && \text{(4.10a)}\\
p_{13} &= R^* N_{qp}^2/2V & \delta n_{13} &= 2, && \text{(4.10b)}\\
p_{21} &= \Gamma_d N_t & \delta n_{21} &= 1, && \text{(4.10c)}\\
p_{31} &= R(N_{qp}^T)^2/2V & \delta n_{31} &= 1. && \text{(4.10d)}\\
& & & && \text{(4.10e)}
\end{aligned}$$

This results in the matrices,

$$\mathbf{M} = \begin{pmatrix} \Upsilon(N_t^{max} - N_t^0) + \Gamma_{R^*} & -\Upsilon N_{qp}^0 - \Gamma_d \\ -\Upsilon(N_t^{max} - N_t^0) & \Gamma_d + \Upsilon N_{qp}^0 \end{pmatrix}, \tag{4.11a}$$

$$\mathbf{B} = \begin{pmatrix} \begin{matrix} \Upsilon(N_t^{max} - N_t^0)N_{qp}^0 \\ +2(N_{qp}^0 + N_{qp}^T)R^*/V \\ +\Gamma_d N_t^0 \end{matrix} & \begin{matrix} -\Upsilon(N_t^{max} - N_t^0)N_{qp}^0 \\ -\Gamma_d N_t^0 \end{matrix} \\ \\ \begin{matrix} -\Upsilon(N_t^{max} - N_t^0)N_{qp}^0 \\ -\Gamma_d N_t^0 \end{matrix} & \begin{matrix} \Upsilon(N_t^{max} - N_t^0)N_{qp}^0 \\ +\Gamma_d N_t^0 \end{matrix} \end{pmatrix}, \tag{4.11b}$$

$$\Gamma_{R^*} = 2R^* N_{qp}^0/V. \tag{4.11c}$$

We set the number of traps to $N_t^{max} = 9 \times 10^8$, i.e. assuming every Fe atom results in a trapping state. The trapping constant is set to $\Upsilon = 1/(N_t^{max} \times 700\,\mu\text{s})$, to model the low temperature lifetime saturation. Note that by this choice for Υ, only the ratio N_t^{max}/Γ_d matters. The detrapping rate is again set to $\Gamma_d = 1/(1 \times 10^5\,\text{ms})$. The resulting spectra are displayed in Figure 4.10a. The same calculation, but for $\Gamma_d = 1/(2\,\text{ms})$ is seen in Figure 4.10c.

We see that for the $\Gamma_d = 1/(2\,\text{ms})$ case, we retrieve the results from the previous model, Figure 4.8b. In fact, by choosing these parameters we ensured that $\Gamma_d \gg \Upsilon N_{qp}^T$, as ($1/2\,\text{ms} \gg N_{qp}^T/(9 \times 10^8 \times 0.7\,\text{ms})$), or ($3.2 \times 10^8 \gg N_{qp}^T$), which is the case for these temperatures ($N_{qp}^T \approx 1 \times 10^7$ for 400 mK). For $\Gamma_d = 1/(1 \times 10^5\,\text{ms})$ we see that for KID2 we retrieved qualitatively the desired behaviour for all three spectra. The FNL drop seems the same in these spectra, but the saturation lifetimes differ. For KID3, we see that the phase has a double Lorentzian shape. The cause for this must lie in the phonon trapping factor, used to calculated R^*, as this is the only difference in used parameters in KID2 and KID3.

The lifetimes and FNLs extracted from these calculated spectra can be seen in Figure 4.11, together with the measured amplitude, phase and cross PSDs. The model prediction for phase is missing for KID3, as we cannot extract a single FNL and lifetime from a double Lorentzian shape.

Again, the amplitude predictions are close to the measured lifetimes and FNLs, but the phase and cross predictions deviate. That is, if we assume trapped quasiparticles not to contribute to the losses, whereas data suggest otherwise. Furthermore, we find that in amplitude ($S_{N_{qp},N_{qp}}$), a peak in lifetime has appeared. Comparing the FNL drop with Figure 4.9, we see that also a sharper knee has appeared at the same temperatures, indicated by the dotted orange lines. This is very similar to the effects of read power seen in Section 3.4.6.

Further investigation shows that the detrapping rate governs this behaviour, as shown in Figure 4.12. The detrapping rate is still very small, which makes the low frequency feature insignificant. However, as we have seen, a lower detrapping rate causes the trapping to become dominant at lower temperatures, when the quasiparticle lifetimes are higher. The saturation lifetime is determined by TN_t^{max}, which is still set to 1/(700 μs), thus resulting in a peak in lifetime and later, but steeper FNL drop. When extending the comparison to the read power effect, a higher read power would result in a lower detrapping rate.

In conclusion, the predicted amplitude response is close to the data, if we assume that trapped quasiparticles do not contribute to the amplitude response. The adjustment of the detrapping rate causes a similar effect on the lifetime and FNLs, as observed for read power. The predicted lifetimes for the phase and cross PSDs are not close to data. Moreover, when trapped quasiparticles do contribute

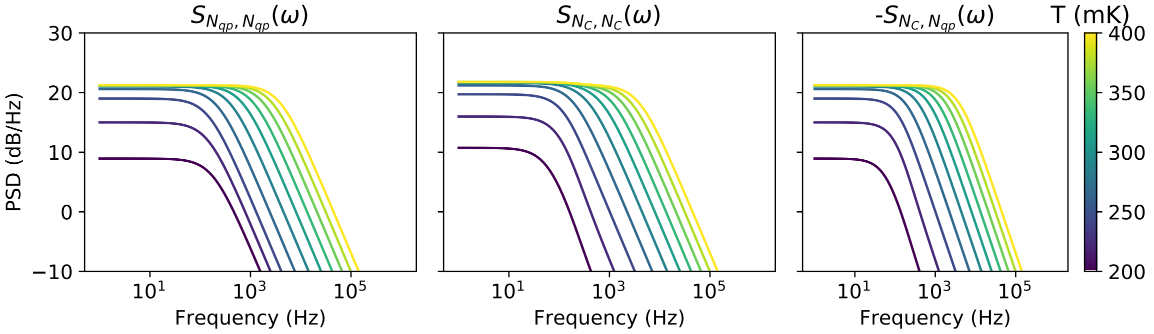

(a) KID2, $\Gamma_d = 1/(1 \times 10^5\,\mathrm{ms})$

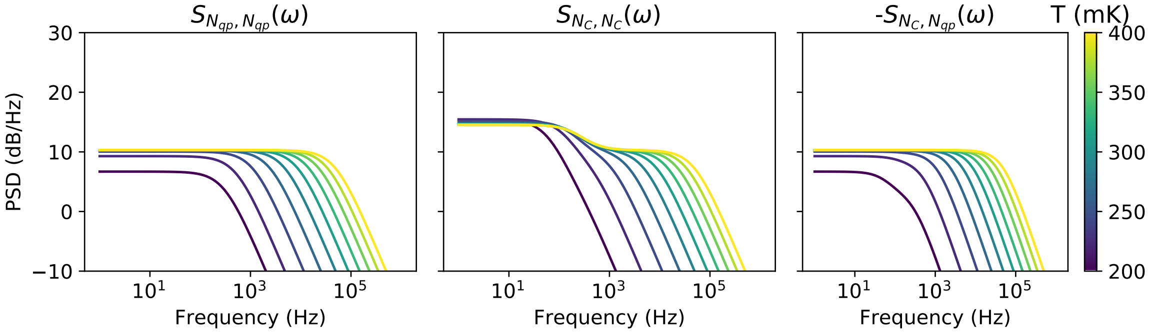

(b) KID3, $\Gamma_d = 1/(1 \times 10^5\,\mathrm{ms})$

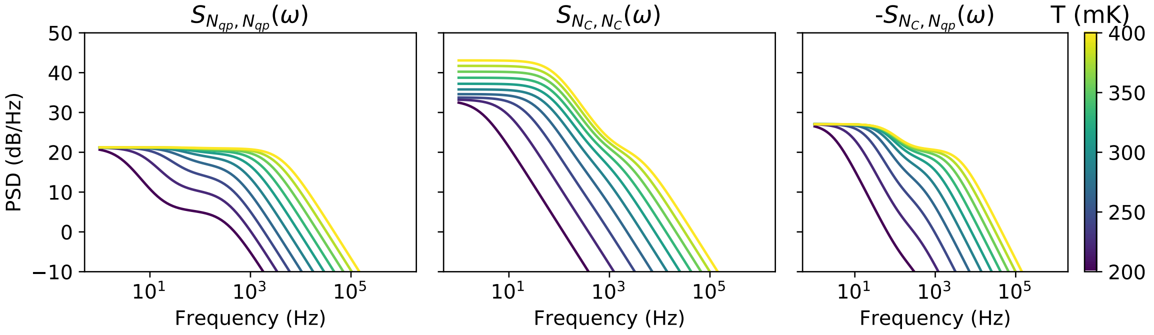

(c) KID2, $\Gamma_d = 1/(2\,\mathrm{ms})$

Figure 4.10: Calculated PSDs from the trapping model, with the trapping constant is set to $\Upsilon = 1/(N_t^{max} \times 700\,\mu\mathrm{s})$ and $N_t^{max} = 9 \times 10^8$. Parameters are for LT165, KID2 and KID3 respectively.

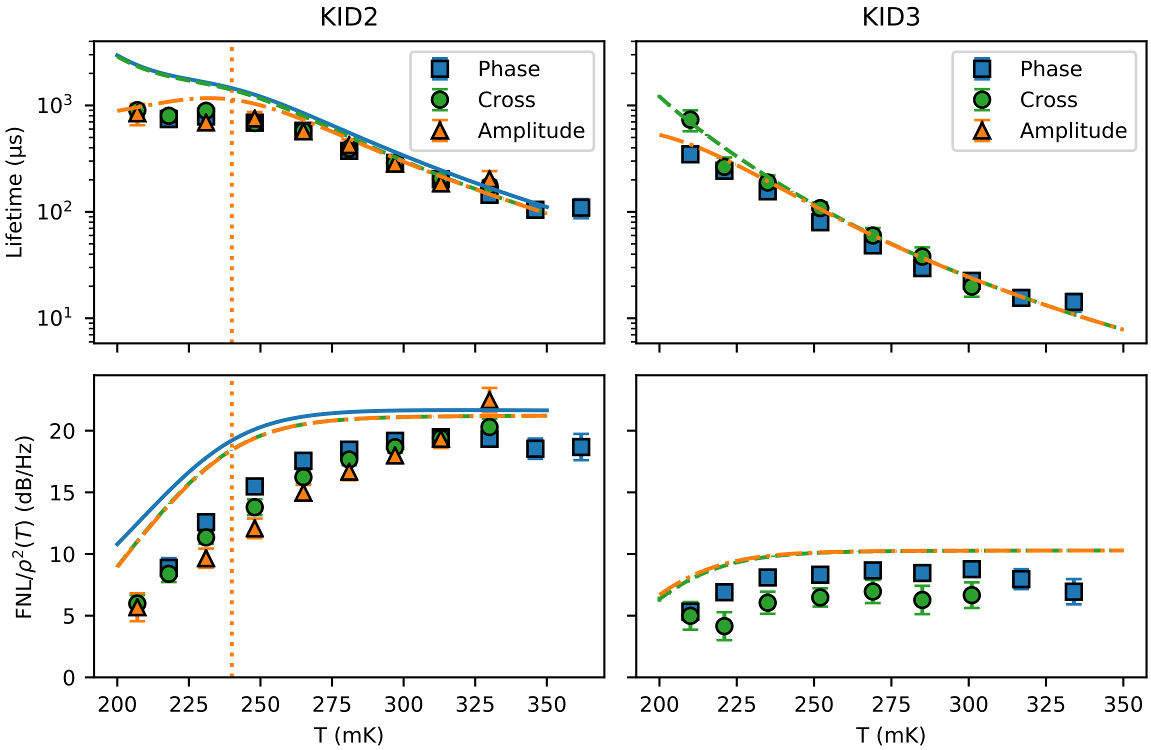

Figure 4.11: Lifetime and FNLs (divided by the appropriate responsivity squared: $\rho^2(T)$) from cross (●) and amplitude (▲) PSDs of LT165 KID2 and KID3 at −101 dBm and −99 dBm, respectively. The orange lines give the model predictions from the $S_{N_{qp},N_{qp}}$, the blue from S_{N_C,N_C} and the green lines are from the $-S_{N_C,N_{qp}}$ spectra. As model input, a trapping rate of 1/(900 µs) and detrapping rate of 1/(1 × 10^8 µs) are used. The orange dotted lines corresponds to 240 mK

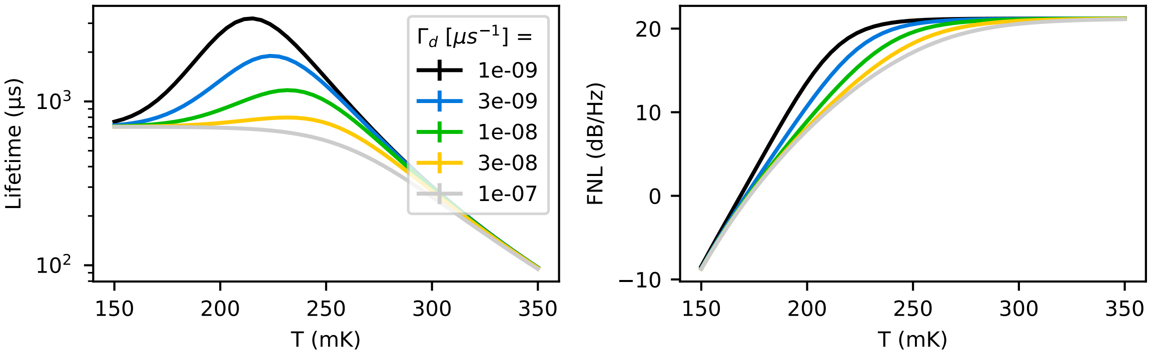

Figure 4.12: Lifetime and FNLs from the calculated $S_{N_{qp},N_{qp}}$ spectra, for different values of the detrapping rate. The trapping constant is set to $\Upsilon = 1/(N_t^{max} \times 700\,\mu s)$ and $N_t^{max} = 9 \times 10^8$. The parameters for LT165 KID2 are used.

to the amplitude response, this model cannot follow the data. Again, this can be attributed to the fact that also this model is set up by considering the behaviour of $S_{N_{qp},N_{qp}}$ (after which we also look at S_{N_C,N_C} and S_{N_qp,N_C}, which could not follow the data). Specifically, the trapping process (Γ_t) was used to model the lifetime saturation, which implies only the free quasiparticle lifetimes saturate.

4.5. Read Power Effects: Creation of Excess Quasiparticles

As stated in Section 3.4.6, read power can cause excess quasiparticles [7] and redistribution of quasiparticles and phonons [6, 71, 72], when read powers are lower than the onset of bifurcation [74]. Modelling of the redistribution of quasiparticles and phonons has been done successfully via the kinetic equation approach of Chang and Scalapino [71] in [6, 47], but is rather extensive. The creation of excess quasiparticles, can however be modelled in a much simpler way. Namely, by adding a generation term to the rate equations (of Section 4.3),

$$\frac{dN_{qp}}{dt} = -\frac{RN_{qp}^2}{V} + \Gamma_d N_t - \Gamma_t N_{qp} + 2\Gamma_B N_\omega + \frac{\eta_{read} P_{abs}}{\Delta}, \tag{4.12a}$$

$$\frac{dN_t}{dt} = \Gamma_t N_{qp} - \Gamma_d N_t, \tag{4.12b}$$

$$\frac{dN_\omega}{dt} = \frac{RN_{qp}^2}{2V} - \Gamma_B N_\omega - \Gamma_{es}(N_\omega - N_\omega^T), \tag{4.12c}$$

$$\tag{4.12d}$$

Here, η_{read} is the efficiency with which read power breaks Cooper-pairs (on the order of 1×10^{-4} [7]) and P_{abs} is the absorbed power in the resonator, which can be expressed as [6],

$$P_{abs} = \left(\frac{4Q^2}{Q_c Q_i}\right)\left(\frac{Q_i}{Q_{i,qp}}\right)\frac{P_{read}}{2}. \tag{4.13}$$

Here, the first factor in parenthesis is the coupling efficiency and the second factor is the fraction of quasiparticle losses to the total internal resonator losses.

In analogy with Section 2.2.2, this addition alters the steady state quasiparticle number in,

$$N_{qp}^0 = \sqrt{\frac{V(1+\Gamma_B/\Gamma_{es})}{R}\frac{\eta_{read} P_{abs}}{\Delta} + \left(N_{qp}^T\right)^2} = \sqrt{\left(N_{qp}^{ex}\right)^2 + \left(N_{qp}^T\right)^2}, \tag{4.14}$$

where N_{qp}^{ex} is the excess quasiparticles created by the read power. This value changes with temperature, as the quality factors in P_{abs} change, but typically not more than one order of magnitude (maximizing at $Q_i = Q_c$). In contrast, the thermal number of quasiparticles changes exponentially with temperature. Therefore at high temperatures, $N_{qp}^0 \approx N_{qp}^T$ and for low temperatures, $N_{qp}^0 \approx N_{qp}^{ex}$. The trapped quasiparticle number can still be expressed in N_{qp}^0 in the same manner, $N_t^0 = \Gamma_t N_{qp}^0/\Gamma_d$. Intuitively, that means that when lowering the temperature, there is a point after which the quasiparticle number does not decrease, and the lifetimes and FNLs saturate. This is what is observed in Section 3.4.6 in LT145.

The combination of trapping effects at higher temperatures and a FNL and lifetime saturation lower temperatures,is seen in some MKIDs, for example in LT179Wide, KID11. See Appendix D for cross PSD lifetimes and FNLs. Here, we will compare the amplitude lifetimes and FNLs, as we saw in Section 4.3, that the trapping model is only able to predict the amplitude PSDs, when also assuming trapped quasiparticles do not contribute to the amplitude response.
Calculating the steady state values as described above, and using $\eta_{read} = 6 \times 10^{-4}$, $Q_i/Q_{i,qp} = 1$ and the low temperature value for P_{abs}, the model predicts the amplitude FNLs and lifetimes as seen in Figure 4.13.

We see that the lifetime saturation is quite accurately captured by the increase in quasiparticle generation power. The FNLs from the measurement are generally lower than the predicted FNLs, possibly

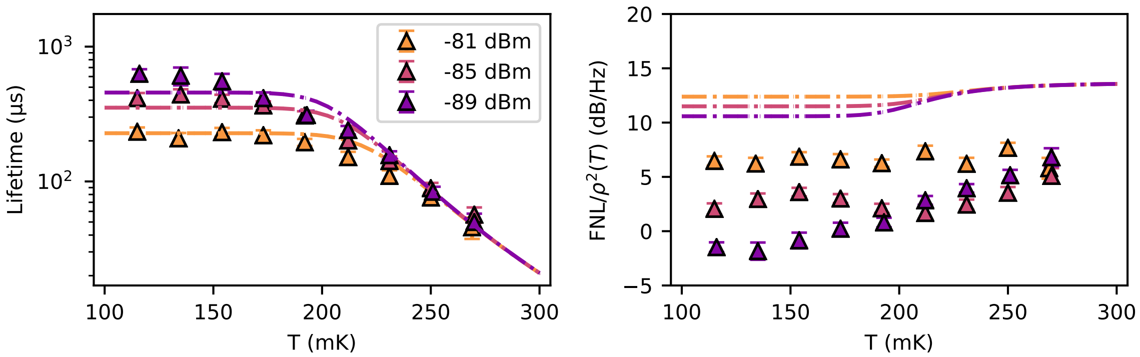

Figure 4.13: Lifetimes and FNLs (divided by responsivity squared: $\rho^2(T)$) from the amplitude PSDs of LT179Wide, KID11 for three different read powers (see legend). The lines give the predicted values for the $S_{N_{qp},N_{qp}}$ spectra, with a generation term added to the model. The parameters for the trapping model are the same as in Section 4.3 ($\Gamma_t = 1/(900\,\mu s)$ and $\Gamma_d = 1/(1 \times 10^8\,\mu s)$) and the generation term parameters are: $\eta_{read} = 6 \times 10^{-4}$ and P_{abs} =9.5 MeV s^{-1}, 2.6 MeV s^{-1} and 1.0 MeV s^{-1}, for −81 dBm, −85 dBm and −89 dBm, respectively.

due to an error in the measured amplitude responsivity. The general behaviour is the same for the model and data: the FNL drop is less apparent at higher read powers. However, in the data this effect is larger. The reason for this could be a read power dependence in trapping parameters (Γ_t, Γ_d), as Grünhaupt et al. [84] argue that detrapping is stimulated by read power. Another possible explanation is that responsivity is dependent on read power, due to the redistribution of quasiparticles. A non-thermal quasiparticle and phonon distributions, alter the electrodynamic response (via Mattis-Bardeen equations, Equation (2.4)) [6].

In conclusion, the creation of excess quasiparticles in MKIDs that exhibit quasiparticle trapping states can be modelled qualitatively by adding a generation term to the free quasiparticle level. To get quantitative agreement, more involved methods are needed, such as the kinetic equation approach by Chang and Scalapino [71].

4.6. Temperature Dependent Detrapping

Kozorezov et al. [10] have calculated relevant quasiparticle transition rates in the presence of magnetic impurities, starting from the Müller-Hartmann and Zittartz model [107, 108]. These calculations give values for the trapping and detrapping rates on microscopic grounds, whereas these rates were fit parameters in the previous sections. Assuming a discrete, subgap trap energy, ϵ_0 (like in Figure 4.6), the expressions for the trapping and detrapping rates are,

$$\Gamma_t = 2\frac{c}{\tau_{sl}}\left(1 - \frac{\epsilon_0}{\Delta}\right)(n(\Delta - \epsilon_0) + 1)(1 - f(\epsilon_0)), \tag{4.15a}$$

$$\Gamma_d = \frac{\sqrt{\pi}}{4}\left(\frac{k_B T}{\Delta}\right)^{\frac{3}{2}} e^{-\frac{\Delta - \epsilon_0}{k_B T}} \tag{4.15b}$$

$$\times\left[\frac{1}{\tau_{ep}}\left(3 + 2\left(\frac{\Delta - \epsilon_0}{k_B T}\right)\right)\frac{k_B T}{\Delta} + \frac{4}{\tau_{sl}}\left(1 + \frac{\Delta - \epsilon_0}{k_B T}\right)\right]. \tag{4.15c}$$

(4.15d)

For the trapping rate, only transitions from the gap edge, Δ are considered. This is justified by the fact that at low temperatures, quasiparticle scattering processes are dominant, which relax the quasiparticles to the gap edge [36]. The times τ_{ep} and τ_{sl} describe the inelastic transitions between the continuum and the subgap state via deformation-potential and spin-lattice interactions, respectively. $n(E)$ and $f(E)$ are the phonon and quasiparticle distribution functions, for which we use the Bose-Einstein and Fermi-Dirac distribution functions. T is the quasiparticle temperature and c is the dimensionless trap density, in units of $2N(0)\Delta$.

In the expression for the detrapping rate, an exponential dependence on temperature is present. Due to this term, detrapping becomes dominant for high temperatures, and conversely trapping becomes

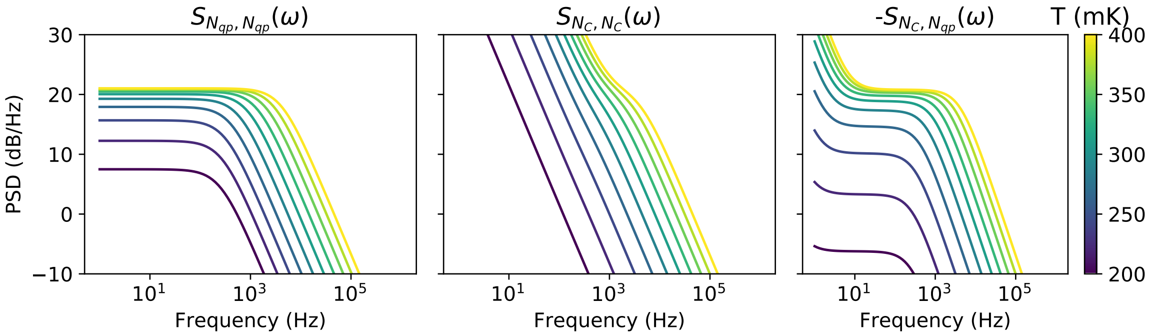

Figure 4.14: Calculated PSDs, with the trapping constant is set to τ_{sl} is set to 5 ms, τ_{ep} = 10 ms, c = 5. Parameters are for LT165, KID2.

dominant for low temperatures. In Section 4.3, we saw that the ratio Γ_t/Γ_d dictated the spectrum behaviour between the thermal (Equation (3.9)) and the spectrum of Equation (4.8), when $\Gamma_d + \Gamma_t \ll \Gamma_R^*$. The potential the trapping model in this section has, is therefore that this crossover is described by the exponential temperature dependence in the detrapping rate. Note that also here, we focus on free quasiparticles fluctuations, ascribing the lifetime saturation to trapping.

Using these rates in the altered Rothwarf-Taylor equations in Equation (4.3), from Section 4.3 and the concentration calculated with 9 × 10^8 traps again ($c = 5$ for LT165, KID2). We set τ_{sl} such that $\Gamma_t = 1/\tau^*_{qp,sat}$, where $\tau^*_{qp,sat}$ is the saturation lifetime of approximately 1 ms.
Note that we chose for the trap concentration the maximum amount, i.e. every Fe atom as a trap. When choosing a lower value, also τ_{sl} must be lowered to keep $\Gamma_t = 1/\tau^*_{qp,sat}$ (see Equation (4.15)). That however, results in a high detrapping rate, producing double Lorentzian spectra, as seen in Figure 4.8b. Therefore, we chose the upper limit from the SIMS analysis.
After trying some values for ϵ_0,τ_{sl} and τ_{ep}, we have set the trap energy to one tenth of the gap $\epsilon_0 = \Delta/10$. τ_{sl} to 5 ms and τ_{ep} to a sufficiently large value (≥10 μs), to avoid extra phonon-electron contributions to the detrapping, resulting in a second Lorentzian shape at low frequencies.

We see that we approximately retrieved the spectra of Section 4.3 (Figure 4.10a). However, we had to set τ_{ep} and τ_{sl} to milliseconds, in order to describe a free quasiparticle lifetime saturation via trapping. Kozorezov et al. [10] estimate τ_{sl} to be of the order of τ_0, the electron-phonon interaction time (440 ns for Al [36]), when traps are assumed to have a localised effect. Also Hijmering et al. [81] show that τ_{ep} and τ_{sl} are in the order of nanoseconds (τ_0 used there is 2 ns, for Ta), when fitting a similar model, but for STJ responsivity.
Furthermore, we saw that all previous models could not describe the phase and cross PSD behaviour. Only when assuming that trapped quasiparticles do not contribute to the amplitude, the amplitude lifetime and FNL behaviour could be modelled via $S_{N_{qp},N_{qp}}$. In all cases where Cooper-pairs contribute to the fluctuations, the models could not follow the data. The measured amplitude, phase and cross PSDs show similar behaviour, which suggest that quasiparticles do contribute to the amplitude response and the spectra relate to S_{N_C,N_C}, i.e. Cooper-pair fluctuations.
Combining these two observations, we conclude that the models we have discussed so far, are set up in a wrong way by attributing the lifetime saturation to the process of trapping (Γ_t). Because also phase and cross PSDs show a lifetime saturation and FNL drop, the process responsible must include transitions to the Cooper-pair level.

4.7. On-trap Recombination

As we concluded that trapping could not be responsible for the lifetime saturation observed in phase, amplitude and cross PSDs, another process must be included. The recombination of trapped and free quasiparticles (on-trap recombination) is a good candidate, as it does involve the Cooper-pair level. This process is depicted in Figure 4.6 as (5) along with the opposite process, on-trap pair-breaking (6).

Kozorezov et al. [10] argue that on-trap recombination is dominant at low temperatures, because the detrapping rate is effectively zero at low temperatures. Therefore, almost all quasiparticles are trapped making it more likely for a free quasiparticle to recombine with a trapped quasiparticle. Including these processes in the Rothwarf-Taylor equations, we get,

$$\begin{aligned}
\frac{dN_{qp}}{dt} &= -\frac{RN_{qp}^2}{V} - \frac{R_t}{2V}N_tN_{qp} + 2\Gamma_B N_\omega + \Gamma_B^{sg}N_\omega^{sg} - \Gamma_t N_{qp} + \Gamma_d N_t, && \text{(4.16a)}\\
\frac{dN_t}{dt} &= -\frac{R_t}{2V}N_tN_{qp} + \Gamma_B^{sg}N_\omega^{sg} + \Gamma_t N_{qp} - \Gamma_d N_t, && \text{(4.16b)}\\
\frac{dN_\omega^{sg}}{dt} &= +\frac{R_t}{2V}N_tN_{qp} - \Gamma_B^{sg}N_\omega^{sg} - \Gamma_{es}^{sg}(N_\omega^{sg} - N_\omega^{sg,T}), && \text{(4.16c)}\\
\frac{dN_\omega}{dt} &= +\frac{RN_{qp}^2}{2V} - \Gamma_B N_\omega - \Gamma_{es}(N_\omega - N_\omega^T). && \text{(4.16d)}
\end{aligned}$$

Here, we have added a level to account for the subgap phonons (N_ω^{sg}) that are emitted from on-trap recombination and are capable of on-trap pair-breaking, thus phonons with energy: $\Delta + \epsilon_0 \leq \Omega < 2\Delta$.

The recombination constants and trapping and detrapping constants, calculated by Kozorezov et al. are,

$$\begin{aligned}
R &= \left(\frac{2\Delta}{k_BT_c}\right)^3 \frac{1}{4N(0)\Delta\tau_0} && \text{(4.17a)}\\
\Gamma_t &= 2\frac{c}{\tau_{sl}}\left(1 - \frac{\epsilon_0}{\Delta}\right)(n(\Delta - \epsilon_0) + 1)(1 - f(\epsilon_0)) && \text{(4.17b)}\\
\Gamma_d &= \frac{\sqrt{\pi}}{4}\left(\frac{k_BT}{\Delta}\right)^{\frac{3}{2}} e^{-\frac{\Delta-\epsilon_0}{k_BT}} && \text{(4.17c)}\\
&\quad \times \left[\frac{1}{\tau_{ep}}\left(3 + 2\left(\frac{\Delta - \epsilon_0}{k_BT}\right)\right)\frac{k_BT}{\Delta} + \frac{4}{\tau_{sl}}\left(1 + \frac{\Delta - \epsilon_0}{k_BT}\right)\right]\\
R_t &= \frac{1}{\tau_{ep}}\frac{1}{N(0)\Delta}\left(1 + \frac{\epsilon_0}{\Delta}\right). && \text{(4.17d)}
\end{aligned}$$

They also calculated an expression for Γ_B^{sg}, the subgap phonon pair-breaking rate. However, this expression diverges for subgap phonons of energy $\Omega = \Delta + \epsilon_0$ because of the assumption of an infinitesimally narrow subgap trapping state energy [8]. Instead, it can be set to be a fit parameter, together with Γ_{es}^{sg}. Furthermore $N_\omega^{sg,T}$ is an added parameter, that describes the number of subgap phonon is the bath (i.e. substrate).

These rate equations (Equation (4.16)) in steady state, (assuming all parameters are known either with rates from Kozorezov et al. or without) do not have a unique solution, due to the non-linear coupling of the N_{qp} and N_t levels, i.e. the on-trap recombination term. This complicates the calculation, as the steady states values are needed for the fluctuation calculations. One could assume that the trapped and free number of quasiparticles are thermal, i.e.,

$$\begin{aligned}
N_{qp}^0 &= N_{qp}^T \approx 2N_0\Delta V\sqrt{\frac{\pi k_bT}{2\Delta}}e^{-\Delta/k_BT}, && \text{(4.18a)}\\
N_t^0 &= N_t^T \approx 2N_0\Delta Vce^{-\epsilon_0/k_BT}, && \text{(4.18b)}
\end{aligned}$$

where the approximation is for low temperatures ($\epsilon_0, \Delta \gg k_BT$), as is done by Hijmering et al. [81]. To account for phonon effects, they define a on-trap phonon trapping factor $\xi = 1 + \Gamma_B^{sg}/\Gamma_{es}^{sg}$ such that $R_t^* = \xi R_t$, and make ξ a fitting parameter.

However, when we try to calculate the fluctuations (instead of the excitation behaviour as Hijmering et al. do for STJs), we find that the on-trap recombination transition involves 3 levels, see Figure 4.15. The framework provided by Wilson and Prober [37], can only account for transitions from one level to another, which complicates this calculation even more. On top of that, we see that the transitions do not occur in pairs and cyclic transitions are possible, enabling non-equilibrium steady states (the multiple

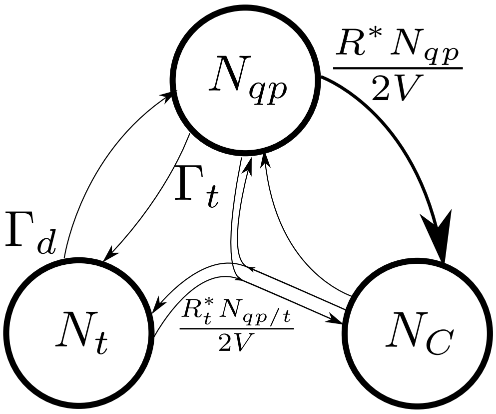

Figure 4.15: Diagram illustrating the different transitions between the levels (free, trapped quasiparticles and Cooper-pairs) for the on-trap recombination fluctuation model. Next to the arrows are the transition rates. When a rate is missing, the equilibrium value of the opposite rate is used, as given by the transition probabilities. The on-trap recombination rate is $R_t^* N_{qp}/(2V)$ for the N_t level and vice versa for N_{qp}, denoted by the $N_{qp/t}$. A thick arrow means that the transition has shot noise of 2.

solutions to the rate equations might already have given us a hint) and super- or sub-Poissonian noise [37].

These complications arise because we are looking at steady state measurements (GR noise). When considering excitation behaviour, the (on-trap) pair-breaking processes can be neglected and the excitation decay can be calculated fairly easily.

More work is needed to be able to describe the MKIDs noise behaviour with this model.

4.8. Quasiparticle Trapping Effects to the Single Photon Response

Apart from the GR noise, we can also look at the single photon response. We simply substitute the Rothwarf-Taylor equations, Equation (2.5), used in Chapter 2 to obtain the quasiparticle number evolution by the rate equations in the previous sections. For the model in Section 4.3 (the most simple one), we use Equation (4.3) and the same trapping and detrapping rates.

Besides substituting the rate equations, we should revisit the method for calculating the quasiparticle temperature. In Chapter 2, we calculated the quasiparticle temperature from the lifetime, which was either extracted from the pulse itself or from GR noise. However, we have seen that another process than recombination limits the quasiparticle lifetime, presumably on-trap recombination, which prevents us from using the lifetime as a probe for quasiparticle temperature. Therefore, we will use the bath temperature. Note that in Section 3.5 we argued that the quasiparticle density is thermal, justifying this approach, at least for temperatures as low as 170 mK (see Figure 3.23).

Furthermore, for low temperatures (120 mK), the Q_i factor from the single photon response model, differs significantly from the measured value as seen in Figure 2.9, because of other loss mechanisms such as TLS. Therefore, when using the bath temperature as quasiparticle temperature, we use the measured Q_i values over temperature instead of the calculated (Equation (2.18)) values. For further details on the single photon response see Chapter 2.

Here, we use the model of Section 4.3, with the same parameters used there: $\Gamma_t = 1/(900\,\mu s)$ and $\Gamma_d = 1/(1 \times 10^8\,\mu s)$. The evolution of the free quasiparticle number is used. The results of this adjusted single photon response model is shown in Figure 4.16.

We see that the model predicts a single exponential decay, with the decay rate equal to the trapping rate. This is expected as at low temperatures, trapping limits the free quasiparticle lifetime. The fitted pair-breaking efficiency is 44%, which is lower than the 69% from Section 2.4.2. This mainly is due to the different method for obtaining Q_i, but also the lower quasiparticle temperature (120 mK instead of 283 mK) lowers the fitted pair-breaking efficiency.

Here again, we should note that phase probes the number of Cooper-pairs, which means we should actually look at the total (trapped and free) quasiparticle evolution. However, trapping and detrapping processes do not alter the total number of quasiparticles and therefore do not alter the phase response.

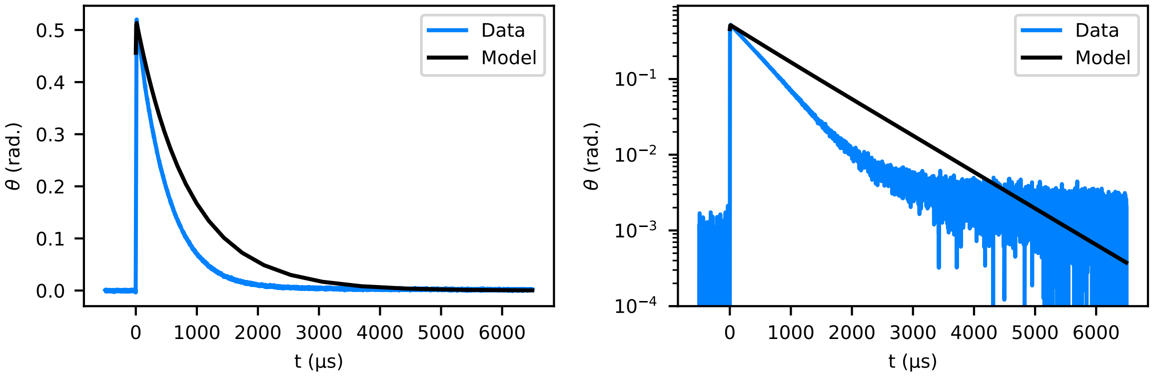

Figure 4.16: Single photon pulse data for 402 nm, LT165 KID2 at −89 dBm read power with single photon response model using the quasiparticle trapping rate equations (Equation (4.3)). Linear scale is shown left and the same data on a log-scale is shown on the right.

Another process is needed to predict a second exponential decay.
The single photon response when using the rate equations and parameters of Section 4.4 and Section 4.6 is qualitatively the same and does not predict a second exponential decay.

The model which includes on-trap recombination has the potential to predict a second exponential decay, considering the non-equilibrium character. More work needs to be done on this model in order to see if this is the case.

4.9. Detector Performance

As mentioned, quasiparticle traps can degrade detector performance. For example, it can decrease the responsivity in STJ's [8]. However, for MKIDs, it is not straightforward what the quasiparticle trapping does to the detector performance. Specifically, the GR noise drop could significantly improve the signal to noise ratio, at first sight. In this section we will qualitatively analyse how the detector performance is influenced by quasiparticle trapping, assuming this is the mechanism behind the FNL drop.

First, we will consider the detection and energy determination of single optical photons. The initial quasiparticles created by the incoming photon are not likely to be affected, as the photon energy down-conversion process occurs at quasiparticle energies much higher than subgap energies [45] and high energetic phonons are not likely to be influenced by the quasiparticle traps. This is supported by the fact that the fitted pair-breaking efficiencies at 120 mK in Section 2.4.2 are not drastically lower than the values at 250 mK, which implies that the responsivity ($d\theta/dN_{qp}$) is not altered much. However, the quasiparticle lifetime is reduced, which results in a faster single photon pulse decay. As the pulse amplitude is calculated from the full pulse, this will lower the energy resolving power. On the other hand, the noise is drastically reduced by virtue of the GR noise drop, which enhances the signal to noise ratio, therefore increasing the resolving power. Considering that the quasiparticle lifetime is limited by other processes when no quasiparticle trapping effects are observed, such as read power induced excess quasiparticles, the reduction in noise would be more significant. That implies that the overall energy resolution would be higher, but experiments should be done to confirm this.

Secondly, we will consider the detection of radiation where no single photon peak can be observed, as for example therahertz radiation [12]. The relevant parameter characterizing this performance is Noise Equivalent Power (NEP), which is the power that can be observed with a signal to noise ratio of one with a bandwidth of 1 Hz. A low NEP is therefore desirable. It is given by [20],

$$NEP = \sqrt{S_{X,X}}\left(\frac{dX}{dP_{rad}}\right)^{-1}\sqrt{1+\tau^2\omega^2}, \tag{4.19}$$

where X is either amplitude or phase, P_{rad} is the radiation power and τ is the limiting timescale. When taking for X, θ, we can rewrite: $\frac{d\theta}{dP_{rad}} = \frac{d\theta}{N_{qp}}\frac{dN_{qp}}{dP_{rad}}$, where the first factor is the responsivity (Equation (2.27b)) and $\frac{dN_{qp}}{dP_{rad}}$ can be obtained from the Rothwarf-Taylor equations (Equation (2.5)), when adding a quasiparticle generation term:

$$\frac{dN_{qp}}{dt} = -\frac{RN_{qp}^2}{V} + 2\Gamma_B N_\omega + \frac{\eta_{pb}P_{rad}}{\Delta}, \tag{4.20}$$

where η_{pb} is the pair-breaking efficiency. Following Section 2.2.2 (replacing I with $\eta_{pb}P_{rad}/\Delta$), we arrive at $\delta N_{qp} = \tau_{qp}^*\eta_{pb}/\Delta$, where τ_{qp}^* is as defined in Equation (2.14), including both the phonon trapping factor and the factor $1/2$ from pair-wise recombination. This gives: $\frac{dN_{qp}}{dP_{rad}} = \frac{\eta_{pb}\tau_{qp}^*}{\Delta}$. So, when probing phase and assuming the quasiparticle lifetime is the limiting lifetime, we thus have,

$$NEP = \sqrt{S_{\theta,\theta}}\left(\frac{d\theta}{dN_{qp}}\frac{\eta_{pb}\tau_{qp}^*}{\Delta}\right)^{-1}\sqrt{1+(\tau_{qp}^*)^2\omega^2}, \tag{4.21a}$$

$$= \sqrt{S_{N_{qp},N_{qp}}}\left(\frac{\eta_{pb}\tau_{qp}^*}{\Delta}\right)^{-1}\sqrt{1+(\tau_{qp}^*)^2\omega^2}, \tag{4.21b}$$

$$= \frac{2\Delta}{\eta_{qp}}\sqrt{\frac{N_{qp}}{\tau_{qp}^*}}. \tag{4.21c}$$

Here we used that the phase spectrum is given by Equation (3.11) in the second equality and that $S_{N_{qp},N_{qp}}$ is given by Equation (4.8) in the last equality. If the quasiparticle system behaves thermal, without quasiparticle trapping, we know that $\tau_{qp}^* \propto 1/N_{qp}$ and thus that $NEP \propto N_{qp}$, meaning that the NEP improves exponentially at low temperatures.

However, in the case of quasiparticle trapping, we have seen that τ_{qp}^* saturates and no longer increases when lowering the temperature. At the same time, the quasiparticle number N_{qp} still seems to behave thermal, as seen in Figure 3.23. That would thus mean that the NEP would improve with $\sqrt{N_{qp}}$, in the quasiparticle trapping temperature regime. For comparison, when the lifetime saturation is caused by excess quasiparticles, both τ_{qp}^* and N_{qp} saturate and no NEP improvement is made when lowering the temperature. Quasiparticle trapping thus improves the detector performance when this process substitutes the creation of excess quasiparticles and the NEP is GR noise limited. Experiments should be set-up in order to confirm this.

4.10. Conclusion

In this chapter, we studied the concept of quasiparticle trapping as an explanation for the FNL drop and second exponential decay seen in Chapters 2 and 3, respectively. After briefly presenting an overview of the theory of quasiparticle trapping by different mechanisms, we proposed magnetic impurities to be the quasiparticle trapping cause in our systems. This is supported by a SIMS analysis showing Fe contamination between the Al film and the substrate. Also the Al geometry dependence of the GR noise drop is consistent with this hypothesis.

The most simple model, containing only a trapping and detrapping term with constant rates, was able to describe the data, when only amplitude was considered and the trapped quasiparticles were assumed to have no contribution to the quasiparticle losses. When this assumption was dropped or another variable was considered (phase or cross PSD), the model could not follow the lifetime saturation and FNL drop, observed in the data.

When introducing a finite number of traps, we saw that a low enough detrapping rate resulted in a peak in lifetime before saturation and a sharp knee in the FNL drop, comparable to the effects we saw as a function of read power in Section 3.4.6. Again, only for the amplitude PSDs when assuming trapped quasiparticles cannot contribute to quasiparticles losses, the model resembled the data.

By adding a quasiparticle generation term to the free quasiparticle level of the simplest model, we were able to qualitatively model one aspect of the read power effects: the creation of excess quasiparticles. Substituting the trapping and detrapping rates in Section 4.3 by the calculated ones from Kozorezov et al. [10], resulted after optimization in the same results. However, the values for the deformation-potential and spin-lattice interaction times obtained from the optimization were orders of magnitude higher than the estimated values in Reference [10] and fitted values in Reference [81]. Moreover, the models could only follow the amplitude data, when trapped quasiparticles do not contribute to the losses. When they do contribute, all spectra could not be described. On top of that, the data suggest that trapped quasiparticles do contribute to the losses, as all three spectra show similar behaviour. These observations led us to conclude that the lifetime saturation is not coupled to the trapping rate, as assumed in these models.

We saw that the introduction of an on-trap recombination term, which is expected to be dominant at low temperatures [10], could have the potential of making the trapping model consistent. However, this term caused the steady state rate equations to have multiple solutions and introduced cyclic transitions between levels. More work is needed to calculate the fluctuations resulting from this model.
Furthermore, we briefly looked at the single photon response predicted by the trapping rate equations. The second exponential decay could not be reproduced, with the present models. However, in future modelling, the single photon response should be altered such that the response is calculated from the total quasiparticle number, instead of only the free. Also the on-trap recombination rate equations should be investigated more, to be able to calculate the quasiparticle evolution upon photon absorption.

From the available data it is inferred that the measured GR noise effects improve detector performance for both single photon detectors and power integration detectors. Here, the assumption is made that the lifetime saturation due to quasiparticle trapping replaces the usually seen lifetime saturation due to read power induced excess quasiparticles. Experiments with and without this effect can justify or falsify this claim.

5

Conclusions and Recommendations

In this thesis we compared two types of MKID measurements with theory: the single photon response and generation-recombination (GR) noise. For the single photon response, a model is developed from the known physics that governs the MKID behaviour. This model includes several non-linearities such as the intrinsic non-linear process of quasiparticle recombination and the non-linearity for large phase values. Read power effects are not included into to model explicitly, but accounted for via an effective quasiparticle temperature, calculated via a measured quasiparticle lifetime, and MKID characterization measurements at different read powers. The only fit parameter included in the model is the pair-breaking efficiency, η_{pb}. All other parameters are determined either from literature (both theory and experiment) or extracted from a separate measurement.
At high temperatures (220 mK and 250 mK), the model predicts the single photon response of 4 different wavelengths, with a single set of parameters. In particular, the effect of phonon trapping is captured by the model as well, which we verified by looking at MKIDs both on substrate and membrane. The fitted values for η_{pb} are close to expected, although somewhat high (30%-60%), which might be caused by the redistribution of quasiparticles due to read power effects [6].
At lower temperatures (120 mK), the model can predict most of the decay as well. The only feature the model can not predict is a second exponential decay, which is observed to have a longer decay time. Moreover, the second decay constant is dependent on read power, with a faster decay for higher read powers. This second decay was visible in both the amplitude and phase, but occurs later in amplitude. The onset of the second exponential decay took place at a constant phase or amplitude value for different wavelengths.

For the GR noise, also an unexpected feature is observed, namely a GR noise drop, where theory predicts a constant noise level over temperature. At temperatures around 250 mK the flat noise level (FNL) of the amplitude, phase and cross power spectral densities (PSDs), drops exponentially with decreasing temperature, to the point where no GR noise signature (i.e. Lorentzian shape) is present in the PSDs. This effect can be made more visible by phonon trapping, as expected by theory. Changing the MKID geometry does not have an effect on the FNL drop, except for increasing the Al film thickness to 150 nm. That can however, be due to read power, as our analysis showed that a high enough read power could mask the effect, most likely due to creation of excess quasiparticles [6, 7]. Assuming the GR noise to be Poissonian in this noise drop regime, implies that the GR noise drop is caused by a process which limits the quasiparticle lifetime, while keeping the quasiparticle density thermal.

We propose an explanation for both these unpredicted measurement results: quasiparticle trapping. This hypothesis was first triggered by the fact that impurities in a superconducting film could enhance the recombination process [83] and that localisation of quasiparticles can cause long lived excitations [84]. In the search for quasiparticle traps in our system, a SIMS analysis (see Appendix A) showed Fe contamination on the substrate-Al film interface. This is the proposed cause for quasiparticle trapping. The location of these traps is consistent with the observation that the GR noise drop is only dependent on the film thickness and not on the Al width or length.
Different models that include quasiparticle trapping as the process that limits the quasiparticle lifetime,

can follow the GR noise drop data, but only for the amplitude PSDs and when assuming that trapped quasiparticles can not dissipate microwave power. In that case, the amplitude PSD is proportional to the free quasiparticle fluctuations, whereas phase and cross PSDs are related to Cooper-pair fluctuations. After implementation of the calculated trapping and detrapping rates by Kozorezov et al.[10], we found that the fit parameters used were orders of magnitude higher than τ_0, which should be of the same order [10, 81]. We combine this with the fact that the models could not predict the Cooper-pair fluctuations, whereas the data suggest that amplitude, phase and cross PSDs all relate to those fluctuations, as opposed to free quasiparticle fluctuations. We thus conclude that trapping itself can not be responsible for the lifetime saturation. On-trap recombination most likely plays a role in the quasiparticle lifetime saturation, as this is a dominant process at low temperatures. However, the fluctuation models including this term involve cyclic transitions and non-equilibrium steady states.

The second exponential decay can not be described by the trapping models considered.

A qualitative analysis on the MKID detector performance (both single photon and radiation power integration) showed that quasiparticle trapping effects can increase the energy resolving power and noise equivalent power at low temperatures, when this effect replaces the usual lifetime saturation due to creation of excess quasiparticles.

Recommendations

To understand the effects of quasiparticle trapping on the noise properties of MKIDs, the process of on-trap recombination needs to be studied in more detail. In particular, the non-equilibrium character of the induced cyclic transitions needs more investigation.

For the trapping effects on the single photon response, the existing model should be altered such that the phase response is proportional to the total (trapped and free) quasiparticles and it includes on-trap recombination.

Besides this modelling work, extra measurements of the single photon response in the intermediate temperatures of 120 mK to 220 mK is recommended to establish a firmer connection between the GR noise data and single photon response data.

To confirm that the Fe contamination causes quasiparticle trapping, new devices, preferably with the same designs as discussed in this thesis, should be made without contamination. To this end, the processing steps should be investigated and adjusted to eliminate the contamination, which should be checked by a SIMS analysis. The same data analysis should be done on these new devices, focussing on the GR noise drop and second exponential decay.

The claim that quasiparticle trapping increases the performance of both single photon and radiation power integration detectors, can be verified with these new devices as well. When experiments show that this is indeed the case, quasiparticle trapping can be introduced in MKIDs in a controlled way, for example via ion-implementation (such as in Reference [9]), to increase energy resolution and noise-equivalent power. Such devices can also be used for fundamental studies on the effect of disorder in superconductors.

As for data analysis, comparing different MKIDs is difficult due to read power effects. A detailed analysis of the microwave power absorption in the Al film is therefore needed.

A

SIMS Analysis

The SIMS analysis is done at EAG laboratories in Eindhoven. The full report can be provided upon request. Here, only a brief description of the important results is given.

Both a 50 nm and a 200 nm Al film on a sapphire substrate are analysed. The relative concentrations of different elements is shown in Figures A.1 and A.2. The green curve, showing the AlO$^+$ elements, probes the Al concentration, as the SIMS analysis is executed with a (2 keV) O$_2{}^+$-ion beam. The Al films are extreme clean, as almost no other element concentrations are found inside the film. However, at the Al film-substrate interface other elements are detected, mainly, Si and Fe.

Figure A.3 shows the quantified concentrations. Inside the film, the Si and Fe concentrations measured there are on the detection limit, which are 5 ppm for Fe and 50 ppm for Si in this case. At the interface of the film and the substrate, the Si and Fe concentrations peak. As Fe is ferromagnetic, it is particularly interesting in the light of quasiparticle trapping. For Fe, the concentration corresponds to about one tenth of a monolayer. This translates to 160 ppm and 480 ppm for the 150 nm and 50 nm Al films, respectively, when taking the Al atom diameter to be 2.4 Å.

Other elements found at the substrate-film interface include P and Ca, but at concentrations orders of magnitude smaller.

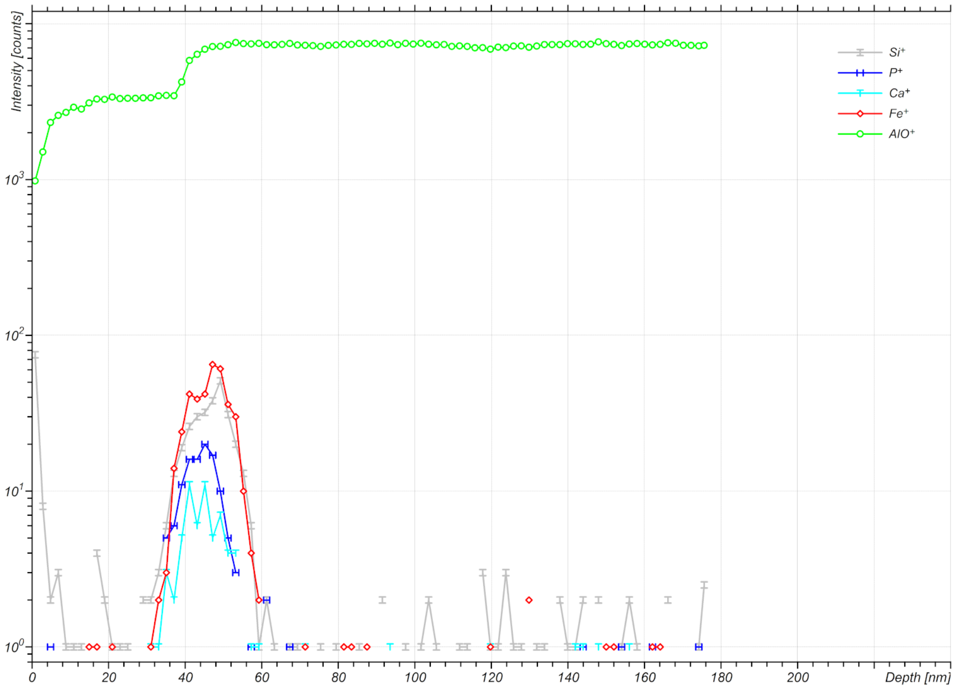

Figure A.1: Intensity of concentrations found in the 50 nm Al film on a sapphire wafer.

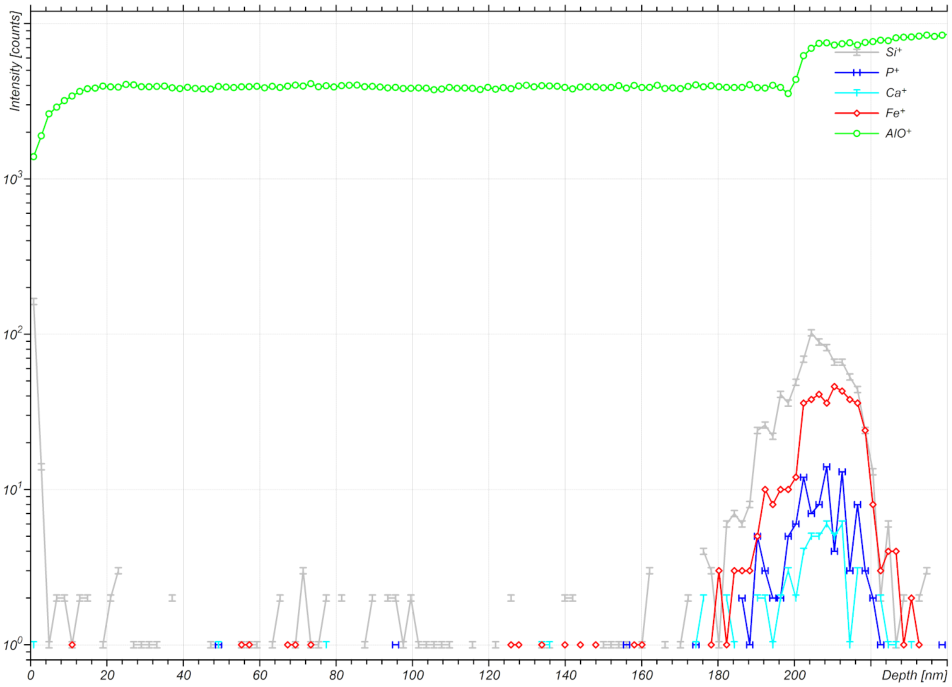

Figure A.2: Intensity of concentrations found in the 200 nm Al film on a sapphire wafer.

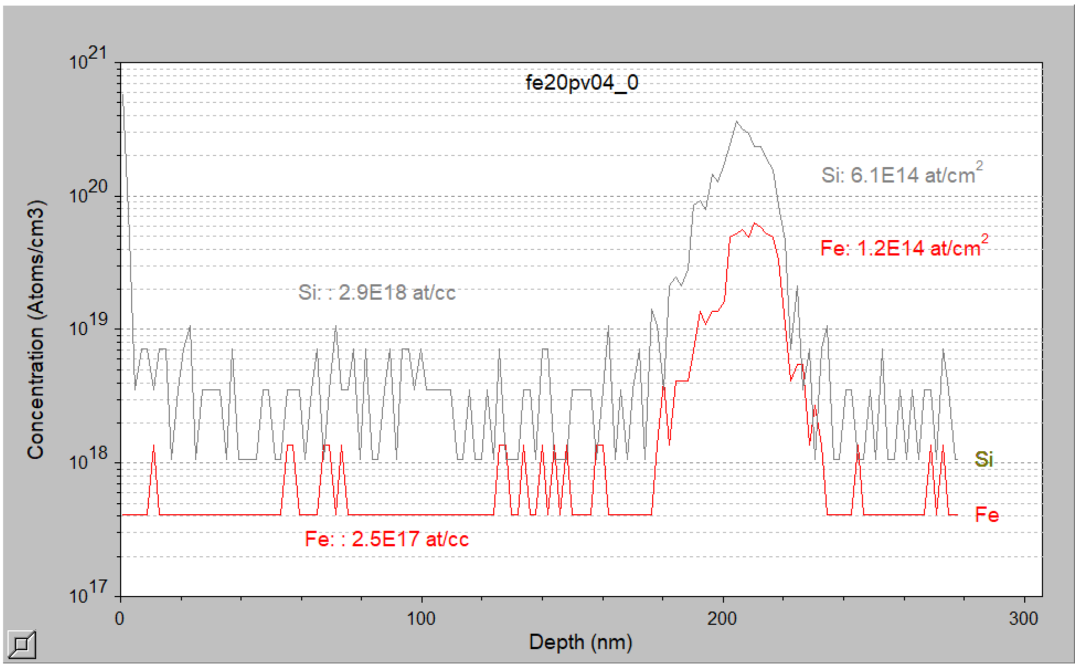

Figure A.3: Depth profiles of Si and Fe concentrations for the 200 nm Al film.

B

Peak Rejection Threshold

Figure B.1 shows the cross PSDs at the lowest measured temperature, 50 mK.The amounts of data that is rejected is on the right. For the biggest value used, 50σ (σ being the standard deviation of the time trace), we see that there is still a clear Lorentzian spectrum visible. When lowering the threshold, more pulses in the data are selected and more pieces of the time trace are thrown out, as seen in the right figure. Along with this, the Lorentzian shape disappears in these low temperature spectra. This disappearing takes place in steps, which is seen by the intermediate value of 20σ. All other data sets show the same behaviour.

From this, we conclude that pulse rejection is necessary, as pulses in the time trace greatly influence the spectra. For the lowest threshold value, 5σ, the rejection rate is not higher than 30%, which leaves enough data for the PSDs. For all data sets, a maximum rejection rate of 70% is seen, which leaves 12 s or 6×10^5 data points. Going lower than 5σ results in a rapid increase in rejection rate. Therefore, the threshold is set to 5σ.

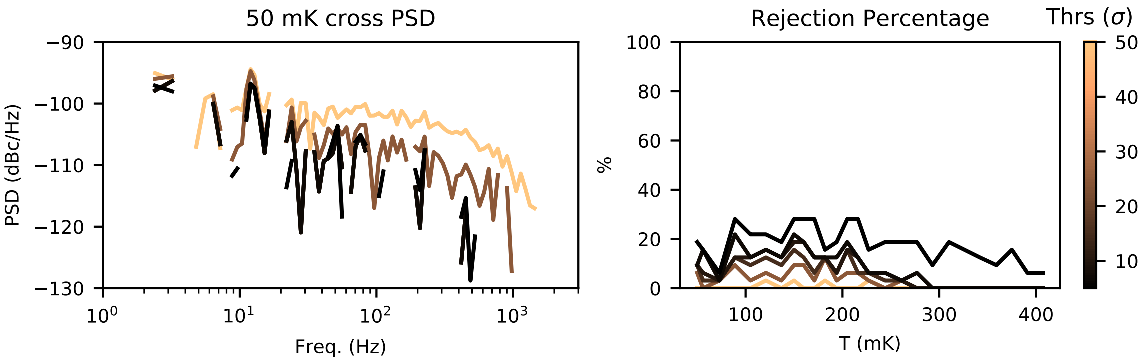

Figure B.1: (*left*): Cross PSD for LT165, at 50 mK, −81 dBm read power for different thresholds used for the peak rejection. (*right*): Amount of rejected data in percentages of the full time trace.

C

Single Photon Peak Results

C.1. LT139

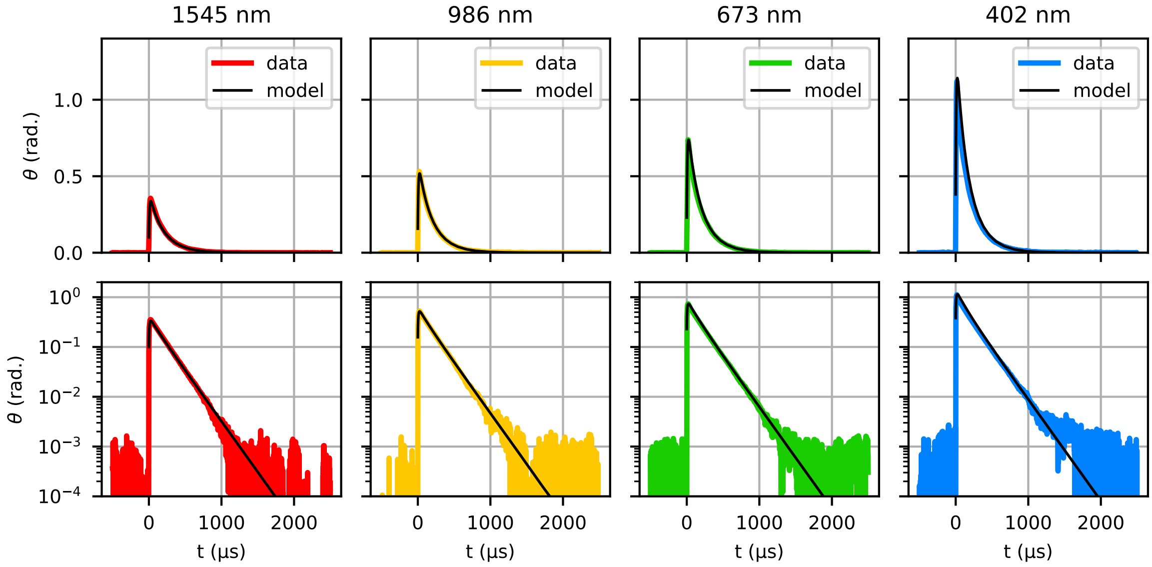

Figure C.1: LT139 at 220 mK, KID1, −92 dBm

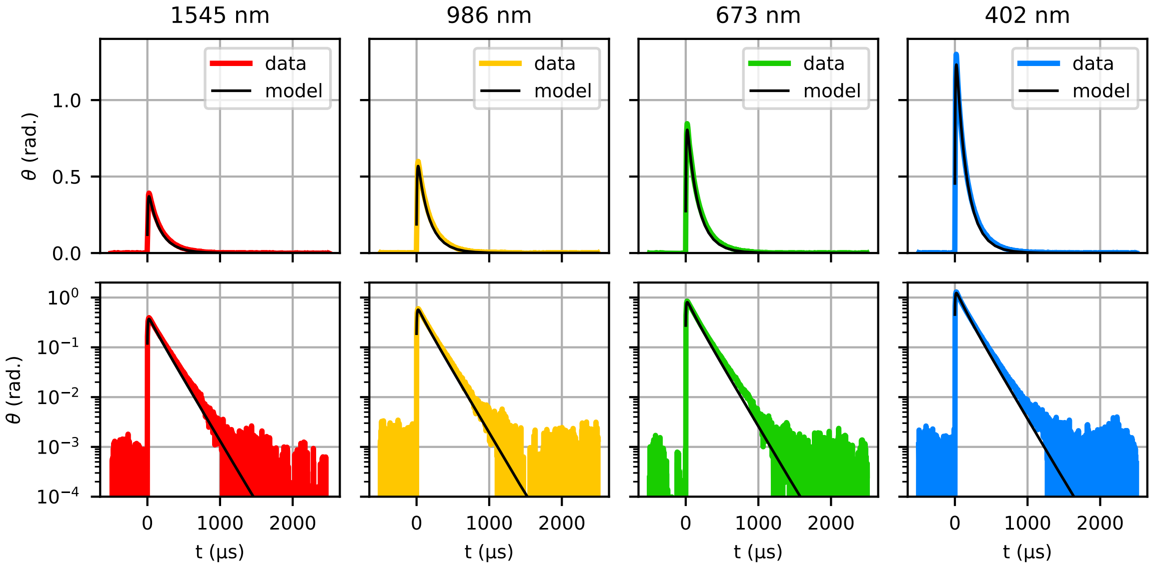

Figure C.2: LT139 at 220 mK, KID1, −96 dBm

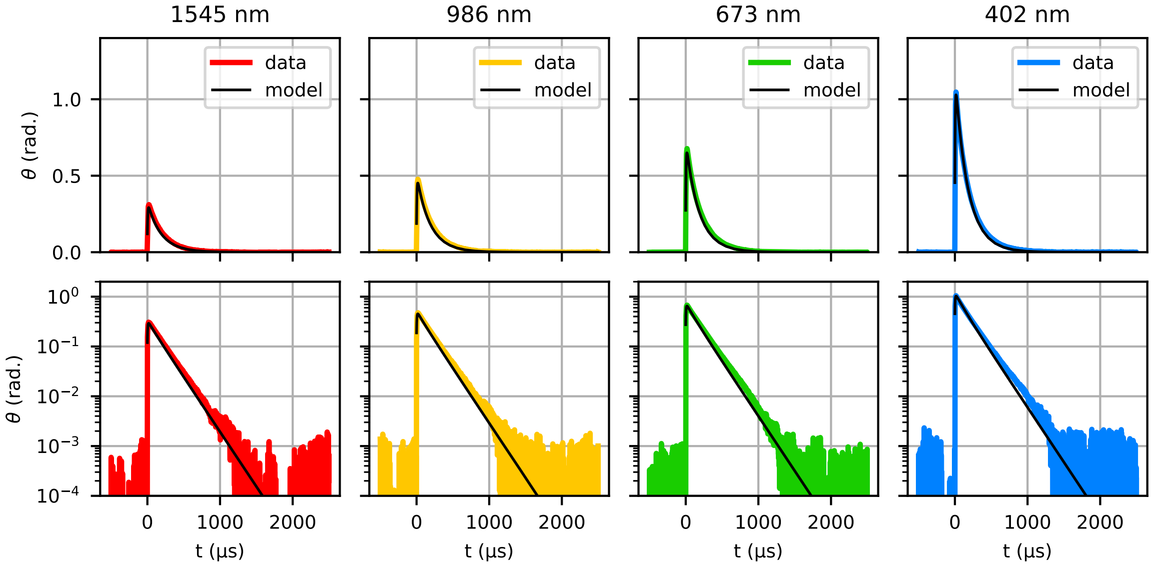

Figure C.3: LT139 at 220 mK, KID6, −92 dBm

Table C.1: LT139, 220 mK, T_{eff} with GR fit

Parameter	KID1 −92 dBm	KID1 −96 dBm	KID6 −92 dBm	KID6 −96 dBm
Q_c	1.58×10^5	1.49×10^5	1.22×10^5	1.15×10^5
$\hbar\omega_0$	20 μeV	20 μeV	21.2 μeV	21.2 μeV
$k_B T_0$	10.3 μeV	10.3 μeV	10.3 μeV	10.3 μeV
$k_B T$	19.5 μeV	19.9 μeV	19.6 μeV	19.2 μeV
V	12.4 μm^3	12.4 μm^3	24.6 μm^3	24.6 μm^3
α_k	0.0288	0.0292	0.0588	0.0591
τ_{esc}	0.161 ns	0.161 ns	0.149 ns	0.149 ns
η_{pb}	0.426	0.511	0.512	0.56

Parameter	Value
d	50 nm
$k_B T_c$	103 μeV
$k_b T_D$	37.3 meV
τ_0	440 ns
τ_{pb}	0.28 ns
$\lambda(0)$	92 nm
N_0	1.72×10^4 $\mu eV^{-1}\,\mu m^{-3}$

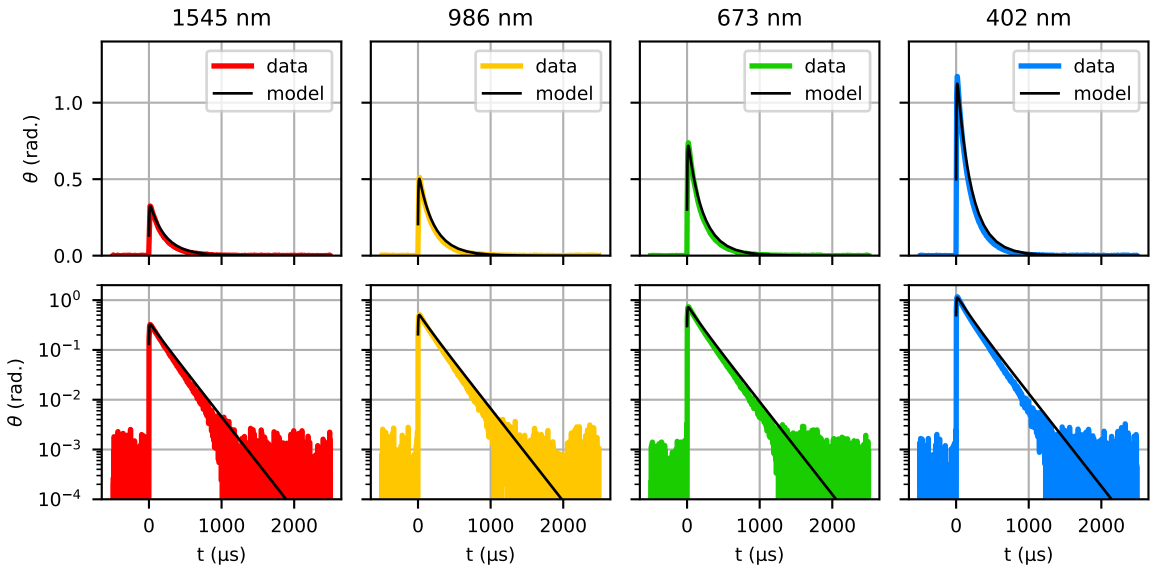

Figure C.4: LT139 at 220 mK, KID6, −96 dBm

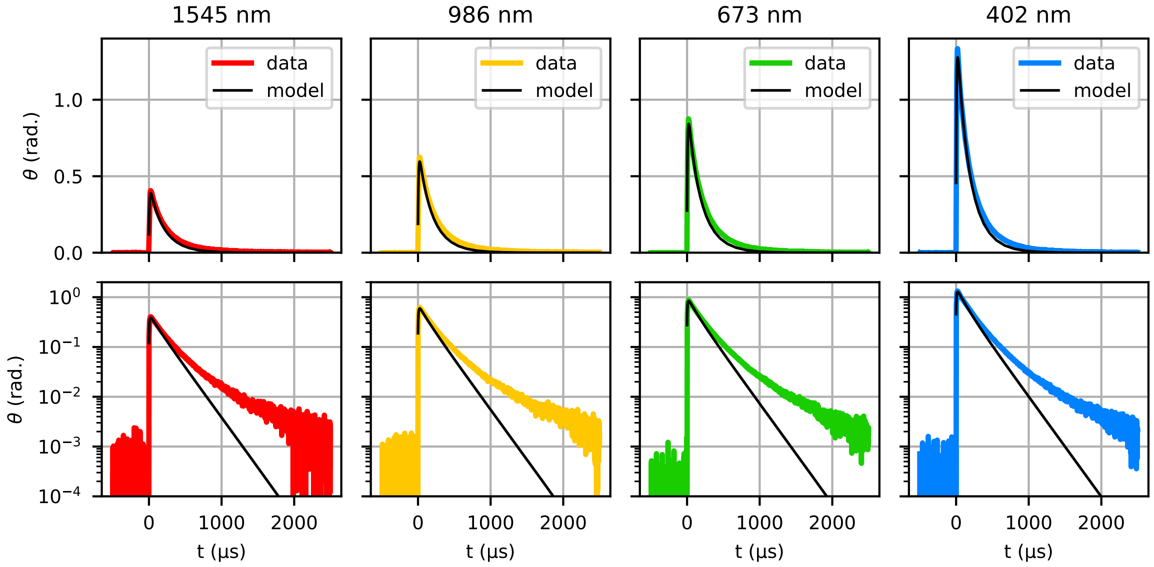

Figure C.5: LT139 at 120 mK, KID1, −96 dBm

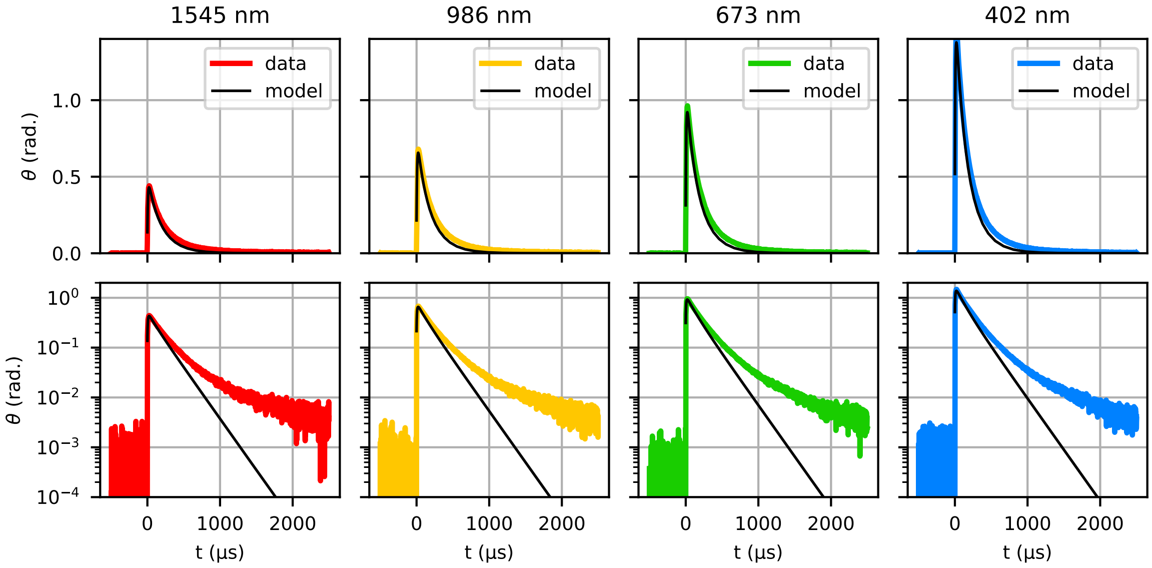

Figure C.6: LT139 at 120 mK, KID1, −100 dBm

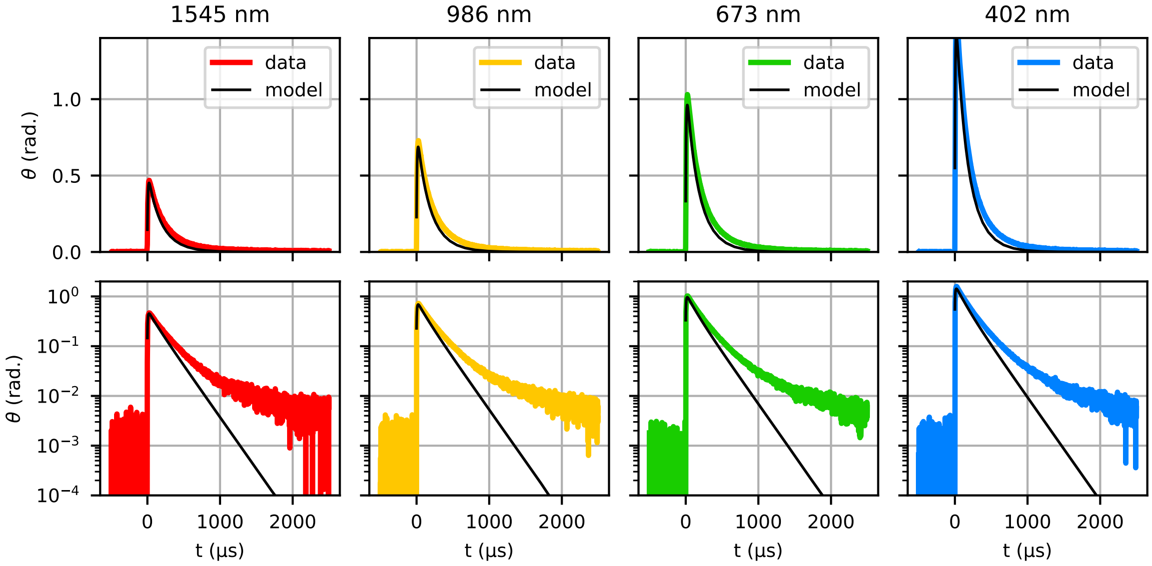

Figure C.7: LT139 at 120 mK, KID1, −104 dBm

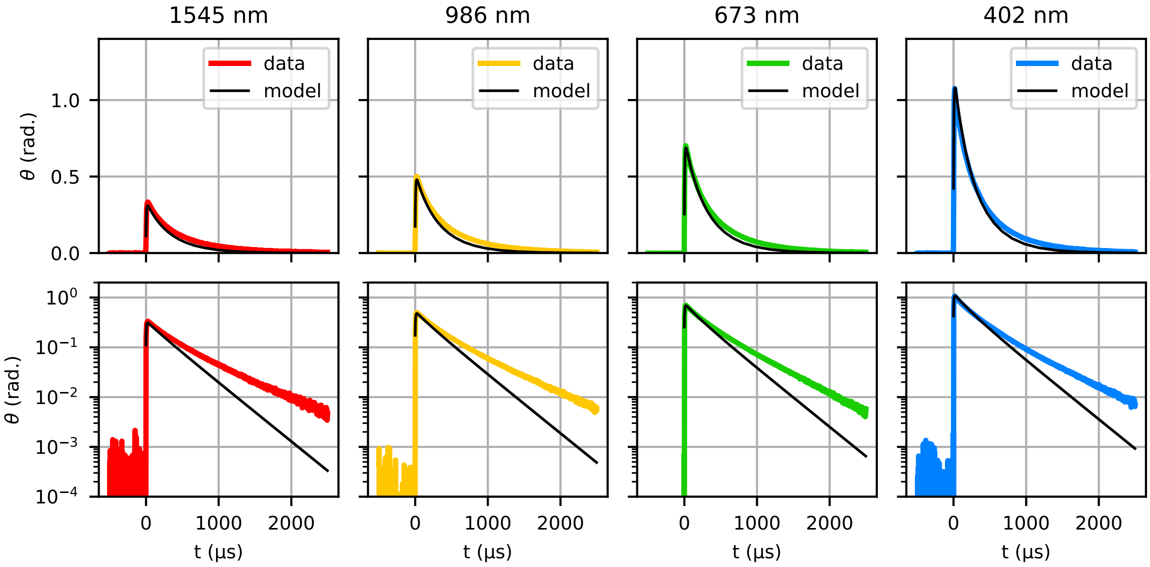

Figure C.8: LT139 at 120 mK, KID6, −92 dBm

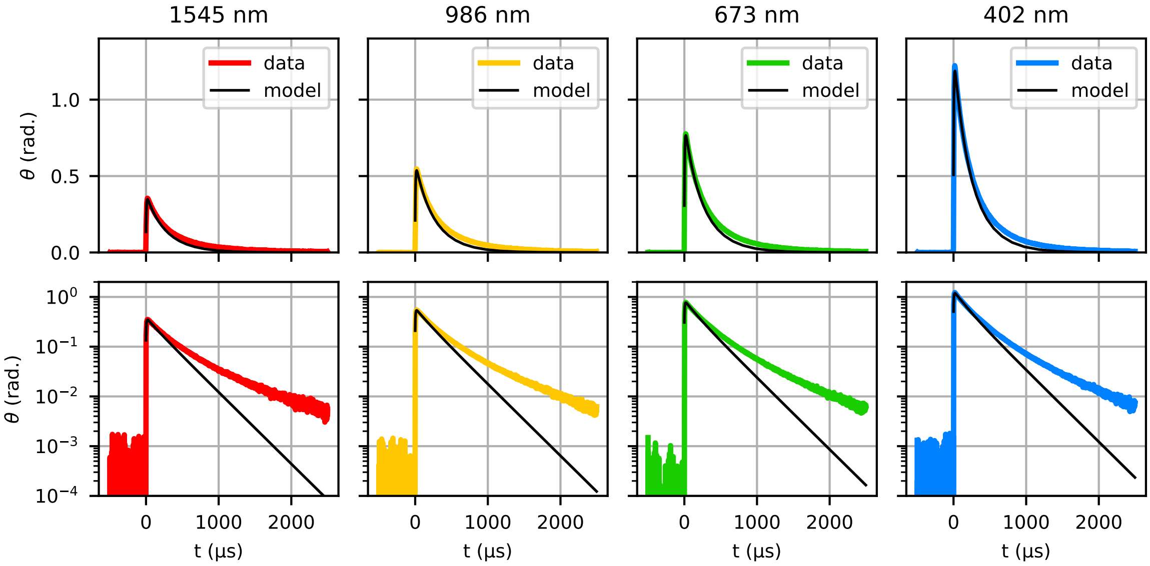

Figure C.9: LT139 at 120 mK, KID6, −96 dBm

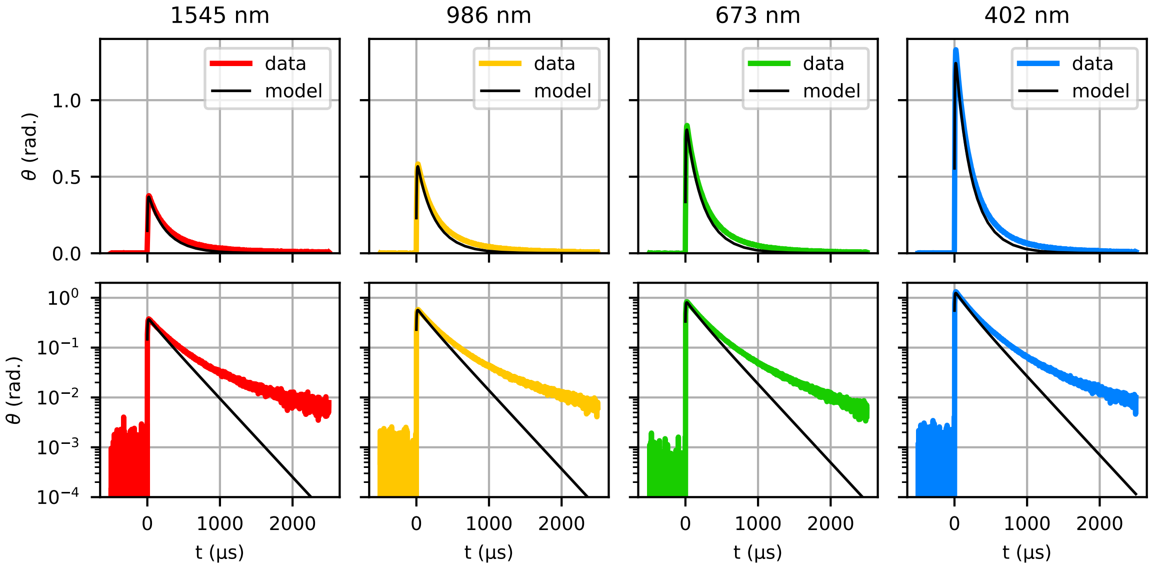

Figure C.10: LT139 at 120 mK, KID6, −100 dBm

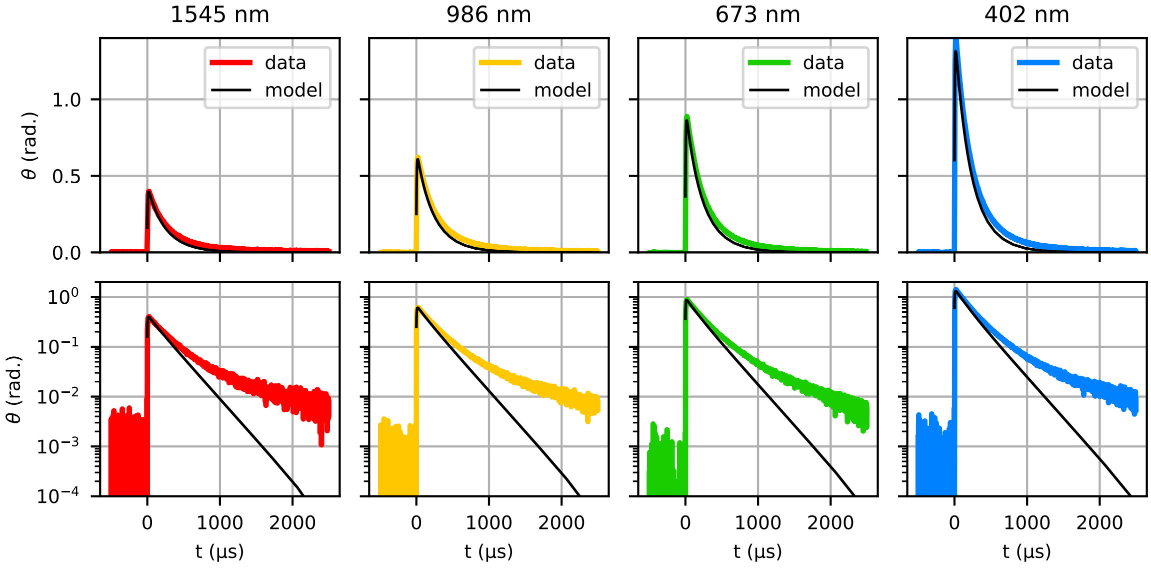

Figure C.11: LT139 at 120 mK, KID6, −104 dBm

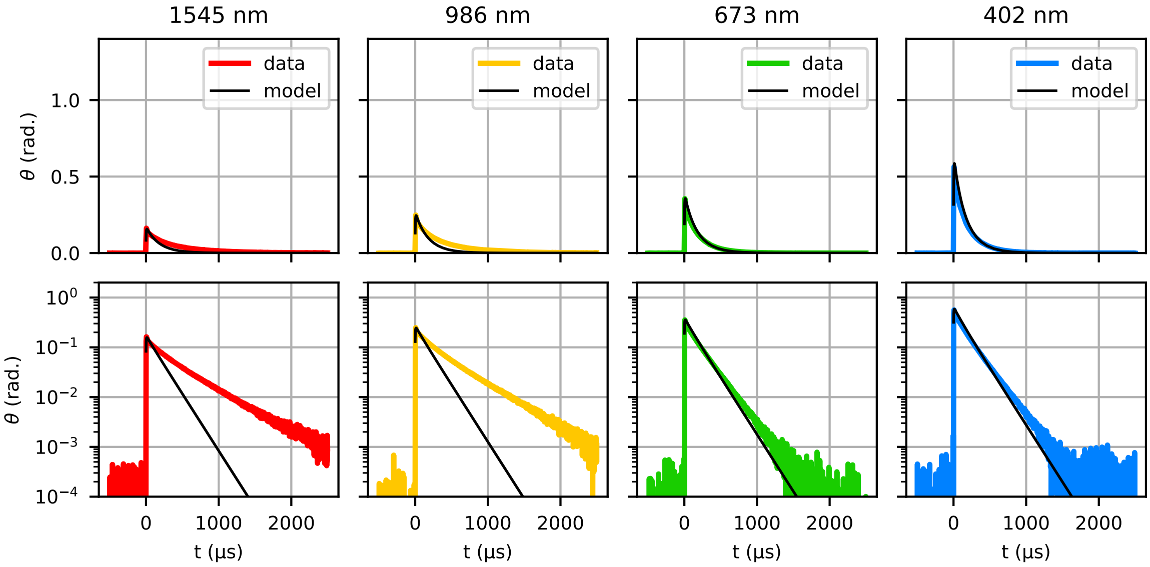

Figure C.12: LT139 at 120 mK, KID7, −88 dBm

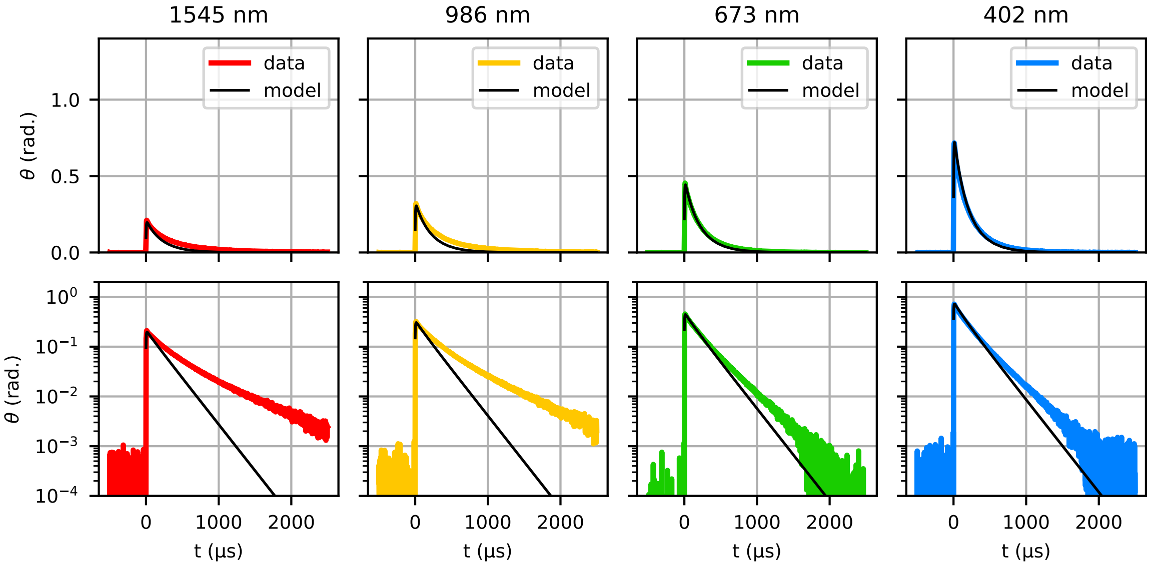

Figure C.13: LT139 at 120 mK, KID7, −92 dBm

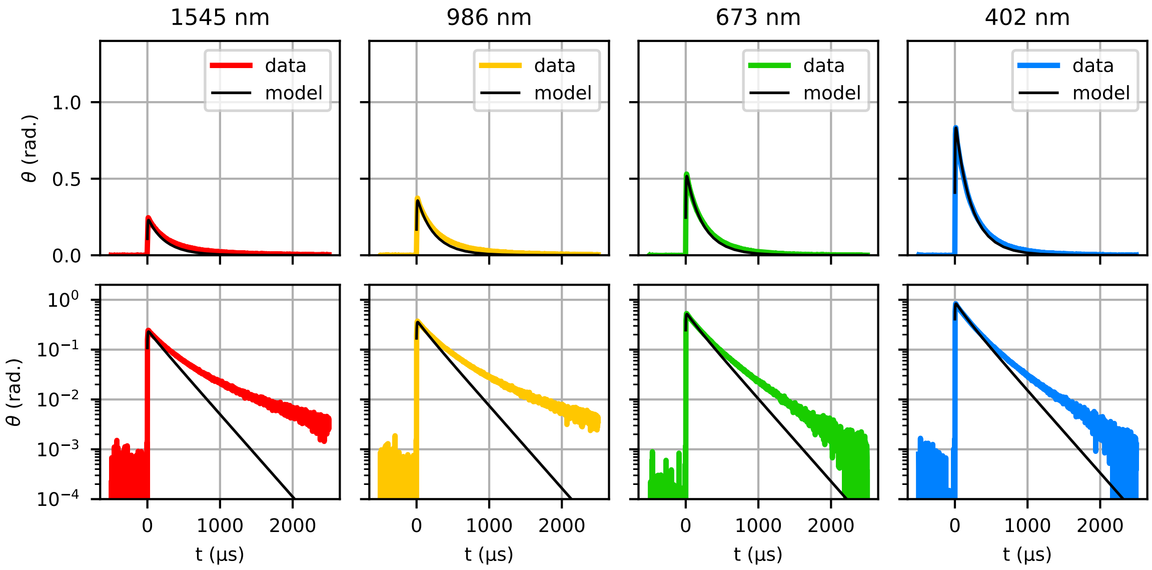

Figure C.14: LT139 at 120 mK, KID7, −96 dBm

Table C.2: LT139, 120 mK, T_{eff} with 402 nm peak fit

Parameter	KID1 −96 dBm	KID1 −100 dBm	KID1 −104 dBm	KID6 −92 dBm	KID6 −96 dBm	KID6 −100 dBm	KID6 −104 dBm
Q_c	1.49×10^5	1.44×10^5	1.42×10^5	1.22×10^5	1.15×10^5	1.13×10^5	1.11×10^5
$\hbar\omega_0$	20 µeV	20 µeV	20 µeV	21.2 µeV	21.2 µeV	21.2 µeV	21.2 µeV
$k_B T_0$	10.3 µeV	10.3 µeV	10.3 µeV	10.3 µeV	10.3 µeV	10.3 µeV	10.3 µeV
$k_B T$	19.4 µeV	19.5 µeV	19.5 µeV	18.4 µeV	18.8 µeV	18.9 µeV	19 µeV
V	12.4 µm^3	12.4 µm^3	12.4 µm^3	24.6 µm^3	24.6 µm^3	24.6 µm^3	24.6 µm^3
α_k	0.0292	0.0293	0.0293	0.0588	0.0591	0.0594	0.0593
τ_{esc}	0.161 ns	0.161 ns	0.161 ns	0.149 ns	0.149 ns	0.149 ns	0.149 ns
η_{pb}	0.509	0.58	0.618	0.459	0.562	0.618	0.678

Parameter	KID7 −88 dBm	KID7 −92 dBm	KID7 −96 dBm
Q_c	7.63×10^4	8.37×10^4	8.72×10^4
$\hbar\omega_0$	21.4 µeV	21.4 µeV	21.4 µeV
$k_B T_0$	10.3 µeV	10.4 µeV	10.4 µeV
$k_B T$	19.9 µeV	19.5 µeV	19.3 µeV
V	24.4 µm^3	24.4 µm^3	24.4 µm^3
α_k	0.0543	0.0548	0.055
τ_{esc}	0.214 ns	0.214 ns	0.214 ns
η_{pb}	0.419	0.462	0.51

Parameter	Value
d	50 nm
$k_B T_c$	103 µeV
$k_b T_D$	37.3 meV
τ_0	440 ns
τ_{pb}	0.28 ns
$\lambda(0)$	92 nm
N_0	1.72×10^4 µeV^{-1} µm^{-3}

C.2. LT165

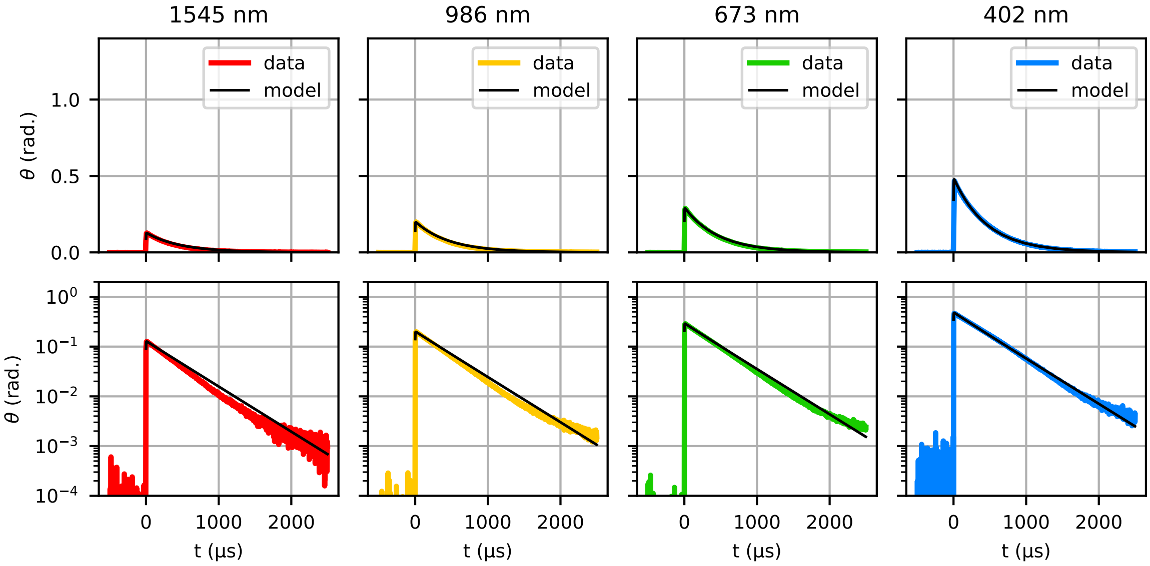

Figure C.15: LT165 at 120 mK, KID2, −85 dBm

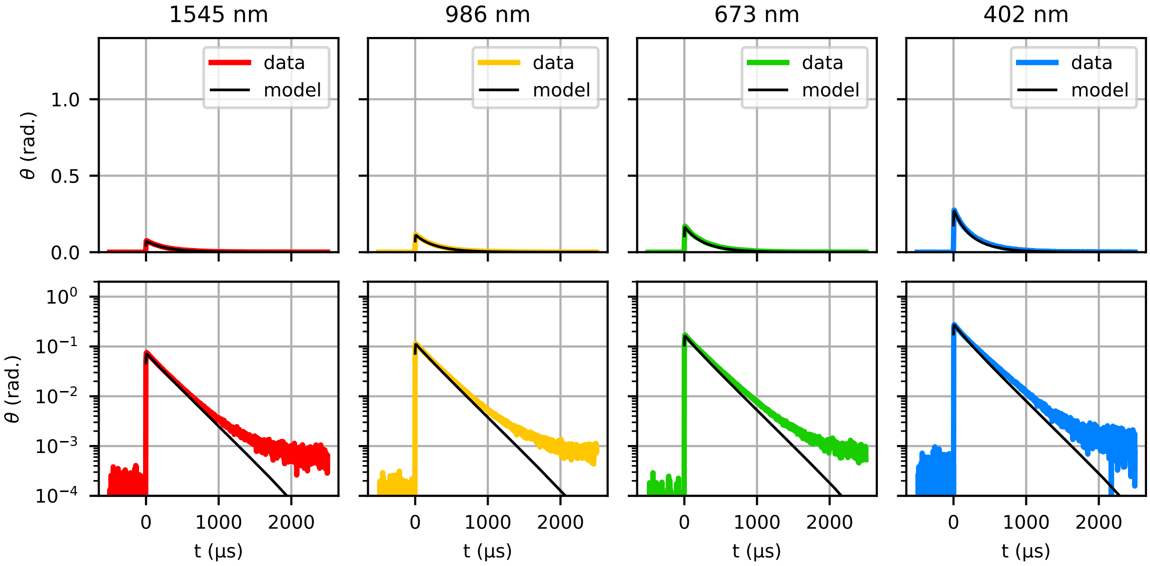

Figure C.16: LT165 at 120 mK, KID3, −83 dBm

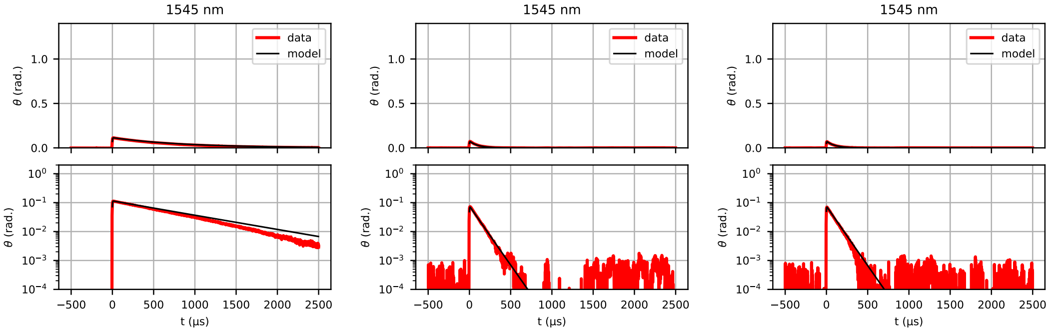

(a) KID2, −85 dBm (b) KID3, −79 dBm (c) KID3, −83 dBm

Figure C.17: Single photon response model results for LT165 at 250 mK.

Table C.3: LT165, 120 mK, T_{eff} with 402 nm peak fit and 250 mK, T_{eff} with GR lifetime

Parameter	KID2 120 mK −85 dBm	KID3 120 mK −83 dBm	KID2 250 mK −85 dBm	KID3 250 mK −79 dBm	KID3 250 mK −83 dBm
Q_c	4.76×10^4	3.8×10^4	4.76×10^4	4.14×10^4	3.8×10^4
$\hbar\omega_0$	17.8 µeV	18.6 µeV	17.8 µeV	18.6 µeV	18.6 µeV
$k_B T_0$	4.3 µeV	4.3 µeV	4.3 µeV	4.3 µeV	4.3 µeV
$k_B T$	24.4 µeV	19.6 µeV	22.7 µeV	21.8 µeV	21.8 µeV
α_k	0.0643	0.0587	0.0643	0.0548	0.0587
τ_{esc}	4.9 ns	0.138 ns	4.9 ns	0.138 ns	0.138 ns
η_{pb}	0.686	0.329	0.496	0.382	0.382

Parameter	Value
V	27 µm^3
d	50 nm
$k_B T_c$	108 µeV
$k_b T_D$	37.3 meV
τ_0	440 ns
τ_{pb}	0.28 ns
$\lambda(0)$	92 nm
N_0	1.72×10^4 µeV^{-1} µm^{-3}

D

GR Results

D.1. LT132

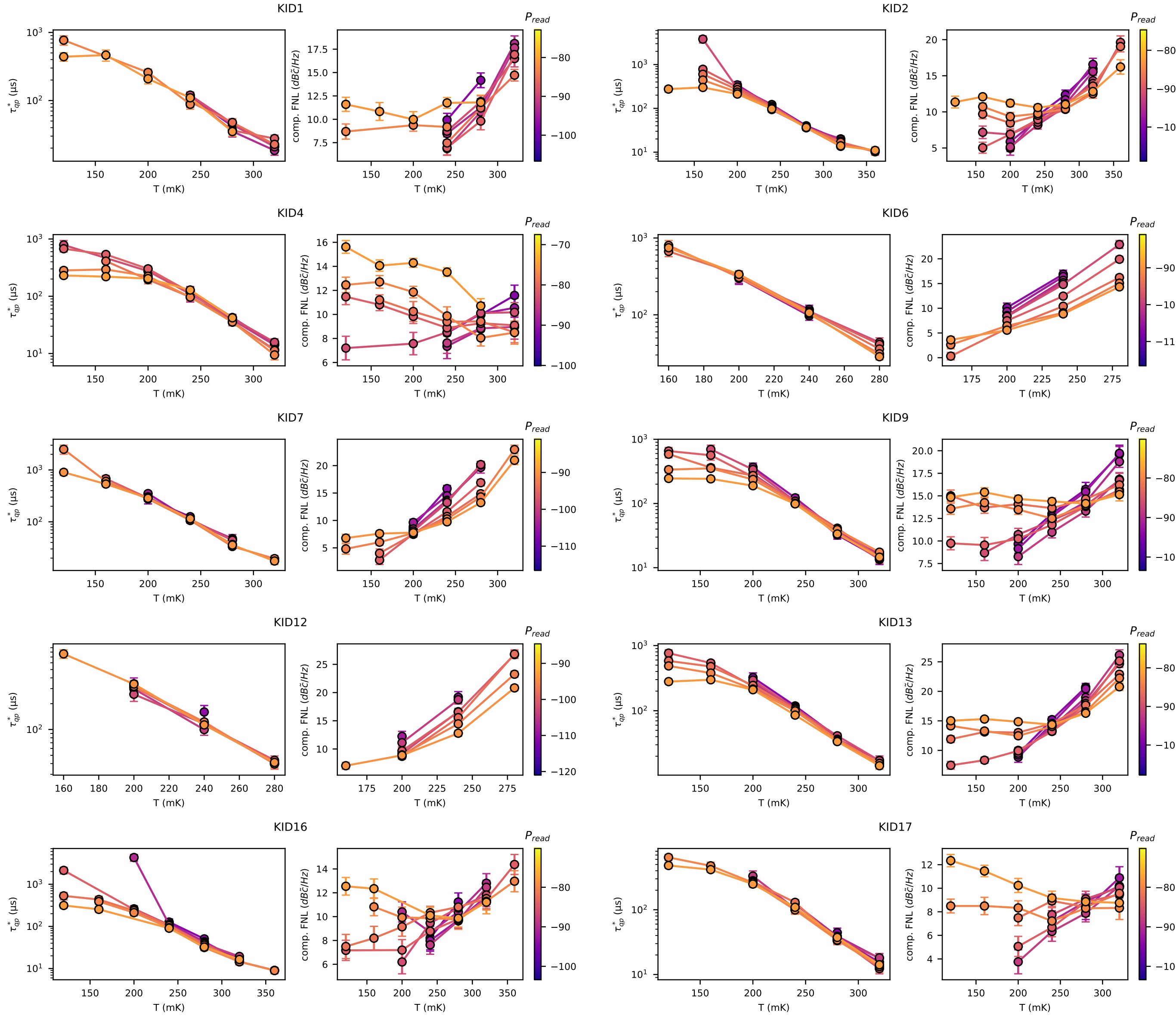

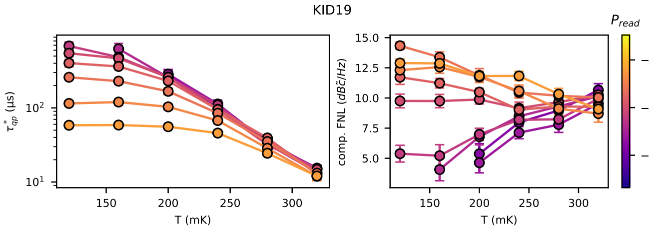
KID19
τ^*_{qp} (μs)
10^1
10^2
150 200 250 300
T (mK)
comp. FNL ($dB\tilde{c}/Hz$)
5.0 7.5 10.0 12.5 15.0
150 200 250 300
T (mK)
P_{read}
−70 −80 −90

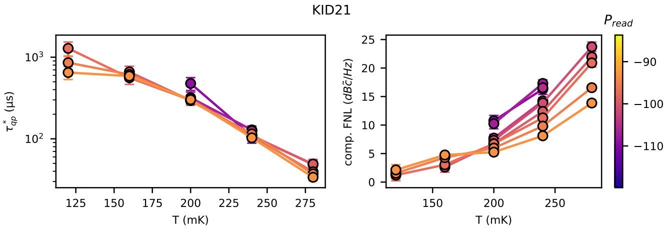
KID21
τ^*_{qp} (μs)
10^2
10^3
125 150 175 200 225 250 275
T (mK)
comp. FNL ($dB\tilde{c}/Hz$)
0 5 10 15 20 25
150 200 250
T (mK)
P_{read}
−90 −100 −110

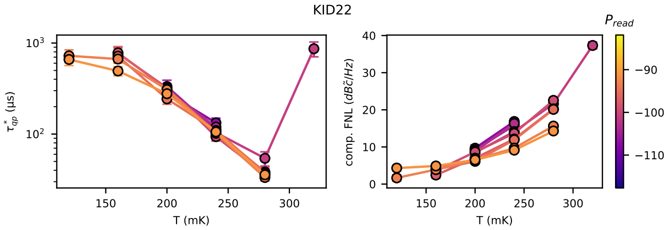
KID22
τ^*_{qp} (μs)
10^2
10^3
150 200 250 300
T (mK)
comp. FNL ($dB\tilde{c}/Hz$)
0 10 20 30 40
150 200 250 300
T (mK)
P_{read}
−90 −100 −110

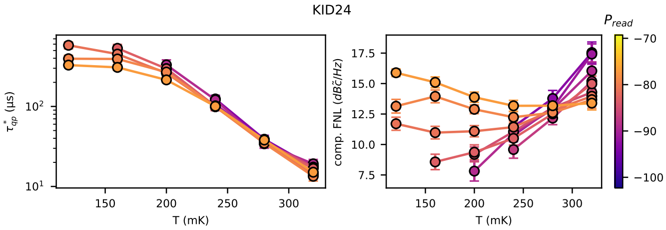
KID24
τ^*_{qp} (μs)
10^1
10^2
150 200 250 300
T (mK)
comp. FNL ($dB\tilde{c}/Hz$)
7.5 10.0 12.5 15.0 17.5
150 200 250 300
T (mK)
P_{read}
−70 −80 −90 −100

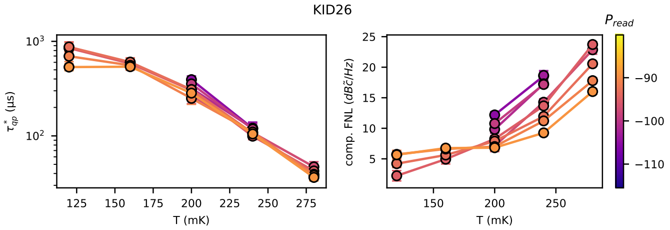
KID26
τ^*_{qp} (μs)
10^2
10^3
125 150 175 200 225 250 275
T (mK)
comp. FNL ($dB\tilde{c}/Hz$)
5 10 15 20 25
150 200 250
T (mK)
P_{read}
−90 −100 −110

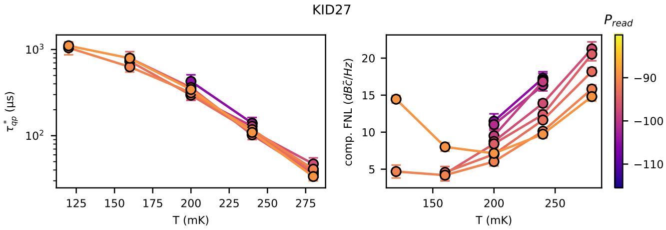
KID27
τ^*_{qp} (μs)
10^2
10^3
125 150 175 200 225 250 275
T (mK)
comp. FNL ($dB\tilde{c}/Hz$)
5 10 15 20
150 200 250
T (mK)
P_{read}
−90 −100 −110

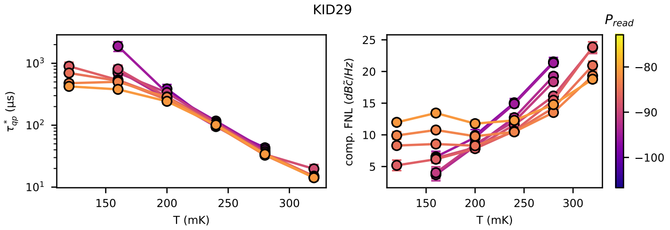
KID29
τ^*_{qp} (μs)
10^1
10^2
10^3
150 200 250 300
T (mK)
comp. FNL ($dB\tilde{c}/Hz$)
5 10 15 20 25
150 200 250 300
T (mK)
P_{read}
−80 −90 −100

D.2. LT139

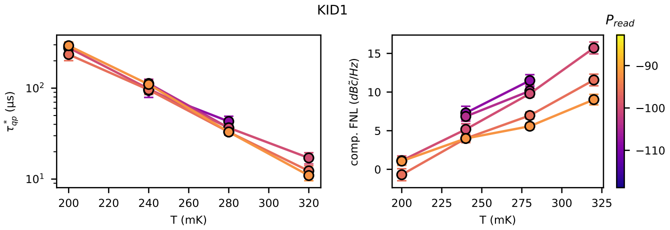
KID1
τ^*_{qp} (μs)
10^1
10^2
200 220 240 260 280 300 320
T (mK)
comp. FNL ($dB\tilde{c}/Hz$)
0 5 10 15
200 225 250 275 300 325
T (mK)
P_{read}
−90 −100 −110

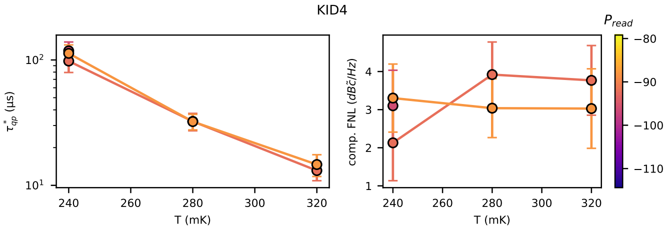
KID4
τ^*_{qp} (μs)
10^1
10^2
240 260 280 300 320
T (mK)
comp. FNL ($dB\tilde{c}/Hz$)
1 2 3 4
240 260 280 300 320
T (mK)
P_{read}
−80 −90 −100 −110

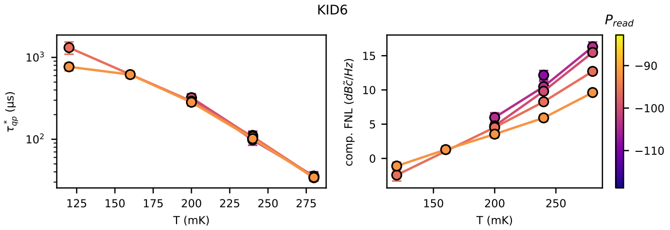
KID6
τ^*_{qp} (μs)
10^2
10^3
125 150 175 200 225 250 275
T (mK)
comp. FNL ($dB\tilde{c}/Hz$)
0 5 10 15
150 200 250
T (mK)
P_{read}
−90 −100 −110

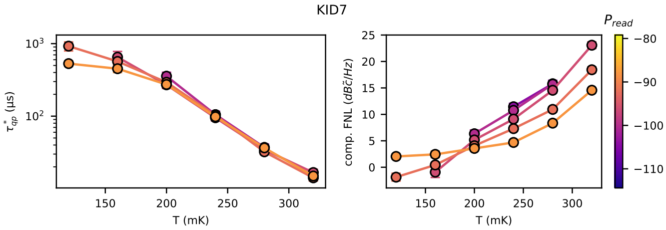
KID7
τ^*_{qp} (μs)
10^2
10^3
150 200 250 300
T (mK)
comp. FNL ($dB\tilde{c}/Hz$)
0 5 10 15 20 25
150 200 250 300
T (mK)
P_{read}
−80 −90 −100 −110

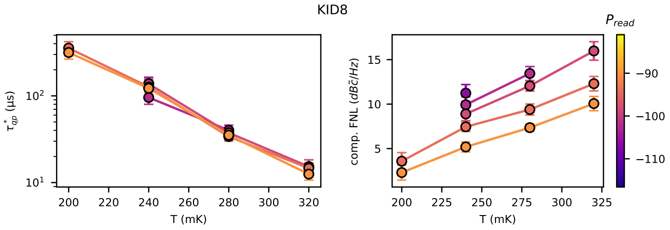
KID8
τ^*_{qp} (μs)
10^1
10^2
200 220 240 260 280 300 320
T (mK)
comp. FNL ($dB\tilde{c}/Hz$)
5 10 15
200 225 250 275 300 325
T (mK)
P_{read}
−90 −100 −110

D.3. LT145

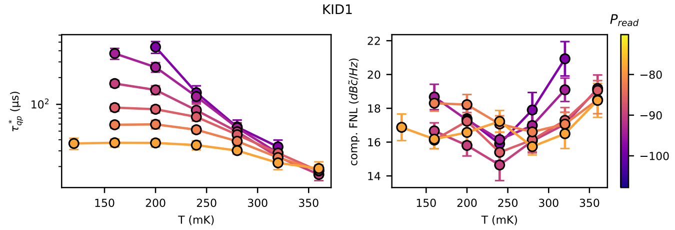

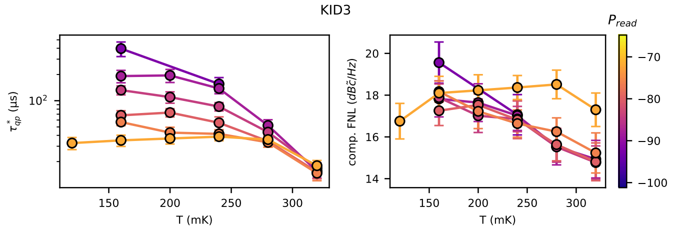

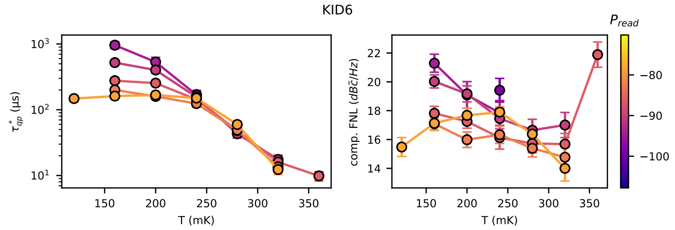

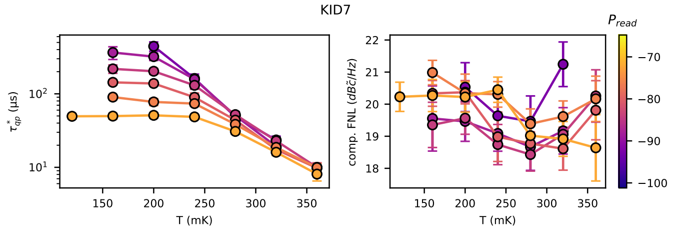

D.4. LT165

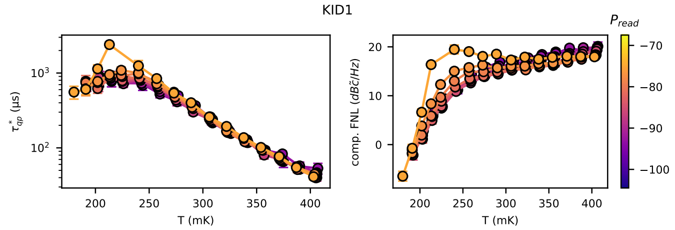

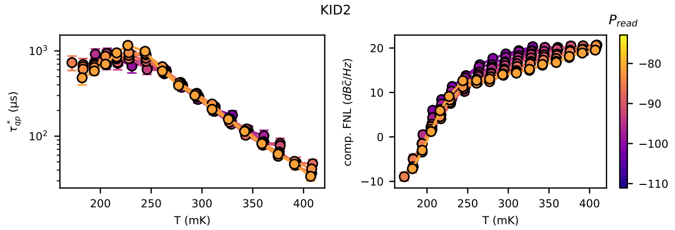

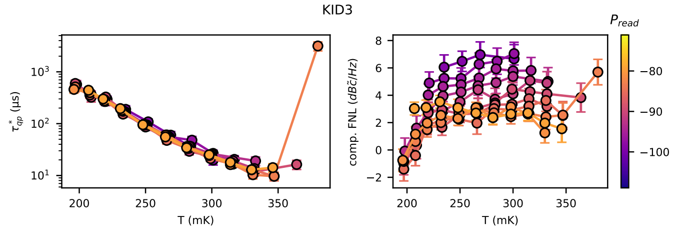

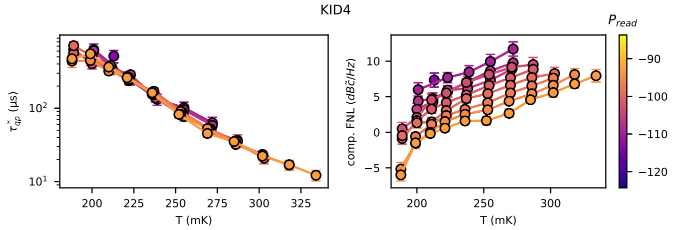

D.5. LT165W2

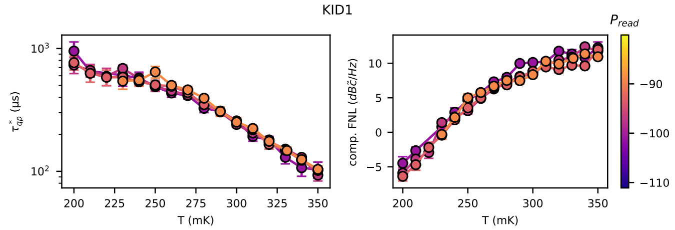

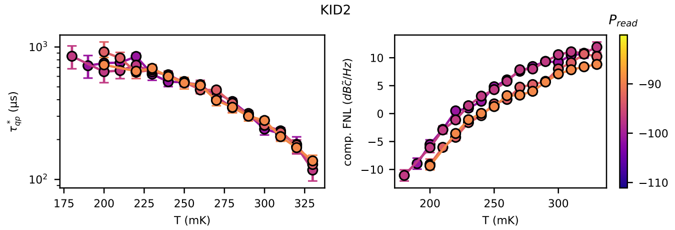

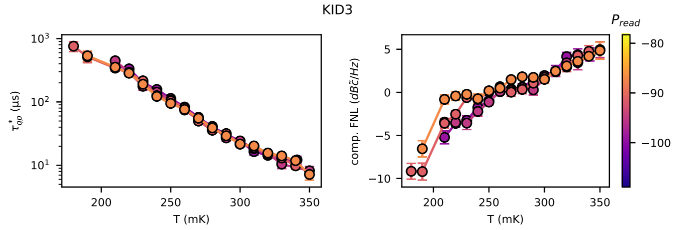

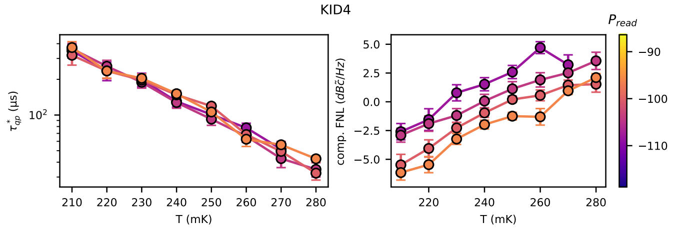

D.6. LT179

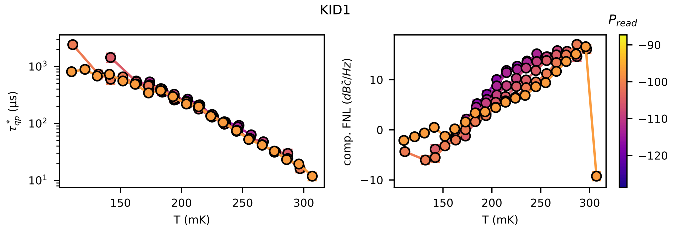

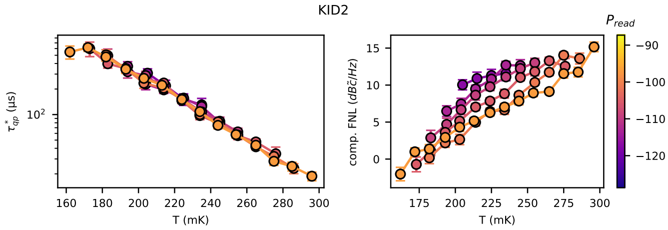

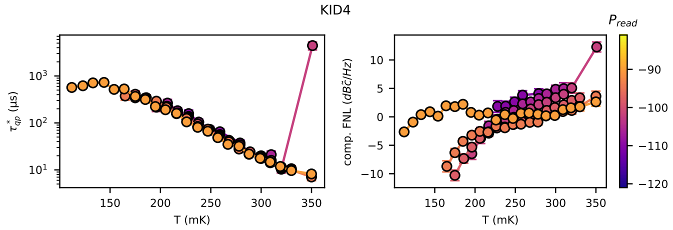

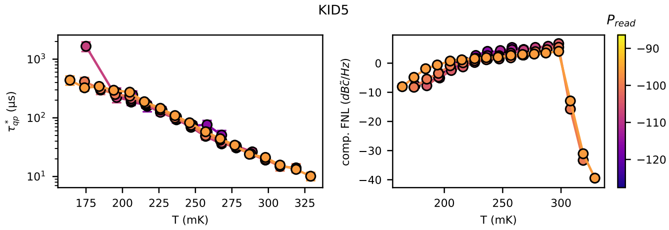

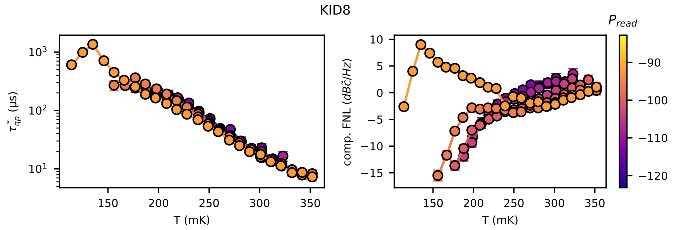

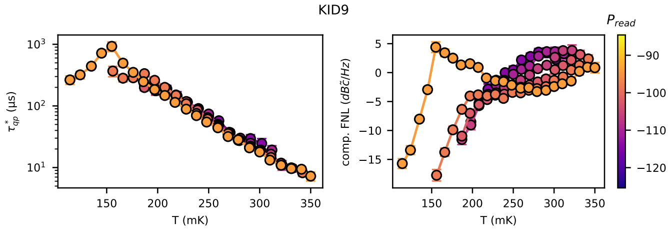

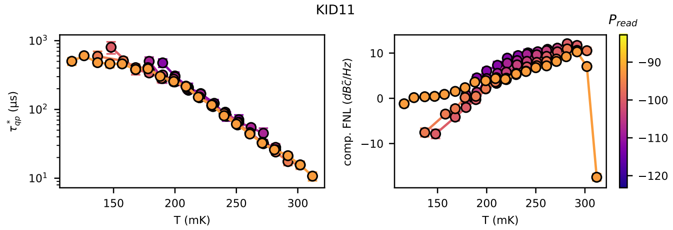

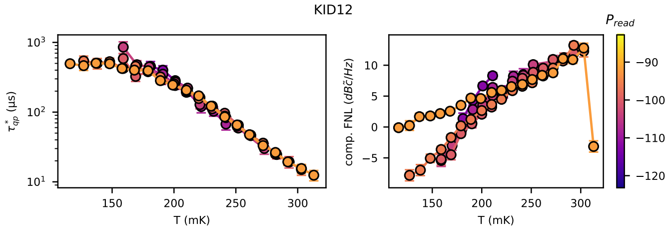

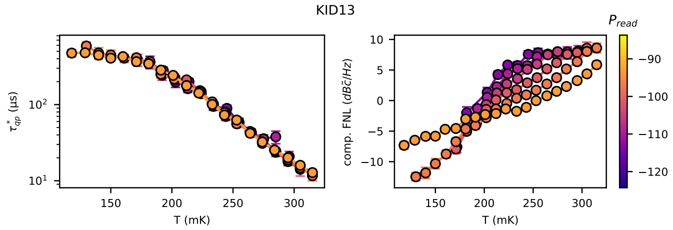

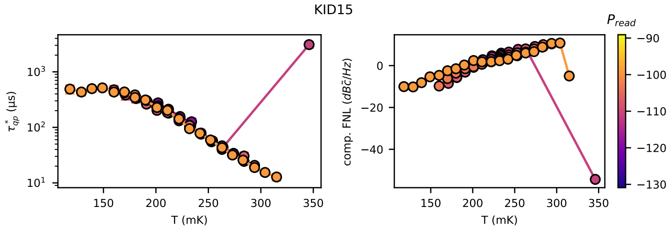

D.7. LT179Wide

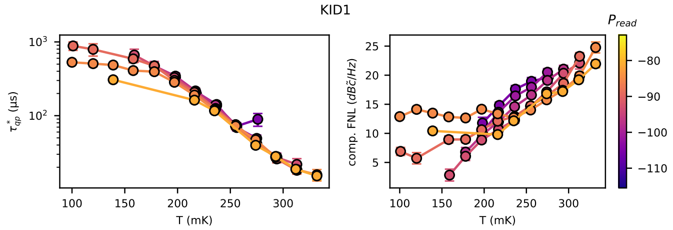

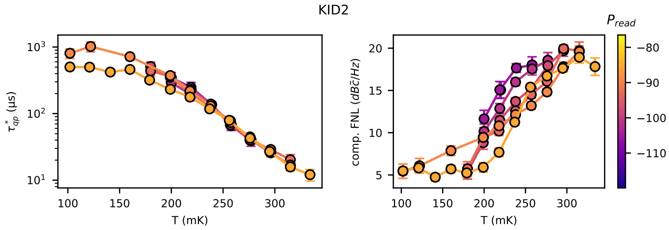

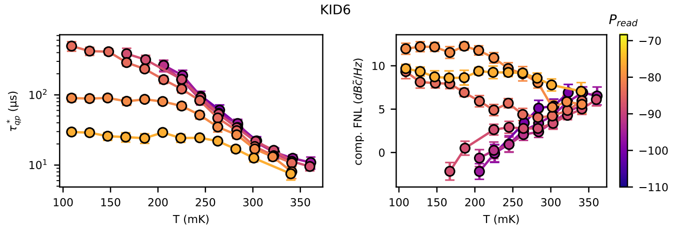

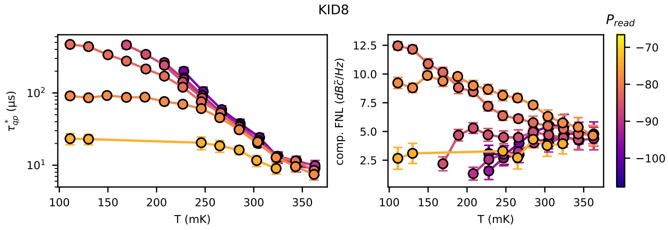

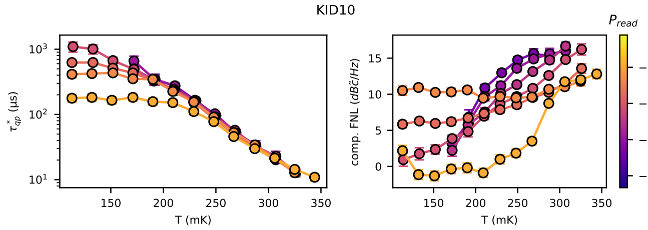
KID10
τ^*_{qp} (µs)
10^3
10^2
10^1
T (mK)
150
200
250
300
350
comp. FNL ($dB\bar{c}/Hz$)
15
10
5
0
P_{read}
−80
−90
−100
−110

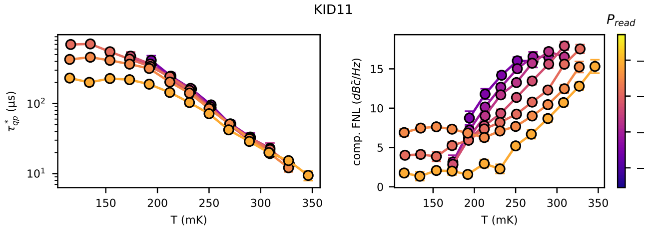
KID11
τ^*_{qp} (µs)
10^2
10^1
T (mK)
150
200
250
300
350
comp. FNL ($dB\bar{c}/Hz$)
15
10
5
0
P_{read}
−80
−90
−100
−110

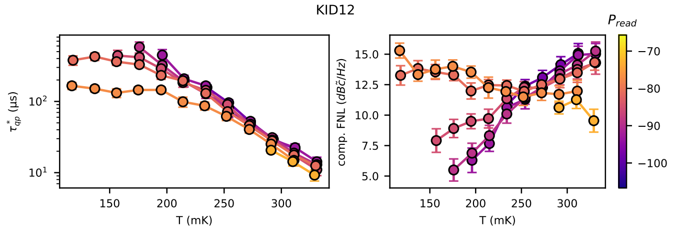
KID12
τ^*_{qp} (µs)
10^2
10^1
T (mK)
150
200
250
300
comp. FNL ($dB\bar{c}/Hz$)
15.0
12.5
10.0
7.5
5.0
P_{read}
−70
−80
−90
−100

Bibliography

[1] B. Mennesson, S. Gaudi, S. Seager, K. Cahoy, S. Domagal-Goldman, L. Feinberg, O. Guyon, J. Kasdin, C. Marois, D. Mawet, et al., in *Space Telescopes and Instrumentation 2016: Optical, Infrared, and Millimeter Wave* (International Society for Optics and Photonics, 2016), vol. 9904, p. 99040L.

[2] M. R. Bolcar, S. Aloezos, V. T. Bly, C. Collins, J. Crooke, C. D. Dressing, L. Fantano, L. D. Feinberg, K. France, G. Gochar, et al., in *UV/Optical/IR Space Telescopes and Instruments: Innovative Technologies and Concepts VIII* (International Society for Optics and Photonics, 2017), vol. 10398, p. 1039809.

[3] B. J. Rauscher, E. R. Canavan, S. H. Moseley, J. E. Sadleir, and T. Stevenson, Journal of Astronomical Telescopes, Instruments, and Systems **2**, 041212 (2016), ISSN 2329-4124, 2329-4221.

[4] A. Rothwarf and B. N. Taylor, Physical Review Letters **19**, 27 (1967).

[5] D. C. Mattis and J. Bardeen, Physical Review **111**, 412 (1958).

[6] P. J. de Visser, D. J. Goldie, P. Diener, S. Withington, J. J. A. Baselmans, and T. M. Klapwijk, Physical Review Letters **112**, 047004 (2014).

[7] P. J. de Visser, J. J. A. Baselmans, S. J. C. Yates, P. Diener, A. Endo, and T. M. Klapwijk, Applied Physics Letters **100**, 162601 (2012), ISSN 0003-6951.

[8] A. G. Kozorezov, A. A. Golubov, J. K. Wigmore, D. Martin, P. Verhoeve, R. A. Hijmering, and I. Jerjen, IEEE Transactions on Applied Superconductivity **19**, 440 (2009), ISSN 2378-7074.

[9] R. Barends, J. J. A. Baselmans, S. J. C. Yates, J. R. Gao, J. N. Hovenier, and T. M. Klapwijk, Physical Review Letters **100**, 257002 (2008).

[10] A. G. Kozorezov, A. A. Golubov, J. K. Wigmore, D. Martin, P. Verhoeve, R. A. Hijmering, and I. Jerjen, Physical Review B **78**, 174501 (2008).

[11] P. K. Day, H. G. LeDuc, B. A. Mazin, A. Vayonakis, and J. Zmuidzinas, Nature **425**, 817 (2003), ISSN 1476-4687.

[12] J. Baselmans, S. J. C. Yates, R. Barends, Y. J. Y. Lankwarden, J. R. Gao, H. Hoevers, and T. M. Klapwijk, Journal of Low Temperature Physics **151**, 524 (2008), ISSN 1573-7357.

[13] R. Adam, A. Adane, P. a. R. Ade, P. André, A. Andrianasolo, H. Aussel, A. Beelen, A. Benoît, A. Bideaud, N. Billot, et al., Astronomy & Astrophysics **609**, A115 (2018), ISSN 0004-6361, 1432-0746.

[14] A. Endo, K. Karatsu, Y. Tamura, T. Oshima, A. Taniguchi, T. Takekoshi, S. Asayama, T. J. L. C. Bakx, S. Bosma, J. Bueno, et al., Nature Astronomy **3**, 989 (2019), ISSN 2397-3366.

[15] A. Endo, K. Karatsu, A. P. Laguna, B. Mirzaei, R. Huiting, D. Thoen, V. Murugesan, S. J. C. Yates, J. Bueno, N. V. Marrewijk, et al., Journal of Astronomical Telescopes, Instruments, and Systems **5**, 035004 (2019), ISSN 2329-4124, 2329-4221.

[16] S. R. Meeker, B. A. Mazin, A. B. Walter, P. Strader, N. Fruitwala, C. Bockstiegel, P. Szypryt, G. Ulbricht, G. Coiffard, B. Bumble, et al., Publications of the Astronomical Society of the Pacific **130**, 065001 (2018), ISSN 1538-3873.

[17] I. Snellen, S. Albrecht, G. Anglada-Escude, I. Baraffe, P. Baudoz, W. Benz, J.-L. Beuzit, B. Biller, J. Birkby, A. Boccaletti, et al., Technical Report, European Space Agency (ESA) (2019).

[18] N. Zobrist, G. Coiffard, B. Bumble, N. Swimmer, S. Steiger, M. Daal, G. Collura, A. B. Walter, C. Bockstiegel, N. Fruitwala, et al., Applied Physics Letters **115**, 213503 (2019), ISSN 0003-6951.

[19] M. Tinkham, *Introduction to Superconductivity* (Courier Corporation, 2004), ISBN 978-0-486-13472-7.

[20] P. J. de Visser, Ph.D. dissertation, Delft University of Technology, Delft (2014).

[21] J. Zmuidzinas, Annual Review of Condensed Matter Physics **3**, 169 (2012), ISSN 1947-5454, 1947-5462.

[22] J. Baselmans, Journal of Low Temperature Physics **167**, 292 (2012), ISSN 1573-7357.

[23] R. Barends, Ph.D. thesis, Delft University of Technology, Delft (2009).

[24] J. Gao, Ph.D. thesis, California Institute of Technology (2008).

[25] G. Catelani, R. J. Schoelkopf, M. H. Devoret, and L. I. Glazman, Physical Review B **84**, 064517 (2011).

[26] B. A. Mazin, B. Bumble, S. R. Meeker, K. O'Brien, S. McHugh, and E. Langman, Optics Express **20**, 1503 (2012), ISSN 1094-4087.

[27] K. D. Irwin, Ph.D. dissertation, Stanford University (1995).

[28] M. E. Eckart, Ph.D. dissertation, California Institute of Technology (2007).

[29] J. Bardeen, L. N. Cooper, and J. R. Schrieffer, Physical Review **106**, 162 (1957).

[30] J. Bardeen, L. N. Cooper, and J. R. Schrieffer, Physical Review **108**, 1175 (1957).

[31] T. Guruswamy, Ph.D. thesis, University of Cambridge, Cambridge (2018).

[32] J. R. Hook and H. E. Hall, *Solid State Physics* (John Wiley & Sons, 2013), ISBN 978-1-118-79088-5.

[33] T. Guruswamy, D. J. Goldie, and S. Withington, Superconductor Science and Technology **27**, 055012 (2014), ISSN 0953-2048.

[34] F. London, H. London, and F. A. Lindemann, Proceedings of the Royal Society of London. Series A - Mathematical and Physical Sciences **149**, 71 (1935).

[35] J. J. Hauser, Physical Review B **10**, 2792 (1974).

[36] S. B. Kaplan, C. C. Chi, D. N. Langenberg, J. J. Chang, S. Jafarey, and D. J. Scalapino, Physical Review B **14**, 4854 (1976).

[37] C. M. Wilson and D. E. Prober, Physical Review B **69**, 094524 (2004).

[38] S. B. Kaplan, Journal of Low Temperature Physics **37**, 343 (1979), ISSN 1573-7357.

[39] J. Gao, J. Zmuidzinas, A. Vayonakis, P. Day, B. Mazin, and H. Leduc, Journal of Low Temperature Physics **151**, 557 (2008), ISSN 1573-7357.

[40] R. M. J. Janssen, A. Endo, P. J. de Visser, T. M. Klapwijk, and J. J. A. Baselmans, Applied Physics Letters **105**, 193504 (2014), ISSN 0003-6951.

[41] R. L. Kautz, Journal of Applied Physics **49**, 308 (1978), ISSN 0021-8979.

[42] R. F. Broom and P. Wolf, Physical Review B **16**, 3100 (1977).

[43] B. A. Mazin, Ph.D. dissertation, California Institute of Technology (2005).

[44] D. M. Pozar, *Microwave Engineering, 4th Edition* (Wiley, 2011), ISBN 978-1-118-21363-6.

[45] A. G. Kozorezov, A. F. Volkov, J. K. Wigmore, A. Peacock, A. Poelaert, and R. den Hartog, Physical Review B **61**, 11807 (2000).

[46] P. J. de Visser, J. J. A. Baselmans, P. Diener, S. J. C. Yates, A. Endo, and T. M. Klapwijk, Physical Review Letters **106**, 167004 (2011).

[47] D. J. Goldie and S. Withington, Superconductor Science and Technology **26**, 015004 (2012), ISSN 0953-2048.

[48] H. K. Leung, J. P. Carbotte, D. W. Taylor, and C. R. Leavens, Canadian Journal of Physics **54**, 1585 (1976), ISSN 0008-4204.

[49] C. C. Chi and J. Clarke, Physical Review B **19**, 4495 (1979).

[50] W. Eisenmenger, K. Laß mann, H. J. Trumpp, and R. Krauß, Applied physics **11**, 307 (1976), ISSN 1432-0630.

[51] A. Kozorezov, Journal of Low Temperature Physics **167**, 473 (2012), ISSN 1573-7357.

[52] P. J. de Visser, S. J. C. Yates, T. Guruswamy, D. J. Goldie, S. Withington, A. Neto, N. Llombart, A. M. Baryshev, T. M. Klapwijk, and J. J. A. Baselmans, Applied Physics Letters **106**, 252602 (2015), ISSN 0003-6951.

[53] J. Wenner, R. Barends, R. C. Bialczak, Y. Chen, J. Kelly, E. Lucero, M. Mariantoni, A. Megrant, P. J. J. O'Malley, D. Sank, et al., Applied Physics Letters **99**, 113513 (2011), ISSN 0003-6951.

[54] J. Gao, M. Daal, A. Vayonakis, S. Kumar, J. Zmuidzinas, B. Sadoulet, B. A. Mazin, P. K. Day, and H. G. Leduc, Applied Physics Letters **92**, 152505 (2008), ISSN 0003-6951.

[55] J. Baselmans, S. Yates, P. Diener, and P. de Visser, Journal of Low Temperature Physics **167**, 360 (2012), ISSN 1573-7357.

[56] J. Bueno, P. J. de Visser, S. Doyle, and J. J. A. Baselmans, Journal of Low Temperature Physics **176**, 1089 (2014), ISSN 1573-7357.

[57] P. J. de Visser, J. J. A. Baselmans, J. Bueno, N. Llombart, and T. M. Klapwijk, Nature Communications **5**, 3130 (2014), ISSN 2041-1723.

[58] R. Barends, J. Wenner, M. Lenander, Y. Chen, R. C. Bialczak, J. Kelly, E. Lucero, P. O'Malley, M. Mariantoni, D. Sank, et al., Applied Physics Letters **99**, 113507 (2011), ISSN 0003-6951.

[59] A. Fyhrie, P. Day, J. Glenn, H. Leduc, C. McKenney, J. Perido, and J. Zmuidzinas, Journal of Low Temperature Physics (2020), ISSN 1573-7357.

[60] J. Gao, J. Zmuidzinas, B. A. Mazin, H. G. LeDuc, and P. K. Day, Applied Physics Letters **90**, 102507 (2007), ISSN 0003-6951.

[61] A. G. Kozorezov, J. K. Wigmore, D. Martin, P. Verhoeve, and A. Peacock, Physical Review B **75**, 094513 (2007).

[62] R. Kubo, Reports on Progress in Physics **29**, 255 (1966), ISSN 0034-4885.

[63] K. Van Vliet and J. Fassett, Academic Press, New York (1965).

[64] K. Gray, ed., *Nonequilibrium Superconductivity, Phonons, and Kapitza Boundaries*, Nato Science Series B: (Springer US, 1981), ISBN 978-0-306-40720-8.

[65] M. Lax, Reviews of Modern Physics **32**, 25 (1960).

[66] K. M. Van Vliet, Physical Review **133**, A1182 (1964).

[67] K. Karatsu, A. Endo, J. Bueno, P. J. de Visser, R. Barends, D. J. Thoen, V. Murugesan, N. Tomita, and J. J. A. Baselmans, Applied Physics Letters **114**, 032601 (2019), ISSN 0003-6951.

[68] I. Florescu, *Probability and Stochastic Processes* (John Wiley & Sons, 2014), ISBN 978-1-118-59313-4.

[69] R. M. J. Janssen, J. J. A. Baselmans, A. Endo, L. Ferrari, S. J. C. Yates, A. M. Baryshev, and T. M. Klapwijk, Applied Physics Letters **103**, 203503 (2013), ISSN 0003-6951.

[70] P. Chubov, V. Eremenko, and Y. A. Pilipenko, SOV PHYS JETP **28**, 389 (1969).

[71] J.-J. Chang and D. J. Scalapino, Physical Review B **15**, 2651 (1977).

[72] J.-J. Chang and D. J. Scalapino, Journal of Low Temperature Physics **31**, 1 (1978), ISSN 1573-7357.

[73] A. Anthore, H. Pothier, and D. Esteve, Physical Review Letters **90**, 127001 (2003).

[74] L. J. Swenson, P. K. Day, B. H. Eom, H. G. Leduc, N. Llombart, C. M. McKenney, O. Noroozian, and J. Zmuidzinas, Journal of Applied Physics **113**, 104501 (2013), ISSN 0021-8979.

[75] C. Wang, Y. Y. Gao, I. M. Pop, U. Vool, C. Axline, T. Brecht, R. W. Heeres, L. Frunzio, M. H. Devoret, G. Catelani, et al., Nature Communications **5**, 1 (2014), ISSN 2041-1723.

[76] M. Taupin, I. M. Khaymovich, M. Meschke, A. S. Mel'nikov, and J. P. Pekola, Nature Communications **7**, 1 (2016), ISSN 2041-1723.

[77] S. Friedrich, K. Segall, M. C. Gaidis, C. M. Wilson, D. E. Prober, A. E. Szymkowiak, and S. H. Moseley, Applied Physics Letters **71**, 3901 (1997), ISSN 0003-6951.

[78] K. D. Irwin, S. W. Nam, B. Cabrera, B. Chugg, and B. A. Young, Review of Scientific Instruments **66**, 5322 (1995), ISSN 0034-6748, 1089-7623.

[79] A. G. Kozorezov, J. K. Wigmore, A. Peacock, A. Poelaert, P. Verhoeve, R. den Hartog, and G. Brammertz, Applied Physics Letters **78**, 3654 (2001), ISSN 0003-6951.

[80] A. G. Kozorezov, R. A. Hijmering, G. Brammertz, J. K. Wigmore, A. Peacock, D. Martin, P. Verhoeve, A. A. Golubov, and H. Rogalla, Physical Review B **77**, 014501 (2008).

[81] R. A. Hijmering, A. G. Kozorezov, A. A. Golubov, P. Verhoeve, D. D. E. Martin, J. K. Wigmore, and I. Jerjen, IEEE Transactions on Applied Superconductivity **19**, 423 (2009), ISSN 2378-7074.

[82] J. Gao, M. R. Vissers, M. O. Sandberg, F. C. S. da Silva, S. W. Nam, D. P. Pappas, D. S. Wisbey, E. C. Langman, S. R. Meeker, B. A. Mazin, et al., Applied Physics Letters **101**, 142602 (2012), ISSN 0003-6951.

[83] R. Barends, S. van Vliet, J. J. A. Baselmans, S. J. C. Yates, J. R. Gao, and T. M. Klapwijk, Physical Review B **79**, 020509 (2009).

[84] L. Grünhaupt, N. Maleeva, S. T. Skacel, M. Calvo, F. Levy-Bertrand, A. V. Ustinov, H. Rotzinger, A. Monfardini, G. Catelani, and I. M. Pop, Physical Review Letters **121**, 117001 (2018).

[85] D. J. Goldie, N. E. Booth, C. Patel, and G. L. Salmon, Physical Review Letters **64**, 954 (1990).

[86] E. M. Levenson-Falk, F. Kos, R. Vijay, L. Glazman, and I. Siddiqi, Physical Review Letters **112**, 047002 (2014).

[87] R.-P. Riwar, A. Hosseinkhani, L. D. Burkhart, Y. Y. Gao, R. J. Schoelkopf, L. I. Glazman, and G. Catelani, Physical Review B **94**, 104516 (2016).

[88] L. Yu, Chin. J. Phys. (Peking) (Engl. Transl.) **Vol: 21** (1965).

[89] H. Shiba, Progress of Theoretical Physics **40**, 435 (1968), ISSN 0033-068X.

[90] A. I. Rusinov, Soviet Journal of Experimental and Theoretical Physics **29**, 1101 (1969), ISSN 1063-7761.

[91] Y. V. Fominov, M. Houzet, and L. I. Glazman, Physical Review B **84**, 224517 (2011).

[92] A. A. Abrikosov and L. P. Gor'kov, Sov. Phys. - JETP (Engl. Transl.); (United States) **9:1** (1959).

[93] A. A. Abrikosov and L. P. Gor'kov, Sov. Phys. - JETP (Engl. Transl.); (United States) **8:6** (1959).

[94] J. Zittartz, A. Bringer, and E. Müller-Hartmann, Solid State Communications **10**, 513 (1972), ISSN 0038-1098.

[95] P. W. Anderson, Journal of Physics and Chemistry of Solids **11**, 26 (1959), ISSN 0022-3697.

[96] A. Bespalov, M. Houzet, J. S. Meyer, and Y. V. Nazarov, Physical Review Letters **117**, 117002 (2016).

[97] A. Ghosal, M. Randeria, and N. Trivedi, Physical Review B **65**, 014501 (2001).

[98] G. C. O'Neil, D. R. Schmidt, N. A. Tomlin, and J. N. Ullom, Journal of Applied Physics **107**, 093903 (2010), ISSN 0021-8979.

[99] A. B. Kaiser, Journal of Physics C: Solid State Physics **3**, 410 (1970), ISSN 0022-3719.

[100] R. C. Dynes, V. Narayanamurti, and J. P. Garno, Physical Review Letters **41**, 1509 (1978).

[101] A. I. Larkin and Y. N. Ovchinnikov, Soviet Journal of Experimental and Theoretical Physics **34**, 1144 (1972).

[102] A. Bespalov, M. Houzet, J. S. Meyer, and Y. V. Nazarov, Physical Review B **93**, 104521 (2016).

[103] M. V. Feigel'man and M. A. Skvortsov, Physical Review Letters **109**, 147002 (2012).

[104] A. A. Bespalov, Physical Review B **100**, 094507 (2019).

[105] G. O'Neil, D. Schmidt, N. A. Miller, J. N. Ullom, A. Williams, G. B. Arnold, and S. T. Ruggiero, Physical Review Letters **100**, 056804 (2008).

[106] A. Poelaert, A. G. Kozorezov, A. Peacock, and J. K. Wigmore, Physical Review Letters **82**, 1257 (1999).

[107] J. Zittartz and E. Müller-Hartmann, Zeitschrift für Physik A Hadrons and nuclei **232**, 11 (1970), ISSN 0939-7922.

[108] E. Müller-Hartmann and J. Zittartz, Physical Review Letters **26**, 428 (1971).